Functionally Graded Additive Manufacturing of Inconel625 and CuCrZr Alloys

by

Ali Zardoshtian

A thesis

presented to the University of Waterloo

in fulfillment of the

thesis requirement for the degree of

Doctor of Philosophy

in

Mechanical and Mechatronics Engineering

Waterloo, Ontario, Canada, 2025

© Ali Zardoshtian 2025

Examining Committee Membership

The following served on the Examining Committee for this thesis. The decision of the Examining Committee is by majority vote.

External Examiner	SOMAYEH PASEBANI, Ph.D. Associate Professor, Oregon State University
Supervisor	EHSAN TOYSERKANI, Ph.D. Professor, University of Waterloo
Supervisor	HAMID JAHED, Ph.D. Professor, University of Waterloo
Internal Member	Elliot Biro, Ph.D. Associate Professor, University of Waterloo
Internal Member	Marco Alfano, PhD. Professor (Adjunct), University of Waterloo
Internal-External Member	Shirley Tang, Ph.D. Professor, University of Waterloo

Author's Declaration

This thesis consists of material all of which I authored or co-authored: see Statement of Contributions included in this thesis. This is a true copy of the thesis, including any required final revisions, as accepted by the examiners.

I understand that my thesis may be made electronically available to the public.

Statement of contributions

I would like to acknowledge my co-authors who contributed to the research described in this thesis:

Prof. Ehsan Toyserkani: Supervision of the research, providing the original idea for the current thesis, editing and reviewing papers, providing experimental facilities, and funding.

Prof. Hamid Jahed: Supervision of the research, providing the original idea for the current thesis, editing and reviewing papers, and providing experimental facilities.

Dr. Reza Esmaeilizadeh: Providing technical and editorial feedback in the preparation of Chapters 3 & 5 and technical training for carrying out the materials characterization.

Dr. Mohsen Keshavarz: Providing technical and editorial feedback in the preparation of Chapters 3, 5, and 6.

Dr. Mazyar Ansari: Providing editorial feedback in the preparation of Chapter 3.

Dr. Ali Keshavarzkermani: Providing editorial feedback in the preparation of Chapter 3.

Dr. Mahyar Hasanabadi: Providing editorial feedback in the preparation of Chapters 6.

Dr. Jakub Preis: Providing Thermo-Calc software analysis for Chapter 5.

Mr. Ali Rezaei: Providing technical and editorial feedback in the preparation of Chapters 5 & 6.

Abstract

Significant advancements over the past decade have transformed metal additive manufacturing from a prototyping tool into a full-fledged production process. These developments have enabled the use of lighter, stronger, and more cost-effective additively manufactured components in aerospace, automotive, and energy industries. As qualification efforts progress, research is increasingly focused on advanced capabilities such as combining multiple alloys within a single build to create functionally graded structures, eliminating the need for additional joints. In that regard, Functionally Graded Additive Manufacturing (FGAM) is a layer-by-layer process that varies composition and/or microstructure within a component to achieve locally tailored properties. A new class of FGAMs combining highly heat-conductive CuCrZr alloy with Inconel 625 superalloy has gained considerable attention for aerospace applications, leveraging the former's high heat dissipation and the latter's excellent mechanical properties. This can be done through the Laser Directed Energy Deposition (L-DED) technique; however, the implementation remains a material-processing challenge due to the noticeable thermophysical mismatch between the two alloys.

This dissertation provides a comprehensive investigation into the FGAM of IN625-CuCrZr alloys, encircling process parameter optimization, gradient path development, and microstructural and defect formation analysis through advanced characterization, CALPHAD-based thermodynamic simulations, and finite element modeling. In that regard, process parameters have been optimized from single-track to multilayer scales, and the effect of process parameters on the microstructure has been studied, more specifically on CuCrZr alloy as there was a big gap in the literature.

Further, the FGAM of IN625-CuCrZr has been exercised for two geometries of thin wall and cuboid, incorporating both sharp and gradual compositional transitions. Sharp transitions led to delamination at the interface, while gradual transitions resulted in structurally sound builds. In the gradual transition zone, the presence of a metastable miscibility gap between the liquid of the two alloys led to the formation of distinct Cu-lean and Cu-rich phases in the microstructure, a phenomenon predicted through CALPHAD-based thermodynamic simulations. The formation of solidification cracking in the gradient region of the cuboid geometry was further investigated using Kou's cracking susceptibility criterion.

In support of these findings, a multi-step numerical investigation of heat transfer in both thin wall and cuboid geometries was conducted using finite element analysis. First, a hybrid statistical–numerical thermal model was developed and implemented in the scale of single tracks through user-defined subroutines (DFLUX, USDFLD, and FILM) in Abaqus software. This model enabled high-fidelity prediction of melt pool geometry and thermal history and was validated against experimental melt pool dimensions and in-situ thermocouple measurements. Subsequently, the validated heat source model was used to simulate the thermal behavior during FGAM processing of both geometries. The thermal simulations highlighted the critical role of geometry on cooling rates and temperature distributions, providing deeper understanding into cracking behavior and how geometry-dependent thermal history influence microstructure and defect formation during FGAM of IN625-CuCrZr alloys.

Overall, this work establishes a robust experimental–computational framework for FGAM of dissimilar alloys using L-DED process. It introduces a scalable strategy for depositing functionally graded IN625–CuCrZr structures with controlled transitions and minimized defects. The modeling and characterization approaches developed here can be extended to other material systems, while the insights into miscibility gap, solidification behavior, and cracking mechanisms lay the groundwork for future microstructure design and process control in metal additive manufacturing.

Acknowledgements

The accomplishment of this research would not have been achievable without the assistance and support of many individuals, to whom I extend my sincere gratitude.

First, I extend my profound appreciation to my supervisor, Prof. Ehsan Toyserkani, for his invaluable guidance and kind support throughout the completion of my PhD studies at the University of Waterloo. In the same vein, I extend my heartfelt appreciation to Prof. Hamid Jahed, my co-supervisor, for his priceless guidance and encompassing mentorship during this journey.

I express my gratitude to my lab members in the Multi Scale Additive Manufacturing Lab, Dr. Mohsen Keshavarz, Dr. Reza Esmaeilizadeh, Dr. Mazyar Ansari, Dr. Ali Keshavarzkermani, Mr. Ali Rezaei, Mr. Hamid Aghajani for their friendly support and advice.

In addition, I acknowledge the support from Mr. Amirsalar Anousheh and Dr. Bahareh Marzbanrad from FATSLAB for helping with the XRD and Residual stress tests.

Furthermore, I gratefully acknowledge the financial support provided by the Government of Ontario through the Ontario Graduate Scholarship (OGS) throughout my PhD studies.

Lastly, and most importantly, I extend my deepest gratitude to my beloved wife and mother. Their kind support, patience, and encouragement have helped me a lot throughout this journey.

Dedication

To the heart of a beloved WIFE, Alaleh, whose unwavering grace unveiled the true power of love;

To the presence of a brave MOTHER, whose endless support has cultivated a life of purpose;

And to the soul of a benevolent FATHER, whose memory will forever be cherished;

Table of Contents

List of Figures xiii

Chapter 1 : Introduction 1

1.1 Motivation 1

1.2 Objectives 2

1.3 Outline of the thesis 2

Chapter 2 : Background & Literature Review 5

2.1 Functionally graded materials 5

2.1.1 Types and Manufacturing methods 5

2.1.2 Additive Manufacturing of Functionally Graded Materials 7

2.2 Metallic systems in functionally graded additive manufacturing 10

2.2.1 Copper to Nickel-based superalloys gradient 11

2.3 Functionally graded additive manufacturing of Inconel 625-CuCrZr 11

2.3.1 Additive manufacturing of CuCrZr 12

2.3.2 Additive manufacturing of Inconel 625 14

2.3.3 Feasibility and challenges from the metallurgical aspect 15

2.3.4 Feasibility and challenges from the process aspect 17

2.4 X-ray diffraction for phase identification and residual stress measurement 18

2.5 Thermal and thermomechanical modeling of additive manufacturing process 21

2.5.1 Thermal Equilibrium 21

2.5.2 The Heat Input Model 22

2.5.3 The mechanical model 23

2.6 Summary 23

Chapter 3 : Experimental analysis and statistical optimization of additive manufacturing of CuCrZr and Inconel 625 powders 24

3.1 Introduction 24

3.2 Laser directed energy deposition of CuCrZr powders 24

3.2.1 Material and methods 25

3.2.2 Results and discussions; single tracks 28

3.2.3 Results and discussions; cuboid geometry 36
3.3 Laser directed energy deposition of IN625 powders 51
3.3.1 Single-track deposition and optimization 51
3.3.2 multitrack single-layer 52
3.3.3 multilayer cuboid buildup and microstructure 53
3.4 Summary and conclusions 54
Chapter 4 : Development of Inconel 625-CuCrZr gradient 55
4.1 Introduction 55
4.2 FGAM of Inconel 625- CuCrZr 55
4.2.1 Powders 55
4.2.2 L-DED processing setup 56
4.2.3 Fabrication approach 57
4.2.4 Prototypes macroscale perspective 59
4.3 Summary 61
Chapter 5 : Insights into Microstructural Evolution in Functionally Graded Additive Manufacturing of IN625–CuCrZr Alloys 63
5.1 Introduction 63
5.2 Methodology 63
5.2.1 Characterization techniques 64
5.2.2 Thermodynamic simulations 65
5.3 Results and Discussions 66
5.3.1 Overall view of FGAM-made microstructure 66
5.3.2 Compositional transition analysis 68
5.3.3 Phase analysis 73
5.3.4 Grain structure 80
5.3.5 Micro-hardness results 86
5.4 Summary 88
Chapter 6 : Unveiling Defect Formation Mechanisms in Functionally Graded Additive Manufacturing of IN625-CuCrZr alloys 90
6.1 Introduction 90

6.2 Methodology 91
6.2.1 Calculation of crack susceptibility index 92
6.3 Results and Discussion 93
6.3.1 Overview of the Defects in FGAM 93
6.3.2 Porosity 93
6.3.3 Crack formation 97
6.3.4 Effect of composition on cracking 99
6.3.5 Impact of Grain Structure on Cracking Behavior 107
6.4 Conclusions 112
Chapter 7 : A geometrically-optimized heat source model for FE thermal simulation of laser directed energy deposition 113
7.1 Introduction 113
7.2 Materials and Experimental Methods 114
7.2.1 Powders 114
7.2.2 Statistical modeling & design of experiment 114
7.2.3 L-DED processing & Experimental validation 115
7.3 Finite element (FE) modeling 117
7.3.1 Model geometry 118
7.3.2 Material properties 119
7.3.3 Heat transfer governing equation and boundary conditions 119
7.3.4 Heat source model 120
7.3.5 Material deposition modeling 121
7.3.6 Quiet element method 122
7.3.7 Inactive element method 122
7.3.8 Hybrid inactive/quiet element approach 122
7.4 Outline of the statistical-numerical approach 123
7.5 Results and Discussions 124
7.5.1 Statistical analysis of geometrical characteristics 124
7.5.2 Element size optimization 127
7.5.3 Experimental measurements of the melt pool, calibration, and validation results 128

7.5.4 Effect of process parameters on the deposition's dimensions 132
7.5.5 Experimental validation through in-situ temperature measurement 133
7.6 Summary 134
Chapter 8 : On the Cracking Behavior in Functionally Graded Additive Manufacturing of IN625–CuCrZr: A Comprehensive Experimental and Thermal Finite Element Study 136
8.1 Introduction 136
8.2 Materials and methods 137
8.3 Finite element (FE) modeling approach and model geometry 137
8.3.1 Thermophysical material properties 138
8.3.2 Governing equation and boundary conditions 139
8.3.3 Outline of the FE transient thermal modeling of FGAM process 140
8.4 Results and Discussions 140
8.4.1 Cross sectional view of the thin wall and cube and CT scan results 140
8.4.2 Simulated temperature distribution in the thin wall 142
8.4.3 Simulated temperature distribution in the cube 143
8.4.4 Experimental measurement of cooling rate from primary dendrite arm spacing and comparison of the cooling rate between thin wall and cube 144
8.4.5 Comparison of the cooling rate between thin wall and cube in the crack prone regions in the model 146
8.4.6 The mechanism behind the difference in cooling rate between thin wall and cube 149
8.5 Summary 150
Chapter 9 : Conclusions and future work 151
9.1 Conclusions 151
9.2 Recommendations and Future Work 154
Letter of Copyright Permission 156
References 160

List of Figures

Figure 2-1 Schematic diagrams of: (a) stepwise and (b) continuous interfaces in FGMs. (c), (d) and (e) schematic diagrams show stepwise FGMs with gradual change in composition, grain direction and volume fractions of two different particles, respectively. (f), (g) and (h) schematics illustrate continuous FGMs with smooth change in grain size, fiber orientation and volume fraction of precipitations [7] **6**
Figure 2-2 (a) Schemas of FGAM process, (b-d) different types of gradients[10], [11]. **8**
Figure 2-3 Schematic of laser powder bed fusion; from the process to the laser powder interaction and melt pool generation **9**
Figure 2-4 Schematic representation of the LDED process [17] **10**
Figure 2-5 Application of Cu alloys to Ni-based superalloys FGAMs; A: combustion chambers of liquid-fuel rocket engines, B: liquid-fuel rocket nozzles.[22], [23] **11**
Figure 2-6 (a). SEM image and EDS line scan profiles of Cr Kα intensity on the horizontal cross-sections of the as-fabricated LPBF CuCr specimen, (b) optical microscopy image of Cr precipitates in cast CuCrZr, (c) formation of a cellular solidification structure oriented parallel and perpendicular to the image plane, and (d) formation of (probably) ZrO2 on the nano-scale. [28], [30] **13**
Figure 2-7 BSE micrographs of CuCr1Zr built by LPBF showing: (a) the microstructure perpendicular to the building direction, and (b) the microstructure parallel to the building direction. (c) EBSD image of CuCr1Zr: crystal-orientation mapping (IPF) and (d) <100> pole figure according to the orientation data of a (red: high amount, blue: low amount) [28] **14**
Figure 2-8 (a). SEM image of SLM processed IN625 sample (PD- Primary Dendrites; CD- Cell-like Dendrites; B-Building direction; S- Scanning direction). (b). SEM image of LMD processed IN625 sample (PD- Primary Dendrites; CD- Cell-like Dendrites; B- Building direction; S-Scanning direction). (c) solidification microstructure map [29] [31] **15**
Figure 2-9 (a). Isothermal section of Cu-Ni-Cr ternary equilibrium diagram at 930 °C showing miscibility gap. (b), (c), and (d) the binary phase diagrams of the each two elements.[31] **17**
Figure 2-10 Potential defects in FGAM processing of CuCrZr-IN625 (a) delamination and macro cracks as a result of a high amount of residual stresses, (b) different types of porosities and unmelted powders.[2] **18**
Figure 2-11 a) Schematic of the XRD experiment. b) 2D diffraction pattern recorded in the detector. The intensity rings present diffractions from different lattice planes of the crystal.[36] **20**
Figure 2-12 thermal modeling of LMAM process; (a) schematic of the semi-spherical heat source model with 3D Gaussian intensity distribution, (b) FE simulated melt pool[40-42] **22**
Figure 3-1 CuCrZr powders (a) morphology, (b) particle size distribution **25**
Figure 3-2 L-DED processing setup with a magnified view of the deposition **26**
Figure 3-3 (a) 3D scanned and (b) optical micrograph of a transverse cross-section of the single track. **27**
Figure 3-4 (a) Optical micrograph from the cross-section of the first DOE samples, (b) An example of RSM analysis on dilution including normal probability plot of residuals, ANOVA, and contour plots of the response vs process parameters, (c) Optimization procedure based on the desirability criteria and the white area in the contour plot showing the desirable processing window. **30**
Figure 3-5 (a) Optical micrograph from the cross-section of the second DOE samples. (b) Optimization procedure based on the desirability criteria. The white area in the contour plot shows the desirable processing window. (c) Confirmation test of the optimum point (red) and its validation for all the predicted responses. **32**
Figure 3-6 (a) SEM secondary electron image of an etched cross-section of a single track showing small dispersed particles, (b) A backscatter image of (a), and (c) EDS elemental map of the same view showing the dispersion of Cr particles in the Cu matrix. **33**
Figure 3-7 (a) EBSD map of the entire cross-section of Sample 3 including (b) SEM image of the same specimen, etched, and from the very bottom of the melt pool area, (c) From the top of the bead, (d) from the substrate area, and (e) columnarity percentage of grain morphology of the selected samples against variation in F/V and P **34**

Figure 3-8 (a) Indentation map of sample 1, (b-f) Microhardness maps of Samples 1 to 5. The red-dashed lines indicate the melt pool boundaries **36**
Figure 3-9 LDED multitrack one-layer deposition and its geometrical characteristics **37**
Figure 3-10 (a) responses and geometrical measurements of a multitrack one-layer, (b) Optimization solution and desirability plot, (c) Confirmation test of the optimization results **41**
Figure 3-11 Schematic of the strategies that have been considered for tool path trajectory planning; (a) infill zigzag trajectory with 90º rotation of scanning direction between layers, (b) the effect of start point rotation for the laser on geometrical accuracy, (c) the effect of addition of profile contouring around the perimeter, (d) the effect of addition of radial pathway at the corners of the contours **43**
Figure 3-12 effect of laser power and scanning speed on surface dimples **45**
Figure 3-13 Lack of fusion map of cuboid samples **46**
Figure 3-14 vaporization and poor wetting as results of excessive and insufficient power per F/V, respectively. **47**
Figure 3-15 General LDED processability map of CuCrZr alloy **48**
Figure 3-16 Microstructural analysis of multilayer CuCrZr (a) EBSD maps and process parameter table of the five samples with almost the same deposition height, (b) Grain structure analysis results **50**
Figure 3-17 Optimization of process parameters for LDED processing of IN625 single tracks **51**
Figure 3-18 optimization of process parameters for LDED processing of IN625 single-layer **53**
Figure 3-19 (a) LDED multilayer cuboid build up of IN625, (b) solidification microstructure **53**
Figure 4-1 Particle size distribution and morphology of feedstock powders; (a) IN625, (b) CuCrZr. **56**
Figure 4-2 In-house robotic L-DED system equipped with a coaxial nozzle and a dual hopper powder feeder system **56**
Figure 4-3 Powder feeder parameter settings: (a) hopper 1 with IN625 powders, (b) hopper 2 with CuCrZr powders **57**
Figure 4-4 FGAM of IN625-CuCrZr, (a) sharp composition transition (b) gradual composition transition **59**
Figure 4-5 (a) FGAM of IN625-CuCrZr prototypes in cuboid geometry, (b) sharp composition transition (c) gradual composition transition **60**
Figure 4-6 Average residual stresses measured on IN625 at the interface of (a) sharp compositional transition, (b) gradual composition transition **61**
Figure 5-1 Schematic of FGAM processing of IN625-CuCrZr thin-wall structure. **64**
Figure 5-2 Overall view from the microstructure of the FGAM-thin wall. (a) Schematic microstructure of the entire FGAM cross-section, BSE images, and EDS mixed elemental map of the microstructure of (b) Cu0, (c) Cu25, (d) Cu50, (e) Cu75, (f) Cu100. ..... **67**
Figure 5-3 EDS elemental map and line scan analysis on compositional transition interface of (a) Cu0/Cu25, (b) Cu25/Cu50, (c) Cu50/Cu75, and (d) Cu75/Cu100 ..... **69**
Figure 5-4 Liquid state miscibility of the two alloys, (a) stitched EDS elemental map of the entire cross-section of the FGAM thin-wall sample, (b) stitched EDS elemental map of the longitudinal section across the Cu 50, Cu75, Cu100 regions, (c) CALPHAD simulation. **70**
Figure 5-5 X-CT 3D images of a thin wall FGAM sample; a) a fine scan of the regions containing the Cu-lean phases shown in isometric and front views, and b) volume of the Cu-lean phases versus height showing their agglomeration in the Cu-75 region **73**
Figure 5-6 CALPHAD's Scheil solidification simulations results for (a) Cu-lean liquid that exists in the range of 0-75% wt. CuCrZr, and (b) Cu-rich liquid existing in the range of 20-100% wt. CuCrZr. **74**
Figure 5-7 XRD spectra at the compositional transition interfaces, (a) from the Cu25 to Cu75 regions, and (b) magnified spectra at 2θ range of 38° to 40°, showing the presence of Mo2C phase at Cu50 and Cu75. ..... **75**
Figure 5-8 BSE images and EDS analysis of microstructure, (a) Cu50, (b) high magnification of a region in (a), (c) Cu75, and (d) high magnification of a region in (c). **80**
Figure 5-9 Analysis results on the grain structure of the FGAM sample; including grain maps of compositional transition interface from (a) Cu0 to (f) Cu100, and (g) average grain size and aspect ratio of each composition. **83**
Figure 5-10 Grain refinement mechanism of Cu-rich liquid around Cu-lean spheroid microstructure; (a) BSE image of Cu75 microstructure, (b) IPF Z EBSD map from a spheroid on which distinct grains have nucleated, (c)

formation of Cu-lean spheroids during cooling their key role as the nucleation site for the Cu-rich liquid during solidification, (d) Scheil simulation results of volume fraction of various phases in Cu-lean and Cu-rich liquids during solidification. **85**
Figure 5-11 Microhardness results of FGAM thin-wall: (a) the hardness maps of the thin-wall sample's cross-section from Cu0 to Cu100 region, (b) Average microhardness of each region on the dashed lines shown in the OM image **88**
Figure 6-1 Cross-sectional view of a FGAM IN625-CuCrZr cuboid sample highlighting the porosity and crack defects across the compositional gradient. **93**
Figure 6-2 Porosity defects in FGAM of IN625-CuCrZr; (a) gas pores, (b) lack of fusions in X and Y directions. **94**
Figure 6-3 Correlation between porosity and process parameters, (a) LoF formation mechanism and melt pool's geometrical characteristics, (b) The porosity level based on Pa and F/V in FGAM of IN625-CuCrZr. **97**
Figure 6-4 Crack formation in FGAM of IN625-CuCrZr sample, (a) OM of the entire cross-section of the sample No.1, (b) low/high magnification micrographs from a crack, initiating in interdendritic region, (c) EDS line scan and elemental map from a crack, highlighting presence of Cu-rich liquid film, (d) SEM-BSE image and EDS map from the tip of a healed crack, highlighting backfilling by Cu-rich liquid film, (e) change in crack morphology from straight to zigzag upon entering Cu50, (f) similar zigzag morphology of the crack in Cu75. **99**
Figure 6-5 The microstructural characteristics across the compositional gradient in a cuboid sample, (a) dendritic structure in Cu0, (b) similar dendritic structure with segregation of Cu in the interdendritic region, (c) & (d) mixed morphology of dendrites and Cu-lean spheroids dispersed in Cu-rich matrix, (e) cellular structure of Cu100, and (f) the liquid state miscibility gap based on the amount of CuCrZr that influence the solidification phenomena in Cu50 and Cu75. **100**
Figure 6-6 The effect of composition on solidification cracking in FGAM of IN625-CuCrZr,(a) BSE and EDS elemental map from the interface of Cu0 and Cu25 where the crack initiates, (b) Kou's CSI calculated based on amount of CuCrZr alloy in the composition and maximized at around 15% wt. CuCrZr, (c) EDS line scan in the vicinity of the crack shown in BSE of (a) shows around 15% wt. of Cu element, (d) DSC cooling curves of Cu0 and Cu25 compositions highlighting larger solidification range of Cu25, (e) schematic of the solidification in the mushy zone of Cu25 highlighting interdendritic Cu liquid film that results in cracking. **103**
Figure 6-7 Cracking behavior and solidification phenomena in Cu50 and Cu75 regions; (a) BSE and EDS mixed elemental map illustrating crack branching and navigating around the Cu-lean spheroids, (b) X-CT analysis of the FGAM cuboid sample representing cracks in 3D, navigating around Cu-lean spheroids without penetrating them **105**
Figure 6-8 solidification phenomena in Cu50 and Cu75 regions; (a) DSC cooling curves highlighting two distinct consecutive solidification peaks in Cu50 and Cu75 compositions as a result of the miscibility gap between the liquids of IN625 and CuCrZr alloys, (b) ThermoCalc's Scheil solidification calculations for each of Cu-lean and Cu-rich liquids of Cu75 composition, (c) schematic of the mushy zone in Cu75 composition demonstrating distinct solidification paths of each liquids that results in the mixed dendritic and spheroidal microstructure along with OM of a lightly etched melt pool splash of Cu75 composition highlighting the nucleation of Cu-rich liquid on a Cu-lean spheroid **107**
Figure 6-9 Impact of grain structure on the cracking behavior across different regions of FGAM IN625-CuCrZr cuboid; (a) OM of sample No. 4 and the different regions that underwent the EBSD analysis, (b) IPF (Y) map of the crack initiation in Cu25, (c) IPF (Y) map of the crack propagation path along HAGBs, (d) IPF (Y) map of the crack in Cu75 highlighting its elimination among fine equiaxed grain structure, (f) stitched IPF (Y) maps from the entire of a crack underscoring the contribution of the grain structure transition along the compositional gradient to the cracking behavior, (g) average grain size and aspect ratio of grain structure in each composition. **111**
Figure 7-1 (a) L-DED setup, (b) schematic of the deposition process and its geometrical characteristics, (c) thermal validation setup including DAQ data recorder, thermocouple, and conductive silver epoxy to mount the thermocouple into the substrate **117**

Figure 7-2 FE numerical model, (a) x-symmetry computational domain for thermal modeling of IN625 single track fabrication by L-DED, (b) meshing layout applied for the model where element size is reduced toward the deposition for high-precision calculations **118**
Figure 7-3 Schematic of the cylindrical heat source model with Gaussian distribution interacting with the deposition profile **121**
Figure 7-4 Hybrid inactive/quiet element activation approach **123**
Figure 7-5 Outline of the statistical-numerical approach to study temperature distribution of the L-DED deposition. **124**
Figure 7-6 The correlation of the geometrical characteristics of a) height, b) width, c) depth of deposition and the combination of process parameters (P/√V, F/V) **127**
Figure 7-7 Mesh sensitivity analysis; a) measurement result's path, b) temperature distribution along the path for different element sizes **128**
Figure 7-8 Geometrical characteristics of depositions in experiments vs. FE results **130**
Figure 7-9 Geometrical characteristics of depositions in experiments vs. FE results **131**
Figure 7-10 Geometrical characteristics of depositions in experiments vs. FE results **133**
Figure 7-11 The validation of temperature distribution: (a) predicted in FE vs. (b) experimentally measured results via thermocouple **134**
Figure 8-1 (a) Schematic of FGAM processing IN625-CuCrZr alloys for (b) cuboid and thin-wall geometries **137**
Figure 8-2 FE thermal model geometry of the FGAM processing of IN625-CuCrZr; (a) Thin-wall, (b) cube **138**
Figure 8-3 Outline of the FE transient thermal modeling workflow to study temperature distribution in FGAM processing of IN625-CuCrZr. **140**
Figure 8-4 Cross sectional view of the FGAM IN625-CuCrZr samples; (a) cuboid geometry with cracks highlighted, (b) Thin-wall geometry **141**
Figure 8-5 X-CT analysis of the defects on the FGAM IN625-CuCrZr samples; (a) cuboid geometry with highlighted cracks and porosity, (b) Thin-wall geometry with highlighted porosity **142**
Figure 8-6 Simulated temperature distributions in the thin wall geometry during laser scanning of the final layer for each composition from Cu0 to Cu100. The gray regions correspond to temperatures exceeding the liquidus point of the respective composition, representing the extent of the simulated melt pool. **143**
Figure 8-7 Simulated temperature distributions in the cube geometry during deposition of the final layer for each composition from Cu0 to Cu100. The gray regions correspond to temperatures exceeding the liquidus point of the respective composition, representing the extent of the simulated melt pool. **144**
Figure 8-8 Primary dendrite arm spacing measured from high magnification SEM images from the cross-section of the Cu25 and Cu0 (IN625) regions in: (a) Thin wall and (b) cuboid samples. (d) comparison of the PDAS between thin wall and cube geometries in both compositions, highlighting finer microstructure in cube and (e) higher cooling rates **146**
Figure 8-9 Simulated thermal behavior at the Cu0–Cu25 interface in cube and thin-wall geometries during FGAM; (a) Temperature distribution in the melt pool cross-section with probe locations. (b–c) Nodal temperature histories at probes for Cu0 and Cu25, respectively, showing higher cooling rates in the cube geometry. (d) Comparison of simulated and experimental cooling rates for Cu0. (e) Predicted cooling rates for Cu25 from simulations. Cube geometry consistently exhibits faster cooling rates **149**
Figure 8-10 Effect of the print geometry on heat dissipation characteristics during the L-DED process **150**

Chapter 1: Introduction

1.1 Motivation

Over the past twenty years, the principles of laser cladding have been adapted to create freeform laser-directed energy deposition (L-DED). Advances in L-DED technique have allowed for the creation of functionally graded metallic parts with tailored compositions and microstructure in three-dimension, known as functionally graded additive manufacturing (FGAM). This capability is particularly useful for creating complex net-shaped parts with precise control over the choice of alloy and its resulting properties, all in a single step. There is a growing need for advanced alloys with specialized properties, especially for demanding applications like aerospace structures and the energy sectors. These alloys are required to possess superior resistance to high temperatures, corrosion, and prolonged radiation exposure, but their high cost or mass often makes their use prohibitive. One way to reduce costs and weight is to use multiple cheaper or lighter-weight alloys instead of a single one, wherever possible. But this has traditionally required the use of fasteners or welds, which come with their limitations and vulnerabilities. L-DED offers an attractive alternative, as it allows for the creation of complex structures without the need for unnecessary joints and welds through compositional grading.

In this study, the focus is on employing the L-DED to respond to the need of aerospace industries for the fabrication of parts that have a highly heat-conductive copper alloy on one side and Ni-based superalloy on the other side through one manufacturing step. The main challenge of fabricating such a component is the high thermophysical property mismatch between the two alloys. This can lead to severe residual stresses and delamination at the composition transition interface, which can be tackled by gradually varying the composition from start to finish.

This capability has already been realized and demonstrated previously on other material systems in the literature [1], [2][3], [4]. In that regard, multi-powder feeder L-DED enables the in-situ composition variation through several layers and smooth composition change instead of a sharp. The situation is analogous to dissimilar welding, in which the alloy incompatibilities make achieving strong defect-free bonding a nontrivial exercise. Yet, what is lacking in the L-DED approach is the dedicated consideration of the problem in the contexts of processing and metallurgy to reach defect-free functionally graded parts in both macro and micro scales. Suppose a universal approach is to be established for additive-based compositional grading; in that case, it

must address each alloy's properties and physical metallurgy to identify what prevents them from being joined or graded together in a defect-free part. Once these issues are generalized, strategies can then be conceived to overcome them with the unique capabilities afforded by additive manufacturing.

1.2 Objectives

The principal objective of this proposal, which is both conceptual and experimental in nature, is to develop a pragmatic approach to the successful functionally graded additive manufacturing of dissimilar alloys.

In doing so, the following steps are considered as sub-objectives:

- Investigating the additive manufacturing of each alloy via L-DED process from single tracks to multilayer scales and optimizing the process parameters through empirical/statistical methods
- Studying the effect of process parameters on microstructure evolution
- Establish an interim approach for developing successful defect-free gradients based on experimental efforts and via unique capabilities of additive manufacturing processes, particularly L-DED.
- Studying the microstructural evolution of the FGAM part via a series of experimental characterization methods
- Unveiling the defect formation mechanism in the FGAM process using advanced experimental characterization and CALPHAD methods
- Simulation of the thermal behavior of the FGAM samples during the process
- Comparing the evolution of the microstructure and thermally induced defects in the FGAM samples in cuboid and thin-wall geometries

1.3 Outline of the thesis

The proposed research is summarized as follows: The research goal is identified and introduced in Chapter 1 based on the lack of knowledge in the literature on the topic of FGAM in terms of processability and thermomechanical behavior.

In Chapter 2, a thorough survey in the area of laser metal additive manufacturing of each alloy has been conducted, along with the microstructure evolution of as-printed products. Further, a

feasibility study on the FGAM of these alloys from both manufacturing and metallurgical aspects has been carried out to address prospective challenges. Finally, principles of constitutive modeling of thermomechanical behavior during LMAM have been reviewed at the end of this chapter.

Chapter 3 discusses the additive manufacturing of each alloy in detail, from process parameter optimization to microstructural characterizations. The focus of this chapter is mainly on L-DED of CuCrZr alloy, as there is no piece of work on this subject in the literature. The results, including process parameter optimization and microstructural characterization from single track to multilayer cuboid geometry, are presented in this chapter.

Chapter 4 experimentally investigates the FGAM of IN625-CuCrZr in both sharp and gradual composition transitions via L-DED technique, utilizing the optimum process parameters from the previous chapter.

Chapter 5 investigates the evolution of microstructure across the gradient based on the change in composition, focusing on the role of the miscibility gap between the two alloys. This miscibility gap results in inhomogeneity within the microstructure, which affects the grain structure and microhardness.

Chapter 6 investigates the defect formation mechanisms during FGAM processing of the two alloys. It provides an in-depth analysis of lack of fusion and solidification cracking defects observed in the cuboid sample and highlights the role of the miscibility gap in solidification phenomena, as well as promoting these defects.

Chapter 7 presents a new hybrid statistical–numerical approach for finite element simulation of the material deposition and temperature distribution during the L-DED process at the single-track scale. The model accurately captures the time-dependent temperature evolution while preserving the actual geometric characteristics of the deposited region.

Chapter 8 investigates the influence of print geometry on defect evolution, with a particular focus on cracking during the FGAM process of the two alloys. It compares the thermal histories of the thin wall and cube geometries, simulated by the finite element model developed in Chapter 7, and reveals the underlying reasons for crack initiation in the cube sample, despite their absence in the thin wall.

The final chapter (Chapter 9) presents the overall conclusions drawn from the research conducted throughout this thesis. It summarizes the key findings from each chapter, highlighting the advancements made in process optimization, microstructural control, defect analysis, and thermal modeling of the L-DED process for FGAM of IN625–CuCrZr. Additionally, this chapter outlines several recommendations for future work, emphasizing opportunities to further enhance process reliability, mechanical performance, and modeling capabilities.

Chapter 2: Background & Literature Review

2.1 Functionally graded materials

Functionally graded materials (FGM) are known as the class of multifunctional materials that benefit from spatially varied properties through variation in their composition and/or microstructure [5]. The concept was first introduced in the mid-1980s by Japanese researchers when they were trying to design a coating as a thermal barrier to withstand a 1000°C temperature gradient to be applied in hypersonic space planes. They found out that the only way was creating a metal-ceramic FGM that has an interface that begins with 100% ceramic on one side, which provides thermal resistance and gradually change the composition to reach 100% metal on the other side to achieve a desirable toughness. The key in this case was the use of a smooth gradual transition from ceramic to metal in order to avoid cracking and insolubility issues [6].

2.1.1 Types and Manufacturing methods

Grading materials is a popular area of research as it aims to maximize the engineering properties of materials. Gradients can take several forms, such as controlled porosity, orientation, microstructural, or compositionally. Figure 2-1 schematically illustrates the different forms of FGMs along with the way that gradual transition takes place, i.e. either stepwise or continuously.

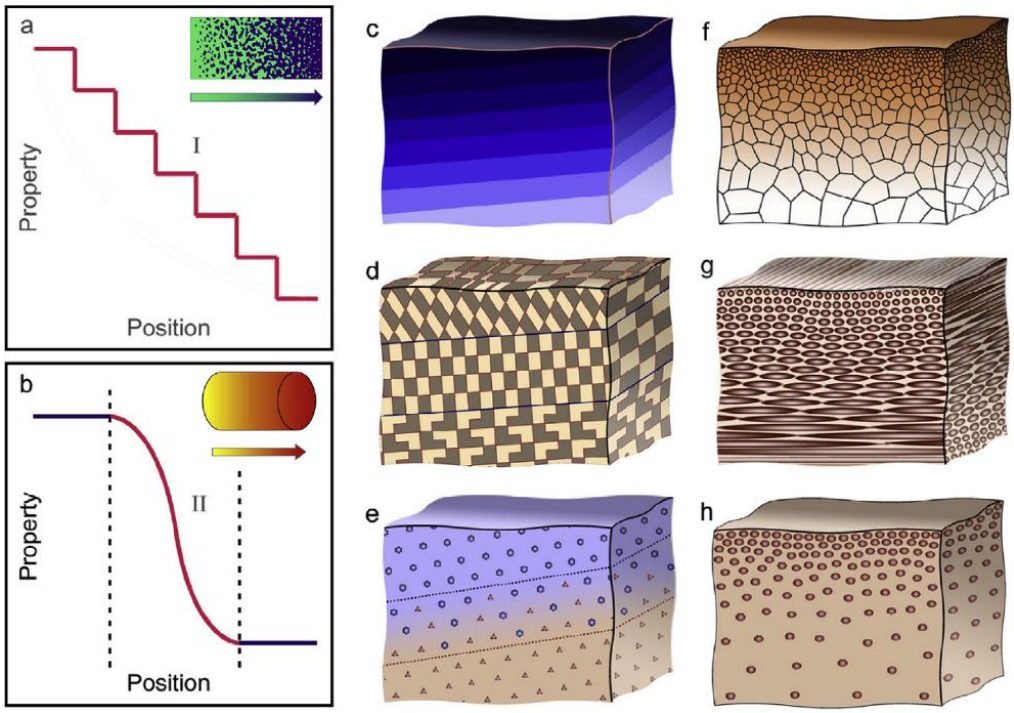


Figure 2-1 Schematic diagrams of: (a) stepwise and (b) continuous interfaces in FGMs. (c), (d) and (e) schematic diagrams show stepwise FGMs with gradual change in composition, grain direction and volume fractions of two different particles, respectively. (f), (g) and (h) schematics illustrate continuous FGMs with smooth change in grain size, fiber orientation and volume fraction of precipitations [7]

Since the concept of FGMs was introduced, several methods have been employed for manufacturing FGM parts. Among them, plasma spray technique as well as chemical and physical vapor deposition (CVD/PVD), were used in creating functionally graded thermal barrier coatings. Yet, due to their slow deposition rate, these methods are not suitable for manufacturing bulk FGMs. On the other hand, powder metallurgy was found to be useful for fabricating bulk FGM parts. Powders are mixed and pressed based on the desired compositional distribution for the part and finally consolidated with some heat treatment steps, such as debinding and sintering. Due to the method's limitations, the size and shape of FGM parts are limited, and porosity always exists as a drawback for this method. As sintering temperatures and time vary based on the materials, it is challenging to consolidate a multi-material part. In the fabrication of FGMs, AM has shown its fantastic capabilities with the transition from one material to another via many steps and over a longer distance [2].

2.1.2 Additive Manufacturing of Functionally Graded Materials

Dissimilar to the above-mentioned conventional methods, AM techniques have the great ability to manufacture bulk FGMs with complex geometries. While conventional methods were focused on fabricating ceramic coatings, composites, and simple linear gradients, the AM techniques, which are quite cost-effective, have shown their capability in tailoring geometrically complex metallic gradients with a high resolution in compositional changes. Additive manufacturing of functionally graded materials, also known as functionally graded additive manufacturing (FGAM), encompasses the gradual mixing of materials to manufacture a free-form component with variable properties that can simultaneously benefit from the advantages of both AM and FGM. For instance, commercial laser AM systems are reported to be able to achieve compositional change resolution of 1% with each layer [8]. This capability results in a finely smooth gradient in microstructure and composition through which the detrimental defects in dissimilar metal joining such as cracking, distortion, and residual stresses that lead to failure during the process or degrade a joint's service performance will be tackled [9].

FGAM has multiple forms based on the need and specific AM fabrication technique. Figure 2-2 represents the general schematic of the FGAM concept, Figure 2-2 (a), and its different types of compositional gradients. Figure 2-2 (b) illustrates a sharp gradient that is similar to the interface of welded parts, where composition abruptly changes, and it is applied in the bimetallic AM component. However, here the key difference is a layer of powder melts and bounds to the substrate individually, and higher thermal history is introduced in the bimetallic part, which altogether results in better bounding between the two alloys. Figure 2-2 (c) represents a smooth gradient where the alloy (B) has changed gradually and in small steps to alloy (A). A multi-gradient FGAM, where one gradient is printed more than one or two times is shown in Figure 2-2 (d). This type of FGM can benefit from variations in properties such as magnetism or thermal expansion. Finally, a schematic of FGAM with two gradients through three different materials is illustrated in Figure 2-2 (e). As an application for this type, where more than two materials are desired based on the application need or the two main materials are greatly incompatible that a filler alloy is needed to ensure a safe transition. Except for the first type of FGAM, which is achievable by both powder-fed and powder-bed processes, the rest gradient types are only possible through powder-fed AM processes due to the unlimited capability of simultaneously depositing different powders.

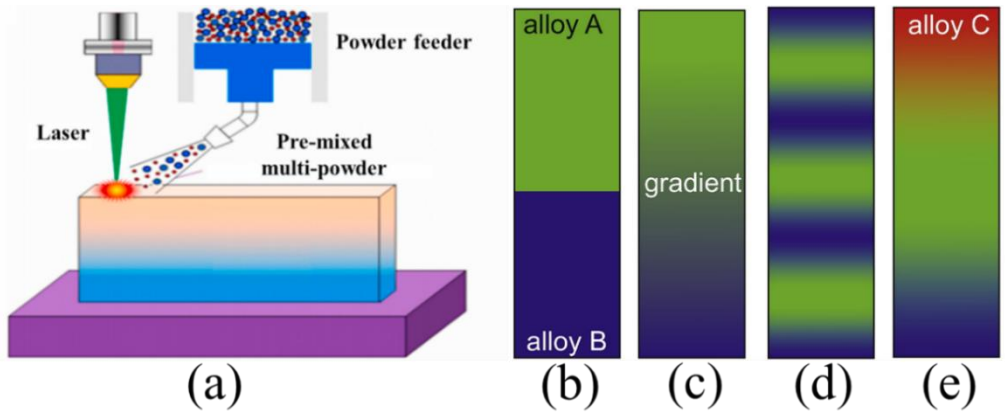


Figure 2-2 (a) Schemas of FGAM process, (b-d) different types of gradients[10], [11].

2.1.2.1 Powder-bed additive manufacturing processes

Powder bed additive manufacturing is a process in which a heat source, either a laser or an electron beam, selectively scans a layer of powder and generates molten materials which subsequently solidify and deposit new rigid material on top of previously built layers. This process will be repeated layer-by-layer until the entire CAD file is fabricated. Among powder bed additive manufacturing processes, laser powder bed fusion (L-PBF) is very well-developed and identified as a versatile technique which is also known as selective laser melting (SLM) and direct metal laser sintering (DMLS). Figure 2-3 schematically shows the LPBF technique from the process to the laser powder interaction and melt pool generation. Although this process benefits from high resolution, shape complexity, and high strength-to-weight ratio, it cannot simultaneously use multiple powder feed stock due to the limitation of the powder bed concept and powder recycling. Therefore, one alloy should be printed first; then, the powder bed needs to be changed to the other alloy, and print will be resumed to reach a bimetallic part with a sharp gradient similar to Figure 2-2 (b). This process has been frequently reported to be used for manufacturing bimetallic FGAM parts made of dissimilar alloys such as different classes of steels, copper to steel, Ni-based superalloys to steel, and copper to Ni-based superalloys[10], [11] [12].

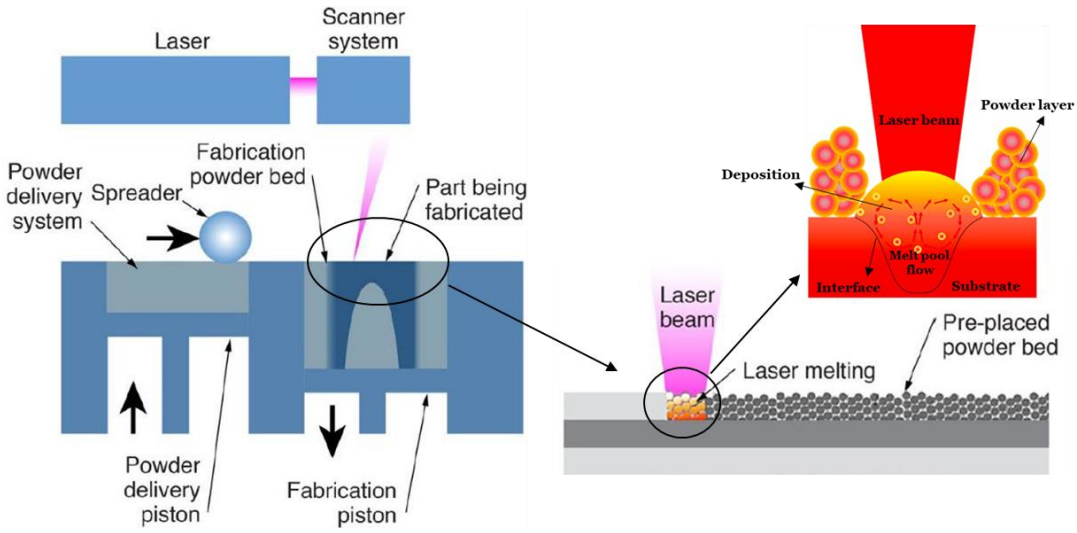


Figure 2-3 Schematic of laser powder bed fusion; from the process to the laser powder interaction and melt pool generation

2.1.2.2 Powder-fed additive manufacturing process

Powder-fed additive manufacturing is a process in which metal powders are fed into a heating zone that is actively scanned by a laser beam, which subsequently led to generating a melt pool. This process is also known as Laser Directed Energy Deposition (L-DED) powder-fed and one of the most efficient techniques among metal AM methods, which is schematically represented in Figure 2-4. Thanks to its capability of printing an unlimited range of materials at very low cost and high production rates, it has been used for a variety of applications such as repair and cladding, rapid prototyping, manufacturing moderately large and complex geometries [13], [14], and functionally graded materials [2]. Among AM techniques, the L-DED-PF has been found to be the best candidate for FGAM application due to its unique ability to adjust the feedstock material in situ and relatively small feedstock loss. Using L-DED-PF technique, there have been several material systems implemented in FGAM applications that are briefly explained in the next section.

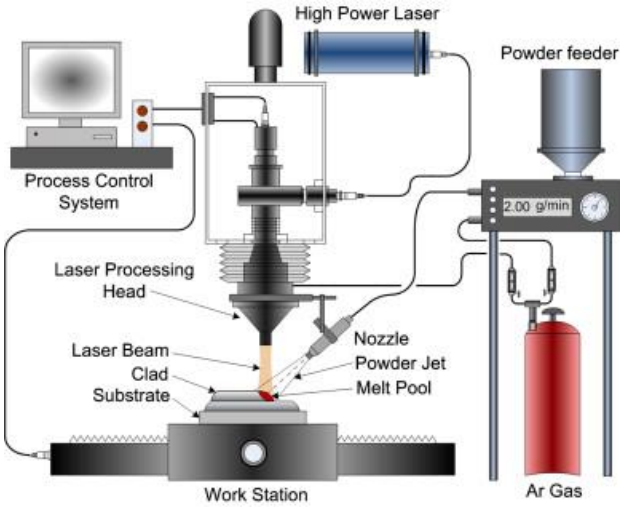


Figure 2-4 Schematic representation of the LDED process [17]

2.2 Metallic systems in functionally graded additive manufacturing

The FGAM concept has gained much attention amongst researchers for several material systems. Titanium-based alloys, different types of steel, nickel, and copper alloys are among the most reported material systems used via L-PBF and L-DED processes. Table 2-1 briefly summarizes the common material systems that have been implemented in FGAM, along with their application. Yet, among different metallic systems, gradients made of copper to Ni-based superalloys have gained significant interest to be investigated more and it is the focus of the current proposal, which is discussed thoroughly in the following section.

Table 2-1 FGAMs of different material systems with their application

Material systems	Application
Ti-based to refractory metals (Nb, Mo, Cr, V)	β-Ti stabilizer and exceptional mechanical properties, in biomedical and aerospace industries[3]
Ti-based to Fe-based alloys	high-quality joints in nuclear/aerospace industry[15]
Fe-based to Ni-based alloys	Improving corrosion resistance and mechanical properties, automotive and oil industry [16]
Ni-based to Ti-based alloys	Thermal protection and reduced thermal stress, aerospace and oil industry [17]
austenitic to ferritic steels	limiting carbon diffusion and better joints, nuclear and fossil-fired power plants [2]
Fe-based to Cu-based alloys	Easing the working temperature, dies and molds, tool industry [18]

2.2.1 Copper to Nickel-based superalloys gradient

Copper and its alloys are excellent options for applications that need high thermal conductivity and oxidation resistance, particularly in salt and alkaline atmospheres. Nickel established its credit as a major element of high-temperature alloys, recognized as Ni-based super alloys, with high mechanical strength at elevated temperatures. Oxidation resistance is another advantage of nickel-based super alloys. Combining the superior thermal properties of copper and the high-temperature strength of Ni-based superalloys can result in an FGM component that benefits from long cycles of service under harsh environments. This material type FGM, has recently caught industries that need high heat-flux cooling, such as the aerospace industry. Figure 2-5 shows some Cu-Ni superalloy FGM parts, which are additively manufactured due to their complex geometries. [19][20]

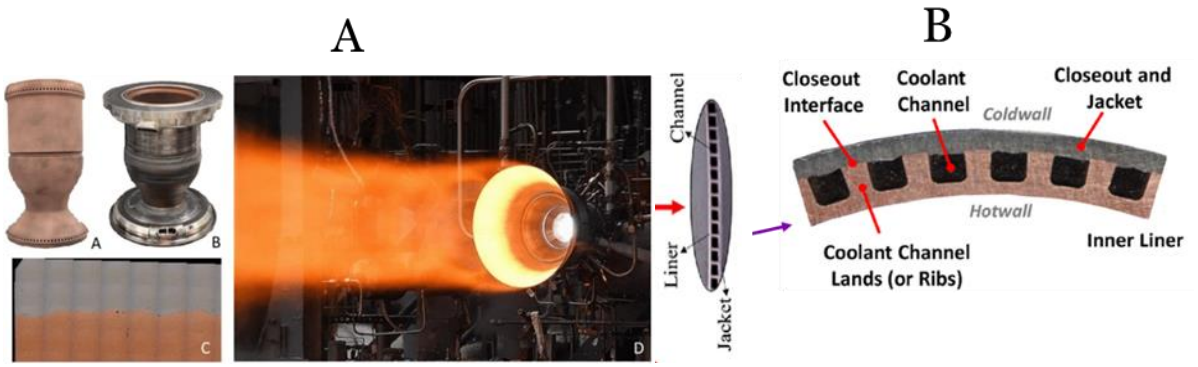


Figure 2-5 Application of Cu alloys to Ni-based superalloys FGAMs; A: combustion chambers of liquid-fuel rocket engines, B: liquid-fuel rocket nozzles.[22], [23]

2.3 Functionally graded additive manufacturing of Inconel 625-CuCrZr

CuCrZr alloy has excellent thermal and electrical conductivity and relatively high hardness and strength, making it an excellent option for applications that need high thermal conductivity and oxidation resistance [21]. Inconel 625 is a well-known superalloy that has high corrosion resistance and mechanical strength up to 650 °C, which drops significantly and constrains their applications in high heat flux cases such as rocket engines and nozzles [10][22]. Therefore, it would be beneficial in such cases to have an FGM component that is made of CuCrZr on one side and Inconel 625 on another side to enhance the cooling process (up to 300% higher thermal diffusivity [22]) while properly benefiting from the corrosion resistance and high mechanical strength [19].

Yet, in terms of the manufacturability of such FGM components, some major challenges urge studying the L-DED processing of each alloy first.

2.3.1 Additive manufacturing of CuCrZr

Due to their outstanding thermal and electric conductivity in combination with wide-range alloying abilities, copper and its alloys are highly significant in the development of new electronic and heat-exchanging units, e.g., in electro-mobility and novel power generation and distribution units. The originally poor strength of Cu alloys can be increased by precipitation hardening, without losing the outstanding electric and thermal conductivity properties. In that regard, one of the robust precipitation-hardening Cu alloys is the Copper–Chromium–Zirconium (Cr: 0.5–1.2 wt%; Zr: 0.03–0.3 wt%) which offers high electrical, thermal, and mechanical properties that recently gained significant attention from AM industry for fabrication of electrical components such as motor rotors, commutators, and heat-transfer parts such as heat exchangers. However, additive manufacturing of CuCrZr is not without its challenges. [23],[24]

Challenges

The main challenge during L-DED of CuCrZr powders is to reach the complete and defect-free melting: (i) at the wavelength of 1050nm, which is the wavelength of most commercial lasers, the laser beam reflection is very high (approximately 75%). A large beam reflection results in a low process efficiency since the major amount of the laser power is reflected and not available for powder melting. (ii) the high thermal conductivity of CuCrZr causes a rapid loss of the spot energy required for heating and melting of the surrounding material. Therefore, with an inadequate local energy supply, the L-DED of CuCrZr is associated with the risk of not reaching dense and defect-free components. [25]

Microstructure

As shown in Figure 2-6, within this alloy Cr precipitates are formed during solidification or aging based on the temperature and cooling rate. Also, fine cellular/dendritic structure, which is a typical microstructure in laser processing of alloys, within a solidified melt pool is visible in Figure 2-6 (c). The formation of a cellular solidification structure oriented parallel and perpendicular to the image plane is a result of high values of a local thermal gradient, G, and relatively low solidification rate, R, that leads to a relatively high G/R ratio which in turn controls the solidification microstructure. [26]

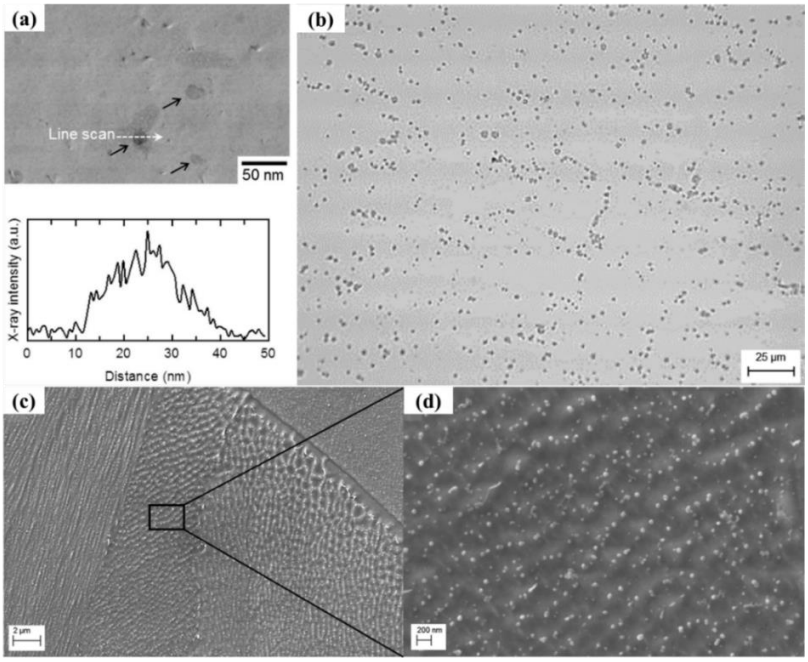


Figure 2-6 (a). SEM image and EDS line scan profiles of Cr Kα intensity on the horizontal cross-sections of the as-fabricated LPBF CuCr specimen, (b) optical microscopy image of Cr precipitates in cast CuCrZr, (c) formation of a cellular solidification structure oriented parallel and perpendicular to the image plane, and (d) formation of (probably) ZrO2 on the nano-scale. [28], [30]

Figure 2-7 shows SEM images of backscattered electrons (BSE) of the grain structure of additively manufactured CuCrZr alloy, perpendicular and parallel to the building direction, respectively. Within the BSE micrographs, the grain structure perpendicular and parallel to the building direction is visible. Figure 2-7 (b) reveals that elongated grains were formed along the building direction with lengths exceeding 10 µm. A deviation of the elongated grains compared to the building direction of about 40◦ is visible within the BSE images. Perpendicular to the building direction, in Figure 2-7 (a) the grains are smaller and equiaxed. Figure 2-7 (c) shows the Inverse Pole Figure mapping (IPF) from the EBSD analysis, which reveals the formation of elongated grains along the building direction. The <100> pole figure in Figure 2-7 (d), shows a deviation from the z0 building direction (accumulation within the pole figure, red area) at approx. 40° and a resulting tilt in the x0 and y0 direction due to synergic effects of (i) the rotation by 67° of the scanning direction with every new layer and (ii) high heat dissipation within the highly conductive CuCrZr alloy.

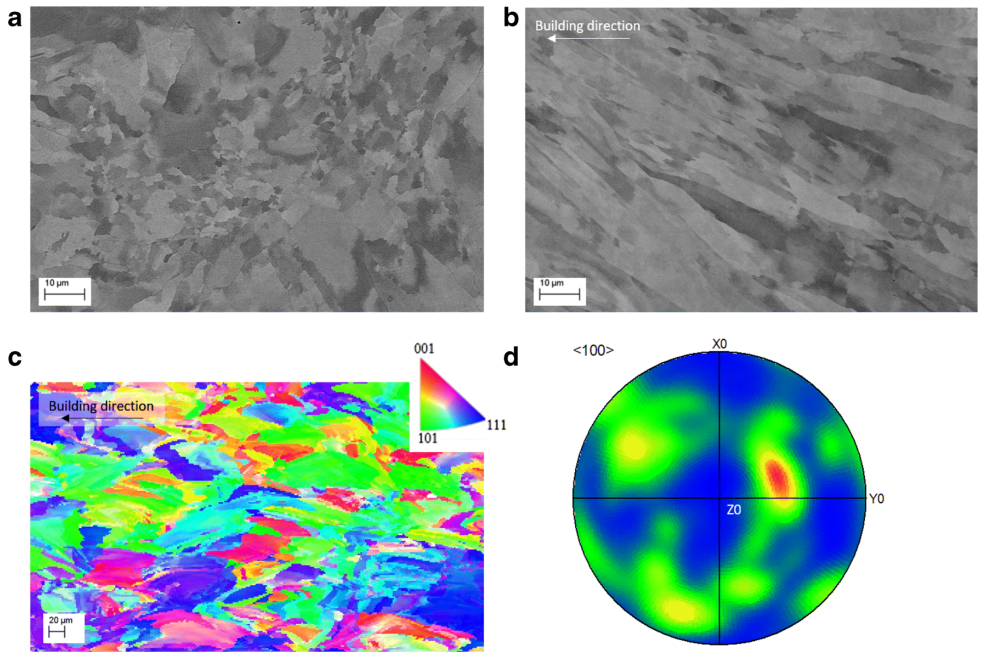


Figure 2-7 BSE micrographs of CuCr1Zr built by LPBF showing: (a) the microstructure perpendicular to the building direction, and (b) the microstructure parallel to the building direction. (c) EBSD image of CuCr1Zr: crystal-orientation mapping (IPF) and (d) <100> pole figure according to the orientation data of a (red: high amount, blue: low amount) [28]

2.3.2 Additive manufacturing of Inconel 625

Inconel 625 is a solid solution strengthened nickel-based superalloy with face centered cubic (FCC) structure. It is used extensively in aerospace, pressure vessels, chemical, and nuclear applications. IN625 usage is preferred in high temperature and high-pressure applications such as gas turbine products due to its excellent mechanical properties and oxidation/corrosion resistance at elevated temperatures [27]. This alloy's composition consists of nickel (62.10%), chromium (22.0%), molybdenum (9.0%), niobium (4.0%), Fe (2.50%), Mn (0.2%), Si (0.2%). Within this alloy, primary and secondary carbides (MC, M6C and M23C6), γ″ (Ni3Nb), δ, and Ni2(Cr, Mo) intermetallic phases can be exist based on different thermal exposure. Undesirable precipitates and phases such as Laves, Si-rich particles, α-Cr particles, μ TCP (Topologically Close Pack) phase can also be found under thermal aging [28], [29], [30]. Unlike its great mechanical and corrosion properties, it has been reported that the machining process of IN625 is faced with many challenges due to poor machinability and increased tool wear rate. Therefore, additive manufacturing processes have been extensively exercised for the fabrication of complex geometries made of this alloy.

Microstructure

Microstructure of additively manufactured IN625 by both L-PBF and L-DED processes are shown in Figure 2-8 (a) and (b), respectively where cellular and dendritic microstructures are evident in both micrographs. As previously mentioned, the microstructure of LMAM products are directly controlled by both the local temperature gradient, G and the solidification rate, R. As it is illustrated in Figure 2-8 (c), the ratio of G over R (G/R) determines the morphology of microstructure while the multiplication of them (G*R), also known as cooling rate, controls the size. From melt pool cross sections, epitaxial grain growth through a perpendicular direction to the build direction is observed, which leads to the formation of elongated columnar grains in both L-PBF and L-DED-made IN625's microstructure.

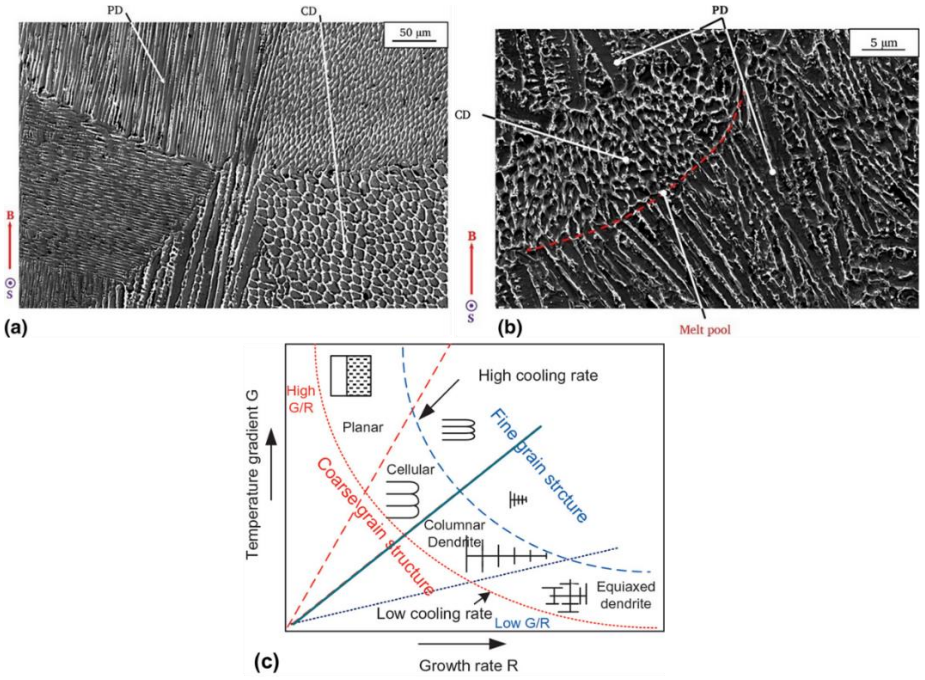


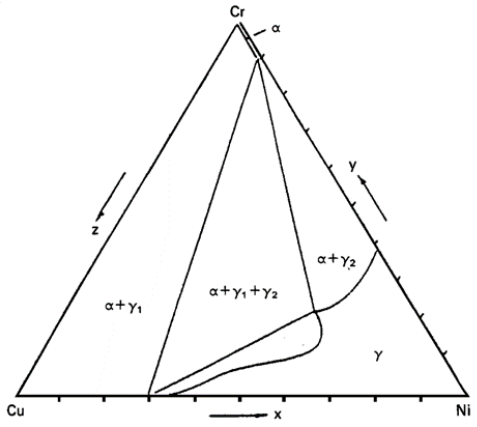
Figure 2-8 (a). SEM image of SLM processed IN625 sample (PD- Primary Dendrites; CD- Cell-like Dendrites; B- Building direction; S- Scanning direction). (b). SEM image of LMD processed IN625 sample (PD- Primary Dendrites; CD- Cell-like Dendrites; B- Building direction; S-Scanning direction). (c) solidification microstructure map [29] [31]

2.3.3 Feasibility and challenges from the metallurgical aspect

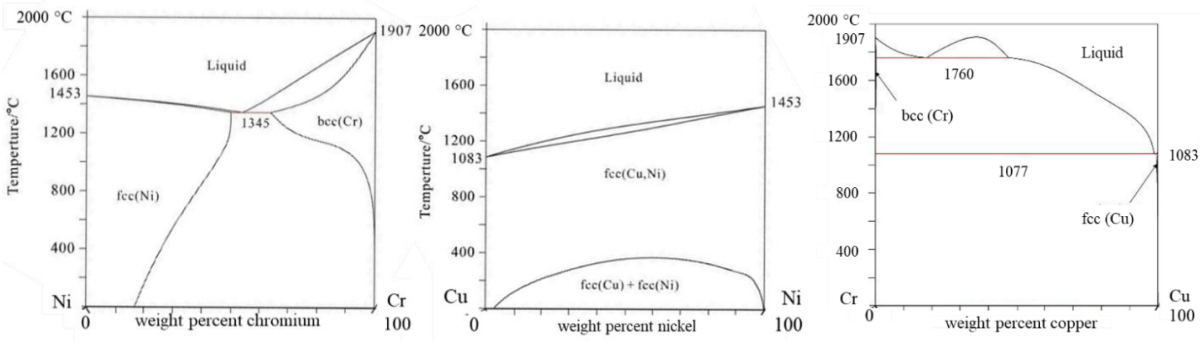
A gradient composed of the IN625 and CuCrZr alloys should first be studied from a metallurgical aspect to predict any metallurgical challenges. As such, intermetallic formation, segregation of different phases, and crack formation can adversely affect the microstructure and mechanical properties of the FGM. In that regard, considering the phase diagram of the main elements of the

gradual composition, which are Cu, Ni, and Cr, can be quite insightful. Though it should be noted that during the L-DED process, solidification does not happen in equilibrium conditions. This may result in a discrepancy between what is predicted from the phase diagrams and real observations. Figure 2.9 shows the equilibrium ternary and binary phase diagrams of these elements where (a) the miscibility gap based on the amount of each element can be predicted at 930 °C where all are completely solidified. While in IN625 alloy, the ratio of Cr to Ni is designated in a way to get a solid solution composition (Figure 2.9 (b)), from Figure 2.9 (c) and (d) the chance of solidification cracking and limited solubility in Cu-Ni system as well as the immiscibility issue in Cu-Cr composition can be predicted, respectively.

Solidification cracking: Solidification cracks, also referred to as "hot tears," mainly occur within the "mushy zone", where the material is in a semisolid state. Based on the portion of each alloy in the gradient region, the material system can have a large solidification range of couple hundreds of degrees °C, which is known to promote the chance of solidification cracking. In that regard, a portion of the liquid phase is entrapped in the interdendritic regions at which the solidifying stress is concentrated and finally leads to the tearing of the liquid films and the formation of solidification cracks[26].



(a)



(b) (c) (d)

Figure 2-9 (a). Isothermal section of Cu-Ni-Cr ternary equilibrium diagram at 930 °C showing miscibility gap. (b), (c), and (d) the binary phase diagrams of the each two elements.[31]

2.3.4 Feasibility and challenges from the process aspect

Alongside metallurgical phenomena that may happen in the case of CuCrZr-IN625 FGAM, there could be a quite few challenges during the process mainly due to the mismatch between the thermophysical properties of these alloys, shown in table 2.2. In fact, differences in melting point and specific heat capacity may lead to poor mixing and the presence of unmelted powder inclusions, and porosities in the melt pool of LMAM of these alloys. Moreover, CuCrZr featured low absorption of infrared laser radiation, indicating most of the energy is reflected and due to the high heat conductivity, less amount of heat accumulates to bond these materials together. Therefore, more challenges will be added to the challenges of LMAM of CuCrZr when it comes to depositing it with IN625 which has higher laser absorptivity and lower heat conductivity[27].

Table 2.2 Thermophysical properties of CuCrZr and Inconel 625. [32][33]

Material	Melting range (°C)	CTE (10^{-6}/°C)	K (W/m.K)	Cp (J/g.K)	Laser beam absorption (%)
CuCrZr	1065-1083	17	200	0.38	25
IN625	1290-1350	12.8	9.8	0.43	65

Residual stress

Residual stress is a common phenomenon in LMAM products as a result of large thermal gradients during the processes. In fact, residual stresses are highly concentrated near the substrate interface, and they may lead to macro cracks and delamination when exceeding the local UTS stress, shown in Figure 2.10 (a). In the FGAM of CuCrZr-IN625, due to the high variation in the thermophysical

properties of these materials, it is expected to have a high amount of residual stress, particularly in its bimetallic form.

Porosity

Porosity is a common defect in LMAM parts and can negatively affect mechanical properties. It can be categorized into process-induced porosity, such as the lack of fusion, and powder-induced porosities such as the oxidized powder particles, shown in Figure 2.10 (b). In the case of CuCrZr-IN625 FGM, both types of porosities can happen as a result of the lack of fusion and oxidation of CuCrZr powders.[14]

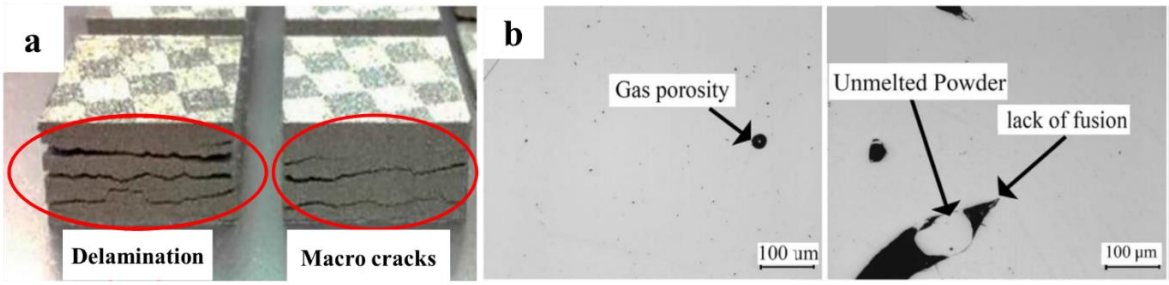


Figure 2-10 Potential defects in FGAM processing of CuCrZr-IN625 (a) delamination and macro cracks as a result of a high amount of residual stresses, (b) different types of porosities and unmelted powders.[2]

2.4 X-ray diffraction for phase identification and residual stress measurement

X-ray diffraction (XRD) is a widely used non-destructive method for analysis of phases and residual stresses, relying on the principle that each crystalline phase produces a characteristic diffraction pattern due to constructive interference of X-rays satisfying Bragg's law:

$$n\lambda = 2d \sin\theta \qquad \text{(equation 2-1)}$$

Each phase yields a unique set of diffraction peak positions and intensities that serve as a "fingerprint," so by comparing them to standard reference databases, one can identify the crystalline phases present in an unknown sample. This approach is widely applied in material science for analyzing multi-phase alloys and compounds. In addition, the Full Width at Half Maximum (FWHM) of X-ray diffraction (XRD) peaks serves as a critical parameter for probing microstructural features such as crystallite size and lattice strain in polycrystalline materials. Peak broadening in XRD patterns arises from both the finite size of coherently diffracting domains and the presence of microstrain, which introduces distortions in the crystal lattice. To decouple these contributions, the Williamson–Hall (W–H) method is commonly used. It assumes that the

observed peak broadening (β, in radians) is a combination of size and strain effects and follows the equation:

$$\beta \cos\theta = \frac{k\lambda}{D} + 4\varepsilon \sin\theta \qquad \text{(equation 2-2)}$$

where θ is the Bragg angle, k is the shape factor (typically ~0.9 for FCC structure), λ is the X-ray wavelength, D is the crystallite size, and ε represents the lattice microstrain. By plotting $\beta \cos\theta$ against $\sin\theta$, one can extract both crystallite size (from the intercept) and microstrain (from the slope) from the linear fit. This approach provides a convenient and non-destructive means of characterizing structural defects, though it assumes uniform deformation and isotropic strain distribution, which may not always hold true. Nonetheless, the Williamson–Hall method remains widely used in materials science for quick estimation of microstructural parameters from XRD data[34], [35].

Moreover, X-ray diffraction (XRD) can be used to measure residual stresses by detecting shifts in the positions of diffraction peaks, which correspond to changes in interplanar spacings (d-spacing) caused by elastic strain. When a material is under stress, the lattice planes are either compressed or stretched, leading to a measurable change in the diffraction angle (2θ) according to Bragg's law. By comparing the measured d-spacing in a stressed region to that of an unstressed reference, the elastic strain (ε) can be calculated. This strain is then related to the residual stress (σ) using Hooke's law for elastic deformation, typically through the equation:

$$\sigma = \frac{E}{1+\nu} . \varepsilon_{\psi} \qquad \text{(equation 2-3)}$$

The strain is measured at different tilt angles (ψ), and a plot of $d\psi$ versus $\sin^2 2\psi$ is used to determine the residual stress from the slope. Here, E is Young's modulus, and ν is Poisson's ratio. This technique is particularly useful for measuring in-plane residual stresses near the surface (typically within a few micrometers depth), and is widely applied in welds, coatings, and shot-peened components. However, plastic stress, which results from permanent deformation such as dislocation motion, slip, and twinning, cannot be measured directly using standard XRD residual stress methods, because plastic deformation alters the lattice in a non-recoverable and often non-uniform way. That said, XRD can provide indirect insights into plastic deformation through several indicators such as peak broadening in PID tests. Plastic deformation increases the density of

dislocations, which introduces local lattice distortions. This manifests as broadening of diffraction peaks (i.e., increased FWHM). Line profile analysis techniques (e.g., Williamson–Hall, Warren–Averbach, or Convolutional Multiple Whole Profile fitting) can help estimate dislocation density and strain anisotropy associated with plasticity.

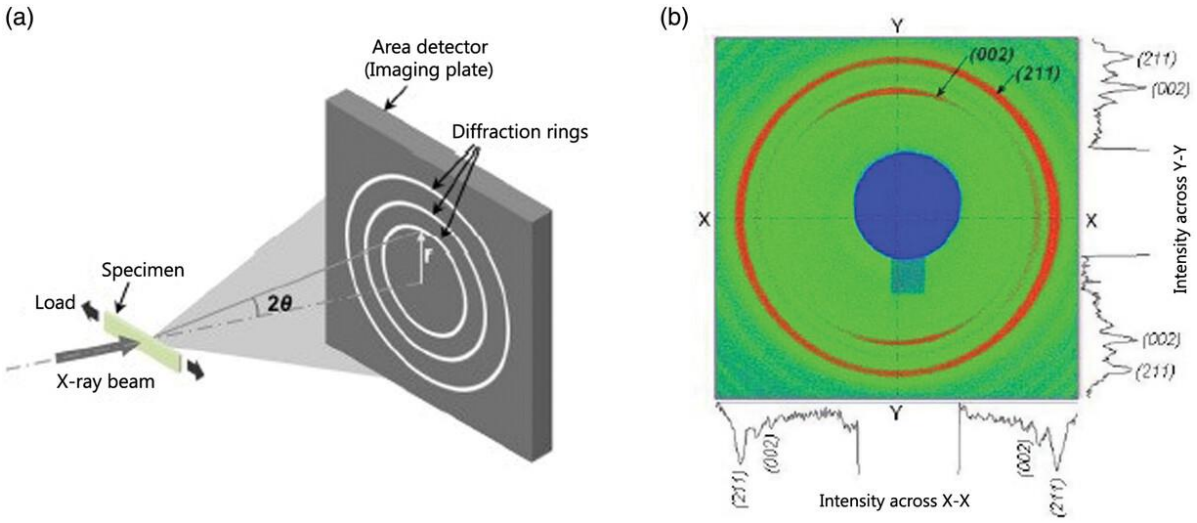


Figure 2-11 a) Schematic of the XRD experiment. b) 2D diffraction pattern recorded in the detector. The intensity rings present diffractions from different lattice planes of the crystal.[36]

Grain size has a significant effect on the reliability of residual stress measurements using X-ray diffraction (XRD), particularly in coarse-grained or columnar-structured materials such as L-DED samples:

Reduced grain statistics: XRD measures lattice strains based on averages from many crystallites. In materials with large grains (hundreds of microns), fewer grains fall within the X-ray beam footprint, leading to poor grain sampling and increased random errors in peak positions and stress estimates.

Peak asymmetry and noise: Coarse grains tend to generate asymmetric diffraction patterns, as shown in Figure 2-11 (patchy Debye rings), complicating peak fitting and reducing precision in the stress–$\sin^2\psi$ plot.

According to guidelines, grain sizes should ideally be under ~100 µm (preferably < 30 µm) to ensure high accuracy. Beyond this, XRD measurements become unreliable without corrective strategies.[36], [37], [38]

2.5 Thermal and thermomechanical modeling of additive manufacturing process

During the L-DED process, the high thermal gradient due to the fast melting and solidification leads to the expansion and contraction of both the added material and previously printed layers, which consequently result in high residual stresses and distortion in the part. Therefore, having a model that can predict the thermomechanical behavior of a part would be highly useful, even necessary, to avoid costly repeated runs [39][40]. In that regard, Finite Element Method (FEM) is a useful tool to predict the thermomechanical behavior of AM products during the process. Moreover, FE numerical models have been extensively used for studying the heat transfer problems and thermal stress analyses of FGMs [41]. Yet, as the concept of FGAM is recent, there is a big gap in the literature about the thermomechanical modeling of AM of FGM parts. In fact, the thermomechanical FE modeling is worth employing for the case of Inconel 625-CuCrZr FGAM to predict the residual stresses.

2.5.1 Thermal Equilibrium

The first step to modeling the thermomechanical behavior of a part during the LMAM process is thermal modeling. The thermal model is mainly conducted in 3D dimensions and in three major scales of micro, meso, and macro based on the methodology and requirements. Conduction is the main mode of heat transfer during the process whereas radiation and convection from the top layer still exist and should be considered in the boundary conditions. The applied heat input which is from the laser, is partially absorbed to melt the powder particles and the rest of it transfers mainly through conduction and a slight amount of convection and radiation. The thermophysical properties of the powder such as density and reflectivity are the most important features affecting both the heat input and heat transfer during the process. The general thermal equilibrium is described as follows [39]:

$$Q_{Laser} = Q_{Melting} + Q_{Conduction} + Q_{Convection} + Q_{Radiation} \quad \text{(equation 2-4)}$$

Another shape of the above equation for a body with constant density, ρ, and an isotropic specific heat capacity, Cp is represented as follows:

$$\rho\, Cp\, dT/dt = -\nabla \cdot q(r,t) + Q(r,t) \quad \text{(equation 2-5)}$$

where T is the temperature, t is the time, q is the heat flux, Q is the absorbed heat input, and r is the relative coordinate from the reference. In the case that there is not any preheating, the initial boundary condition for temperature is $T_0 = T_\infty$, which is the ambient temperature. The heat losses

from the surface through radiation and convection should also be considered in the boundary. The heat dissipation through the substrate is described by Fourier's conduction equation as follows:

$$q = -k\nabla T \quad \text{(equation 2-6)}$$

where k is the isotropic thermal conductivity coefficient, which is temperature-dependent. To solve the above equations, one has to consider the boundary conditions mentioned earlier as well as apply a proper heat input model that matches the actual laser-powder interaction.

2.5.2 The Heat Input Model

The laser beam that incidents the powder particles is usually modeled as a volumetric heat flux that follows a Gaussian intensity distribution [13], [42]. Figure 2-12 schematically shows the semi-spherical heat source model and its 3D Gaussian intensity distribution which follows the below equations:

$$I(x,y,z) = q_0 . \exp\left[-2\frac{x^2+y^2+z^2}{\eta^2}\right] \quad \text{(equation 2-7)}$$

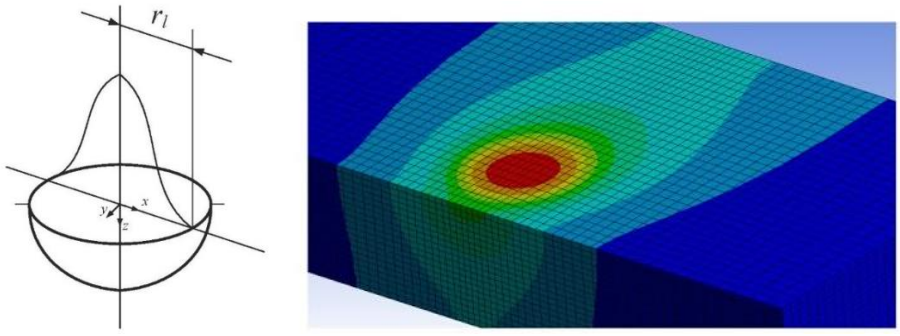
While,

$$\beta . P = \int_0^{\infty}\int_{-\infty}^{\infty}\int_{-\infty}^{\infty} q_0 . \exp\left[-2\frac{x^2+y^2+z^2}{\eta^2}\right] dxdydz \quad \text{(equation 2-8)}$$

The q_0 will be equal to:

$$q_0 = \frac{2^{5/2}\beta P}{\pi^{3/2}\eta^3} \quad \text{(equation 2-9)}$$

$$I(x,y,z) = \frac{2^{5/2}\beta P}{\pi^{3/2}\eta^3} . \exp\left[-2\frac{x^2+y^2+z^2}{\eta^2}\right] \quad \text{(equation 2-10)}$$



(a) (b)

Figure 2-12 thermal modeling of LMAM process; (a) schematic of the semi-spherical heat source model with 3D Gaussian intensity distribution, (b) FE simulated melt pool[40-42]

2.5.3 The mechanical model

After completing the thermal simulation, a temperature history for each node is derived, besides a quasi-static equilibrium of stress is determined for each time step. The small deformation theory applies in modeling of LMAM processes, in which the total strain can be calculated as follows:

$$\varepsilon_{Total} = \varepsilon_e + \varepsilon_p + \varepsilon_T \quad \text{(equation 2-11)}$$

where ε_{Total}, ε_e, ε_p, and ε_T are the total strain, elastic strain, plastic strain, and thermal strain, respectively. The governing stress equilibrium equation is:

$$\nabla . \sigma = 0 \quad \text{(equation 2-12)}$$

where **σ** is the stress. The constitutive equation that relates stress, strain, and material properties is as follows:

$$\sigma = C\varepsilon_e \quad \text{(equation 2-13)}$$

whereε_e is elastic strain and **C** is the fourth order stiffness tensor. [39]

2.6 Summary

As stated in this chapter, the FGAM (Functionally Graded Additive Manufacturing) of CuCrZr-IN625 material system poses various challenges. On one hand, due to the significant mismatch between the thermophysical properties of these alloys, the bimetallic form (sharp transition) would face poor bounding and delamination as a result of the high amount of residual stresses. On the other hand, in the smooth gradient form, there is a high chance of solidification cracking and segregation of different phases in the compositional gradient zone, degrading the mechanical properties of such components. Based on the application and potential needs, both cases are already, while could be more in the future, in demand. So far, there is no study on the FGAM of this material system in the literature. Moreover, although the concept of FGAM has gained a lot of interest and is remarkably extending, there is a big gap in the literature on their thermal and thermomechanical modeling during the process. Consequently, the objective of this thesis is to comprehensively investigate both the sharp and smooth gradients of this material system at both macro and micro scales, followed by the identification of effective solutions to the aforementioned challenges through the use of experimental and modeling approaches.

Chapter 3: Experimental analysis and statistical optimization of additive manufacturing of CuCrZr and Inconel 625 powders

3.1 Introduction

Laser Directed Energy Deposition (LDED) is one of the most efficient processes among metal Additive Manufacturing (AM) techniques, in which metal powders/wire are fed into a melt pool produced by a laser beam. In LDED, a product is fabricated by horizontal and/or vertical addition of single tracks. Further, by printing these single-tracks and adjoining them both horizontally then vertically in a way that properly overlap each other, and a successful part can be fabricated. Therefore, in this chapter a thorough investigation has been carried out to optimize the process parameters from single tracks to multilayers to successfully fabricate cuboid geometry for CuCrZr alloy first. It is worth mentioning that CuCrZr alloy has been the focus of this chapter due to the challenges associated with its laser processing along with the big gap in the literature for LDED of this material. Further, the similar methodology has been followed for successful LDED processing of Inconel 625 alloy. In addition, the effects of main process parameters, which are laser power (P), powder feed rate (F), and scanning speed (V), on the evolution of microstructure have been studied. Finally, the knowledge obtained from this chapter will be applied in the next chapter for successful fabrication and characterization of these two alloys together as FGAM.

3.2 Laser directed energy deposition of CuCrZr powders

Copper and its alloys have been extensively used in aerospace, particularly in high heat flux applications where high cooling rates are needed to cool down engine parts [43]. Among the copper alloys, CuCrZr has been widely used in combustion chambers and cooling channels of rocket nozzles not only because of its high heat conductivity but also due to its superior mechanical properties at high temperatures such as creep resistivity [43], [44]. Moreover, the geometrical complexity of those parts on one hand, and the need for cost-effective and fast production, have made AM techniques robust candidates for manufacturing aerospace parts composed of CuCrZr alloy [45]. In spite of the fact that there are several studies on LPBF of CuCrZr alloy, to date, there is not any systematic investigation on LDED of this alloy. Moreover, it has been reported that this technique is employed for building nozzles made of CuCrZr alloy due to its capability for manufacturing large-scale parts [19], [20].

Due to the large gap in the literature, the present work thoroughly investigates the processability and microstructure of CuCrZr fabricated by powder-fed LDED from the scale of single tracks to multilayers. The original contribution of this study are as follows: 1) a novel two-step process optimization approach is established through response surface methodology to achieve a proper deposition with desirable geometrical characteristics; 2) general processability map in which the optimum processing window is identified based on key process parameters; 3) the microstructure of selected samples made by different process parameters are studied to comprehend the influence of process parameters.

3.2.1 Material and methods

CuCrZr powders

Gas atomized CuCrZr powder was used as the feedstock material in this study. Table 3-1 shows the chemical composition of the powder, and Figure 3-1 shows its main characteristics; morphology, and particle size distribution (D10: 30.61 µm, D50: 42.56 µm, D90: 59.91µm). The substrate material was pure copper, which was sandblasted before the experiments.

Table 3-1 Chemical composition of the CuCrZr powders (wt.%)

Cu	Cr	Zr
balance	0.5-1.5	0.05-0.15

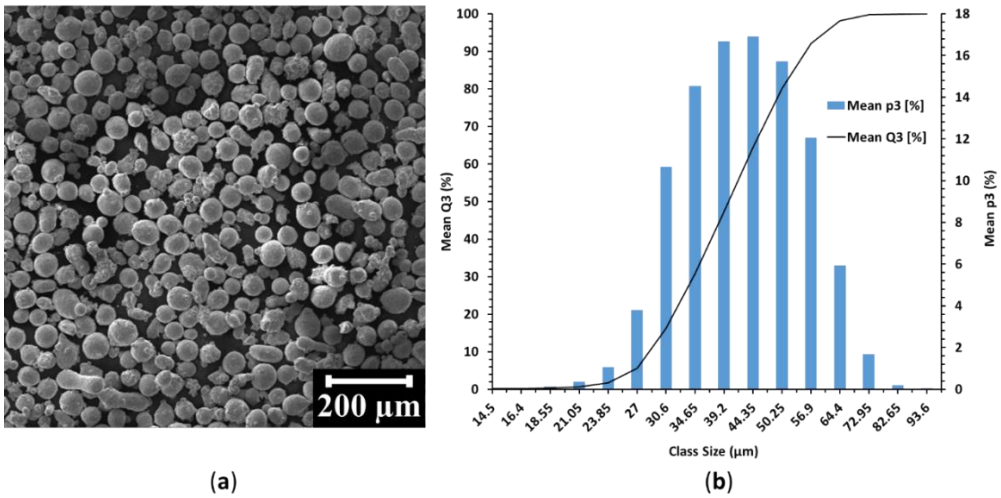


Figure 3-1 CuCrZr powders (a) morphology, (b) particle size distribution

L-DED setup and settings

Single tracks with a length of 35 mm and 3 replicates per each condition were deposited on the substrate by a powder-fed L-DED system (IC106, DM3D Technology) equipped with a robot (ABB IRB 140) that is armed with a coaxial nozzle and a disk laser (TruDisk 2000, TRUMPF) with up to 2000 W power capacity. Figure 3-2 shows the L-DED processing setup. During the experiments, the laser spot size was kept at 1.4 mm. The laser power (P, 700-1900 W), scanning speed (V, 2-14 mm/s), and powder feed rate (F, 4-12 g/min) are considered variable input parameters. Figure 3-2 shows a single track sample consisting of three discrete zones: deposition zone, heat-affected zone (HAZ), and substrate.

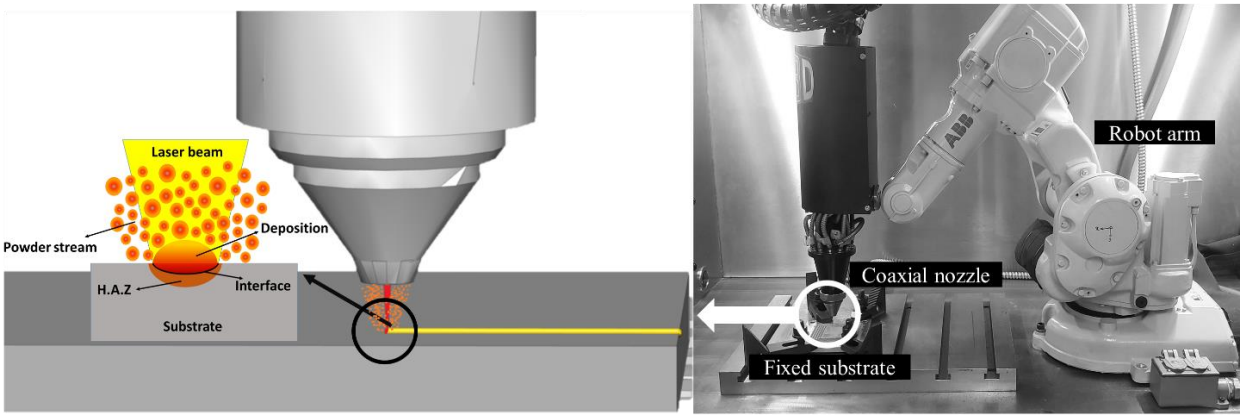


Figure 3-2 L-DED processing setup with a magnified view of the deposition

Geometrical and microstructural characterizations

Metallographic characterization was done to inspect the geometrical characteristics and microstructure of the samples. First, the samples were cross-sectioned and hot-mounted in a conductive epoxy resin. Then, the samples were ground and polished on a Struers Labopol-20 auto-polisher using SiC grinding papers from 120 to 4000 grit sizes and the 1µm alumina slurry, respectively. Finally, polished samples were etched using 50% HNO_3 diluted in Ethanol for 30~35 seconds in order to reveal their microstructure.

Using a Keyence VHX-7000 digital microscope, the optical microscopy was carried out to scan the entire track from the top, as shown in Figure 3-3 (a), and for melt pool observation on the metallographically prepared samples, Figure 3-3 (b), where it shows the geometrical characteristics of a single track; the height (h) and width (w) of the bead as well as the melt pool penetration depth to the substrate (b). In this study, the combination of geometrical characteristics

and input parameters, i.e. the dilution ($D= b/h+b$), the powder efficiency ($PE= A*V*\rho/F$), which is the ratio of the deposited material to the fed powder, and the deposition rate ($DR=A*V$) were considered as the outputs for the statistical analysis where ρ is the density of the alloy (8.9 g/cm^3) and $A=2/3h*w$ is the cross-section area of a track.

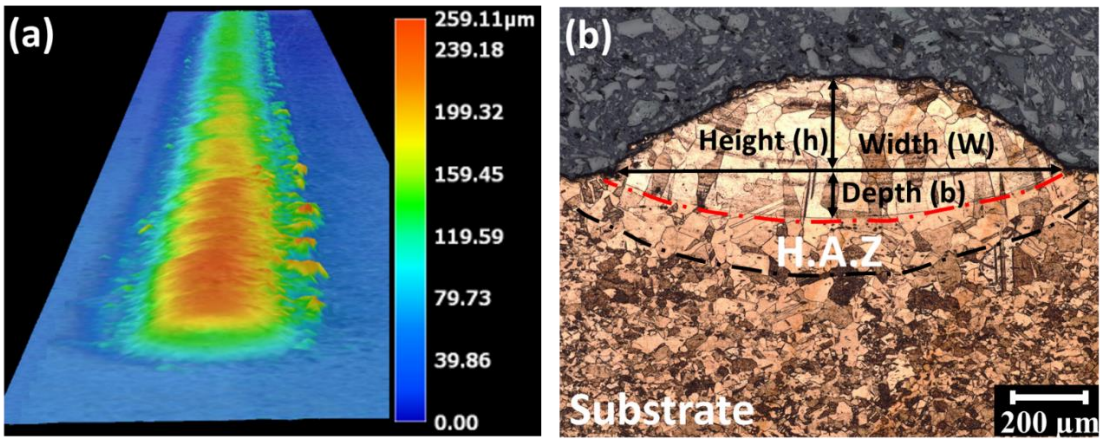


Figure 3-3 (a) 3D scanned and (b) optical micrograph of a transverse cross-section of the single track.

Furthermore, the microstructure and chemical composition of the samples were examined by a Tescan VEGA3 scanning electron microscope (SEM) equipped with an energy-dispersive X-ray spectroscope (EDS) detector. The morphology and size of grains were explored via a Bruker QUANTAX electron backscatter diffraction (EBSD) which was carried out at the voltage of 20 kV and scanning step size of 4 µm that was finally analyzed with ESPRIT2 software. The aspect ratio of grains was measured, and the grains with values less than 0.5 were considered columnar.

Design of experiments and data analysis

For the statistical data analysis, the response surface methodology (RSM) was employed for a three-step statistical approach. As the printability of CuCrZr powder is challenging due to its high laser reflectivity and thermal conductivity [25], [46], a screening phase was initially carried out through a set of preliminary runs to find out the feasible range of process parameters through which minimum quality requirements are met (e.g., being free from delamination and a minimum clad height produced). Then, using the central composite design (CCD) method, the design of experiment (DOE) was conducted for the second set of experiments, followed by the regression scheme on the measured responses (the geometrical characteristics) to establish the correlation between track features and the process parameters. The dilution (D), the powder efficiency (PE), and the deposition rate (DR), were also considered as the objectives of the compliance function.

All the data analysis procedures from the DOE to the optimization were carried out through Minitab 19 software. For the first DOE, a three-factor CCD matrix with an alpha value of 1.68 (standard, orthogonal) was considered, which consists of 8 cube points, 6 axial points, and 3 central points. It is frequently reported in the literature that a second-order equation best describes the correlation between inputs and responses of the L-DED process [47], [48], hence, the full quadratic model was employed for the regression analysis, which was conducted in the stepwise approach with backward elimination of insignificant factors.

3.2.2 Results and discussions; single tracks

Process parameter optimization

Figure 3-4 (a) reveals a general view of the cross-section of all single tracks of the first DOE, where the input variables and the output responses are presented in Table 3-2. A few of the trials got rejected due to the poorly wetting the substrate and/or over deposition, which resulted in high wetting angles [49]. After measuring all the responses, the RSM analysis was performed. Figure 3-4 (b) shows the regression analysis results for the dilution response (D) as an instance. This figure also shows the normal probability plot of residuals, scatter plots of residuals vs fitted values, which prove the validity of the raw data for regression, the table of ANOVA, showing the significant process parameters for the response, and contour plots of D vs different levels of the significant process parameters. The mathematical equation from the regression analysis is as follows:

$$D = 82.4 + 0.03541P - 18.57F - 5.30V + 0.498F^2 + 1.224F * V \quad \text{(equation3-1)}$$

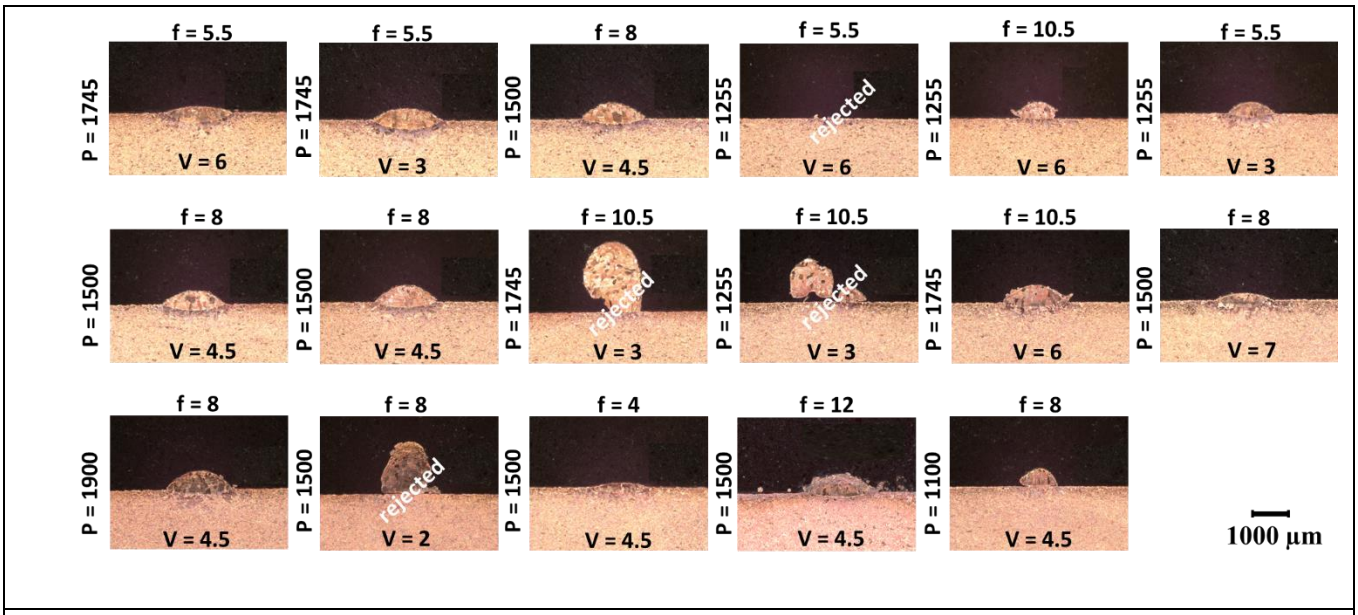
Optimizing the process parameters is then followed, as shown in Figure 3-4 (c). The compliance function was set to maximize both *PE* and *DR* while reaching the target of 30% for *D*, as they are the average values that are reported to be acceptable for the L-DED process[50], [51]. Based on the optimization solutions, F was around 12 gr/min in all the solutions with high desirability values. The white area in the contour plot shows the desirable processing window.

Table 3-2 the first step DOE input variables and output responses

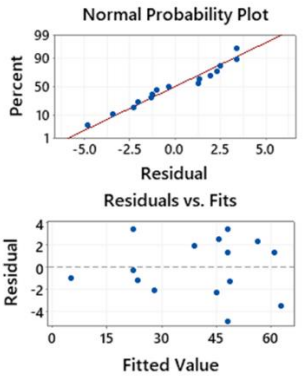
Track NO.	Process parameters (input variables)	Geometrical measurements (output responses)

	P **(W)**	***F*** **(g/min)**	***V*** **(mm/s)**	***h*** **(µm)**	***w*** **(µm)**	***b*** **(µm)**	***DR*** **(µm³/s)**	***D*** **(%)**	***PE*** **(%)**
1	1745	5.6	6.03	88.30	1222	146	0.44	62.31	3.98
2	1745	5.6	2.97	154.90	1559	221	0.48	58.79	4.38
3	1500	8.0	4.50	159.60	1583	122	0.76	43.32	4.82
4	1255	5.6	6.03	73.00	925	0	0.27	0.00	2.49
5	1255	10.4	6.03	166.20	1185	58	0.80	25.87	3.86
6	1255	5.6	2.97	103.30	1194	72	0.25	41.07	2.24
7	1500	8.0	4.50	142.90	1442	140	0.62	49.49	3.93
8	1500	8.0	4.50	140.90	1465	150	0.62	51.56	3.94
9	1745	10.4	2.97	396.80	1569	22	1.24	5.25	6.00
10	1255	10.4	2.97	431.70	1432	18	1.23	4.00	5.96
11	1745	10.4	6.03	198.90	1583	150	1.27	42.99	6.17
12	1500	8.0	7.00	97.50	1382	91	0.63	48.28	4.00
13	1900	8.0	4.50	169.70	1513	153	0.77	47.41	4.90
14	1500	8.0	2.00	384.40	1651	29	0.85	7.01	5.38
15	1500	4.0	4.50	53.90	1320	79	0.21	59.44	2.72
16	1500	12.0	4.50	285.20	1623	108	1.37	27.46	6.49
17	1100	8.0	4.50	140.20	1114	18	0.47	11.37	2.98

a) First step specimens



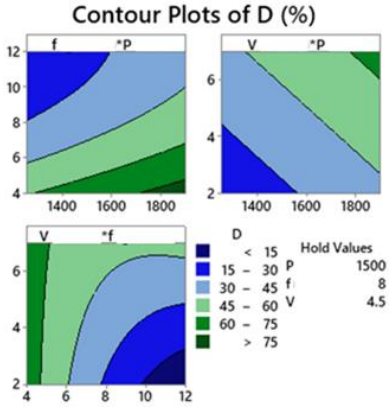
b) Regression analysis on dilution



ANOVA

Source	DF	Adj SS	Adj MS	F-Value	P-Value
Model	7	3852.56	550.37	42.26	0.000
Blocks	2	322.08	161.04	12.36	0.005
Linear	3	3288.06	1096.02	84.15	0.000
P	1	610.10	610.10	46.84	0.000
f	1	1801.92	1801.92	138.35	0.000
V	1	548.51	548.51	42.11	0.000
Square	1	73.04	73.04	5.61	0.049
f *f	1	73.04	73.04	5.61	0.049
2-Way Interaction	1	134.68	134.68	10.34	0.015
f *V	1	134.68	134.68	10.34	0.015
Error	7	91.17	13.02		
Lack-of-Fit	5	54.44	10.89	0.59	0.725
Pure Error	2	36.73	18.37		
Total	14	3943.73			

R^2 97.69%
Adj-R^2 95.38%
Pred-R^2 85.54%



c) Optimized process parameter window

Desirability criteria

Response	Goal	Lower	Target	Upper	Importance
PE (%)	Maximum	2.23853	6.4882		1
D (%)	Target	4.00267	30.0000	62.3133	1
DR	Maximum	0.21451	1.5375		1

Optimization solutions

Solution	P (W)	f (gr/min)	V (mm/s)	PE (%) Fit	D (%) Fit	DR Fit	Composite Desirability
1	1523.18	11.9192	4.75890	6.49268	30.0147	1.53978	0.999848
2	1479.60	12.0000	4.87184	6.42860	29.4653	1.52587	0.985530
3	1569.67	11.7293	3.28434	5.90672	29.1085	1.53687	0.940978
4	1499.30	12.0000	5.34287	6.31874	34.5856	1.51497	0.932112
5	1613.01	11.7798	5.26441	6.36209	37.9806	1.51212	0.894896
6	1414.01	12.0000	6.03646	5.79185	38.0785	1.39036	0.822959
7	1503.81	11.5916	2.95154	6.84563	13.5998	1.53708	0.717287

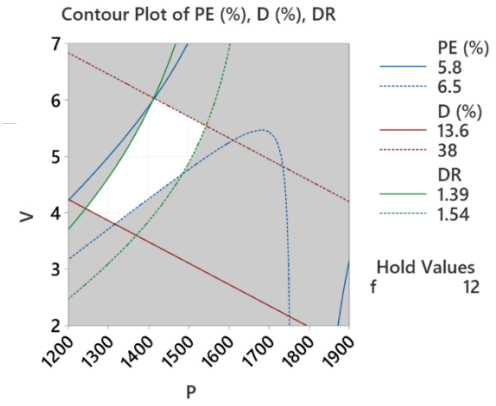
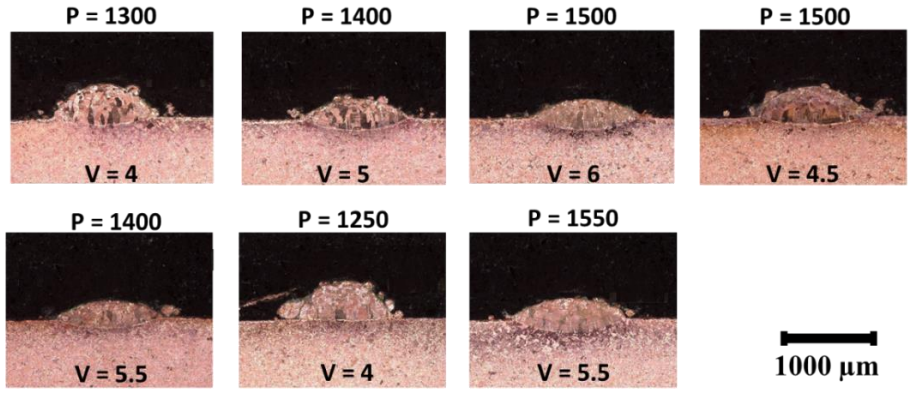


Figure 3-4 (a) Optical micrograph from the cross-section of the first DOE samples, (b) An example of RSM analysis on dilution including normal probability plot of residuals, ANOVA, and contour plots of

the response vs process parameters, (c) Optimization procedure based on the desirability criteria and the white area in the contour plot showing the desirable processing window.

Further, to achieve the optimum set of process parameters for the aforementioned responses, the second DOE was conducted in which the ranges of inputs were narrower. This was necessitated by the fact that in the LDED process there are multi-physics phenomena that not only make the process complex, but also add environmental and process disturbances to the process zone that in turn result in low accuracy of the statistical model. For example, the rejected tracks, shown in Figure 3-4 (a), can cause a discrepancy in the statistical prediction. Therefore, another set of DOE was designed from the previous step's processing window. To this end, Figure 3-5 (a) shows the cross-sectional views of the printed tracks, all of which are acceptable in terms of geometrical characteristics. After measuring the responses and performing the regression analysis, the optimization phase was carried out with the same criteria as the previous step, and the results are shown in Figure 3-5 (b). The optimization solution is shown as the red point in the contour plot. To confirm this set of process parameters as the optimum ones and validate the optimization procedure, it was printed with three replicates, and the result is shown in Figure 3-5 (c) in which the mean values of experimental measurements were in good agreement with both low and high 95% confidence levels of the predicted responses.

a) Second step specimens



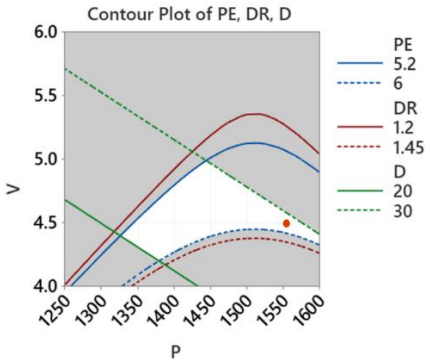
b) Optimized process parameter window

Desirability criteria

Response	Goal	Lower	Target	Upper	Importance
PE	Maximum	4.71289	5.9175		1
DR	Maximum	1.11680	1.4023		1
D	Target	8.24801	30.0000	40.3587	1

Optimization solutions

Solution	P	V	PE Fit	DR Fit	D Fit	Composite Desirability
1	1550.00	4.47567	5.91751	1.40225	28.8215	0.981604
2	1550.00	4.47570	5.91747	1.40224	28.8218	0.981583
3	1550.00	4.47528	5.91813	1.40240	28.8177	0.981544



c) Model confirmation test

Validation

Response	Predicted	SE Pred.	No. replicates	95% C.L. low	Exp. Mean	95% C.L. high
PE	5.91	0.21	3	5.37	**5.97**	6.46
DR	1.4	0.05	3	1.27	**1.41**	1.57
D	28.82	3.28	3	21.07	**26.3**	36.57

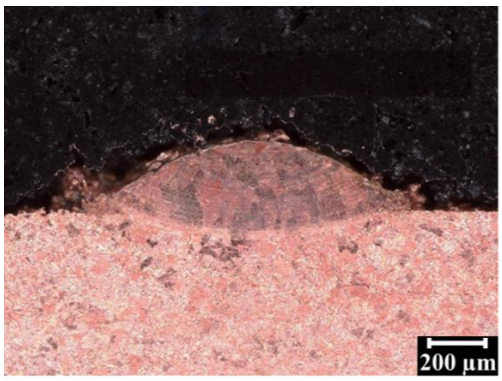


Figure 3-5 (a) Optical micrograph from the cross-section of the second DOE samples. (b) Optimization procedure based on the desirability criteria. The white area in the contour plot shows the desirable processing window. (c) Confirmation test of the optimum point (red) and its validation for all the predicted responses.

Microstructural results

To understand the effect of process parameters on the microstructure in the LDED of CuCrZr alloy, five samples with different process parameters were selected from the last set of DOEs. Table 3-2 represents the samples with their process parameters.

Table 3-2 Selected specimens for microstructural characterization with their process parameters

Sample No.	***P*** (W)	***F*** (g/min)	***V*** (mm/s)	***F/V*** (g/mm)
1	1300	12	4	0.050
2	1400	12	5.5	0.036
3	1250	12	4	0.050

4	1550	12	5.5	0.036
5	1550	12	4.5	0.044

Figure 3-6 shows the result of microstructural observations in the deposition area of Sample 1. SEM SE and BSE are shown in Figure 3-6 (a) and (b), respectively, in which the cellular structure is evident [52], [53]. In fact, the interaction between thermal gradient (G) and solidification rate (R), G/R, determines the morphology of the solidification structure[26]. In this study, the high heat conductivity of the copper substrate leads to high heat dissipation, hence resulting in relatively high values of G which resulted in the cellular morphology of the microstructure. Moreover, shiny spherical particles, as shown in Figure 3-6 (a), with different contrast from the matrix in the backscatter image in Figure 3-6 (b), were found to be the chromium particles based on the results of the EDS analysis map shown in Figure 3-6 (c). This observation is comparable to what is reported from the microstructure of LPBF-manufactured CuCrZr alloy[21], [25].

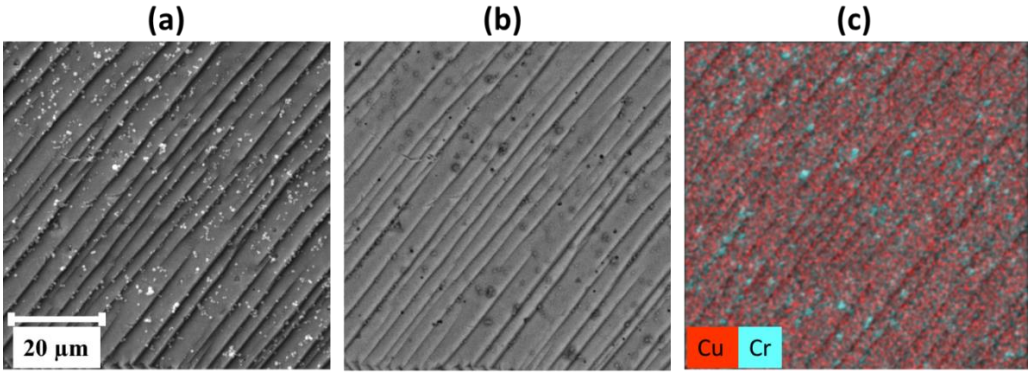


Figure 3-6 (a) SEM secondary electron image of an etched cross-section of a single track showing small dispersed particles, (b) A backscatter image of (a), and (c) EDS elemental map of the same view showing the dispersion of Cr particles in the Cu matrix.

Figure 3-7 depicts a set of microstructural features from the substrate to the top of the track for Sample 3. From the EBSD Inverse Pole Figure (IPF) map, shown in Figure 3-7 (a), epitaxial grain growth is evident for the grains located at the melt pool boundary that are highly columnar. This happens for molten material at the liquid-solid interface, where the crystallographic orientation of the adjacent solid grain is preferred to solidify and grow in the thermal gradient direction. Figure 3-7 (b) also verifies this, where the growth direction of cells is mainly upward and along the printing direction. This phenomenon has been frequently reported and justified in the literature in

detail [54], [55]. Due to a couple of synergic mechanisms, the top half of the bead consists of a fine and equiaxed grain structure, as shown in Figure 3-7 (c). There are a couple of synergic mechanisms behind this. One is the interaction of the shielding gas with the melt pool, which provides a suitable condition for heterogeneous nucleation [56], [57]. Moreover, in LDED, the melt pool is always under the bombardment of powder particles and based on how far the heat source is from the melt pool, some of them may completely melt and dissolve in the molten metal, while others may partially melt or attach to the edge of the bead. Having these partially melted particles is highly likely in the relatively cold top half region, where they act as potential nuclei and cause grain detachment [58]. Lastly, the microstructure of the substrate material, made of pure copper, is displayed in Figure 3-7(d).

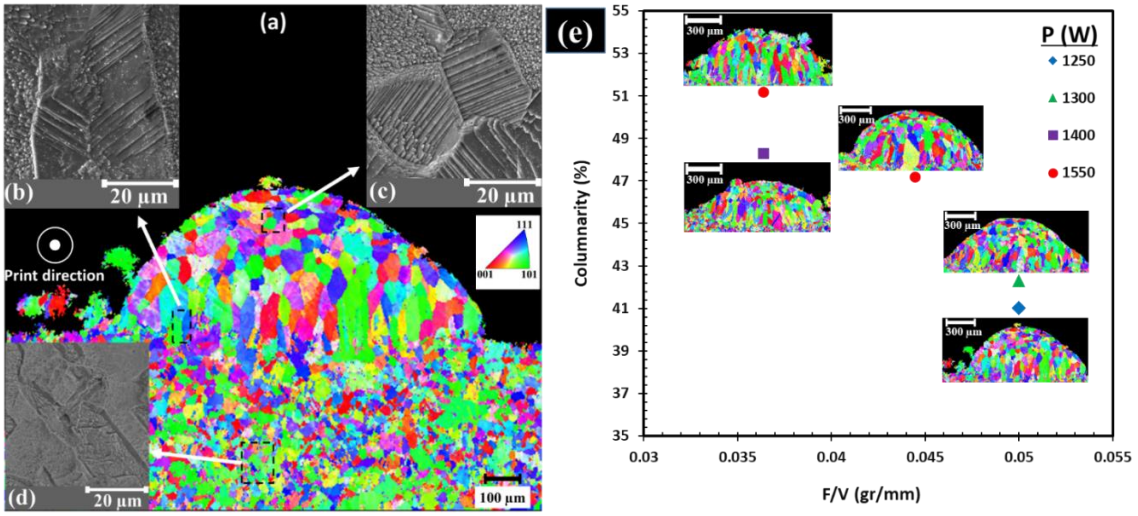


Figure 3-7 (a) EBSD map of the entire cross-section of Sample 3 including (b) SEM image of the same specimen, etched, and from the very bottom of the melt pool area, (c) From the top of the bead, (d) from the substrate area, and (e) columnarity percentage of grain morphology of the selected samples against variation in F/V and P

Similar characterizations are done on the microstructure of the other specimens and the results from the analysis of grain structure morphology were considered against the process parameters for each sample. The grains with an aspect ratio of less than 0.5 were considered columnar. Figure 3-7 (e) shows the plot of the columnarity of the grain structure against (F/V) in different P values. While the laser spot size was kept constant, the higher values of (F/V) indicate that more powders are fed into that distance, which not only increases the deposition height but also provides more nucleation sites. Therefore, at the fixed laser power, the higher the (F/V), the lower the columnarity. On the other hand, at the fixed values of (F/V), the higher the power, the higher the

columnarity. The reason for the latter could be justified by the fact that higher laser power results in a higher thermal gradient which leads to higher columnarity of grains' morphology. In addition, the higher laser powers result in deeper and wider melt pools observed in the current study and others, indicating that more area of the liquid-solid interface, which results in more epitaxially growing grains that are the main portion of columnar grains of each track [58], [59].

The hardness maps of the five selected samples are represented in Figure 3-8, in which the red dashed lines show the melt pool boundaries. The hardness indentation pattern of Sample 1, as an example, is shown in Figure 3-8 (a). As illustrated, all five hardness plots follow the same trend, having the maximum hardness values at the top half of the bead, whereas the minimum values are under the melt pool boundary, in the HAZ zone.

However, the value of the maximum hardness of each sample is different, as seen in Figure 3-8 (d) that shows the highest maximum hardness value (104 HV, Sample 3), and Figure 3-8 (b) that shows the second-highest (99 HV, Sample 1). Interestingly, these are samples with the minimum columnarity that results in the finest grain structure based on Figure 3-7. Hall [60] showed that the hardness of polycrystalline materials, including copper alloys, is correlated to the grain size through the following equation:

$$H = H_0 + K_H d^{-1/2} \qquad \text{(equation3-2)}$$

where H_0 and K_H are material's constants, and d is the grain size [61]. This properly justifies the variation of hardness between the samples as well as across the deposition area by the observed finer grain structures at the top of the bead in all samples compared to the coarse-columnar structure in the bottom of the melt pool. From the hardness maps (Figure 3-8), the pure wrought copper substrate is generally softer than the deposition zone, particularly in the HAZ (76 ±4 HV) in which the grain structure is coarser (see Figure 3-8 (b)) as a result of the grain growth [62]. While the deposited tracks are composed of ~99% wt. copper, there is ~1% wt. chromium, that apparently leads to precipitation hardening mechanism [63]. Moreover, the existing cellular microstructure increases the hardness of the deposition area [64].

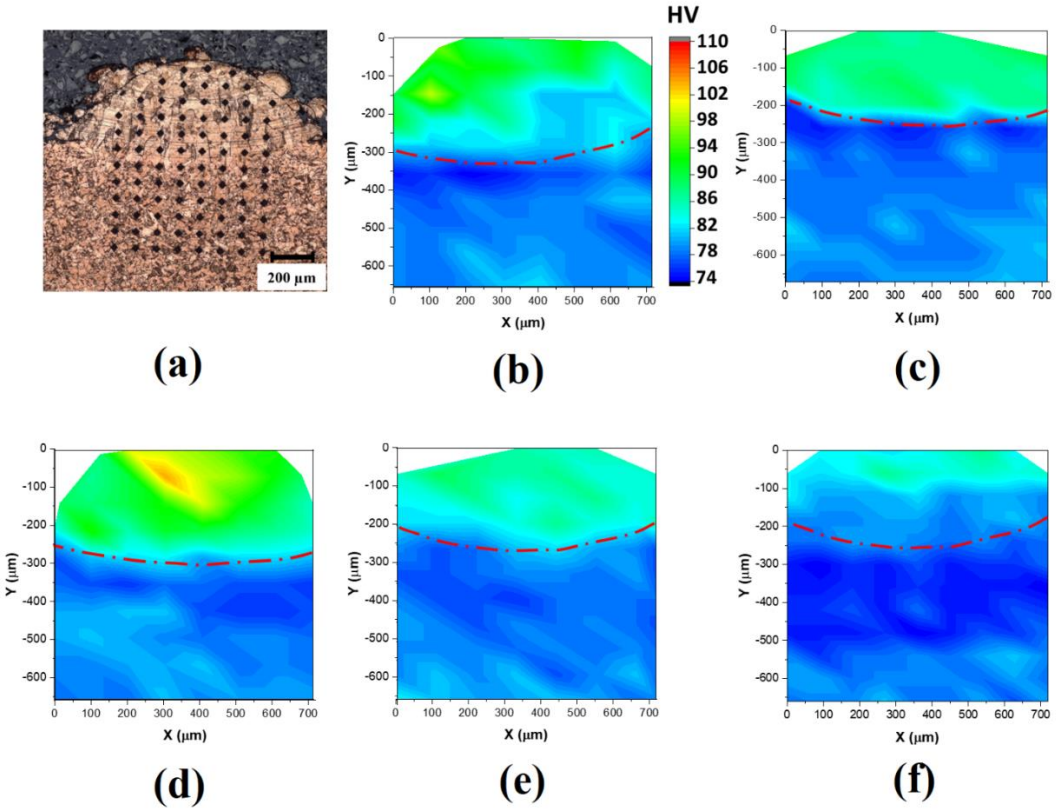


Figure 3-8 (a) Indentation map of sample 1, (b-f) Microhardness maps of Samples 1 to 5. The red-dashed lines indicate the melt pool boundaries

3.2.3 Results and discussions; cuboid geometry

Process parameter optimization of single-layer multitrack

After optimizing the process parameters for single tracks, it was about the time to adjoin them horizontally with a proper overlapping ratio through the bidirectional (zigzag) strategy to form a single-layer deposition so so-called "multi tracks". In that regard, the key process parameters are the ones introduced in the previous section, plus the overlap ratio (OR), which is defined as the ratio of the overlapping distance of two clads over the total distance from one end to the other. The responses in this study are the average deposition height (h_{avg}), dilution (D), flatness ratio (S), and surface roughness (Sa). Figure 3-9 schematically shows the geometrical characteristics of a multitrack deposition. Table 3.3 details the input variables and output responses of the DOE matrix for the cuboid geometry.

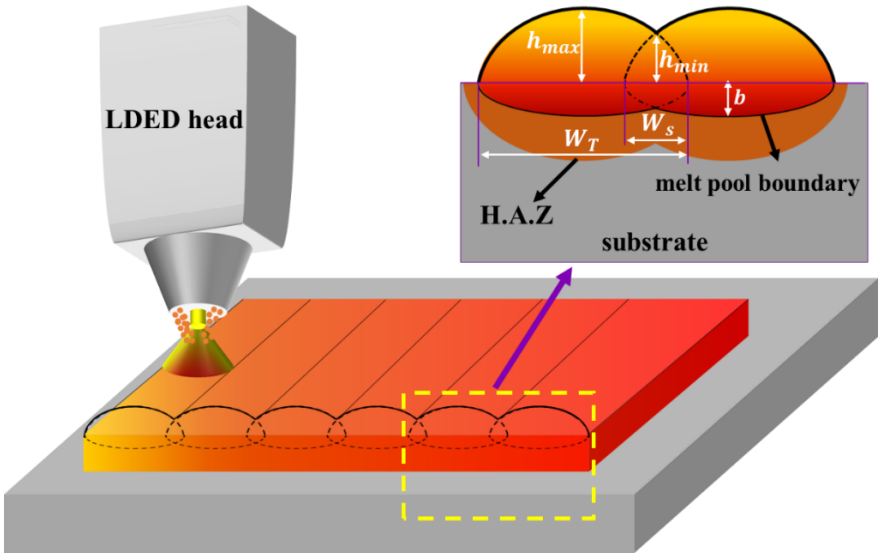


Figure 3-9 LDED multitrack one-layer deposition and its geometrical characteristics

Table 3.3 the input variables and output responses of the DOE

Track NO.	**Process parameters (input variables)**				**Geometrical measurements (output responses)**			
	***P* (W)**	***V* (mm/s)**	***F* (g/min)**	***OR***	$h_{avg}(\mu m)$	***Sa(μm)***	***D(%)***	***S***
1	1250	6	6	0.2	91.15	17.37	55.75	0.57
2	950	4	4	0.2	60	41	0	1
3	1550	6	6	0.4	163.47	32.25	56.15	0.61
4	950	8	4	0.6	193.23	33.13	0	0.43
5	1250	6	6	0.6	232.39	47.13	38.39	0.52
6	1250	8	6	0.2	71.13	15.83	57.70	0.50
7	950	6	6	0.4	205.59	55.7	0	0.26
8	950	8	4	0.2	56.93	31.51	0	1
9	1250	6	6	0.4	122.90	27.1	48.30	0.63
10	950	4	8	0.4	282.35	88.12	0	0.51
11	1550	4	8	0.6	615.88	243.17	4.34	0.88
12	1550	4	4	0.4	88.92	22.64	54.17	0.64
13	950	6	6	0.6	313.47	60	0	0.44

14	1550	8	8	0.6	308.20	65.83	22.10	0.52
15	1250	8	6	0.4	102.92	20.21	48.53	0.57
16	1250	6	6	0.4	117.44	24.73	55.22	0.66
17	950	4	8	0.2	204.32	62.15	0	0.59
18	950	4	4	0.6	184.37	34.71	0	0.51
19	1250	4	6	0.4	162.44	29.81	34.98	0.56
20	1250	4	6	0.6	247.34	42.57	26.10	0.53
21	1550	4	8	0.4	387.72	91.31	6.73	0.59
22	1550	8	8	0.4	217.29	46.55	28.70	0.62
23	1550	6	6	0.6	231.85	46.88	47.44	0.59
24	1250	6	8	0.4	188.85	39.91	16.48	0.63
25	1250	6	4	0.4	122.01	19.79	38.27	0.52
26	950	8	8	0.2	314.77	72.25	0	0.35
27	950	4	8	0.6	613.93	167.2	0	0.60
28	1250	4	6	0.2	132.34	34.19	39.77	0.69
29	1250	6	6	0.2	95.90	22.5	60.16	0.66
30	1250	6	6	0.4	110.35	30.11	56.75	0.81
31	1550	4	8	0.2	268.99	81.82	9.42	0.69
32	1250	8	6	0.6	128.76	29.42	42.98	0.54
33	1250	6	8	0.6	393.95	124.56	8.64	0.74
34	950	8	8	0.6	1213.51	495.21	0	0.80
35	950	8	4	0.4	68.60	20.87	0	0.70
36	1550	8	4	0.4	70.18	15.77	71.27	0.67
37	1250	6	6	0.2	95.48	18	60.27	0.61
38	1250	6	6	0.6	192.06	45.45	42.99	0.79
39	950	8	8	0.4	408.05	106.92	0	0.48
40	950	4	4	0.4	96.73	26.44	0	0.59
41	1250	6	8	0.2	141.32	30.94	20.87	0.62
42	950	6	6	0.2	137.46	35.87	0	0.45
43	1550	6	6	0.2	97.60	21.79	68.20	0.73
44	1550	4	4	0.2	71.49	19.13	59.52	0.71

45	1550	8	4	0.6	154.72	25.1	52.95	0.55
46	1250	6	4	0.2	76.86	20.79	49.60	0.70
47	1550	8	4	0.2	59.02	11.96	74.68	0.56
48	1550	4	4	0.6	186.34	43.39	36.06	0.65
49	1250	6	4	0.6	213.10	50.9	26.19	0.60
50	1550	8	8	0.2	187.88	42.54	31.76	0.63
51	1250	6	6	0.6	235.54	52.49	38.078	0.64

Figure 3-10 (a) reveals a general view of geometrical measurement of a multitrack deposition by microscope. After measuring all the responses, the RSM analysis was performed and optimizing the process parameters is then followed. The compliance function was set to maximize the average height (h_{avg}) and minimizing both the flatness ratio (S), and surface roughness (Sa), while keeping the dilution (D) in the range of 20-30% [48], [50]. The optimization solution, shown in Figure 3-10 (b), offered the set of process parameters for P, V, F, and OR to be 1500 W, 4.5 mm/s, 4 g/min, and 0.4, respectively that altogether would result in the highest desirability criteria (1). To confirm this set of process parameters as the optimum ones and validate the optimization procedure, it was printed with three replicates, and the result is shown in 3-10 (c). The mean values of experimental measurements were in good agreement with both low and high 95% confidence levels of the predicted responses.

a) responses and geometrical measurements of a multitrack one-layer

- **Flatness ratio:**

$$S = (h_{max}\text{-}h_{min})/h_{max}$$

- **Dilution:**

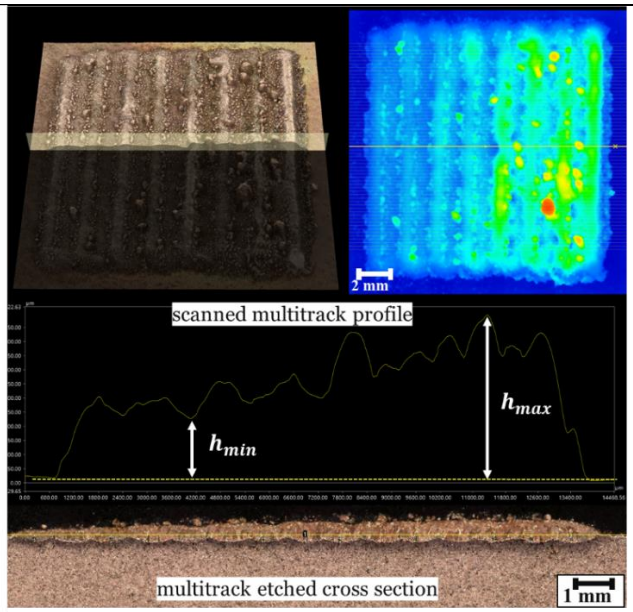
$$D = b_{avg}/(h_{avg} + b_{avg})$$

- **Average height:**

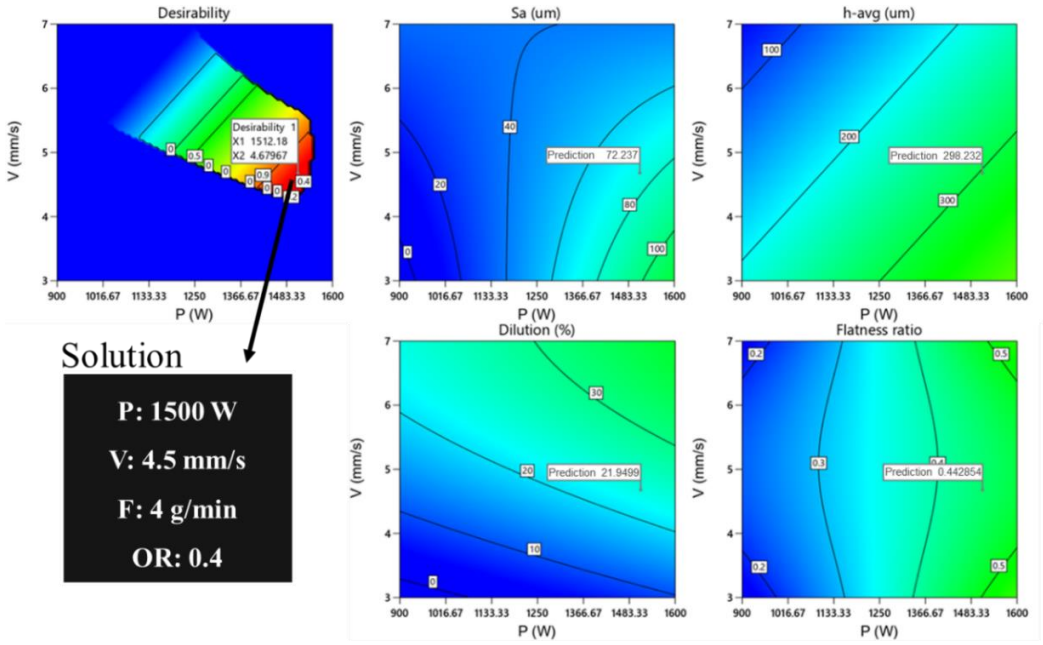
$$h_{avg} = \sum_0^n h_i / n$$

- **Surface roughness:**

$$S_a = \frac{1}{A}\iint Z_{(x,y)}\,dxdy$$



b) 2D contour plots of desirability and optimization results



c) validation of optimization results

Confirmation

Two-sided Confidence = 95%

Analysis	Predicted Mean	Std Dev	n	SE Pred	95% PI low	Data Mean	95% PI high
Sa	72.237	17.7657	1	20.5838	72.7542	92.92	114.72
h-avg	298.232	28.2745	1	33.0176	229.93	315	366.534
Dilution (%)	21.9499	3.61594	1	4.02561	13.659	19.99	30.2408
Flatness ratio	0.442854	0.0912731	1	0.0995823	0.23816	0.544	0.647548

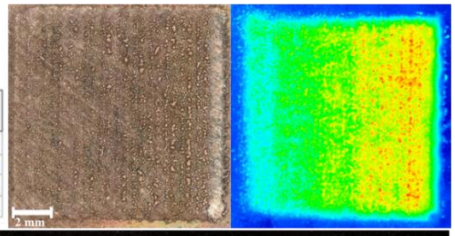




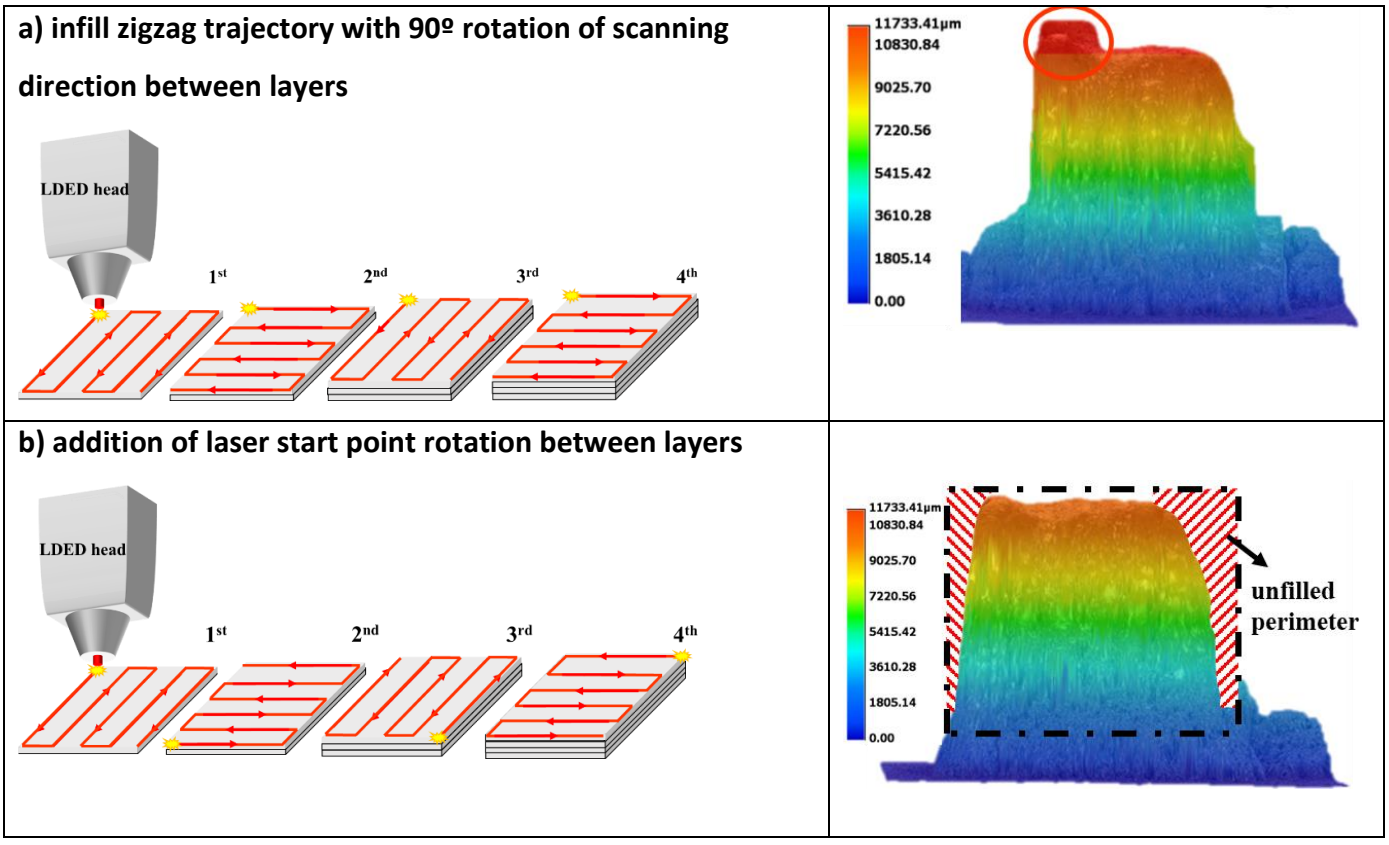
Figure 3-10 (a) responses and geometrical measurements of a multitrack one-layer, (b) Optimization solution and desirability plot, (c) Confirmation test of the optimization results

Multi-layer build-up and trajectory planning

In order to build up a multilayer cuboid geometry, the multitrack one-layer needs to be deposited on top of each other repeatedly using the optimum set of process parameters. Yet, even if the single layer height is uniform, which is practically not, the superimposition of single layers seldom leads to a high dimensional accuracy over multiple layers. More specifically, in robotic LDED systems, the movement of the robot arm during deposition can be categorized into three distinct phases: initial acceleration to attain the desired speed, consistent uniform motion, and eventual deceleration as the process concludes. In the acceleration and deceleration phases, employing a reduced scan speed contributes to elevated heat input. As a result, this translates into an increased deposition rate and heightened accumulation of heat. Furthermore, insufficient deposition rates in proximity to edges primarily trigger deviations and the emergence of raised formations during the build-up process. [31]. Therefore, proper build-up strategies and techniques must be considered for tool path trajectory planning to reach near net shape of the desired geometry.

Figure 3-11 shows the schematics of the multiple techniques that were implemented in tool path trajectory planning along with their effect on the shape accuracy. As shown in Figure 3-11 (a), in this study, the zigzag deposition strategy with 90-degree rotation in the deposition direction between each layer is selected as the standard infill method. The unidirectional strategy (offset pattern) was not chosen due to the low deposition rate. Spiral inward/outward pattern is also not suitable for regular cuboid geometries because they cause varying scan-length and potentially higher heat accumulation near the center due to shorter cooling intervals between overlapping laser

passes. In addition, as depicted in Figure 3-11 (b), the starting point was constantly rotated after each layer to balance out varying deposition height in each layer. Figure 3-11 (c) shows the profile contouring after the infill deposited layer and its effect that was considered to avoid the common dome-shaped issue. In fact, due to the lower deposition rate at the edges of the cuboid, the perimeter remained unfilled to some extent which was tackled by adding one-line contouring with a proper amount of overlap with the previously deposited infill layer. Although the profile contouring maintained the squareness of the cuboid built-up, it resulted in arisen corners due to the higher deposition at those regions. Thus, as shown in Figure 3-11 (d), for the corners of the contour's path an arc with a radius of 0.7mm, which is half of the melt pool width, was considered. This resulted in avoiding sharp corners which creates a delay in changing direction and therefore higher deposition at the corners. All the aforementioned techniques were employed to reach the cuboid build-up with acceptable shape accuracy shown in Figure 3-11 (d).



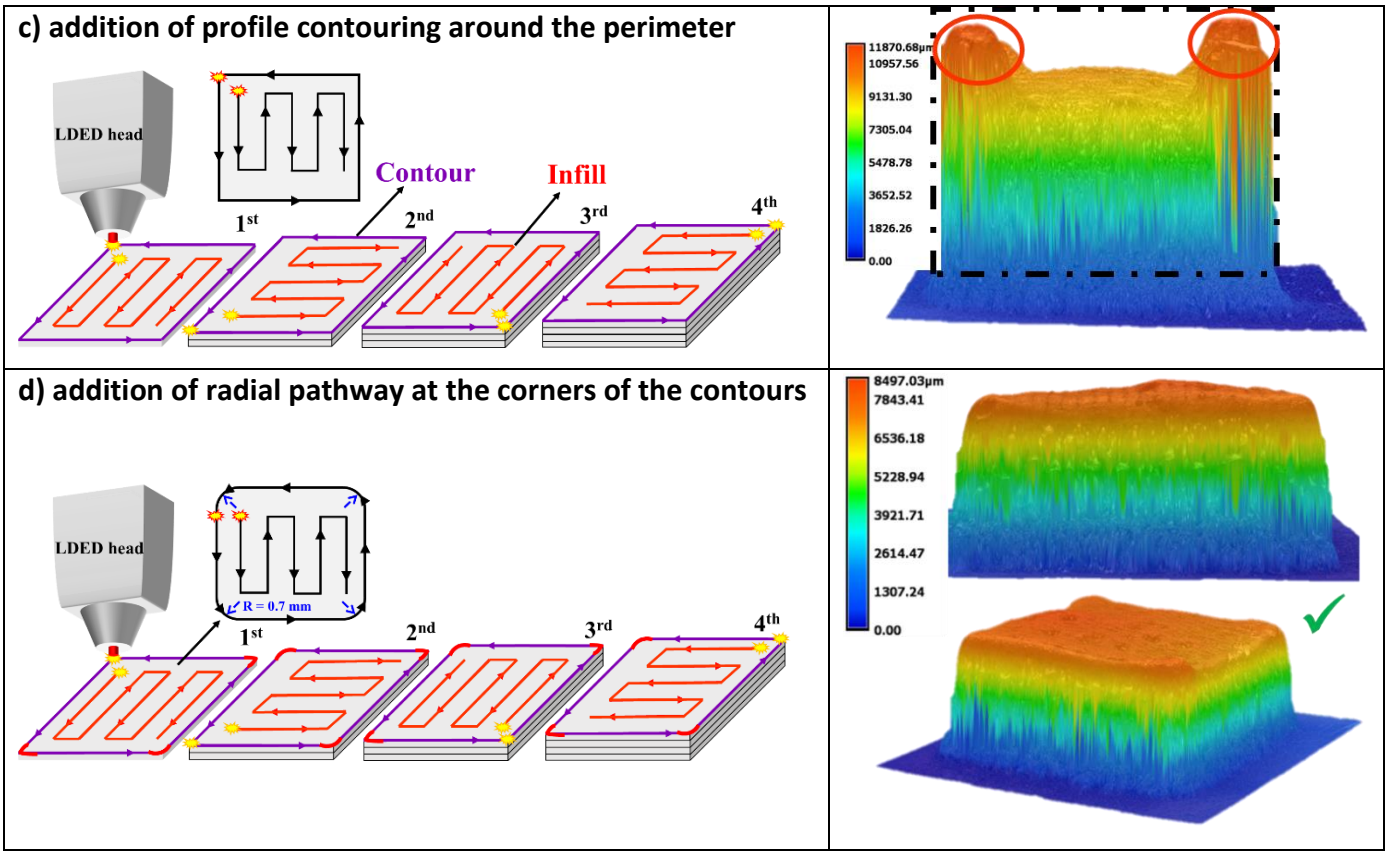


Figure 3-11 Schematic of the strategies that have been considered for tool path trajectory planning; (a) infill zigzag trajectory with 90º rotation of scanning direction between layers, (b) the effect of start point rotation for the laser on geometrical accuracy, (c) the effect of addition of profile contouring around the perimeter, (d) the effect of addition of radial pathway at the corners of the contours

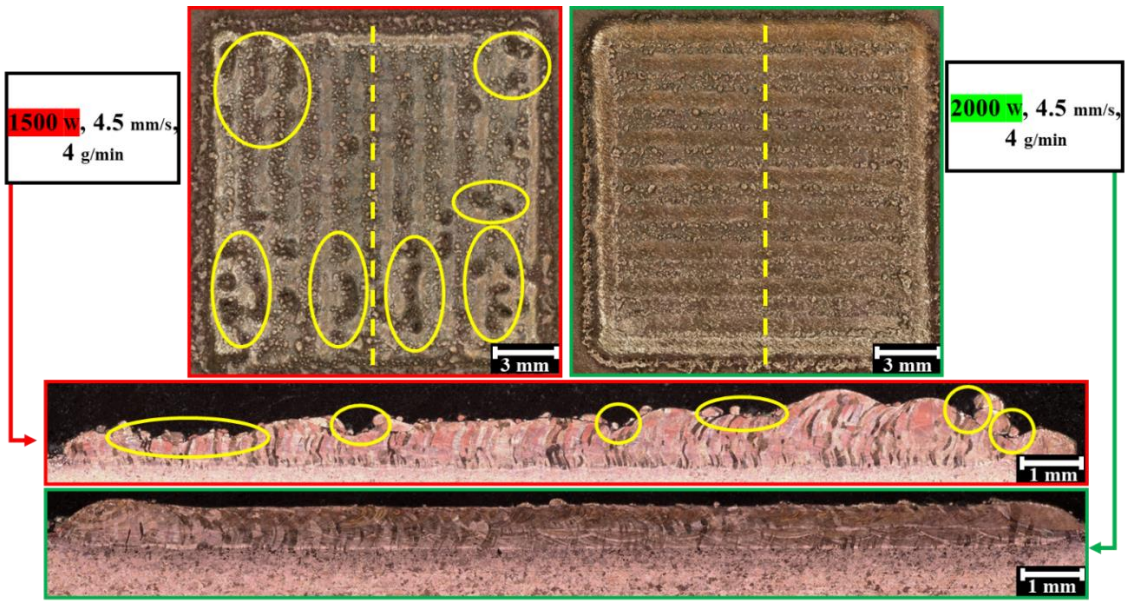
Defects and processability map

Beside the process parameter optimization and correct toolpath trajectory planning, there are some other issues that appear through multilayer fabrication and need to be tackled. As such surface dimples have been seen on the top layer of some specimen with specific process parameters. In that regard, investigation has been conducted on the effect of process parameters on the surface dimples effect and results have been illustrated in Figure 3-12. Using the set of process parameters that was optimized for multitrack single-layer and the coorect tool path trajectory, surface dimples was appeared as shown in Figure 3-12(a) from top view and in the cross-section. Yet, increasing the laser power from 1500 to 2000 W resolved this issue. Moreover, in another case shown in Figure 3-12(b) increasing the scanning speed from 4 to 8 mm/s also resulted in disappearing these defects. After giving a precise look at the cross section of the samples and putting all the parameters

together, it was concluded that the source of the surface dimples is in fact the lack of fusion, which is one of the most common issues in LDED.

LOF porosity can be identified by its large and irregularly shaped pores and often contain unmelted powder particles similar to what have been observed from the cross section of defective samples in Figure 3-12. These defects are normally attributed to incorrect processing parameters and/or condition such as oxidation during the deposition process that is the case in this study as the process take place in ambient atmosphere and decrease the efficiency of input energy such that not all powder are compeletly melted or the previously deposited layer not sufficiently remelted to fuse with the new layer. For the CuCrZr multilayer processing parameters investigated and it can be readily observed that LOF porosity occupies the low laser power, and low scanning speed that leads to high F/V which indicate the amount of powder that are fed to the meltpool and the deposition thickness. It is worth mentioning that although the lower scanning speed increase the energy density to some extend, its effect on F/V value is stronger based on the observations in this study. This behavior agrees well with the general hypothesis that points to low power input per amount of material or alternatively low energy density as the primary source of LOF porosity.

a) effect of Laser power on the surface dimple defects:



b) effect of scanning speed on surface dimple defects:

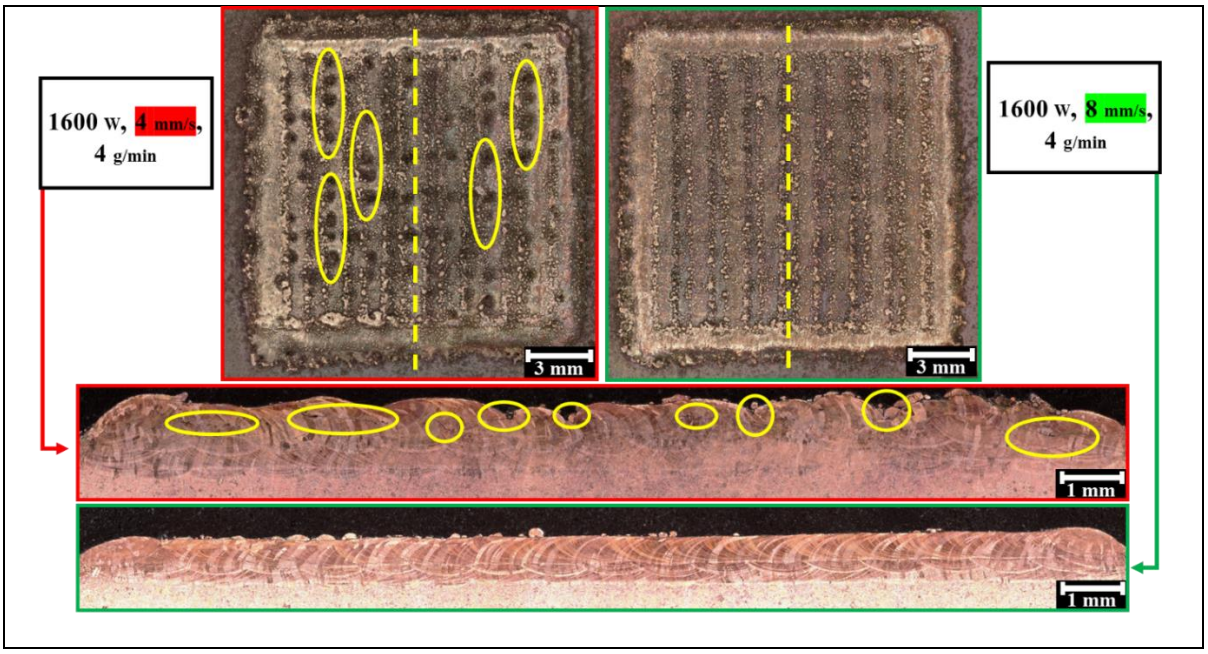


Figure 3-12 effect of laser power and scanning speed on surface dimples

In that regard, Tang et al. [65] developed the Equation 3-3 that predicts the LOF defect happening based on the geometrical parameters and characteristics of the melt pool:

$$\left(\frac{h}{b}\right)^2 + \left(\frac{H}{W}\right)^2 \leq 1 \qquad \text{(equation 3-3)}$$

in which h is the deposition height, b is the melt pool penetration depth, H is the hatching distance, and W is the melt pool width. Based on this equation, measurements were conducted on some defective and fine samples and results are plotted in Figure 3-13 where four samples were selected for porosity analysis using CT scan technique. As shown in the plot both sample 1 and 2 are inside the LOF quadrant which do not have any sign of LOF defects, while the sample 3 and 4 are located in the outside of the criterion and have noticeable amount of LOFs. These results show that the CuCrZr buildup follow the LOF geometric criterion very well. As attained in the optimization procedure, the H/W (OR) value was defined to be 0.4, which consequently leaves the melt pool penetration depth and the deposition height as the only crucial parameters. Where the former is mainly controlled by the laser power and the later is defined by F/V value. Therefore, maintaining a constant value of energy density, which is the ratio of P to F/V, can avoid LOF in CuCrZr build up.

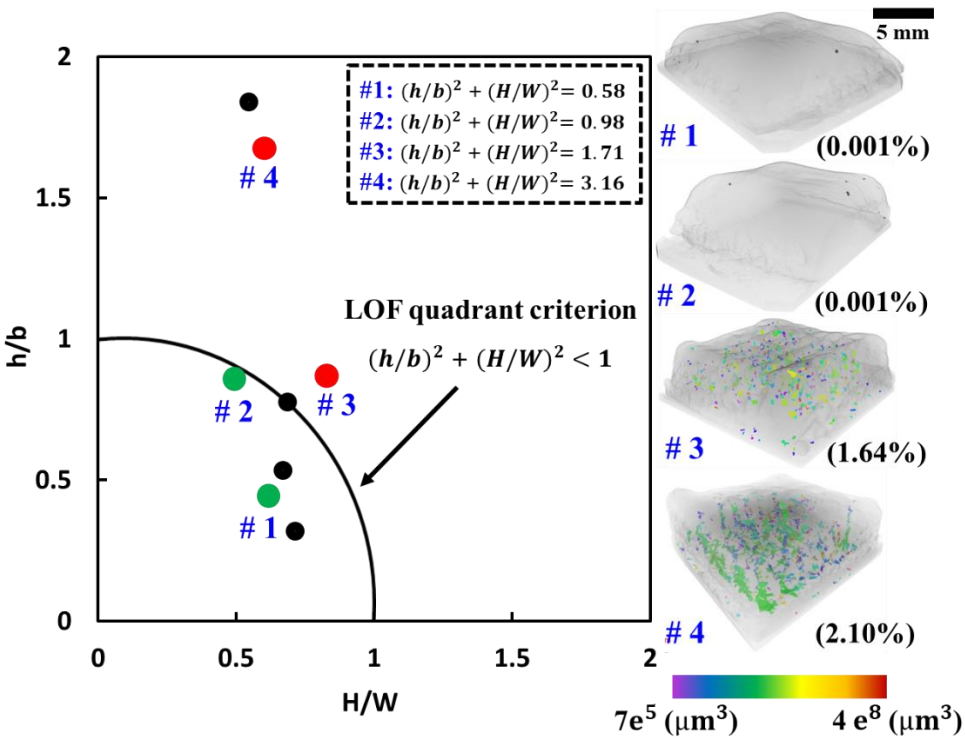


Figure 3-13 Lack of fusion map of cuboid samples

Vaporization

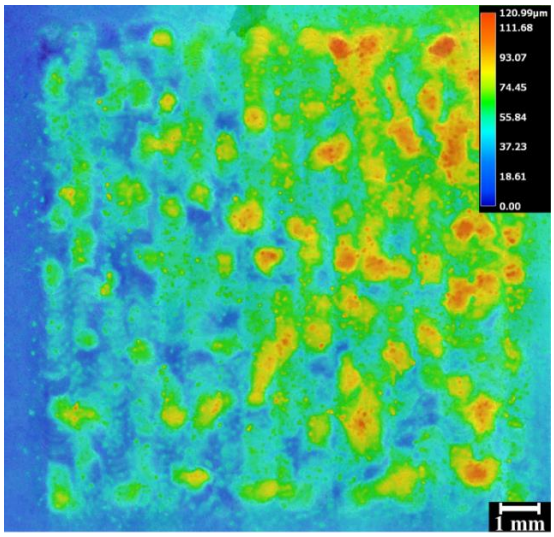
The nature of a high intensity laser beam with high power densities (>10^5 W/mm^2) and short interaction times (micro to milliseconds) leads to vaporization and ejection of molten material during the deposition process which are not desirable in LDED and more preferable for laser drilling/cutting [66]. This vaporization results in a loss of alloying elements and keyhole formation particularly in multilayer build up that adversely affect the mechanical properties and microstructure. As shown in as seen in Figure 3-14 (a), vaporization took place due to too much power (from 1800 to 2000 W) per low F/V values (from 0.003 to 0.005 g/mm) that lead excessive energy density and evaporation of material from the substrate instead of deposition.

Balling

Balling, which is the formation of the small ball-shape discontinuous deposition of melted powders on top of the substrate or previous layer [67], was observed in the single-layer multitrack samples. In fact, whenever the laser power is not sufficient to melt the both substrate and powders together, a stable melt pool cannot be formed and only partially melted powders that have relatively high solid–liquid interfacial free energy γ_{SL} join together and poorly connect to the substrate instead of

properly wetting it as seen in Figure 3-14 (b). The parameters that cause balling in single-layer can often bring about defects when they are used for multilayer buildup. These defects include large pores, inclusions, and poor surface roughness [68].

a) vaporization in LDED of CuCrZr samples:



b) poor wetting in LDED of CuCrZr samples:

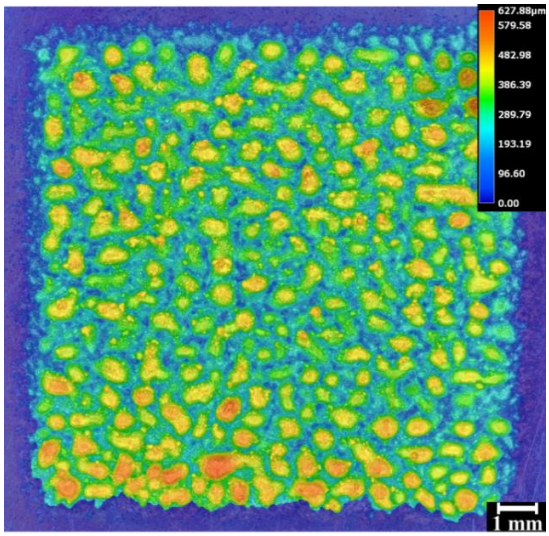


Figure 3-14 vaporization and poor wetting as results of excessive and insufficient power per F/V, respectively.

General processability map

Placing all the data together, the general processability map of CuCrZr via LDED technique is drawn based on the key process parameters of laser power (P) per F/V values. As seen in the yellow region, the green straight line shows the minimum laser power of 1100 W that is needed for the fed powders to properly melt and wet the previous layer/substrate and form a stable melt pool and avoid the balling defect. Above the green line in the blue region, the blue line is fit to the data that have a few LOF defects and draws the boundary between the blue and green regions, which define the LOF-rich and fine deposition regions, respectively. In the green region, only few spherical gas porosity was seen in the samples, that is common and acceptable in LDED as there are always gas pores that are entrapped in the powder particles and/or oxidation during the process. Separated by the red line from the green region, the red region stands for too high values of power per relatively low values of F/V that results in vaporization of the powder and substrate material which is not a desirable phenomenon in LDED. Therefore, as shown in Figure 3-15 to correctly deposit CuCrZr

alloy and avoid the aforementioned major defects/instabilities, both the P and F/V values must be kept in the green deposition region.

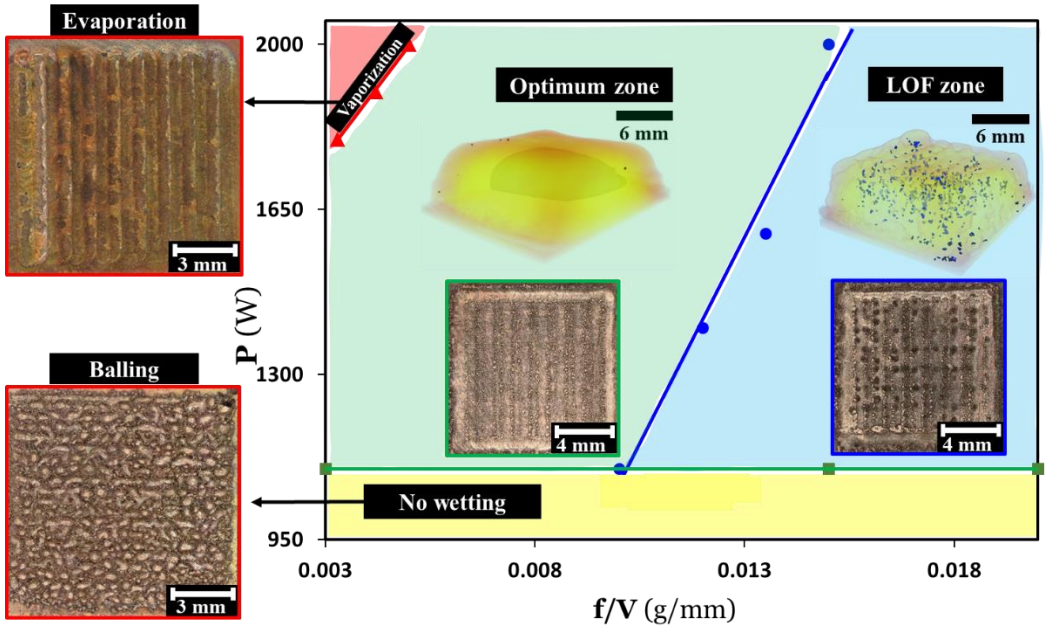


Figure 3-15 General LDED processability map of CuCrZr alloy

Grain structure analysis

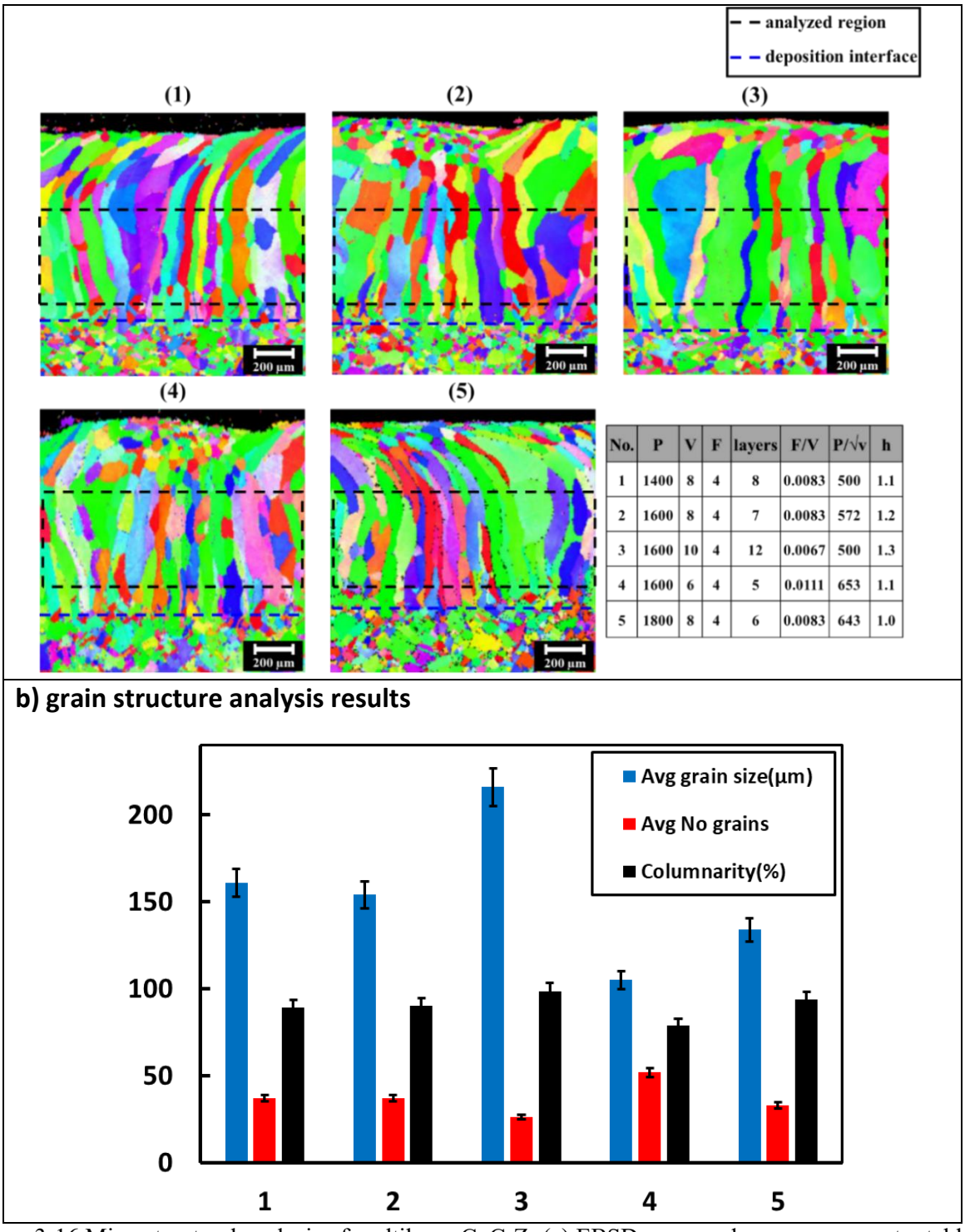
The microstructure of the LDED deposited samples is directly influenced by the main process parameters. As such laser power, scanning speed, powder feed rate, and number of layers are the parameters that have been frequently identified as the key parameters influencing the microstructure during multilayer deposition[57], [69]. In a single melt pool, solidification is directly influenced by the laser power, scanning speed, and feed rate that altogether control the geometry, thermal gradient, solidification speed, and number of nucleation sites. On the other hand, during the multilayer build-up process with LDED, the multiple deposition of single layers on top of each other leads to re-melting and inducing thermal cycles in the previously deposited material that leads to recrystallization and grain growth in the microstructure [69].

To identify the effect of process parameters on the microstructure, five cuboid samples are printed with almost the same height but different process parameters that are still in the green region of the processability map, and results from EBSD analysis are shown in Figure 3-16. The grain structure of all the samples with their process parameters are illustrated in Figure 3-16 (a) in which highly columnar grains are grown from the fusion zone interface with the substrate towards the

curved top surface of the deposit. Near the boundary of the pool, where the pool is nearly orthogonal to the observed cross-section, the grain growth direction is approximately in plane with the transverse section, as a result of epitaxial grain growth mechanism and high values of G/R [70][58]. Yet in the very top region and close to the surface, fine equiaxed grain structure can be seen due to the relatively low values of G/R and more nucleation sites [71], [72]. A certain area of the deposition region in the samples is selected for further analysis. The average grain size, average number of grains, and columnarity of the grain structure are illustrated in Figure 3-16 (b). Based on the average grain size results, sample 3's grain structure is significantly coarser than sample 4 while its average number of grains is much smaller.

It is possible that the lower value of F/V, which identifies the amount of powder that is fed to the melt pool distance, leads to a reduced number of nucleation sites [58], [59], which contributes to the number of grains and therefore their size. Additionally, a higher number of layers in sample 3 resulted in more cycles of reheating and cooling of the previously deposited material, and this in turn affects the temporal evolution of the grains and their sizes. The proposed mechanisms are further supported by the observation of a higher columnarity of the grain structure in sample 3. This suggests that the factors influencing the growth of the grains in this sample are consistent with the proposed mechanisms and highlights the importance of considering multiple factors in understanding the evolution of grain structure. Therefore, different grain structures, which influence the mechanical properties [73] can be achieved for the same deposition height while still being in the optimum processing window.

a) EBSD maps of the five samples with their process parameters table



No.	P	V	F	layers	F/V	P/√v	h
1	1400	8	4	8	0.0083	500	1.1
2	1600	8	4	7	0.0083	572	1.2
3	1600	10	4	12	0.0067	500	1.3
4	1600	6	4	5	0.0111	653	1.1
5	1800	8	4	6	0.0083	643	1.0

Figure 3-16 Microstructural analysis of multilayer CuCrZr (a) EBSD maps and process parameter table of the five samples with almost the same deposition height, (b) Grain structure analysis results

3.3 Laser directed energy deposition of IN625 powders

A similar systematic investigation has been done for LDED processing of IN625 to optimize the process parameters hierarchically from single tracks to multilayer cuboid geometry. The same methodology of statistical optimization as for CuCrZr was followed, and the analysis results for each step are illustrated in the following.

3.3.1 Single-track deposition and optimization

Figure 3.17 briefly illustrates the optimization of the main process parameters, which are laser power (P), powder feed rate (F), and scanning speed (V), the procedure for single tracks. Here the responses are deposition rate (DR) and dilution (D). Due to the limited thermal conductivity of IN625 and to avoid too much heat accumulation a theoretical criterion of laser energy per feed rate (LEPF) has been defined, which is directly calculated based on the following equation:

$$LEPF = P/VF \qquad \text{(equation 3-4)}$$

In fact, it has been frequently reported that high values of LEPF lead to high thermal gradients that consequently result in a high amount of residual stresses [39], which is detrimental, as discussed in chapter 2. Based on the optimization solutions offered by the statistical model, it has been found that the optimum set of parameters is as follows: P: 526 (W), F:10 (g/min), V:5 (mm/s), which is shown by the green point in the contour plot.

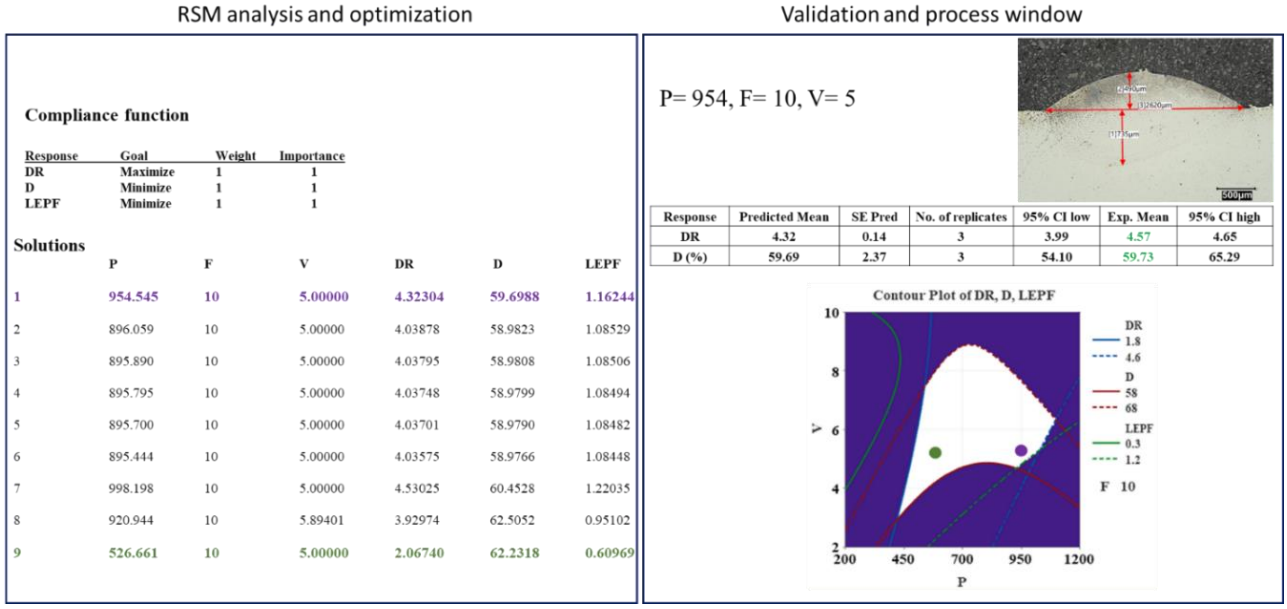


Figure 3-17 Optimization of process parameters for LDED processing of IN625 single tracks

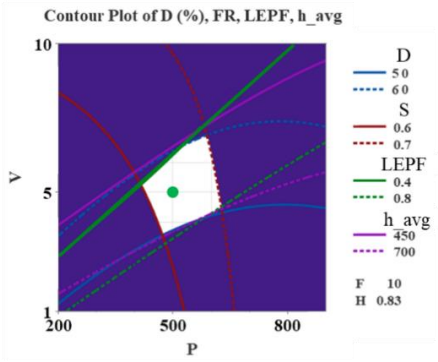
3.3.2 multitrack single-layer

Further, similar procedure has been conducted to optimize the process parameters for single-layer multitrack, and the compliance function was set to minimize the flatness ratio and dilution while maximizing the average height with minimum LEPF. It is worth mentioning that for this case, the hatching distance has been considered directly as an input parameter instead of the overlap ratio, as the melt pool width was found to be in the range of 1500 to 3000 µm in the range of the input parameters and a function of both P and V. Figure 3-18 shows the optimization procedure of single layer multi-track and validation of the optimization results. Based on the analysis, the optimum set of process parameters are as follows: P:500 (W), F:10 (g/min), V:5 (mm/s), and H:0.83 (mm) which yields to overlap ratio of 0.5.

a) optimized process parameter window

Compliance function

Response	Goal	Weight	Importance
h_avg	Maximize	1	1
D	Minimize	1	1
LEPF	Minimize	1	1
S	Minimize	1	1



Optimization solutions

	P	F	V	H	D	S	LEPF	h_avg
1	500.000	10.0000	5.00000	0.836066	54.8279	0.640462	0.53937	575.197
2	500.000	10.0000	5.00000	0.836066	54.8279	0.640462	0.53937	575.197
3	500.000	10.0000	5.00000	0.836066	54.8279	0.640462	0.53937	575.197
4	500.000	10.0000	5.00000	0.836066	54.8279	0.640462	0.53937	575.197

b) validation of optimization results

Response	Predicted Mean	95% CI low	Exp.Mean	95% CI high
h_avg	575.20	420.92	**612.05**	729.52
D	54.83	47.55	**54.90**	62.11
S	0.64	0.33	**0.65**	0.95

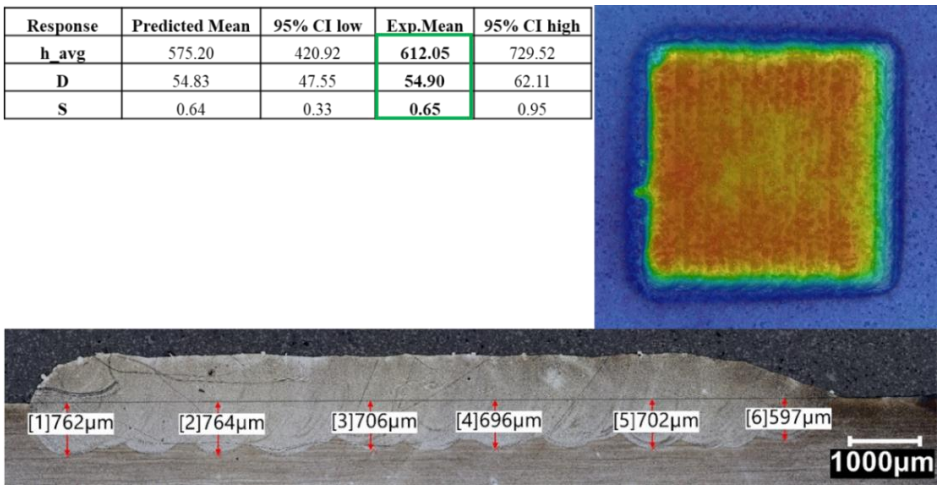
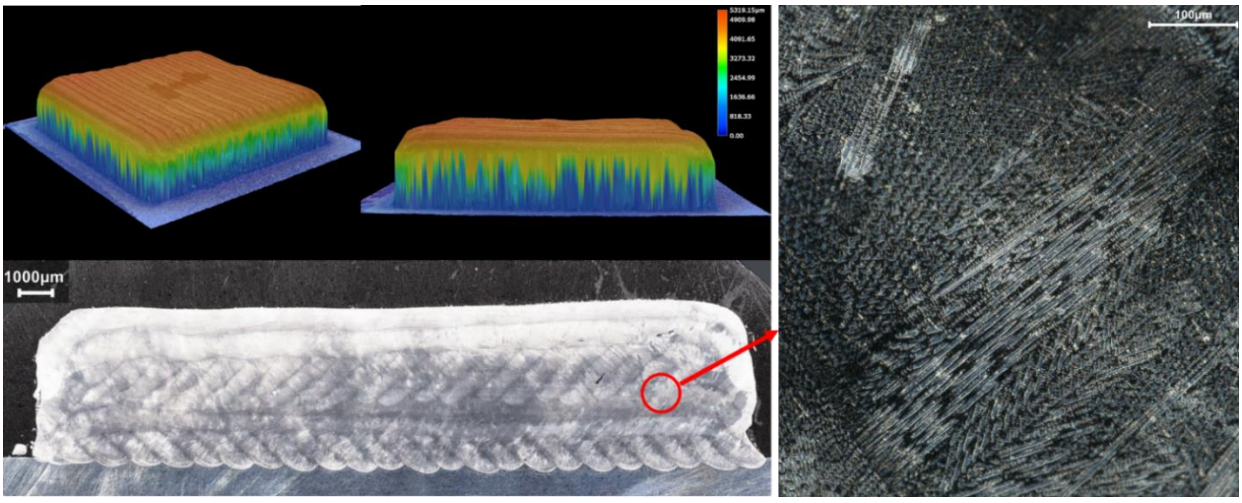


Figure 3-18 optimization of process parameters for LDED processing of IN625 single-layer

3.3.3 multilayer cuboid buildup and microstructure

Having the optimum set of parameters for a single layer of a cuboid geometry, a multilayer build can be exercised to fabricate the cuboid geometry. Therefore, the same tool path strategy optimized for the CuCrZr cuboids was implemented to fabricate near-net-shape cuboids. Figure 3.19 (a) illustrates the 3D scanned view of the fabricated cuboid along with its etched cross-section in which the columnar dendritic microstructure is magnified and shown in Figure 3.19 (b).



(a) (b)

Figure 3-19 (a) LDED multilayer cuboid build up of IN625, (b) solidification microstructure

3.4 Summary and conclusions

In this chapter, additive manufacturing of CuCrZr and Inconel 625 alloys have been exercised separately via LDED-PF process. The present study investigates optimizing the key process parameters, printing strategy, and developing the optimum processing window, from the scale of single track to multilayer, which altogether results in defect-free products. CuCrZr alloy was the focus of this part of the study due to the challenges associated with its laser processing as a result of its high heat conductivity and low laser energy absorption, along with the big gap in the literature for LDED of this material. In addition, microstructural characterization has been done to comprehend the impact of key process parameters. The results of the study can be summarized as follows:

1) The process parameter optimization has been done for each alloy hierarchically from single-tracks to single-layer multitrack through RSM method, and the optimized set of process parameters are in good agreement with the model predicted values with ~95% low and high confidence intervals.
2) Tool path trajectory planning has been conducted to reach the proper build-up strategy that leads to acceptable shape accuracy. For the infill of the geometry, the zigzag strategy with 90º rotation of deposition direction in which the start point also rotates between layers is considered. Further, to compensate for the unfilled perimeter, profile contouring around the perimeter after each infill deposition was considered with a radial pathway at the corners to avoid the bumps that happen as a result of acceleration and deceleration of the robotic arm.
3) For CuCrZr alloy, the general processability map was drawn as it was a gap in the literature and by putting all the data together and based on the P against F/V parameters.
4) The grain structure of the deposition mainly consists of big columnar grains that nucleated from the fusion zone and grew up to the very top layer through epitaxial grain growth mechanism. Yet on the very top layer and close to the surface the fine and equiaxed grain structure has been observed due to the relatively lower values of G vs R and more nucleation sites. Depositing new layer provides reheating and cooling for the formerly deposited layer that leads to grain growth and increasing the grain size.

Chapter 4: Development of Inconel 625-CuCrZr gradient

4.1 Introduction

The aerospace industry desires to develop new advanced materials that offer a longer service life. There is an evolution in the AM sector to manufacture multi-functional parts made of multiple materials that each enable functionality. The concept of Functionally Graded Additive Manufacturing (FGAM) has been introduced recently by which different gradients in the form of either controlled porosity, orientation, microstructure, or composition can be fabricated. For the aerospace industry, cooling the components that are mainly made of Ni-based superalloys such as IN625 can be challenging due to their limited thermal conductivity. Therefore, there is interest in using a highly heat-conductive material like CuCrZr in some sections of the components, such as cooling channels, to ease heat dissipation while maintaining strength and corrosion resistance. In that regard, LDED technology has shown its capability to be employed for FGAM of IN625-CuCrZr. Yet, this material system is difficult to be processed due to large thermophysical property mismatch and high reflectivity issues at near infrared wavelengths for CuCrZr.

This chapter investigates the process route for FGAM of IN625-CuCrZr using a multi-powder feeder LDED system. In situ alteration of the composition followed by process parameters adjustment through various layers is practiced with different types of composition transition to study FGAM of such material system in both macro and micro scales.

4.2 FGAM of Inconel 625- CuCrZr

The initial set of laser-deposited gradients considered in this study consisted of transitions between IN625 and CuCrZr alloy, either by a sharp or gradual composition change. This type of FGAM was fabricated prior to the start of this thesis in the aerospace sector [19], [20], but only in sharp compositional transition cases, while their characteristics had not yet been reported, and there is no systematic study on their fabrication and challenges in the literature.

4.2.1 Powders

Gas-atomized IN625 and CuCrZr powders were used as feedstock materials in this study. The chemical compositions of both powders are shown in Table 4-1, and Figure 4-1 illustrates their morphologies and particle size distributions (PSD). Both powders are mainly spherical with a sparse number of attached satellite particles, according to the SEM micrographs. As shown in

Figure 4-1, the PSD of the powders is in the range of 50 to 125 µm for IN625 (D50 = 75 µm) and 30 to 90 µm for CuCrZr powders (D50 = 58 µm).

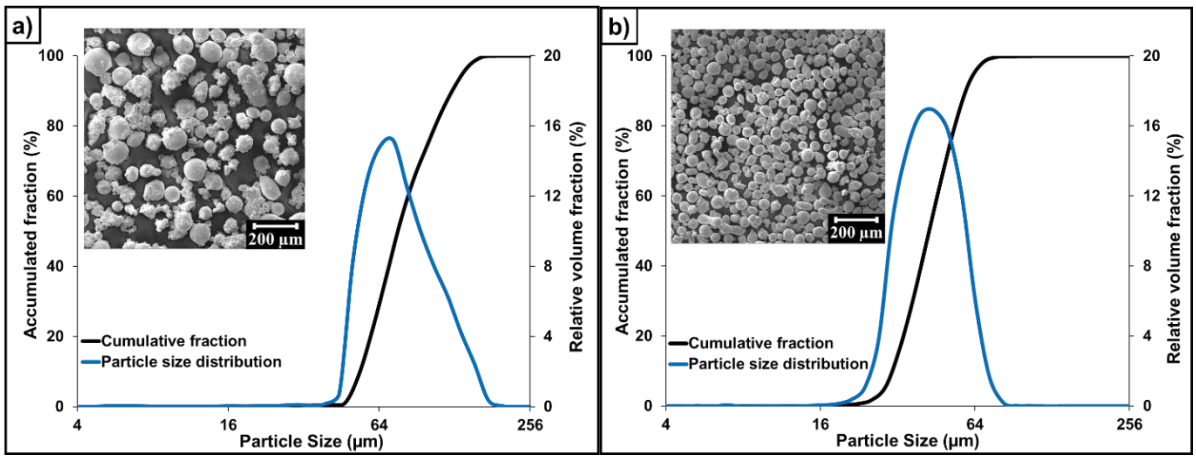


Figure 4-1 Particle size distribution and morphology of feedstock powders; (a) IN625, (b) CuCrZr.

4.2.2 L-DED processing setup

An in-house developed robotics L-DED system, shown in Figure 4-2, was used to perform the experiments. The system is equipped with a 1 kW fiber laser, dual hopper powder feeder, and coaxial nozzle. A laser spot diameter of 1.2 mm at the substrate surface is used for the deposition.

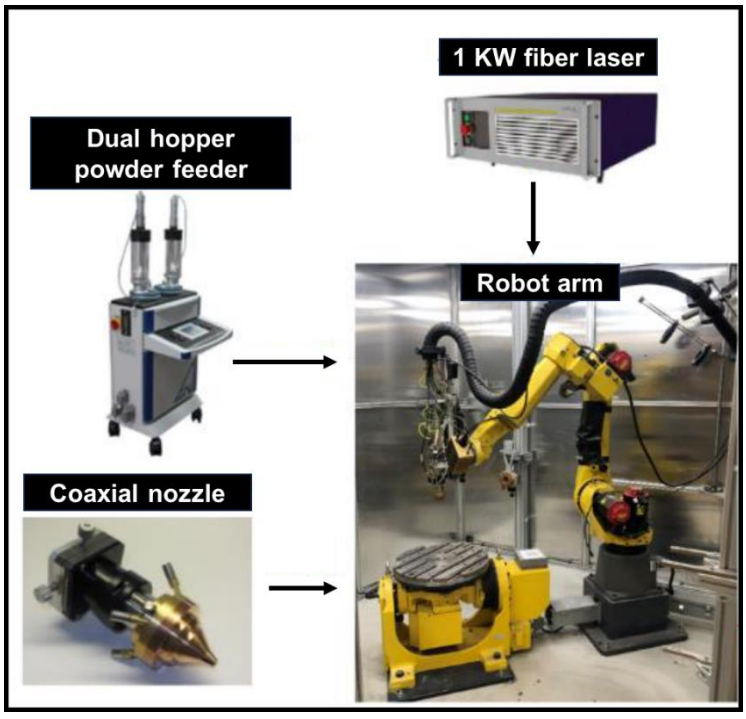


Figure 4-2 In-house robotic L-DED system equipped with a coaxial nozzle and a dual hopper powder feeder system

Figure 4-3 illustrates the powder feeder settings used in the multi-powder feeder system implemented in this study. Figure 4-3(a) displays the feed rate profile for Hopper 1, which contains IN625, while Figure 4-3(b) shows the corresponding parameters for Hopper 2 containing CuCrZr powder. As shown, both feed rates follow a linear function, allowing for precise control over the compositional ratio of the two alloys throughout the FGAM processing.

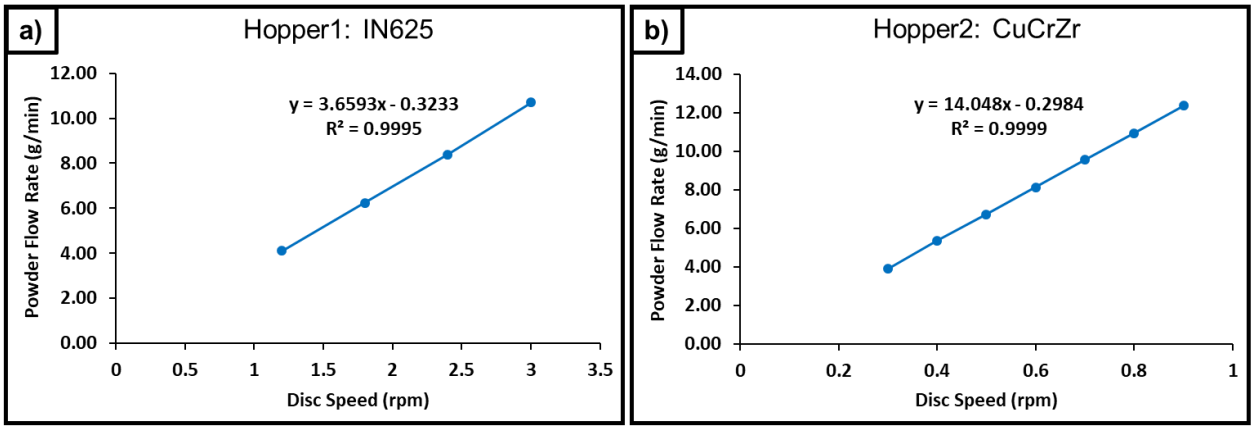


Figure 4-3 Powder feeder parameter settings: (a) hopper 1 with IN625 powders, (b) hopper 2 with CuCrZr powders

Table 4-1 Chemical composition of the IN625 and CuCrZr powders (wt.%).

Powders	Ni	Cu	Cr	Mo	Nb	Fe	Zr
IN625	67.0	-	20.0	9.0	3.0	1.0	-
CuCrZr	-	98.90	1.0	-	-	-	0.1

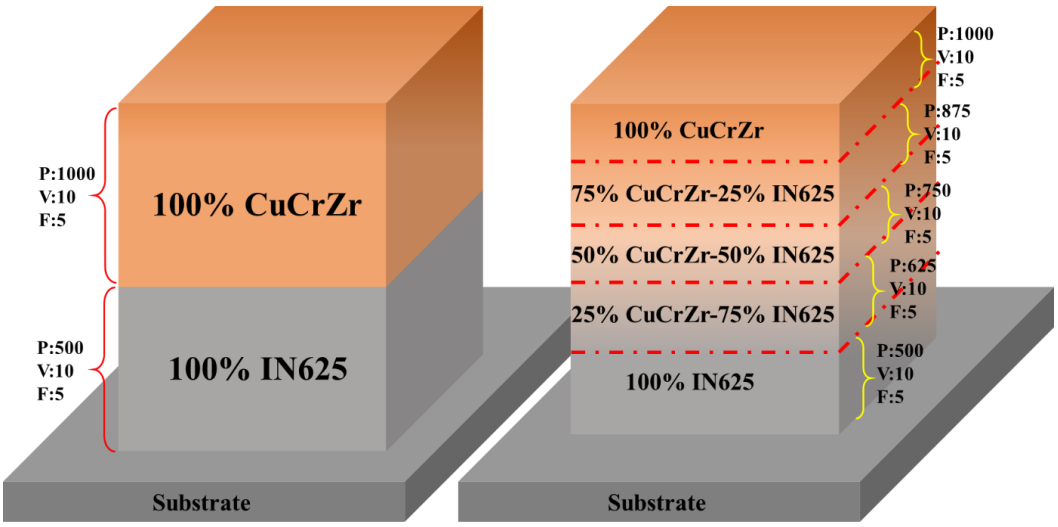
4.2.3 Fabrication approach

Figure 4-4 schematically shows the prototypes along with their composition gradient and according to process parameters made by the multi-powder feeder LDED system. Figure 4-4 (a) represents the prototype with a sharp composition transition in which it begins with 10 layers of 100% IN625 deposition on a 10 mm thick steel substrate. During this step, hopper 1, which was carrying IN625 powders, was switched on, and hopper 2, which contained CuCrZr powders was off. Right after finishing the first 10 layers, hopper 1 was turned off, hopper 2 was engaged, and 10 layers of CuCrZr were deposited on previously deposited IN625. For the gradual composition transition case shown in Figure 4-4 (b), the deposition process started with 100% IN625 and

CuCrZr gradually has been added with a 25% (weight) increment through every four layers until 100% CuCrZr composition has been reached. In both cases, only the laser power was adjusted based on the composition, and other process parameters, including laser spot size, overlap ratio, scanning speed, and feed rate were held constant throughout the deposition. A laser power of 500 W was employed for IN625, while 1000 W was utilized for CuCrZr, with adjustments made linearly for each composition and considering the proportion of each alloy. It is worth mentioning that other process parameters, such as F, V, and OR were kept constant during the process. The fraction of alloys in the powder blend at each deposited region, with respective designated labels, and laser beam absorptivity are comprised in Table 4-2. The absorptivity values for IN625 and CuCrZr are reported to be around 65% and 25%, respectively [74], [75],[76], while intermediate values for compositional mixtures are derived using the rule of mixtures.

Table 4-2 The composition of each section in the FGAM sample and the corresponding laser beam absorptivity

Region in FGM	Nominal portion of IN625 (wt.%)	Nominal portion of CuCrZr (wt.%)	Laser beam absorptivity (β)
Zone 1	100	0	0.65
Zone 2	75	25	0.55
Zone 3	50	50	0.45
Zone 4	25	75	0.35
Zone 5	0	100	0.25



(a) (b)

Figure 4-4 FGAM of IN625-CuCrZr, (a) sharp composition transition (b) gradual composition transition

4.2.4 Prototypes macroscale perspective

Figure 4-5 represents the isometric (Figure 4-5 (a)) and front views (Figure 4-5 (b), (c)) of the prototypes in macroscale. As shown in Figure 4-5 (b) macro cracking occurred in the sharp composition transition case and at the interface region that, resulted in the delamination of the CuCrZr from the IN625. However, in the gradual composition transition case shown in Figure 4-3 (c), there is neither sign of macro cracks nor any other macroscale defects. In general, the occurrence of macro cracking can be due to different reasons, such as the existence of intermetallic at the interface region that suffers from high brittleness [77], and/or a high amount of thermal stresses [78], which is more likely happened in this case. As previously stated, in the LDED process, the material is rapidly heated to the melting temperature, then cooled and solidified at an extremely fast cooling rate, and is repeatedly affected by the subsequent deposition process that yields to high thermal gradient and thermo-mechanical imbalance. This imbalance is associated with high thermal stress that results in macro cracks and delamination when exceeding the local UTS stress; otherwise remains as residual stress in the fabricated part. Here, firstly, the abrupt change of laser power from 500 to 1000 W, which was necessary to deposit the CuCrZr properly, induced a high amount of thermal gradient and thermal stress as a consequence. In addition, the mismatch in the CTE and elastic modulus between those materials also intensified thermally induced stresses at the interface region[79]. Therefore, it seems that a combination of abrupt changes in both laser power and material properties induced a high amount of thermal stress that results in crack initiation, while the cyclic heating and cooling of the LDED process also creates

expansion and contraction during the multi-layer deposition that resulted in the propagation of the crack [80]. As previously stated, in the LDED process, the material is rapidly heated to the melting temperature, then cooled and solidified at an extremely fast cooling rate and is repeatedly affected by the subsequent deposition process that yields to high thermal gradient and thermo-mechanical imbalance. This imbalance is associated with high thermal stress that results in macro cracks and delamination when exceeding the local UTS stress; otherwise remains as residual stress in the fabricated part. Here, firstly, the abrupt change of laser power from 500 to 1000 W, which was necessary to deposit the CuCrZr properly, induced a high amount of thermal gradient and thermal stress as a consequence. In addition, the mismatch in the CTE and elastic modulus between those materials also intensified thermally induced stresses at the interface region [66]. Therefore, it seems that a combination of abrupt changes in both laser power and material properties induced a high amount of thermal stress that results in crack initiation, while the cyclic heating and cooling of the LDED process also creates expansion and contraction during the multi-layer deposition that resulted in the propagation of the crack [67].

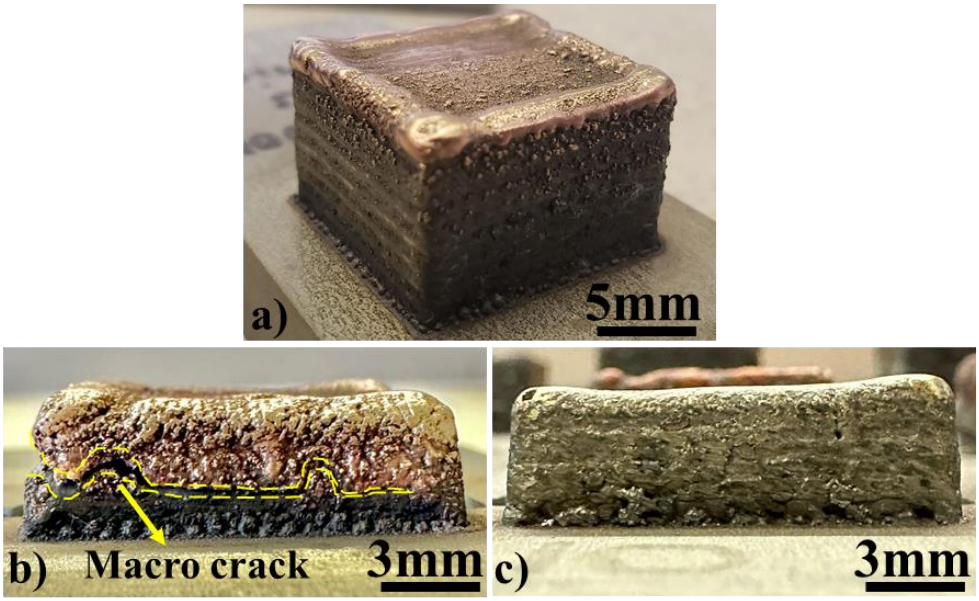


Figure 4-5 (a) FGAM of IN625-CuCrZr prototypes in cuboid geometry, (b) sharp composition transition (c) gradual composition transition

Figure 4-6 illustrates the effect of composition gradient on residual stress at the interface between Inconel 625 and CuCrZr in FGAM structures. In Figure 4-6 (a), where a sharp transition from 100% IN625 to 100% CuCrZr is implemented, the measured tensile residual stress in the IN625 substrate reaches 200 MPa. This high stress level is attributed to the abrupt high energy input that

was applied to deposit CuCrZr, along with the mismatch in thermal expansion coefficients and mechanical properties between the two dissimilar alloys, leading to significant thermal and plastic incompatibilities during cooling. In contrast, in Figure 4-6 (b) where the gradual compositional transition has been employed, progressing through low to intermediate energy input before reaching 100% CuCrZr. This graded transition significantly reduces the residual stress in the IN625 substrate to 44 MPa, likely due to the smoother thermal cycles across the gradient. The lower peak stress indicates that functionally graded transitions effectively mitigate interfacial stress concentrations by smoothing the mechanical and thermal gradients across layers. These findings underscore the importance of compositional grading in reducing residual stress and enhancing interfacial integrity in multi-material additive manufacturing.

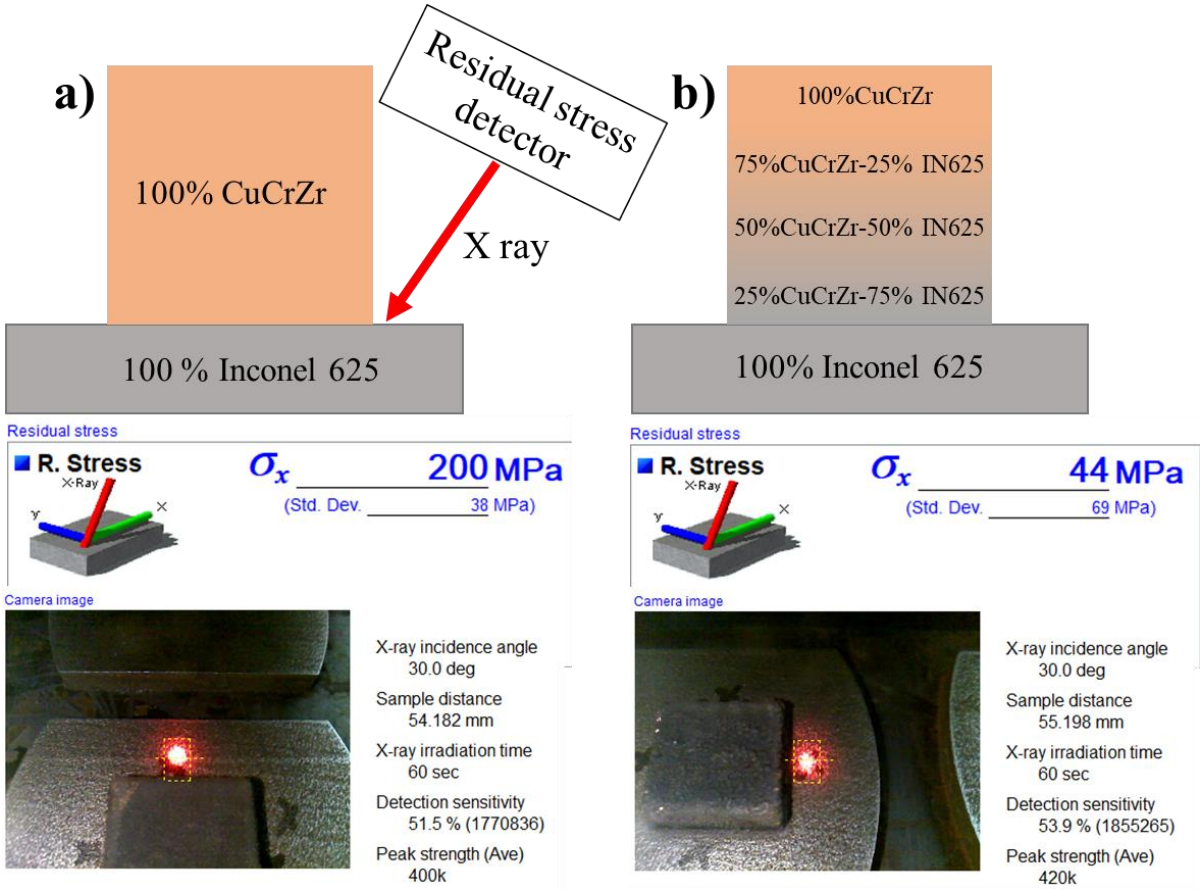


Figure 4-6 Average residual stresses measured on IN625 at the interface of (a) sharp compositional transition, (b) gradual composition transition

4.3 Summary

This chapter presented the systematic development of the FGAM of IN625-CuCrZr using a multi-powder feeder laser-directed energy deposition (L-DED) system. Initial trials revealed that a direct

transition between the two alloys led to severe macro-cracking and delamination at the interface, primarily due to the substantial differences in process parameters, particularly the high energy input required for depositing CuCrZr, along with the mismatch in thermophysical properties, which generated significant thermal stresses. To mitigate these issues, a step-wise gradient strategy was implemented by gradually varying the composition from 100% IN625 to 100% CuCrZr in 25 wt.% increments every four layers. Simultaneously, laser power was linearly adjusted in accordance with the evolving composition's absorptivity to ensure stable deposition. While the developed FGAM strategy proved successful from a macroscale perspective, a comprehensive microscale investigation remains necessary. The subsequent chapters will therefore examine the influence of compositional gradients on microstructure evolution and defect formation in both thin-wall and cuboid samples, as representatives of the main geometries in additive manufacturing. A comparative analysis of these geometries will also be conducted to elucidate the role of part geometry on the overall FGAM processability and material behavior of the IN625-CuCrZr system.

Chapter 5: Insights into Microstructural Evolution in Functionally Graded Additive Manufacturing of IN625–CuCrZr Alloys

5.1 Introduction

As previously described in Chapter 1, the ultimate goal of this thesis is to develop a pragmatic approach to the successful functionally graded additive manufacturing of dissimilar alloys. In this chapter, the successful FGAM of IN625 superalloy and CuCrZr alloy was demonstrated for the thin-wall samples without any major defects, such as cracks or lack of fusion. The samples were fabricated by gradually varying the composition via a dual powder feeder laser directed energy deposition (L-DED) system. Further, comprehensive thermodynamic simulations using CALPHAD methods, along with detailed microstructural characterization, are conducted to evaluate the effect of compositional change on grain size, morphology, and chemical segregation along the deposition direction. Furthermore, the influence of the compositional change on mechanical behavior is examined through microhardness testing, which captures the associated phase transformations on hardness variation across the gradient.

5.2 Methodology

Thin-wall samples were fabricated via an in-house developed robotic L-DED system shown in Figure 5-1 which schematically shows the FGAM process along with the compositional gradient path. Table 5-1 summarizes the nominal portion of each alloy at each compositional step, along with the corresponding labels and laser power settings, which were taken from previous studies [81], [82].

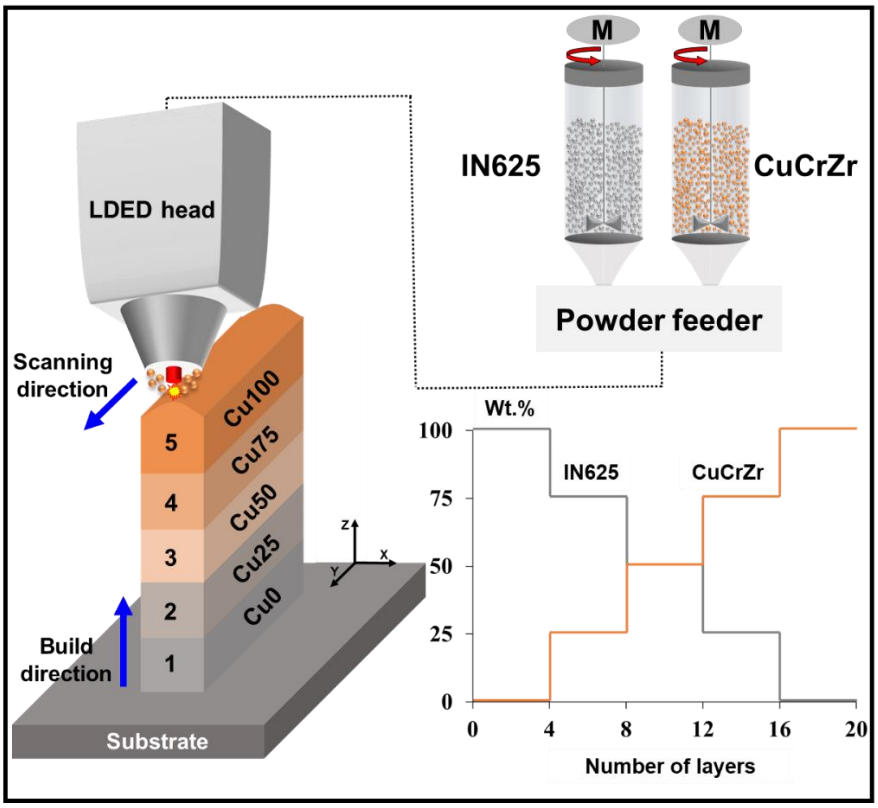


Figure 5-1 Schematic of FGAM processing of IN625-CuCrZr thin-wall structure.

Table 5.1 The content of used alloys in each section of the FGAM sample and the corresponding labels

Region in FGM	Nominal portion of IN625 (wt.%)	Nominal portion of CuCrZr (wt.%)	Label	Laser Power (W)	Scanning speed (mm/s)	Feed rate (g/min)
Zone 1	100	0	Cu0	500	10	2
Zone 2	75	25	Cu25	625	10	2
Zone 3	50	50	Cu50	750	10	2
Zone 4	25	75	Cu75	875	10	2
Zone 5	0	100	Cu100	1000	10	2

5.2.1 Characterization techniques

The FGAM-made thin-wall samples were fabricated and then cut in cross-sections, allowing for all composition steps present to be assessed with spatial continuity. A Struers Accutom-50

precision cutter was used to cross-section the completed thin-wall structures. The samples were hot-mounted using a conductive mold and polished with SiC grinding papers with grit levels ranging from 320 to 4000 grit sizes. Fine polishing was performed in alumina slurry (0.05 μm particle size) and colloidal silica suspension (particle size) in the vibratory polisher for 2h and 1h respectively, afterward washed with distilled water and subjected to ultrasonic cleaning. Finally, the polished thin-wall sample was etched using Kalling's No.2 reagent solution for 10 ~ 15 s to reveal the microstructure of each region.

A section of the entire thin-wall sample was examined for the distribution of secondary phases using ZEISS Xradia 520 Versa X-ray computed tomography (X-CT). Overall, 1801 2D projections were performed at 10 W, 145 kV with an exposure time of 8 s per image and voxel size of 5 μm. A beam hardening constant of 0.05 was used for reconstruction and the 3D images were analysed via Dragonfly 3.1 software.

A Keyence VHX-7000 optical microscope was used to examine the microstructure of the prepared FGAM. A Tescan Vega3 scanning electron microscope (SEM) equipped with a Bruker XFlash 6/10 energy dispersive X-ray spectroscopy (EDS) detector was used to study the microstructure and chemical composition of deposited thin-wall. Electron backscatter diffraction (EBSD) analysis was performed using Bruker QUANTAX detector to investigate the grain size and crystallographic texture throughout the gradient at 20 kV voltage, employing a scanning step size of 4 μm. X-ray diffraction (XRD) patterns were obtained using a Bruker D8 Discover diffractometer equipped with a VANTEC500 detector and Cu Kα radiation (λ = 1.5418 Å). The analysis was conducted over a 2θ range of 30° to 100°, offering insights into existing phases in each compositional mixture of the FGAM sample. For the evaluation of the mechanical properties of the FGAM structure microhardness (Vickers) test was conducted via Clemex CMT automated hardness tester at a load of 50 gf and a dwell time of 10 s.

5.2.2 Thermodynamic simulations

The CALPHAD (CALculation of PHAse Diagrams) method was employed to perform a computational investigation of both equilibrium and non-equilibrium phases (using the Scheil-Gulliver model without back-diffusion) to aid in analyzing the solidification path for various compositions. The Scheil–Gulliver model was selected to approximate the solidification behavior

under the non-equilibrium, rapid solidification characteristic of the L-DED process. This model is particularly well-suited due to the key assumption of negligible diffusion in the solid phase. In this work, we assumed that the cooling rates are high enough that solid-state diffusion is kinetically suppressed. In addition, the literature argues that considering back-diffusion in the presence of high undercooling makes the calculation complicated. The study utilized the Thermo-Calc software (version 2023a) and the TC-python API along with a custom Python script to determine the phases as functions of temperature and composition. The optimized databases TCCU5 for Cu-based alloys [27], and TCNI12 for Ni-based alloys [28] were employed. To reduce computational expense, the simulations included only the primary elements (Cu, Ni, Cr, Mo, Nb, Fe, and Zr).

5.3 Results and Discussions

5.3.1 Overall view of FGAM-made microstructure

Figure 5-2 reveals an overview of the microstructure of each composition. Figure 5-2(a) schematically represents the microstructure of each composition from the cross-section of the FGAM thin-wall. Figures 5-2(b) to 5-2(f) represent the backscattered electrons (BSE) images of the etched microstructure along with the mixed elemental EDS map of each composition from Cu0 (100% IN625) to Cu100 (CuCrZr), respectively. Dendritic/cellular microstructure [83] was observed in Cu0 (Figure 3(b)) as well as Cu25 (Figure 5-2(c)), in which Cu is predominantly present in the interdendritic regions. Figure 5-2(d) and (e) show peculiar microstructure in Cu50 and Cu75 regions, respectively. In fact, the microstructure of these regions consists of multiple phases with dendritic and spherical morphologies (spheroid). The formation of these spheroids is due to the presence of a metastable miscibility gap [84],[85], which has been previously reported in similar alloy mixture systems by other researchers [86], [87], though they may sometimes be misinterpreted as partially/un-melted powder particles. Moreover, from the EDS mixed elemental map, it can be seen that these spheroids are lean in Cu and enriched with the rest elements. The rapid solidification inherent to the L-DED process [88], [89] implies the formation of the spheroids in the liquid state, driven by poor miscibility between Cu and other elements in the melt pools. It is important to note that at the very top region of the sample, the microstructure of Cu100 is shown in Figure 5-2(f), which consists of a relatively fine cellular structure that has been previously studied in more detail by the authors [81], [82].

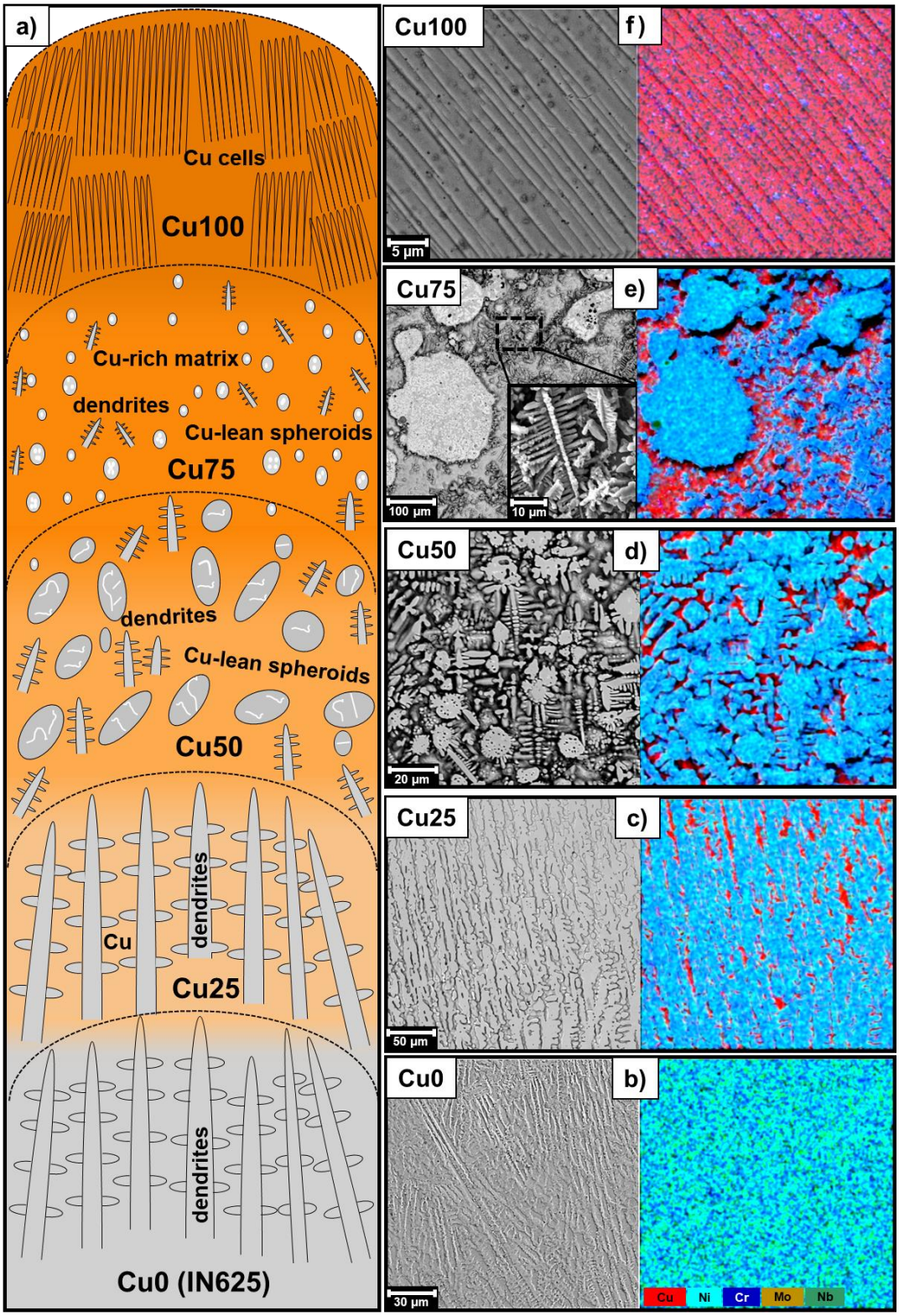


Figure 5-2 Overall view from the microstructure of the FGAM-thin wall. (a) Schematic microstructure of the entire FGAM cross-section, BSE images, and EDS mixed elemental map of the microstructure of (b) Cu0, (c) Cu25, (d) Cu50, (e) Cu75, (f) Cu100.

5.3.2 Compositional transition analysis

Figure 5-3 provides a schematic illustration of the thin-wall FGAM sample, highlighting the interfaces of compositional transitions, which were subjected to EDS analysis to study compositional transitional changes at each step. Figures 5-3(a) to (d) show the EDS mixed elemental map at the interface of each composition transition, accompanied by a 2 mm line scan analysis along the yellow arrow. The corresponding results are shown in the right panel. As seen from the mixed elemental map of Figure 5-3(a), the two alloys blend well at the Cu25 due to turbulent flows within the melt pool [66], with no evidence of immiscibility. This is also further confirmed by the smooth elemental profiles in the line scan results, indicating the actual composition step is around 80/20 IN625-CuCrZr. The slight deviation from the nominal composition is likely attributed to the difference in the PSD of the powders, which may cause minor powder separation in the powder stream [90].

Figure 5-3(b) illustrates the elemental composition at the Cu25 to Cu50 interface. The mixed elemental map shows a smooth transition between these compositions. However, the line scan results for the Cu50 region reveal significant fluctuations in elemental profiles, indicating a multiphase composition, as previously shown in Figure 5-2(d). These fluctuations reveal an inverse relationship between Cu and other elements, where Cu depletes, the other elements are enriched, and vice versa. This confirms that the Cu50 region consists of a multiphase composition of distinct Cu-rich and Cu-lean phases.

Similarly, the Cu75 region exhibits a dual-phase structure with prominent Cu-rich and Cu-lean regions. The final compositional transition from Cu75 to Cu100 is depicted in Figure 5-3(d). Both the mixed elemental map and line scan results indicate that the compositional inhomogeneity observed in the Cu75 region has disappeared upon entering the Cu100 region, which consists only of Cu-rich phase(s). These observations, besides the spherical microstructure seen in Figures 5-2(d) and (e), confirm the presence of a miscibility gap within the liquid phase of the two alloys in Cu50 and Cu75 compositional mixtures, which will be discussed in more detail in the following section.

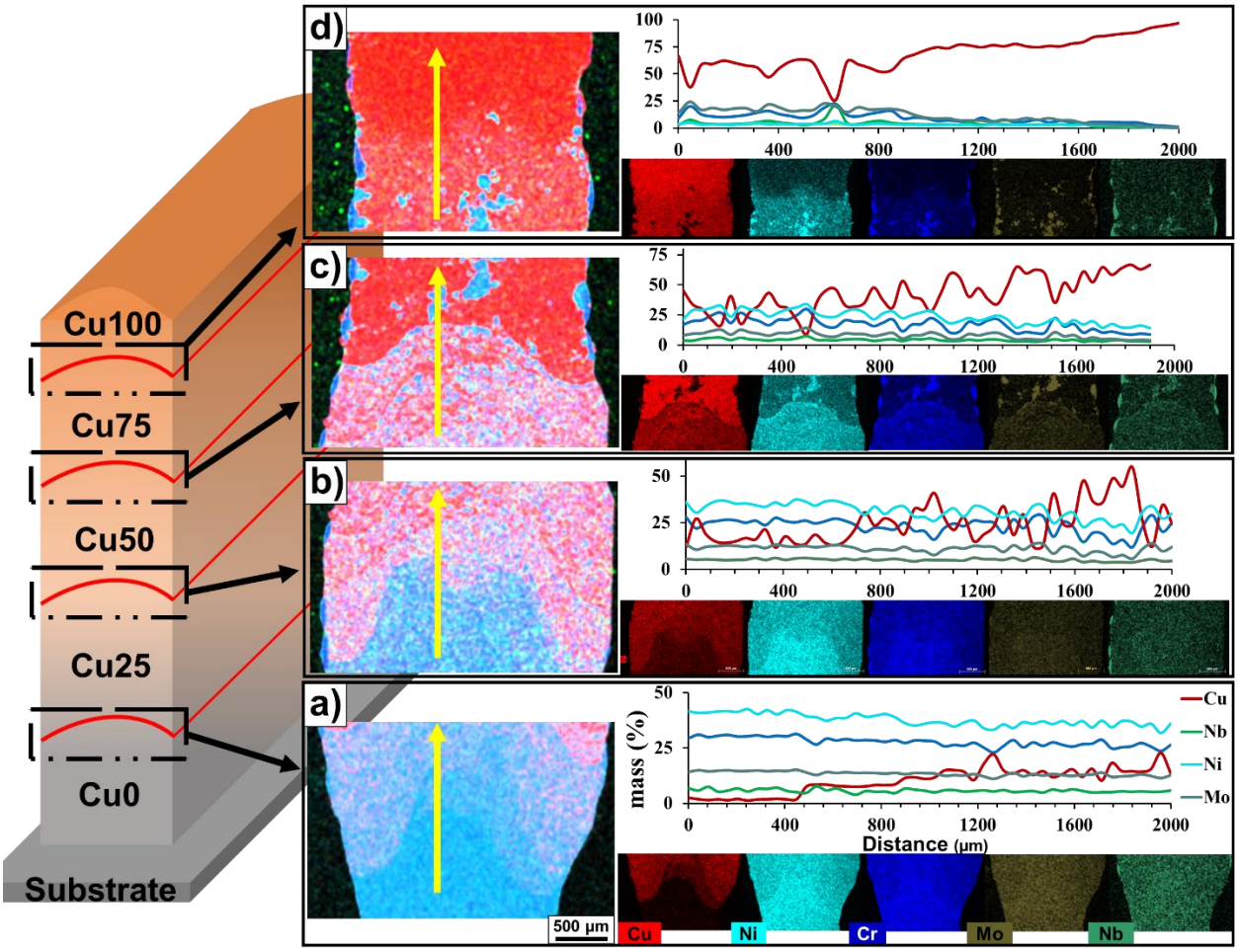


Figure 5-3 EDS elemental map and line scan analysis on compositional transition interface of (a) Cu0/Cu25, (b) Cu25/Cu50, (c) Cu50/Cu75, and (d) Cu75/Cu100

The stitched EDS maps of the cross-section and longitudinal section of the FGAM thin-wall sample are presented in Figures 5-4(a) and (b), respectively. To further elucidate the presence of the Cu-rich and Cu-lean phases, CALPHAD simulations were conducted. The simulation results indicate a lack of liquid-state miscibility at the liquidus temperature. The volume fraction of liquid phases, as a function of the CuCrZr content (wt.%), is depicted in Figure 5-4(c), which predicts the onset of the miscibility gap at approximately 20 wt.% CuCrZr and its closure at 85 wt.%. Moreover, the five compositional regions of the FGAM sample are mapped on the plot according to their CuCrZr content.

From the stitched EDS elemental maps and CALPHAD simulation results, it is evident that the Cu50 and Cu75 regions consist of two immiscible liquids: Cu-rich and Cu-lean. During rapid

solidification, these two distinct regions, one Cu-rich and the other Cu-lean, emerge in the deposition. Besides, this miscibility gap explains the spherical microstructure observed in Figures 5-2(d) and (e). It seems that supercooling of these compositions beyond a critical limit leads to the separation of melt into two liquids due to the metastable miscibility gap of Cu with other elements [86][91]. As noticed from the mixed elemental map of Figures 5-4(a-4 and b-4), the Cu-lean phases in the Cu75 region seem to be coarser and show significant agglomeration. The agglomeration mechanism is discussed in detail in the following section.

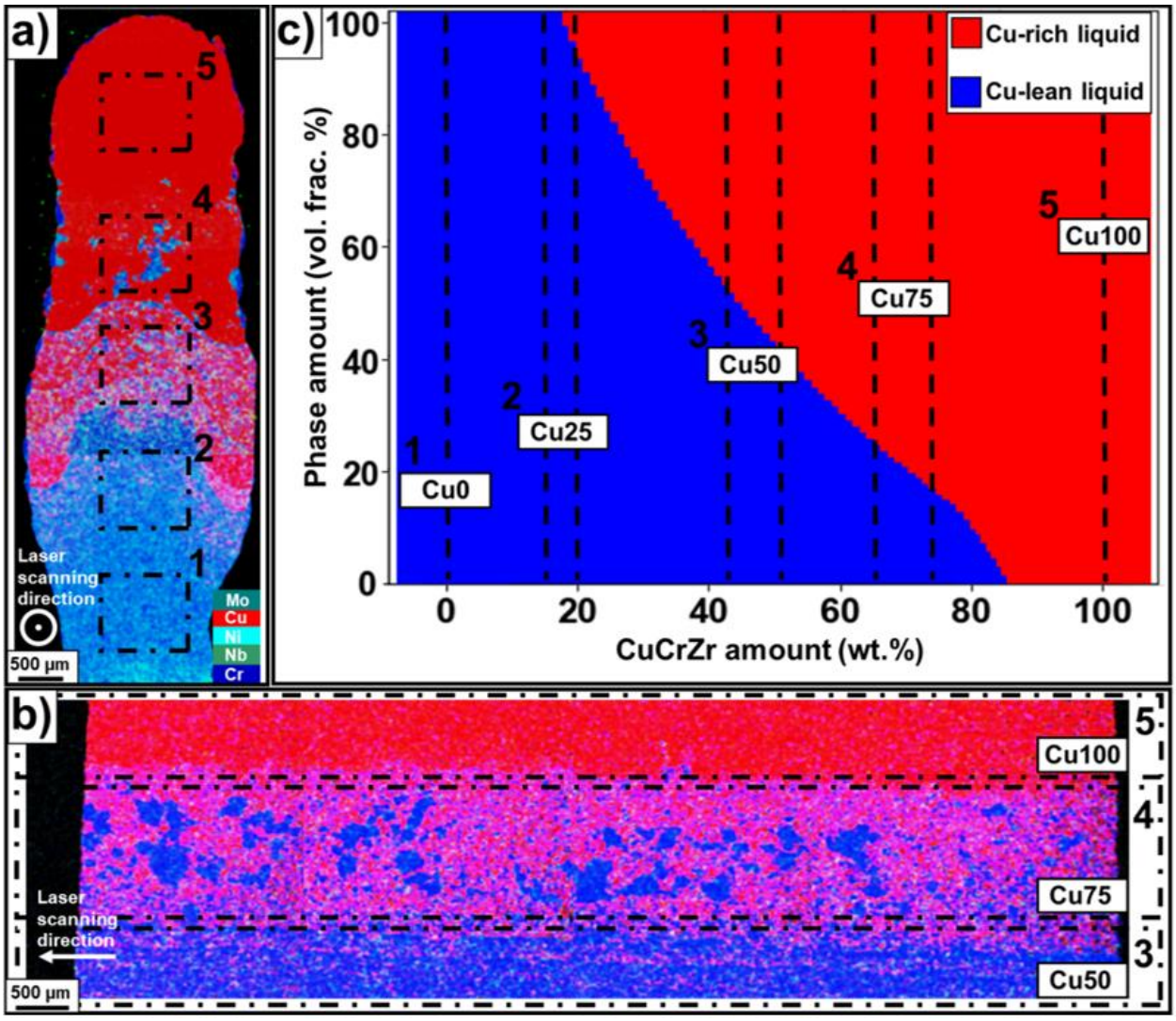


Figure 5-4 Liquid state miscibility of the two alloys, (a) stitched EDS elemental map of the entire cross-section of the FGAM thin-wall sample, (b) stitched EDS elemental map of the longitudinal section across the Cu 50, Cu75, Cu100 regions, (c) CALPHAD simulation of Cu0 to Cu100 compositions at liquidus temperature.

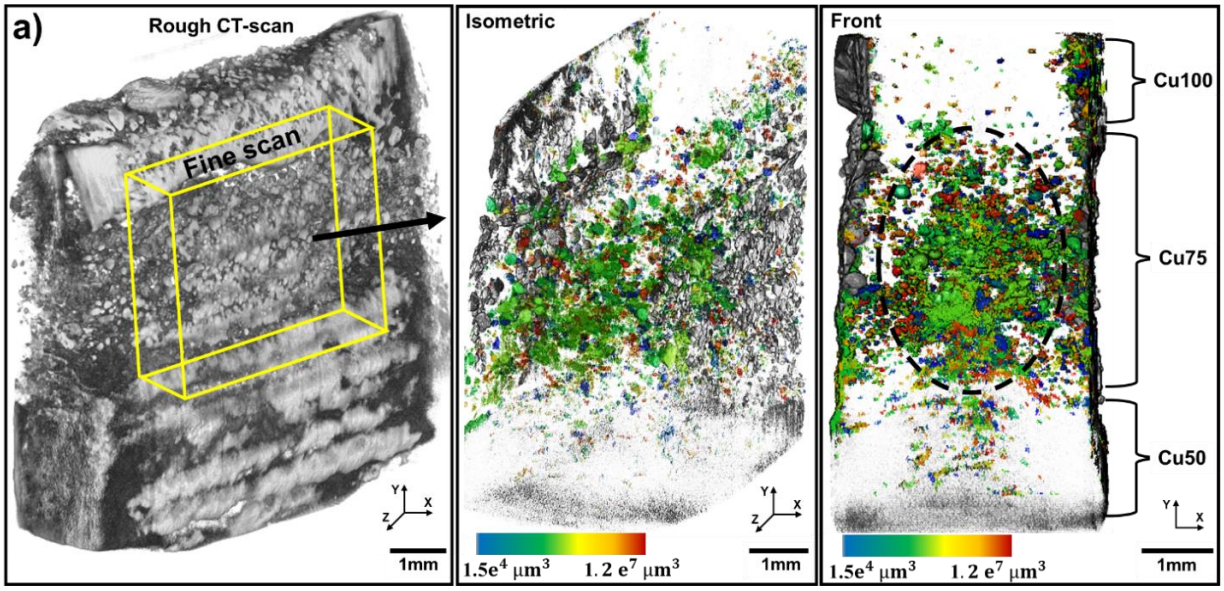
To delve further into the distribution, size, and agglomeration of Cu-lean phases, X-CT was performed on the thin wall sample, and the results are shown in Figure 5-5. Figure 5-5(a) illustrates the analysis of the Cu-lean spheroids, highlighting their distribution and agglomeration within the melt pool of the highlighted finer scan region. The isometric view provides a three-dimensional perspective of the spheroid distribution across different compositions. The front view further demonstrates the agglomeration tendency of the Cu-lean phases, particularly in the Cu75 region. In addition, the distribution of Cu-lean spheroids across successive layers of the fine scan is illustrated in Supplementary Animation 1, which provides a visual representation of their evolution and concentration while highlighting their agglomeration in the central region of the Cu 75. Figure 5-5(b) presents the size of Cu-lean spheroids as a function of their vertical position within the sample. The plot reveals the presence of several large spheroids in the Cu75 region, some of which are approximately ten times larger than the typical spheroids. These observations underscore the pronounced agglomeration occurring in this region. The agglomeration mechanism is likely attributed to Marangoni convection and differences in surface tension and viscosity between the Cu-lean and Cu-rich liquids [92]. Marangoni convection, driven by temperature-induced surface tension variations, plays a critical role in melt pool dynamics [13], [66]. Numerical investigations on melt pool dynamics indicate that temperature and surface tension coefficients, varying with distance from the laser beam center, enhance the Marangoni number. This enhancement results in radial surface flow, either outward or inward over the center of the melt pool [93][94]. Marangoni convection can be quantified using the non-dimensional Marangoni number (*Ma*), defined as follows:

$$Ma = \frac{d\gamma}{dT}\frac{dT}{dx}\frac{L^2}{\eta\alpha} \qquad \text{(equation5-1)}$$

where γ represents surface tension, dγ/dT is the surface tension coefficient, dT/dx is the temperature gradient from the melt pool center, η denotes viscosity, α is thermal diffusivity, and L is the characteristic length. Based on the EDS analysis the Cu-lean's composition is close to that of IN625 while the Cu-rich composition is close to copper. The estimated surface tension of copper at 1400°C is approximately 1.221 N/m, while IN625 has a higher estimated surface tension of 1.756 N/m at the same temperature [95]. This significant difference in surface tension leads to distinct flow behaviors under the influence of Marangoni convection. Due to Cu-lean's higher

intrinsic surface tension, the flow driven by Marangoni forces is resisted, causing Cu-lean phases to remain concentrated near the center of the melt pool, resulting in their agglomeration.

Additionally, the lower viscosity of the Cu-rich liquid (e.g., copper at ~2.5-2.8 mPa·s at 1400°C) [96] allows it to flow more easily than the Cu-lean liquid (e.g., IN625 at ~5-6 mPa·s at 1400°C)[97]. Consequently, the higher viscosity of the Cu-lean liquid contributes to its tendency to agglomerate near the center of the melt pool. Also, the presence of Cu-lean spheroids in the Cu100 region, as shown in Figure 5-5(b) highlights the recurring nature of the agglomeration mechanism. During subsequent layer depositions, new melt pools are formed and partially diluted with previously deposited layers. This repetitive cycle reinforces the agglomeration of Cu-lean phases, leading to their continued presence even in regions initially dominated by the copper alloy. Therefore, the recurring formation and solidification of melt pools in each compositional region enhances the clustering and growth of Cu-lean spheroids.



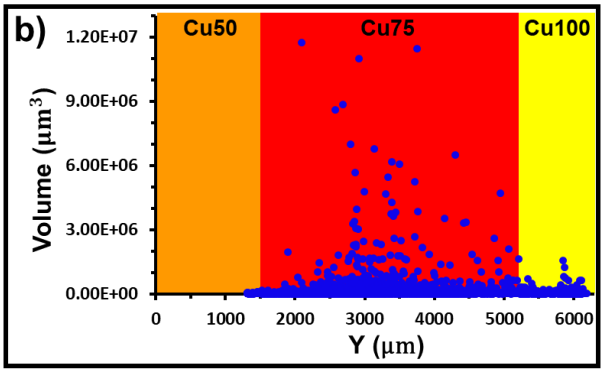


Figure 5-5 X-CT 3D images of a thin wall FGAM sample; a) a fine scan of the regions containing the Cu-lean phases shown in isometric and front views, and b) volume of the Cu-lean phases versus height showing their agglomeration in the Cu-75 region

5.3.3 Phase analysis

The evolution of phases in the FGAM thin wall specimen is notably more complex than in IN625 and CuCrZr alloys individually, particularly in the mixed compositional regions. This complexity arises because of not only existing additional elements but also the aforementioned miscibility gap, which results in inhomogeneity and emerging two distinct Cu-reach and Cu-lean regions, as shown in Figure 5-6. These regions often consist of multiple phases and precipitates. Considering the complexity of the material system and the intricate thermodynamics of the L-DED process, non-equilibrium thermodynamic modeling of phases is crucial. Therefore, using the CALPHAD method and Scheil solidification simulations, the potential phases for Cu-lean and Cu-rich liquids were predicted, as shown in Figures 5-6(a) and 5-6(b), respectively.

As seen from Figure 5-6(a), up to approximately 25% CuCrZr, only a Ni-rich FCC phase is present. Beyond 25%, two additional phases, M_2C and Ni_3Nb, begin to emerge, with increasing volume fractions in Cu50 and Cu75. These phases have been reported in the microstructure of Ni-based superalloys [98], [99], [100] with their volume fraction increasing as CuCrZr content rises, particularly in the Cu75 region. Solidification simulation results for the Cu-rich liquid, depicted in Figure 5-6(b), suggest a Cu-rich FCC as the primary phase with the CrO phase likely in the Cu50 region. With the potential phases established, the next step is to identify the actual phases comprising the microstructure of the manufactured sample.

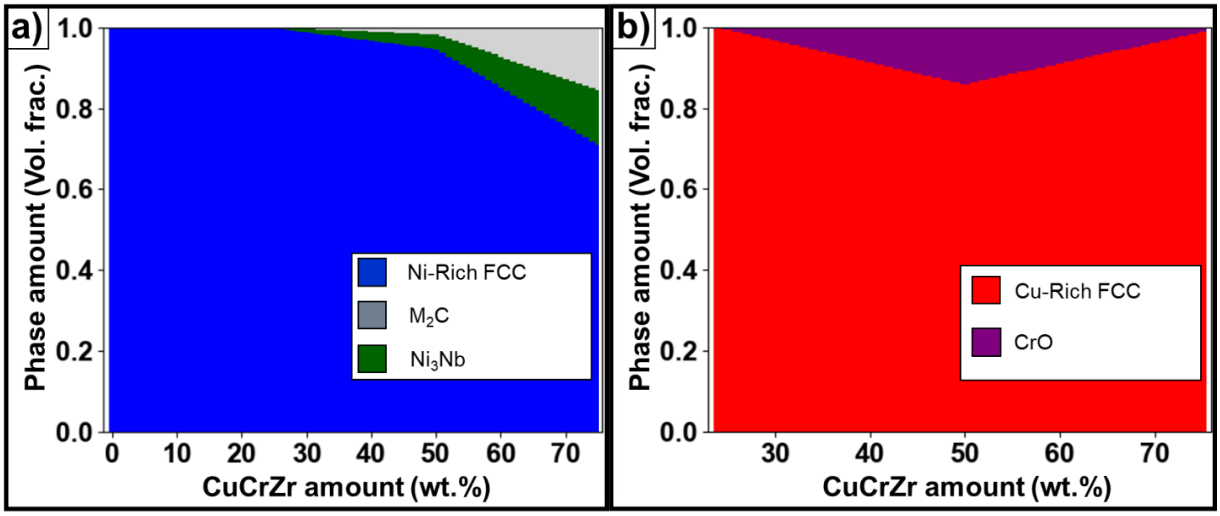


Figure 5-6 CALPHAD's Scheil solidification simulations results for (a) Cu-lean liquid that exists in the range of 0-75% wt. CuCrZr, and (b) Cu-rich liquid existing in the range of 20-100% wt. CuCrZr.

The diffraction pattern from XRD analysis across the compositional transitions in the IN625-Copper alloy system is shown in Figure 5-7. Each scan was conducted at a compositional transition region, i.e. Cu25, Cu50, and Cu75, and XRD patterns are shown in Figure 8(a). The primary phases correspond to the γ-Ni and γ-Cu phases, which are coincident, indicating that these are the main phases present throughout the sample. However, in Cu75, a small peak appeared in the low-angle region, magnified in Figure 5-7(b), revealing the presence of Mo_2C phase. This phase is also detected in Cu50, though with lower intensity, indicating its formation in regions with higher Cu content, particularly in the Cu75 composition. These findings align well with the CALPHAD results shown in Figure 5-6, where FCC Ni-rich and FCC Cu-rich were predicted to be the main phases besides the formation of Mo-rich M_2C phase in both Cu50 and Cu75 regions with higher volume fraction in the latter. It is important to note that the diffraction peak of Ni_3Nb phase is likely masked by the primary diffraction peak of γ-Ni/Cu at 2θ angle of 43.4°[101], [102]. Therefore, a more comprehensive microstructural analysis of these regions is presented in the subsequent section.

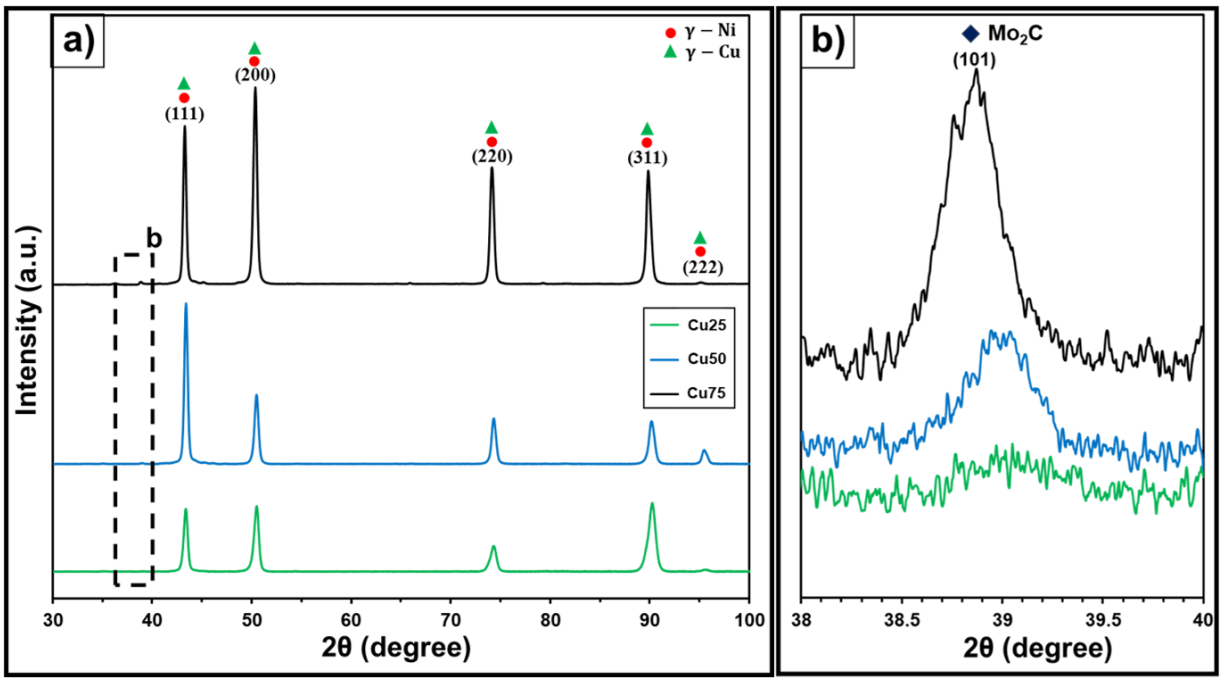


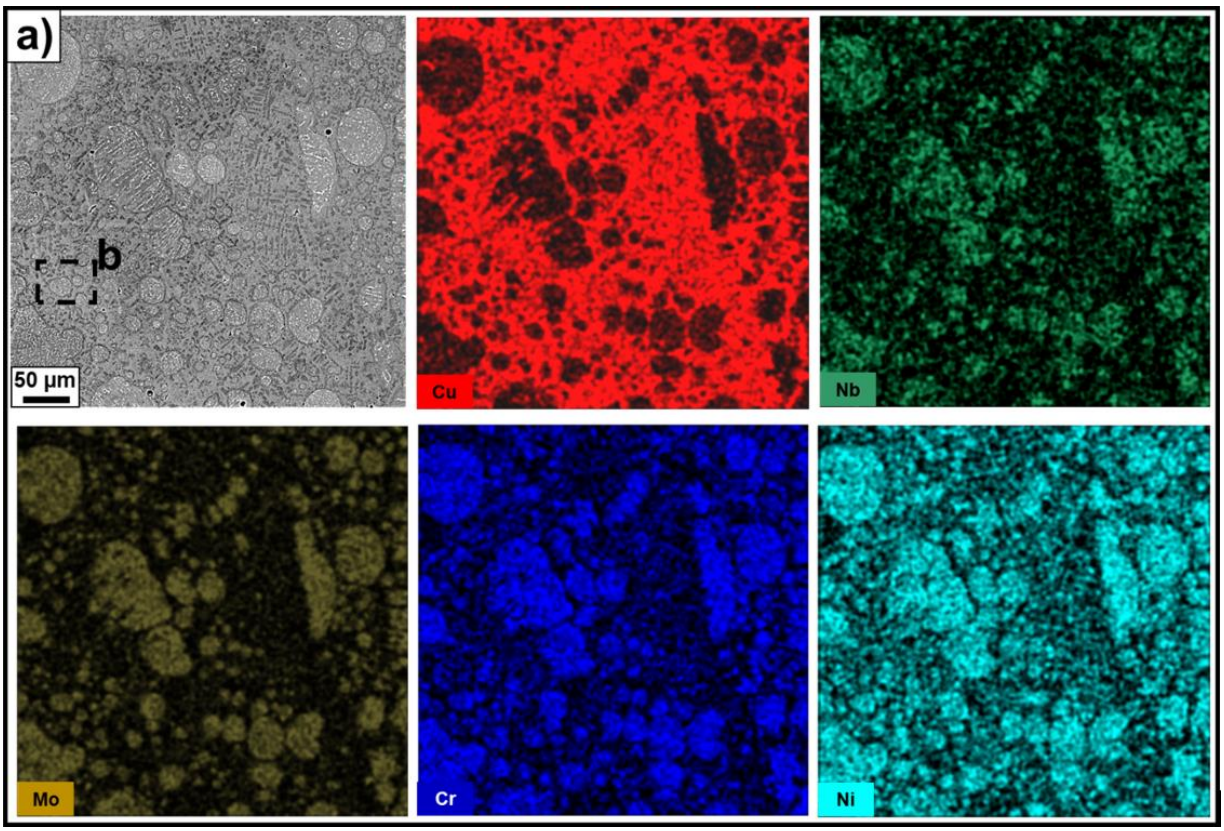
Figure 5-7 XRD spectra at the compositional transition interfaces, (a) from the Cu25 to Cu75 regions, and (b) magnified spectra at 2θ range of 38° to 40°, showing the presence of Mo2C phase at Cu50 and Cu75.

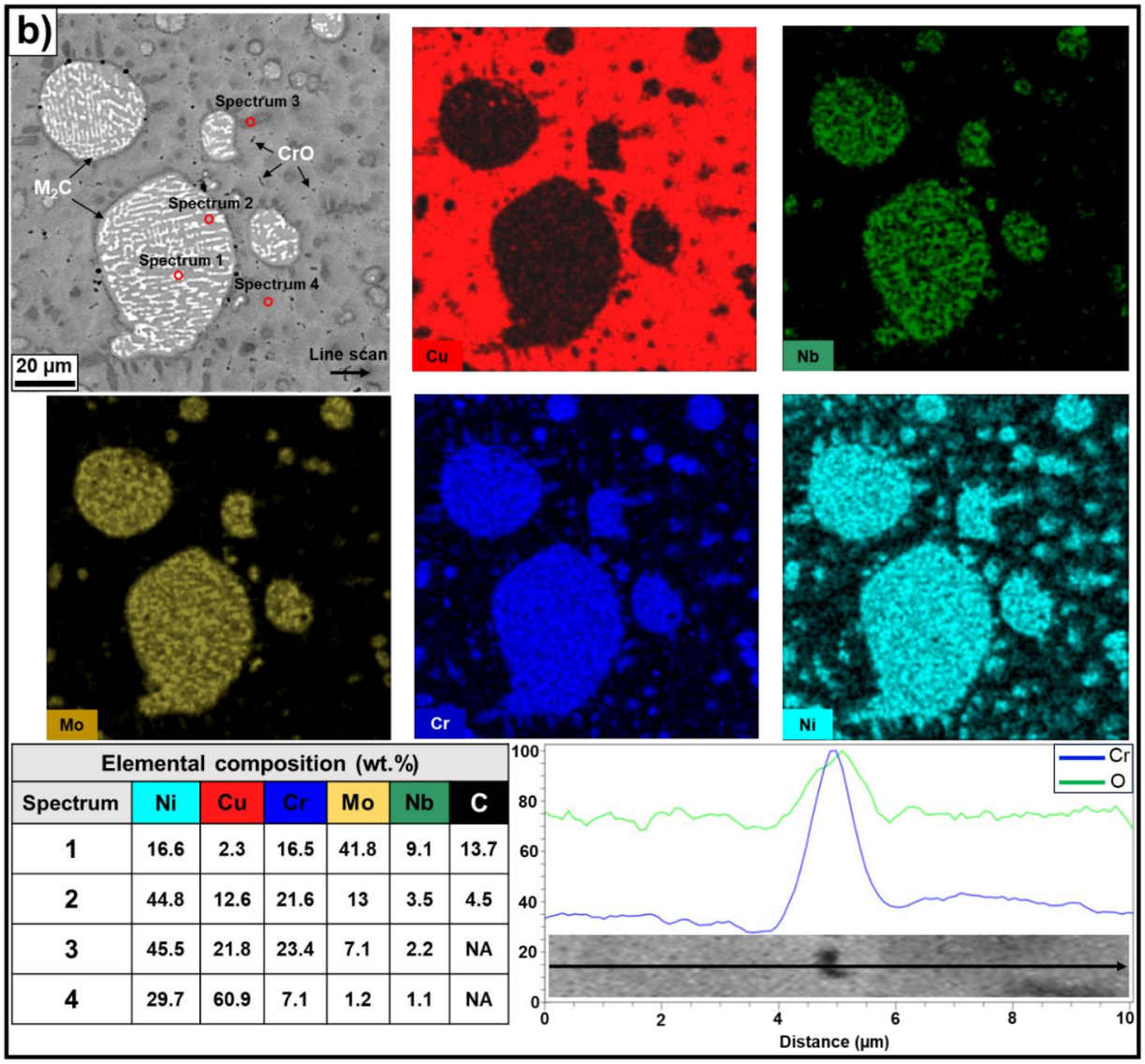
To delve further into the peculiar microstructure of the two multiphase regions, Cu50 and Cu75, a series of BSE imaging with EDS analysis was conducted, with the results depicted in Figure 5-8.

- **Cu50 region:** The BSE image in Figure 5-8(a) reveals a spheroid microstructure with bright precipitates, surrounded by a dendritic structure within a Cu-rich matrix. EDS elemental maps show Cu-lean spheroids rich in Ni, Cr, Nb, and Mo, formed due to the miscibility gap creating two distinct liquids before solidification. Higher magnification (Figure 5-8(b)) confirms multiple phases in the spheroids: Bright precipitates rich in Mo, Cr, Nb, and C (Spectrum 1) suggest M_2C-type carbides, as predicted by CALPHAD and XRD results.

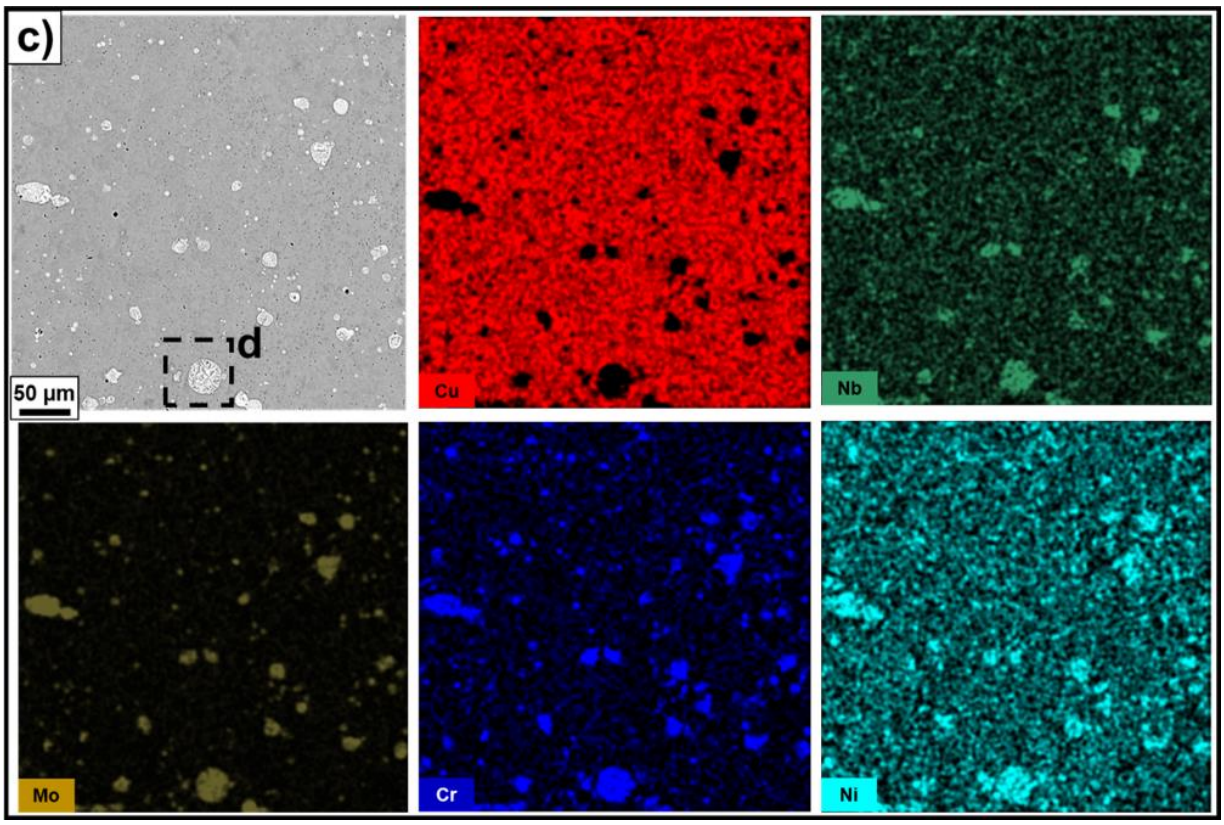
  Another area within the spheroid (Spectrum 2) contains Ni, Cr-rich phases, corresponding to the Ni-rich FCC phase predicted by CALPHAD. The dendritic structure (Spectrum 3) shows Ni-rich FCC phases with substantial Ni, Cr, and Cu. The Cu-rich matrix (Spectrum 4) contains a high concentration of Cu, Ni, and smaller amounts of other elements, confirming the Cu-rich FCC phase. Additionally, the presence of small CrO precipitates in the matrix that was previously predicted by CALPHAD, is verified by the line scan EDS analysis.

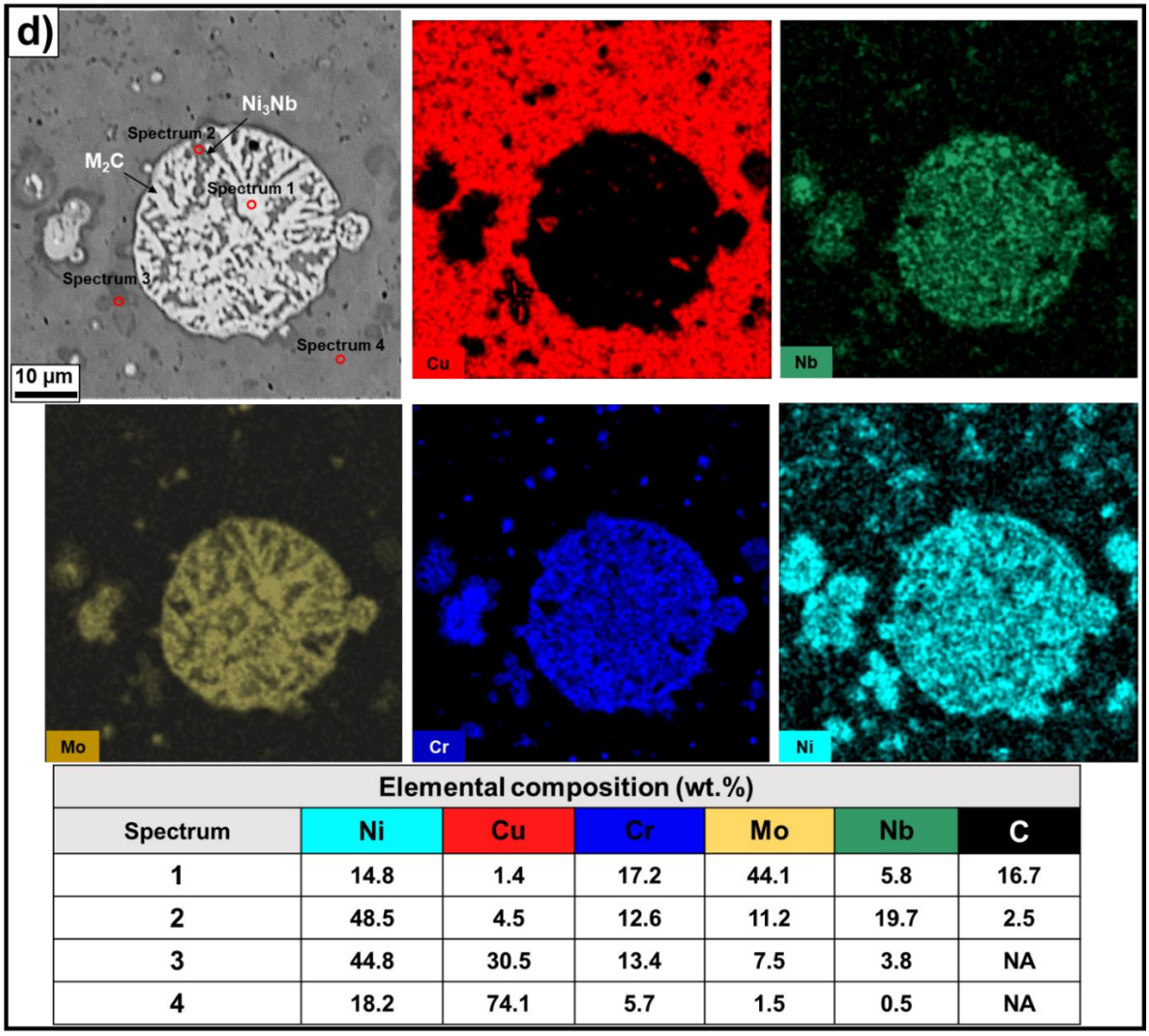
- **Cu75 region:** Figure 5-8(c) shows the BSE image of the Cu75 microstructure, featuring dendritic structures and spheroids similar to those in the Cu50 region. However, the Cu75 spheroids contain more bright precipitates. The surrounding Cu-rich matrix embeds dendrites where Ni is evenly distributed but in lower concentrations than within the spheroids, as shown by EDS elemental maps. A higher magnification view in Figure 5-8(d) reveals a complex microstructure with phases concentrated in specific regions. Spectrum 1 highlights significant Mo and C enrichment in the spheroids, indicating the formation of M_2C-type carbide, consistent with CALPHAD predictions and a stronger Mo_2C XRD peak in the Cu75 composition. Spectrum 2 along with the EDS elemental maps reveal Ni and Nb enrichment, suggesting the formation of the Ni_3Nb phase [100], also predicted by CALPHAD. Outside the spheroids, Spectrum 3 shows the dendritic structure is rich in Ni and Cu, confirming a Ni-rich FCC phase. Also, spectrum 4 reflects the Cu-rich matrix composition, dominated by Cu with some Ni, confirming the Cu-rich FCC phase as the predominant matrix. The detailed phase analysis presented here provides crucial insights into the microstructural evolution and phase stability. In the following section, the correlation between these phases and the resultant grain structure of each composition is investigated.


a)
b
50 µm
Cu
Nb
Mo
Cr
Ni



Elemental composition (wt.%)						
Spectrum	Ni	Cu	Cr	Mo	Nb	C
1	16.6	2.3	16.5	41.8	9.1	13.7
2	44.8	12.6	21.6	13	3.5	4.5
3	45.5	21.8	23.4	7.1	2.2	NA
4	29.7	60.9	7.1	1.2	1.1	NA


c)
d
50 µm
Cu
Nb
Mo
Cr
Ni



Elemental composition (wt.%)						
Spectrum	Ni	Cu	Cr	Mo	Nb	C
1	14.8	1.4	17.2	44.1	5.8	16.7
2	48.5	4.5	12.6	11.2	19.7	2.5
3	44.8	30.5	13.4	7.5	3.8	NA
4	18.2	74.1	5.7	1.5	0.5	NA

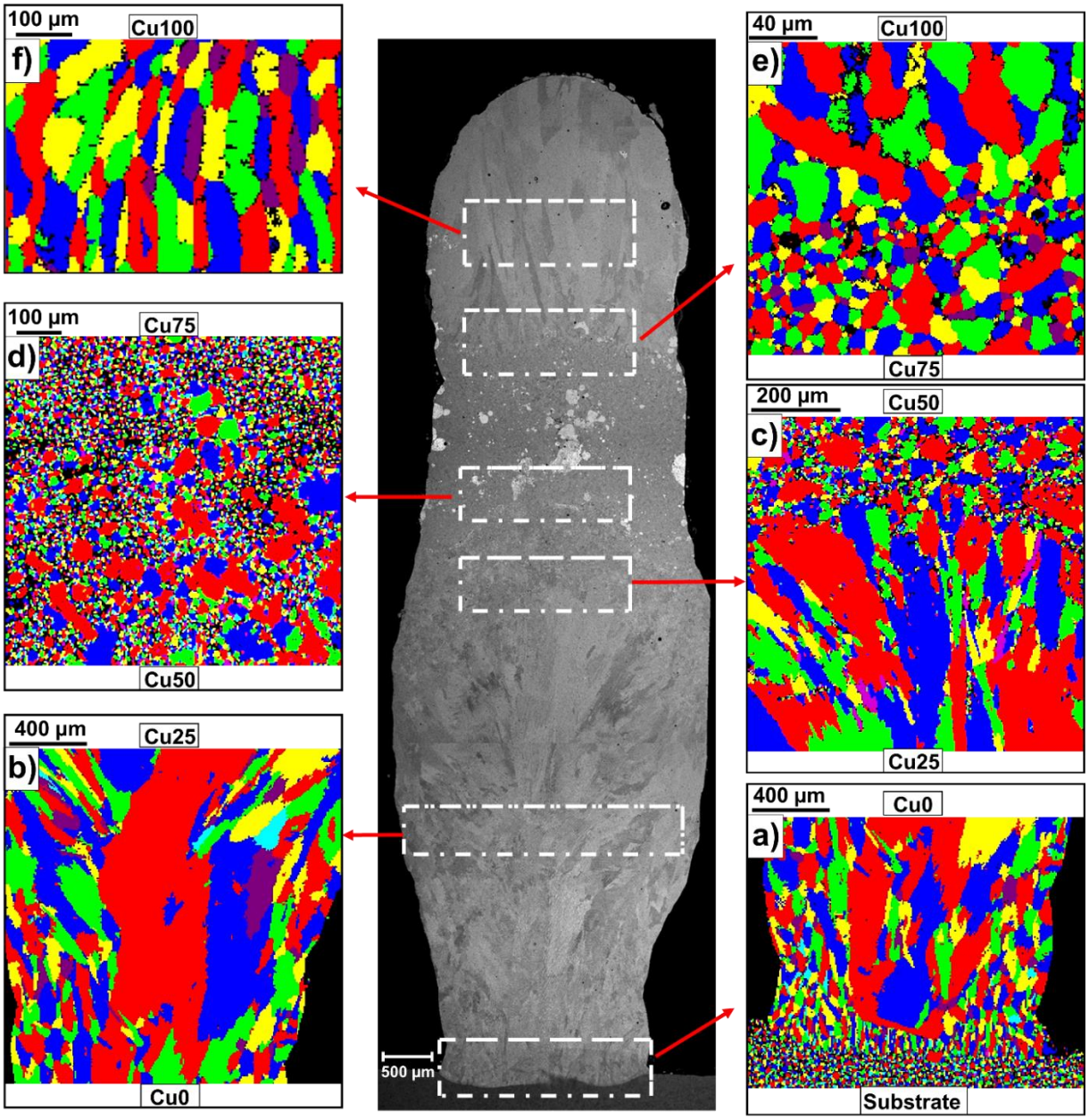
Figure 5-8 BSE images and EDS analysis of microstructure, (a) Cu50, (b) high magnification of a region in (a), (c) Cu75, and (d) high magnification of a region in (c).

5.3.4 Grain structure

The evolution of chemical composition can impact grain structure evolution, affecting the grain size and aspect ratio from the substrate to the top of the FGAM sample, as illustrated in Figure 5-9. The observation per each region is summarized below:

- **Cu0 region**: large grains can be seen in Figure 5-9(a) where the growth direction is parallel to the build direction across multiple deposited layers. As depicted quantitatively in Figure 5-9(g), the average grain size and aspect ratio are 125 µm and 0.35, respectively, indicating full columnarity of the grain structure in this region [103], [104].

- **Cu25 region**: As shown in Figure 5-9(b), coarse grain structure persists, with the grains aspect ratio of 0.31, indicating minimal impact from the compositional change. This stability aligns with the phase analysis, which only identified a single Ni-rich FCC phase in this region.
- **Cu50 region**: A significant change in grain structure occurs as the composition reaches 50 wt.% CuCrZr, as shown in the interface of the Cu25 and Cu50 regions in Figure 5-9 (c), where the coarse columnar grains notably transform to fine equiaxed ones with an average grain size of 32 μm and 0.6 aspect ratio. This change correlates with the introduction of the miscibility gap in this region as well as the additional phases alongside the γ matrix.
- **Cu 75 region**: More conspicuously, as depicted in Figure 5-9(d), the grain structure becomes fully equiaxed and even much finer with a 7 μm average grain size and 0.69 aspect ratio. This refinement is attributed to the increased microstructural complexity caused by the miscibility gap and the formation of multiple phases. The grain refinement mechanism will be explored in more detail in the subsequent section.
- **Cu 100 region**: As shown in Figure 5-9(e), the grain structure transitions from the fine equiaxed grains of Cu75 to a coarser columnar structure in the Cu100 region, with an average grain size of 45 μm and an aspect ratio of 0.38, as depicted in Figure 5-9(f).


100 µm
Cu100
f)
100 µm
Cu75
d)
Cu50
400 µm
Cu25
b)
Cu0
500 µm
40 µm
Cu100
e)
Cu75
200 µm
Cu50
c)
Cu25
400 µm
Cu0
a)
Substrate

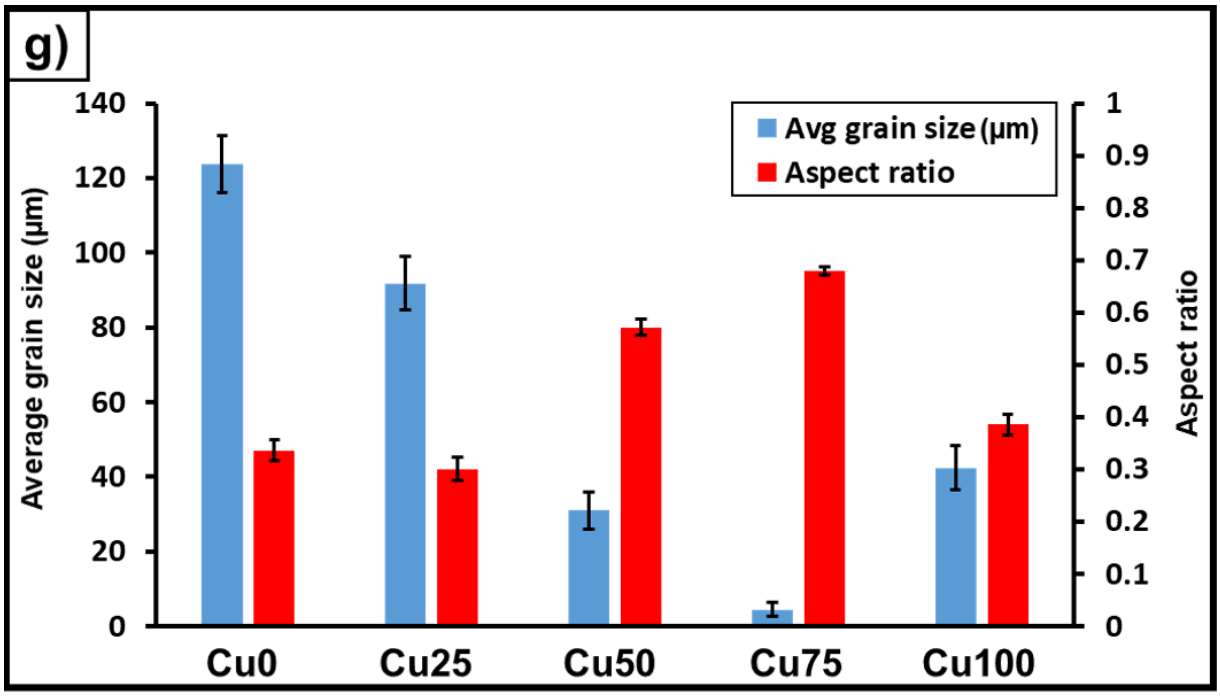


Figure 5-9 Analysis results on the grain structure of the FGAM sample; including grain maps of compositional transition interface from (a) Cu0 to (f) Cu100, and (g) average grain size and aspect ratio of each composition.

In general, the grain morphology and size in additive manufacturing (AM) are influenced by two primary factors: process-related and composition-related parameters [105]. In L-DED, the key process parameters, laser power (P) and scanning speed (V), govern the thermal gradient (G) and solidification rate (R), respectively [72]. In fact, the grain morphology is primarily determined by the G/R ratio, where an increase in G/R promotes columnar grain growth, whereas a decrease favors the formation of equiaxed grains [26], [106], [107]. In this study, V remains constant during the process and as the composition transitions from Cu25 to Cu50 and Cu75 only P increases, resulting in a higher G/R ratio. Based on classical solidification theory, this should promote columnar grain growth. However, the grain structure transitions into a highly fine equiaxed morphology (Figure 5-9(c & d)), highlighting the dominant role of compositional effects. The composition-related parameters can have more pronounced impact such as existence of inuclants that provides nucleation sites and leads to grain refinement during solidification [108][109][110].

As demonstrated in Figure 5-2(d) & (e), the microstructure of the Cu50 and Cu75 regions comprises multiple phases with dendritic and spherical morphologies, where the formation of dendrites from the spheroids is particularly evident. Also, as discussed earlier these spheroids are identified as the Cu-lean phases formed as a result of miscibility gap between the liquids of Cu

with other elements. To delve further into the grain refinement mechanism, a series of detailed analyses were conducted in the Cu75 region, with results shown in Figure 5-10. Figure 5-10(a) reveals a heterogeneous microstructure in which grains nucleate on the spheroids. Figure 5-10(b) presents the IPF Z map of the grain structure around a spheroid, showing disruption of the surrounding grain structure and suggesting its role as a nucleation site for Cu-rich liquid during solidification. The presence of fine grains around these spheroids indicates effective grain refinement in their vicinity. According to the CALPHAD data, the Cu-rich and Cu-lean liquids are separated once the Cu75 alloy cools down to the miscibility gap area from 1920 °C to 1190 °C. As schematically shown in Figure 5-10(c-I), this process begins with the separation of Cu-lean liquid from Cu-rich liquid and their growth by diffusion of solutes [111]. The solidification process was obtained from CALPHAD simulation and is indicated in Figure 5-10(d) for each of Cu-lean and Cu-rich liquids. The liquidus and solidus temperatures of Cu-rich (T_L:1130 °C, Ts:1045 °C) and Cu-lean (T_L:1230 °C, Ts:1050 °C) show that the solidification first triggers in the Cu-lean liquid at ~1230 °C by the formation of Ni-rich FCC phase while the Cu-rich liquid is still in the liquid state. In fact, the Cu-rich liquid starts to solidify at 100 °C lower temperature (~1130 °C) than T_L of Cu-lean, at which approximately 75% of the Cu-lean spheroids are solidified, including 65% of Ni-rich FCC and 10% of M_2C carbides (Figure 5-10(d)). This stage is schematically shown in Figure 5-10(c-II). In such circumstances, the semi-solid spheroids can act as nucleation sites and facilitate the heterogeneous nucleation once the Cu-rich matrix begins to solidify (see Figure 5-10(c-III)) [112]. Heterogonous nucleation of grains on the spheroids has been previously observed in immiscible Cu alloys by other researchers as well [91]. Overall, the presence of Cu-lean spheroids was found to be effective grain refiners through heterogeneous nucleation for the remaining liquid and their dispersion in the matrix provides frequent nucleation sites, leading to a uniform highly fine grain structure.

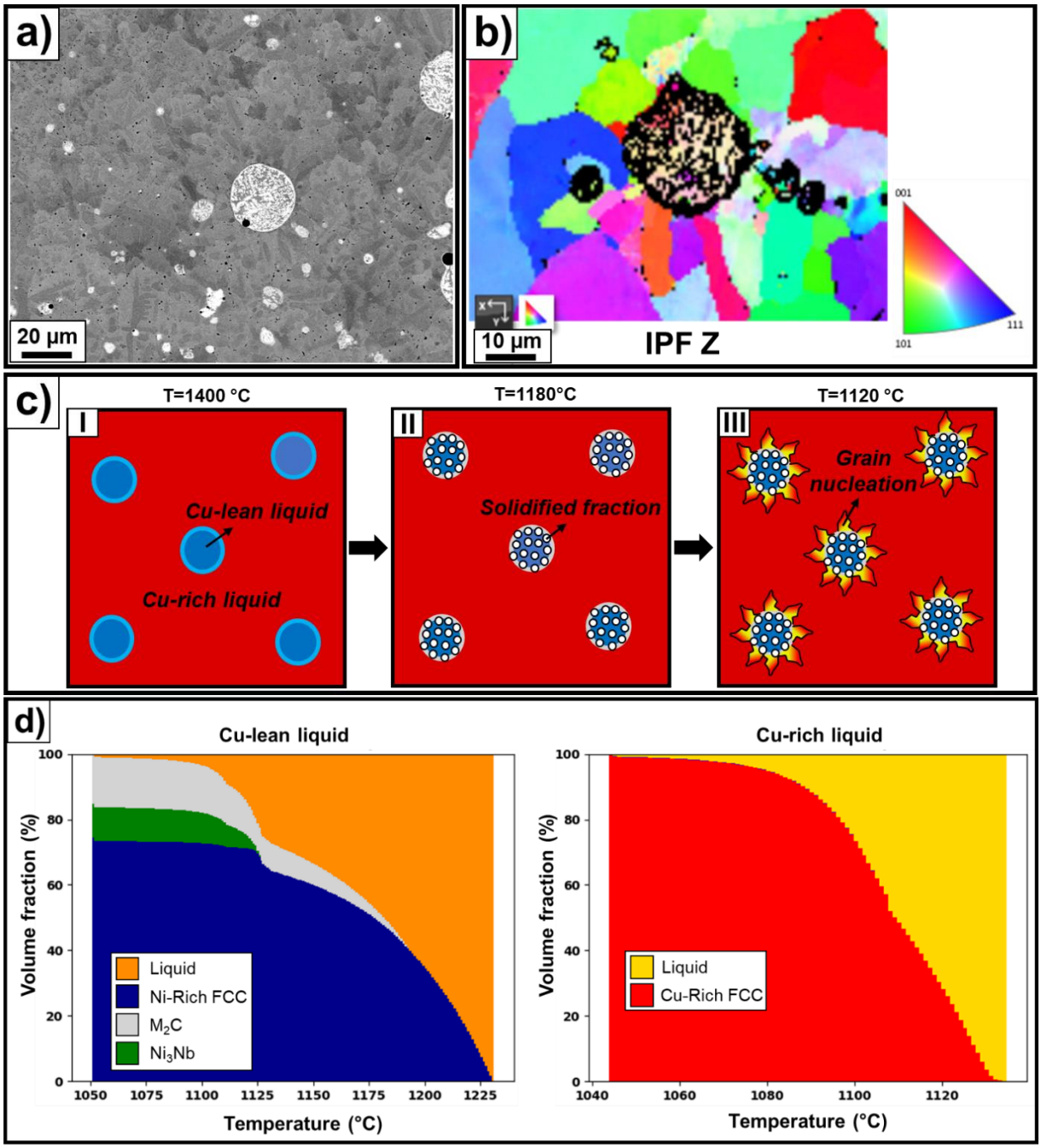


Figure 5-10 Grain refinement mechanism of Cu-rich liquid around Cu-lean spheroid microstructure; (a) BSE image of Cu75 microstructure, (b) IPF Z EBSD map from a spheroid on which distinct grains have nucleated, (c) formation of Cu-lean spheroids during cooling their key role as the nucleation site for the Cu-rich liquid during solidification, (d) Scheil simulation results of volume fraction of various phases in Cu-lean and Cu-rich liquids during solidification.

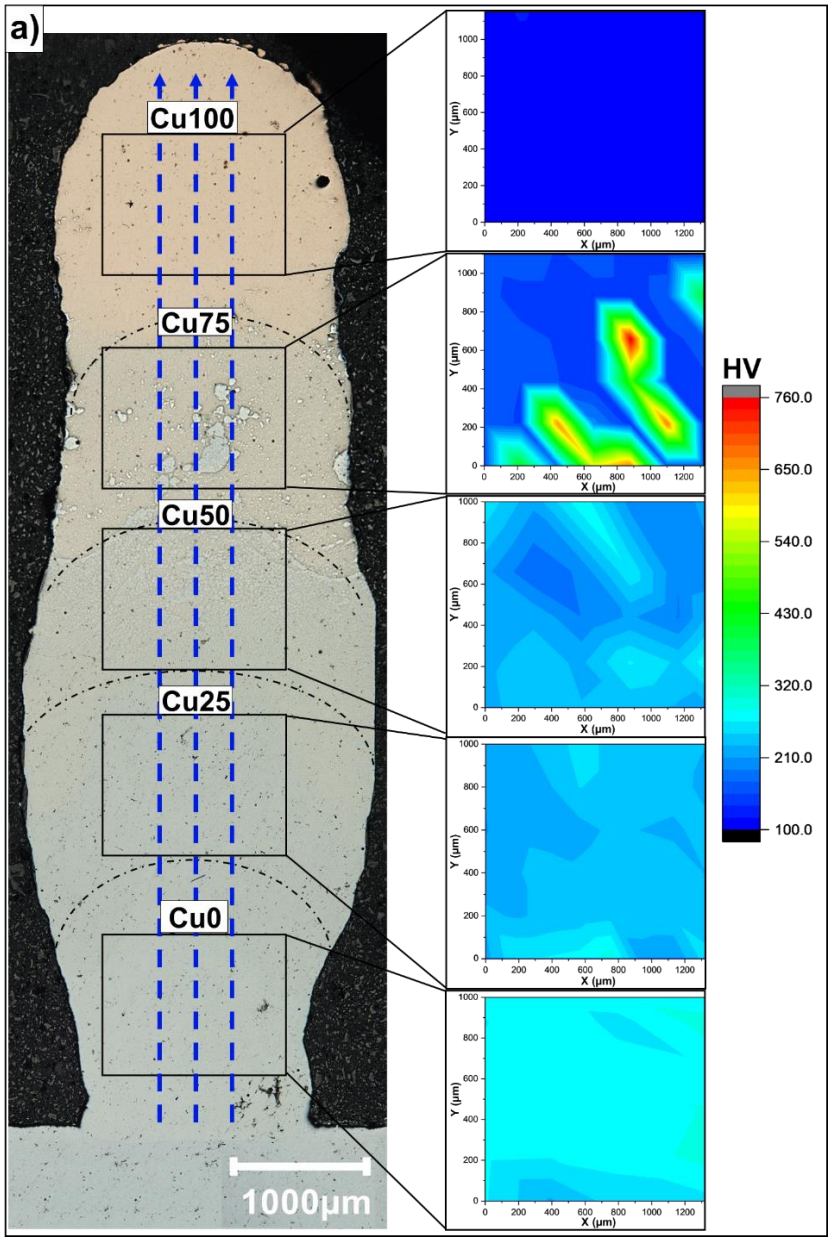
5.3.5 Micro-hardness results

To understand the effect of compositional changes on mechanical properties, micro-hardness measurements were conducted across the cross section of each region of the FGAM thin-wall sample, and the results are illustrated in Figure 5-11. The hardness maps for five regions from Cu0 to Cu 100 are represented in Figure 5-11(a) and the average Vickers hardness from the three dashed lines along the gradient are plotted in Figure 5-11(b).

- **Cu0 region**: The average hardness of 280 HV, is consistent with reported values for as-deposited IN625 via L-DED [113]. The microstructure showed homogeneity, resulting in a smooth hardness profile with a low standard deviation (Figure 5-11(b)).
- **Cu25 region**: A drop in the hardness was observed in this region to 230 HV, attributed to the incorporation of the softer CuCrZr alloy into the IN625 matrix. The single-phase FCC structure in this region contributes to a homogeneous microstructure, and minimal hardness variability (Figure 5-11(b)).
- **Cu50 region**: The hardness further decreased to an average 200 HV, due to the increased copper content. However, a higher standard deviation is observed from the average line hardness measurements (Figure 5-11(b)), which is attributed to the presence of Cu-lean regions within the matrix.
- **Cu75 region:** Significant variability in the hardness is observed, ranging from 160 HV to 760 HV (Figure 5-11(a)). The sharp peaks may be attributed to the notable presence and agglomeration of the M_2C phase in the Cu-lean regions, as previously shown in Figure 9. This variability contributed to the high standard deviation in hardness measurements in this region.

1. **Cu100 region**: The hardness dropped significantly to around 105 HV, which is expected for L-DED of CuCrZr composition lacking additional hardening phases [81]. The homogeneous microstructure resulted in a smooth hardness profile with minimal standard deviation.

In summary, these findings underscore the complex interplay between composition, microstructure, and mechanical properties in the FGAM thin-wall sample.


a)
Cu100
Cu75
Cu50
Cu25
Cu0
1000μm
Y (μm)
X (μm)
HV
760.0
650.0
540.0
430.0
320.0
210.0
100.0

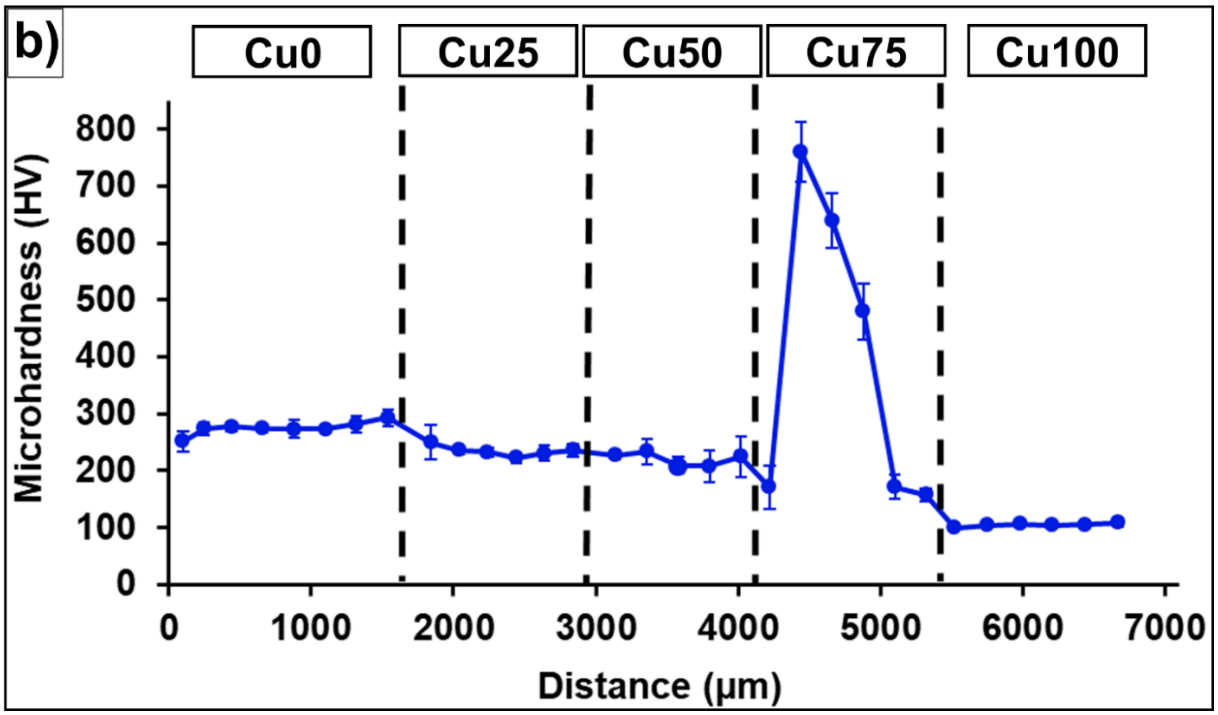


Figure 5-11 Microhardness results of FGAM thin-wall: (a) the hardness maps of the thin-wall sample's cross-section from Cu0 to Cu100 region, (b) Average microhardness of each region on the dashed lines shown in the OM image

5.4 Summary

In this study, we demonstrated successful FGAM of IN625 and CuCrZr in a thin-wall structure using the multi-powder feeder LDED technique. A comprehensive investigation was conducted using thermodynamic simulations and characterization techniques to examine the impact of compositional transitions on the liquid-state miscibility gap and their synergistic effects on the microstructural evolution. The key findings are summarized as follows:

1. At Cu25, the absence of a significant miscibility gap leads to a homogeneous microstructure, where the Cu-rich phase remains dispersed within the interdendritic regions of the IN625 matrix, similar to the structure of Cu0 (IN625) zone.
2. At Cu50 and Cu75 regions, CALPHAD simulations predicted a liquid-phase miscibility gap, leading to Cu-rich and Cu-lean phase separation. Rapid solidification during L-DED preserved this separation, resulting in a dual-phase microstructure.
3. The miscibility gap strongly influenced solidification behavior, promoting spheroidal microstructures with M_2C precipitates while partial dissolution of Ni and Cr in the Cu-rich liquid facilitated dendritic growth within this region.

4. The miscibility gap also promoted grain refinement during solidification by enabling semi-solidified Cu-lean spheroids to act as nucleation sites for the Cu-rich liquid, resulting in a highly fine, equiaxed grain structure (a few microns), unlike the coarse columnar grains in other regions.
5. CALPHAD-predicted phases were largely confirmed by XRD when present in significant volume fractions, while low-volume phases were identified via BSE imaging and EDS, demonstrating the reliability of CALPHAD for phase prediction in FGAM materials.
6. The miscibility gap impacts microhardness, causing significant variability in Cu50 and Cu75, with sharp peaks from M_2C-rich Cu-lean spheroid clusters, while other regions exhibit smooth hardness profiles, underscoring the strong interplay between composition, microstructure, and mechanical properties.

The FGAM thin-wall samples of IN625 to CuCrZr were successfully fabricated without major defects such as lack of fusion or cracks. While Cu-lean spheroids led to grain refinement, their agglomeration caused inhomogeneity in both microstructure and microhardness. Future efforts should focus on developing strategies to prevent or mitigate this issue by tailoring composition gradients and process parameters using thermodynamic tools, as well as applying post-process heat treatments, to minimize the agglomeration and ensure even distribution throughout the deposition.

Chapter 6: Unveiling Defect Formation Mechanisms in Functionally Graded Additive Manufacturing of IN625-CuCrZr alloys

6.1 Introduction

The unique capabilities of FGAM can mitigate the limitations of commonly used valuable alloys by enabling controlled compositional change [8,9]. The FGAM of nickel-based superalloys, known for their high mechanical performance, with highly conductive copper alloys has recently become a focal point for high heat flux applications, particularly in the aerospace industry [10]. Combining nickel-based superalloys with pure copper or copper alloys can improve the overall thermophysical properties such as the thermal conductivity and thermal diffusivity of the structure while preserving the exceptional strength, corrosion, and oxidation resistance of the superalloy [11]. Pan et al. [12] reported the L-DED fabricated crack-free IN625-Copper 110 bimetallic structure with a 100% increase in thermal diffusivity.

Despite these advantages, significant differences in thermophysical and metallurgical properties between the alloys poses challenges to achieving defect-free structures, particularly with abrupt compositional transitions. Lack of fusion (LoF) porosity and cracks are the typical defects that have been reported in FGAM process [13,14]. LoF pores primarily result from insufficient energy input to fully melt the powder and/or provide proper overlap with adjacent tracks. In that regard, compositional transitions can further exacerbate LoF through differences in thermophysical properties such as varying melting temperatures, thermal diffusivity, and laser absorptivity of FGAM alloy powders[15][16]. Crack formation in FGAM is a complex phenomenon with multiple types, each influenced by different factors, such as strain-induced cracks caused by shrinkage and residual stresses after solidification [17]. Solidification cracking is another common crack formation mechanism in FGAM, occurring during the final stages of solidification. When the melting temperature range of the FGAM is large, liquid films of the material with a lower melting point can become trapped in the solidified portion. These trapped liquid films are unable to accommodate the tensile stresses arising during cooling, ultimately leading to solidification crack initiation [18,19].

In this study, FGAM cuboids of IN625-CuCrZr were fabricated using the L-DED process with five compositional layers, transitioning from 100% IN625 to 100% CuCrZr in 25 wt.% increments of CuCrZr. This smooth gradual compositional transition minimized abrupt thermophysical, and mechanical mismatches. Process parameters were optimized by adjusting the proposed absorbed laser power (*Pa*) and combined parameter of powder feed rate over laser scanning speed (*F/V*) to minimize porosity defects. Further, crack formation was thoroughly investigated to identify the mechanisms driving initiation, propagation, and potential arrest. Thermodynamic simulations and microstructural characterizations were used to examine how compositional changes, solidification mechanisms, and the evolution of phases and grain structure influence cracking behavior across the compositional gradient. In this research and for the first time a liquid-state miscibility gap at 50 and 75 wt.% CuCrZr compositional gradients was identified, which forms Cu-lean spheroids that redirect cracks around them rather than through them. Additionally, these spheroids contributed to grain refinement, which enhances strain accommodation and promotes crack arrest.

6.2 Methodology

Cuboid samples with 8mm x 15mm x 15mm dimensions were fabricated by an in-house built robotic L-DED system equipped with 1 kW fiber laser, a dual hopper powder feeder, and a coaxial nozzle. Depositions were conducted on an SS304 substrate using with 9 different sets of process parameters, where the laser power (*P*) adjusted based on the change in composition while the laser spot size and the scanning speed (*V*) was set at 1.2 mm and 10 mm/s, respectively, and powder flow rate (*F*) in the range of 2-6 g/min. Table 6-1 summarizes the process parameters used for the FGAM processing via L-DED. The fraction of alloys in the powder blend at each deposited region, with respective designated labels, and laser beam absorptivity are included in Table 6-2. The absorptivity values for IN625 and CuCrZr are reported to be around 65% and 25%, respectively [33][74], [75] while intermediate values for compositional mixtures are derived using the rule of mixtures.

Table 6-1 Input process parameters for FGAM processing of the cuboid samples via L-DED

Sample No.	*P (W)*	*F (g/min)*	*V (mm/s)*
1	550-1000	2	10
2	550-1000	4	10
3	550-1000	6	10
4	500-900	2	10
5	500-900	4	10
6	500-900	6	10
7	450-800	2	10
8	450-800	4	10
9	450-800	6	10

Table 6-2 The composition of each section in the FGAM sample and the corresponding laser beam absorptivity

Region in FGM	Nominal portion of IN625 (wt.%)	Nominal portion of CuCrZr (wt.%)	Label	Laser beam absorptivity (β)
Zone 1	100	0	Cu0	0.65
Zone 2	75	25	Cu25	0.55
Zone 3	50	50	Cu50	0.45
Zone 4	25	75	Cu75	0.35
Zone 5	0	100	Cu100	0.25

6.2.1 Calculation of crack susceptibility index

Solidification simulations for the mixed compositional sections of IN625-CuCrZr FGAM were conducted by CALPHAD (CALculation of PHAse Diagrams) software under non-equilibrium conditions following the Scheil model (with no back diffusion). Additional simulations, namely the calculation of crack susceptibility index, were conducted on each 1 wt.% incremental composition and up to 25 wt.% CuCrZr employing Thermo-Calc 2023 software with TCCU5 thermodynamic database for Cu-based alloys [114], and TCNI12 for Ni-based alloys [115].

6.3 Results and Discussion

6.3.1 Overview of the Defects in FGAM

Figure 6-1 provides a cross-sectional view of a FGAM IN625-CuCrZr cuboid sample, showcasing the two primary types of defects observed in most of samples: porosity and cracks. Porosity, identified as rounded or irregular voids, is predominantly located in the upper regions of the sample. On the other hand, cracks, categorized as narrow elongated discontinuities, are mainly observed in the lower compositional regions and align along the build direction (BD). The variety of defects along the gradient reflects the influence of compositional changes on the formation mechanism of porosity and cracks, each of them will be explored in more detail in the following sections.

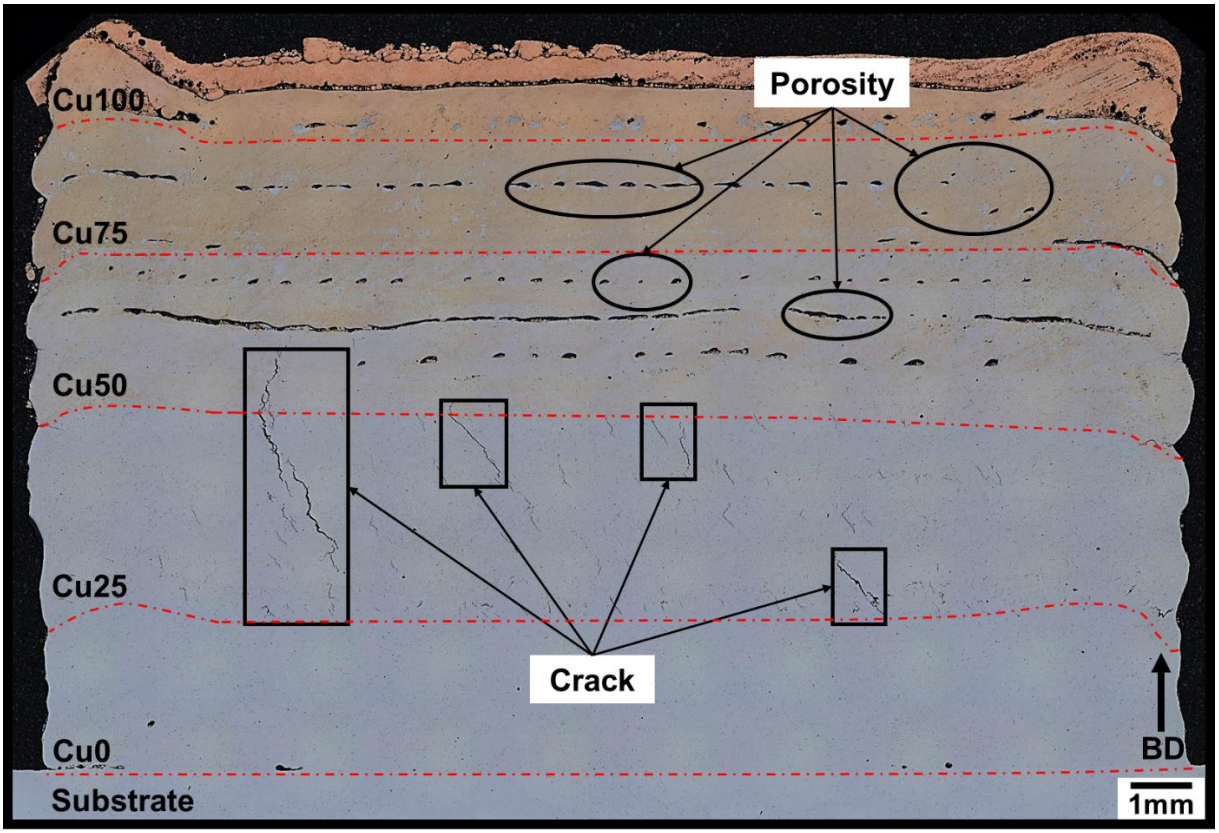


Figure 6-1 Cross-sectional view of a FGAM IN625-CuCrZr cuboid sample highlighting the porosity and crack defects across the compositional gradient.

6.3.2 Porosity

To understand the types of pores and their formation mechanisms, two samples one with low porosity and one high porosity were analyzed in detail and the results are shown in Figure 6-2. Figure 6-2 (a) presents the micrograph of the low porosity sample with relatively small spherical

pores formed by trapped gas in the powder particles during the powder manufacturing and during the deposition process [116]. The micrograph reveals that the quantity of gas porosities is notably higher in the Cu75 and Cu100 regions, likely due to higher oxidation tendency of the copper during deposition in ambient atmosphere [117]. Figure 6-2 (b) shows the micrograph of the high porosity sample, where coarse, irregularly shaped pores containing unmelted powders are visible, indicative of LoF porosities [118]. This porosity is often associated with insufficient input energy density per amount of powders fed to the melt pool, leading to incomplete bonding between adjacent tracks [65]. The printing strategy includes an alternating 90° rotation after each layer (XY-Scan). Hence, the magnified LoF porosities appear elongated in the X direction and hole-shaped in the Y directions (Figure 6-2(b)).

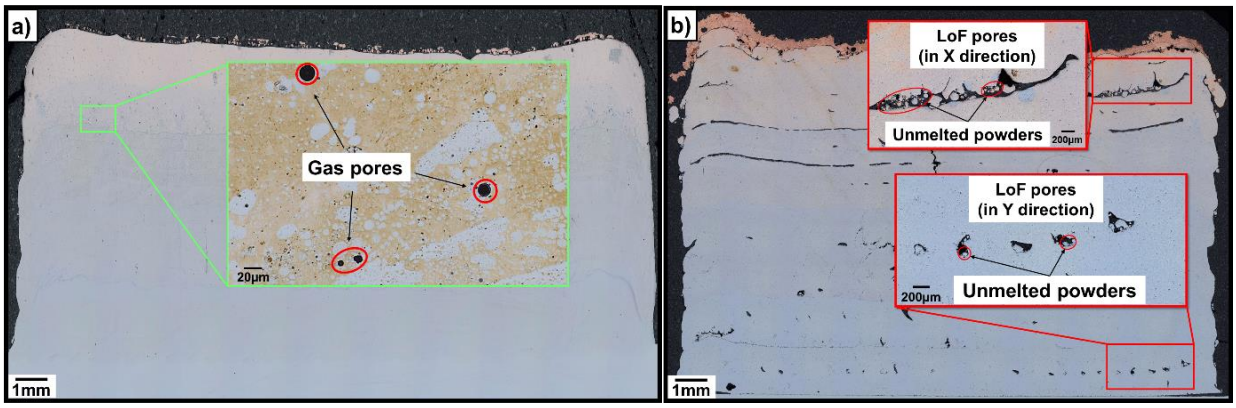


Figure 6-2 Porosity defects in FGAM of IN625-CuCrZr; (a) gas pores, (b) lack of fusions in X and Y directions.

Although the gas porosity is commonly present in L-DED printed samples, particularly when processing in an ambient environment, the LoF porosities are strongly influenced by key processing parameters. These defects can be tackled through process optimization aimed at maximizing energy density, providing sufficient overlap between adjacent tracks in both horizontal and vertical directions. In that regard, Figure 6-3(a) represents a schematic of LoF formation mechanism according to the melt pool characteristics, including their width (W), height (h), hatch distance (H), and depth of penetration (b). The previous work by the authors [119] demonstrated that to avoid LoF porosity, the following criterion must be satisfied:

$$\left(\frac{h}{b}\right)^2 + \left(\frac{H}{W}\right)^2 \leq 1 \qquad \text{(equation 6-1)}$$

Understanding the correlation between these geometrical characteristics and process parameters is critical for mitigating their occurrence. In L-DED, laser power (P) determines b and W, while combined parameter of the powder feed rate-to-scanning speed ratio (F/V) influences h [48], [81].

Therefore, to identify a reliable process window, the porosity level of the samples with different process parameters was measured from micrographs. It is worth noting that the cracks present in all samples were excluded from the porosity measurements and will be investigated separately in the following sections. Figure 6-3(b) illustrates the effect of absorbed laser power (P_a) and the F/V on porosity levels in FGAM IN625-CuCrZr cuboid samples. The absorbed laser power P_a is defined as the actual amount of laser energy absorbed by the material during the process. As the composition changes throughout the print, the laser power needs to be adjusted based on the estimated absorptivity of the composition to ensure that the absorbed laser power remains constant across the entire FGAM sample. This relationship is expressed mathematically as:

$$P_a = P \times \beta \qquad \text{(equation 6-2)}$$

where P is the actual laser power and β is the laser beam absorptivity listed in Table 6-2. Based on the porosity level map shown in Figure 6-3(b), it is evident that higher P_a leads to lower porosity levels, while lower P_a results in increased voids. Similarly, excessive F/V ratios correspond to increased porosity, whereas lower values are associated with reduced porosity. The color-coded zones highlight a clear trend, where the combined effect of these parameters is particularly critical, with optimal conditions shown in green and characterized by higher P_a and lower F/V ratios, resulting in minimized porosity. As an increase in P_a enhances b and W, and a decrease in F/V reduces h, the observed correlation between the proposed parameters and porosity levels aligns with equation 6-1.

These trends highlight the need for careful balancing of the combination of these parameters in achieving proper track overlap to eliminate LoF porosities in FGAM of IN625-CuCrZr. The cracking mechanism will be discussed in more detail in the following sections.

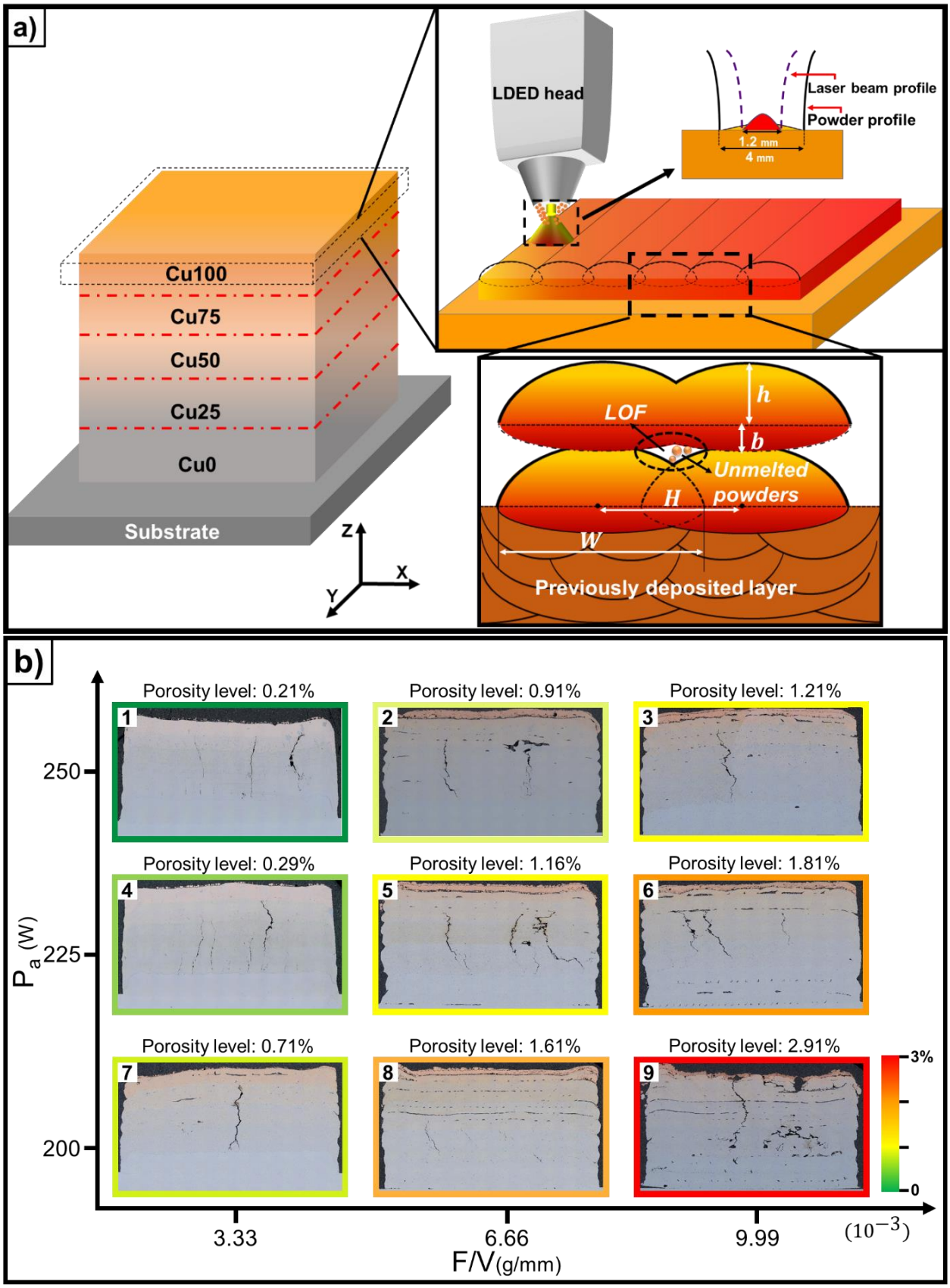

a)
LDED head
Laser beam profile
Powder profile
1.2 mm
4 mm
Cu100
Cu75
Cu50
Cu25
Cu0
Substrate
Z
X
Y
h
LOF
b
Unmelted powders
H
W
Previously deposited layer
b)
Porosity level: 0.21%
Porosity level: 0.91%
Porosity level: 1.21%
Porosity level: 0.29%
Porosity level: 1.16%
Porosity level: 1.81%
Porosity level: 0.71%
Porosity level: 1.61%
Porosity level: 2.91%
1
2
3
4
5
6
7
8
9
250
225
200
P_a (W)
3.33
6.66
9.99
(10^{-3})
F/V(g/mm)
3%
0

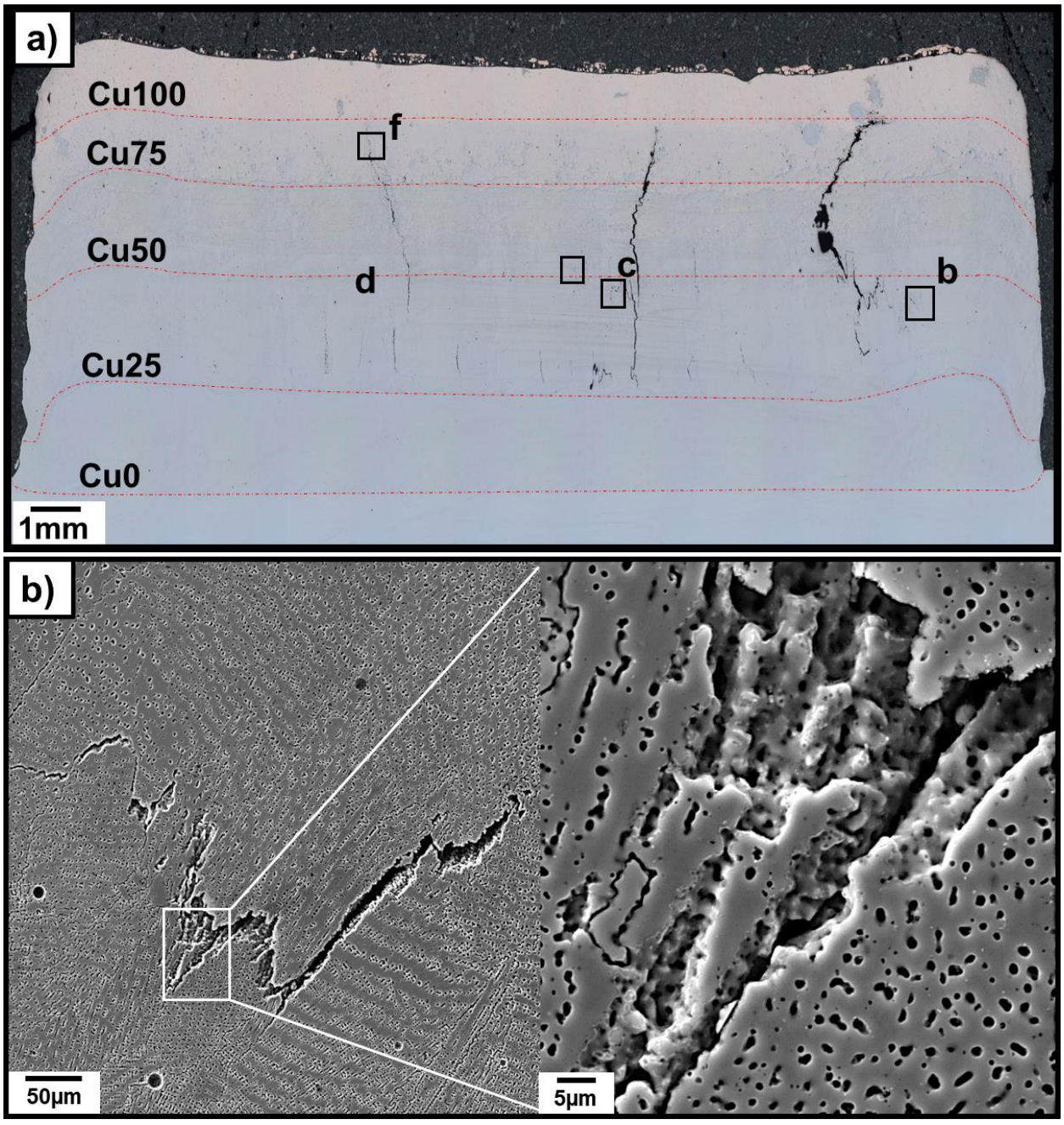
Figure 6-3 Correlation between porosity and process parameters, (a) LoF formation mechanism and melt pool's geometrical characteristics, (b) The porosity level based on Pa and F/V in FGAM of IN625-CuCrZr.

6.3.3 Crack formation

The cracking behavior of the FGAM cuboid samples was examined in detail, with the results shown in Figure 6-4. Figure 6-4(a) displays the cross-section of the printed Sample #1, illustrating the initiation, propagation, and arrest of cracks across various compositional regions. The micrograph shows that all cracks originated in the Cu25 region, with most of them also terminating within the same area. However, some cracks coalesced into larger ones that propagated into the Cu50 region and eventually arrest in the Cu75 region.

Figure 6-4(b) provides SEM-secondary electron (SE) images from the etched microstructure of a crack in the Cu25 region. The higher magnification image reveals the initiation of the crack within the interdendritic regions, indicative of solidification cracking [120], [121]. In addition, the EDS line scan and elemental map from a crack in the Cu25 region in Figure 6-4(c), shows the segregation of Cu around a crack. The pronounced fluctuations in Cu concentration near the crack, along with traces found inside it, indicate the presence of a Cu-rich liquid film prior to completion of solidification [122], [123]. Most cracks, aside from a few coarse ones, were found to arrest within the upper region of Cu25. Figure 6-4(d) shows the SEM-backscattered electron (BSE) image along with the EDS elemental map from the tip of a healed crack, highlighting Cu element that backfilled the crack [122], [124].

Furthermore, due to the high stress concentration, only the coarse cracks in the Cu25 region propagated into the Cu50 region, driven by the thermal stresses introduced during the L-DED process [125]. As shown in Figure 6-4(e), the crack morphology undergoes a significant transformation, transitioning from a relatively straight trajectory in Cu25 to a zigzag pattern upon entering Cu50. A similar zigzag pattern is observed for the crack in the Cu75 region, as depicted in Figure 6-4(f), where it propagated predominantly along the Cu-rich matrix and ultimately arrested within this region. This analysis highlights the interaction between cracks and the different compositions across the gradient. The next section will shed light on the effect of compositional transition on cracking behavior in FGAM of IN625-CuCrZr.


a)
Cu100
Cu75
Cu50
Cu25
Cu0
f
d
c
b
1mm
b)
50µm
5µm

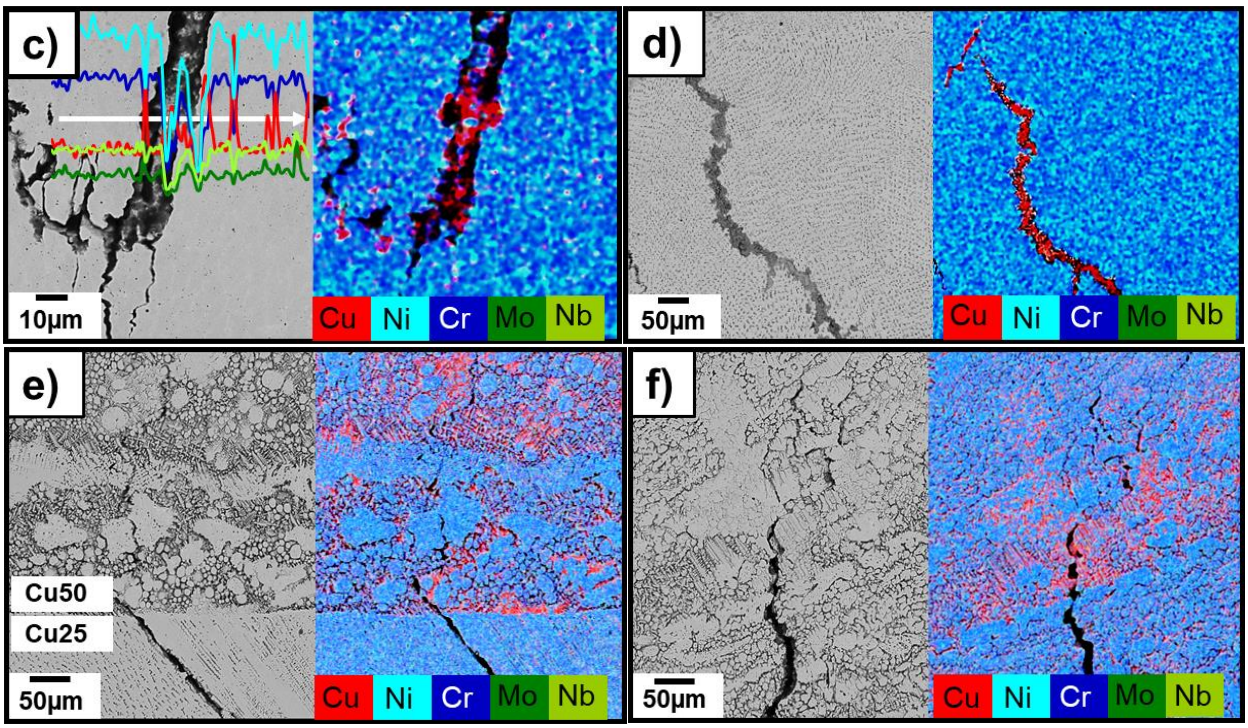


Figure 6-4 Crack formation in FGAM of IN625-CuCrZr sample, (a) OM of the entire cross-section of the sample No.1, (b) low/high magnification micrographs from a crack, initiating in interdendritic region, (c) EDS line scan and elemental map from a crack, highlighting presence of Cu-rich liquid film, (d) SEM-BSE image and EDS map from the tip of a healed crack, highlighting backfilling by Cu-rich liquid film, (e) change in crack morphology from straight to zigzag upon entering Cu50, (f) similar zigzag morphology of the crack in Cu75.

6.3.4 Effect of composition on cracking

To understand the effect of composition on cracking behavior across the gradient, it is essential to first comprehend how compositional changes influence microstructural evolution. In the following sections, the microstructural characteristics of each compositional region will be covered in detail, and then the influence of compositional change on crack initiation will be discussed comprehensively.

Metastable miscibility gap and microstructures across the gradient

The microstructural characteristics across the compositional gradient in one of the cuboid sample is shown in Figure 6-5. As shown in Figure 6-5(a), the Cu0 region consists of dendritic structures, a typical microstructure in L-DED of IN625 [113]. Similarly, Figure 6-5(b) reveals the Cu25 region exhibits a dendritic morphology with some Cu segregation in the interdendritic regions. Figures 6-5(c) and 6-5(d) illustrate the microstructure of the Cu50 and Cu75 regions, respectively, which exhibit a mixed morphology of dendrites and Cu-lean spheroids [91] dispersed within a Cu-

rich matrix. As previously studied by the authors, these distinct microstructures are the result of the metastable miscibility gap between the liquid of two alloys, depicted in Figure 6-5(f). Finally, the Cu100 region is shown in Figure 6-5(e) and characterized by a cellular structure with dispersed Cr-rich particles as previously studied by the authors [81]. These microstructural variations, along with the metastable miscibility gap, impact the solidification phenomena, and consequently, the initiation, propagation, and the arrest of solidification cracks in the FGAM samples. These phenomena will be explored in more detail in the following sections.

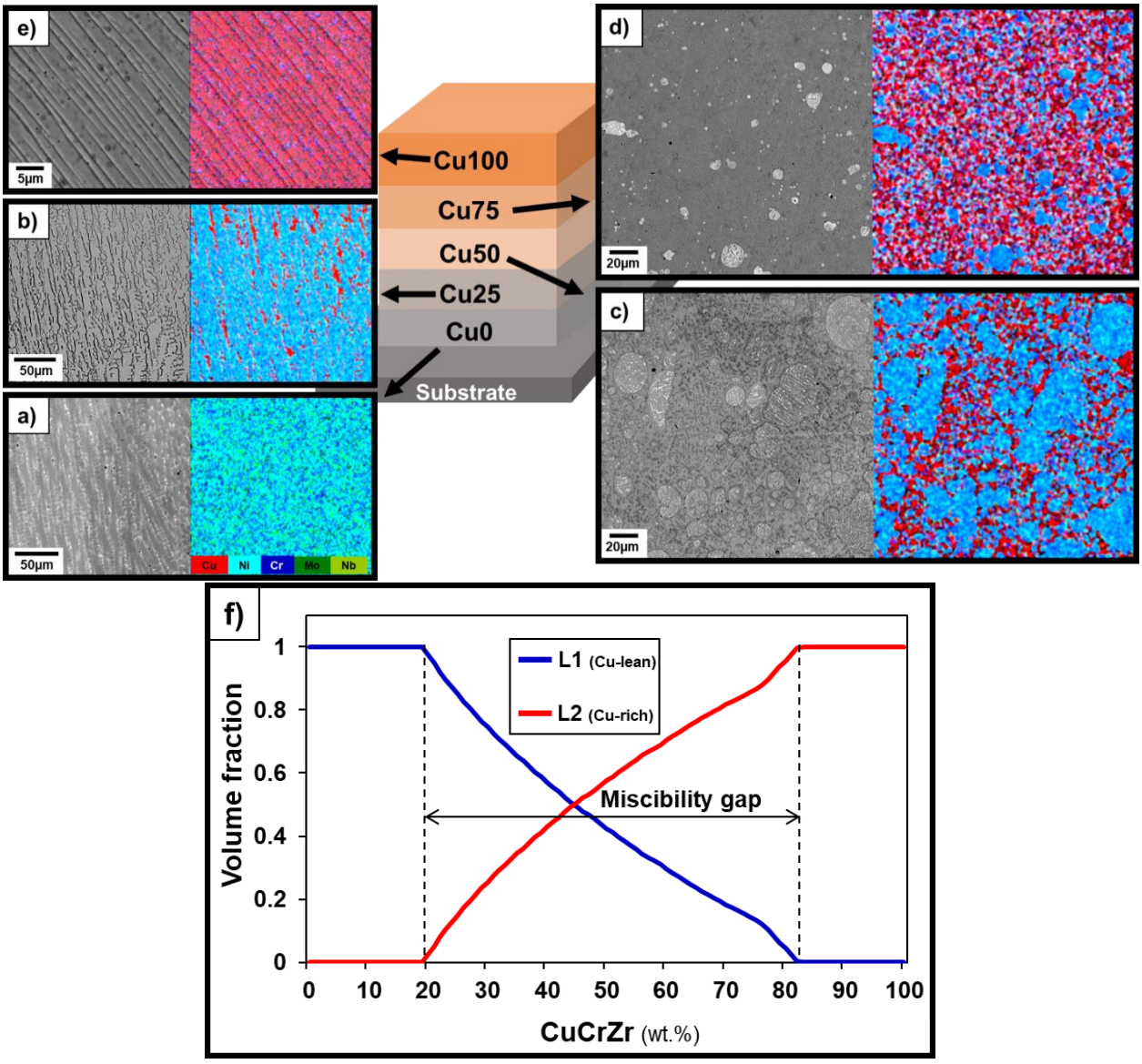


Figure 6-5 The microstructural characteristics across the compositional gradient in a cuboid sample, (a) dendritic structure in Cu0, (b) similar dendritic structure with segregation of Cu in the interdendritic region, (c) & (d) mixed morphology of dendrites and Cu-lean spheroids dispersed in Cu-rich matrix, (e)

cellular structure of Cu100, and (f) the liquid state miscibility gap based on the amount of CuCrZr that influence the solidification phenomena in Cu50 and Cu75.

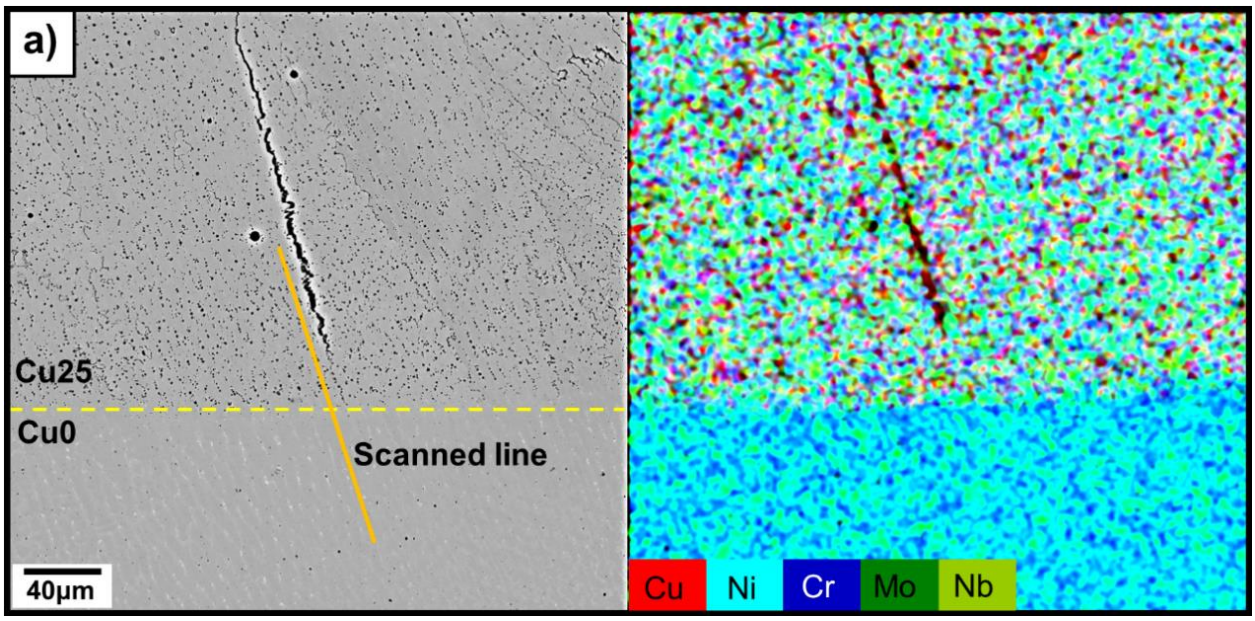
Solidification and crack initiation in Cu25

The evolution of chemical composition across the gradient influences the primary factors of solidification cracking. This includes the solidification temperature range, the existence of the liquid film at the last stage of solidification, and the ability of the liquid film to redistribute and backfill the gaps caused by solidification shrinkage [26]. The impact of chemical composition on the solidification cracking initiation in the FGAM of IN625-CuCrZr cuboid samples has been investigated in detail with the results presented in Figure 6-6. Figure 6-6 (a) illustrates the initiation of a crack originating from the first melt pool in Cu25 region. Apparently, the addition of CuCrZr alloy to the composition prompted the condition for solidification cracking in Cu25. Therefore, to investigate the effect of compositional change via addition of CuCrZr on crack initiation, Kou's solidification cracking susceptibility index (CSI) [126] was calculated for Cu0 to Cu25 on each 1wt.% composition interval of CuCrZr and the results are shown in Figure 6-6 (b). The CSI, in fact, quantifies the likelihood of crack initiation based on the composition as follows:

$$CSI = dT/d(f_s)^{1/2},\ fs \xrightarrow{yields} 1 \qquad \text{(equation 6-3)}$$

where T is the temperature of the mushy zone and f_s is the fraction of solid. Kou's index considers the values close to 1 as the critical range for f_s, where dendritic growth significantly restricts liquid mobility, and the remaining liquid is unable to effectively backfill shrinkage-induced gaps. Solidification calculations were conducted through Thermocalc's Scheil solidification model on 1% incremental chemical compositions from 0 to 25% CuCrZr and IN625 balance. To evaluate the CSI, the square root of the solid fraction $f_s^{1/2}$ from Scheil solidification simulation was used. The CSI was determined from the maximum steepness of the T-$f_s^{1/2}$ curve up to $f_s^{1/2}$= 0.99 [127], and results are shown in Figure 6-6 (b). The susceptibility to solidification cracking from Cu0 to Cu25 increases with the rise in CuCrZr content to the level of 15%, then decreases afterwards, and forms a Λ-shaped curve. Figure 6-6 (c) presents the EDS line scan results along a crack, which is in agreement with the simulation findings. Based on the elemental distribution, the peak in CSI aligns closely with the Cu content (15 wt.%) in the vicinity of the crack. To delve further into the effect of CuCrZr addition, DSC was conducted on Cu0 and Cu25 compositions as shown in Figure

6-6 (d). The DSC cooling curves at a 10°C/min for Cu0 (IN625) and Cu25 compositions highlight the liquidous and solidus points of each composition. Compared to Cu0 with 40°C solidification range (from T_L:1330°C to T_S:1290°C), the DSC curve for Cu25 shows larger solidification range of 90°C (from $\acute{T}_L$:1321 to $\acute{T}_S$:1231°C). In fact, the addition of the CuCrZr alloy with lower melting point to the IN625 alloy increases the solidification temperature range in Cu25, thereby elevating the susceptibility to cracking [26]. This happens by the formation of Cu-rich liquid film at the end of the solidification in Cu25 composition. As shown in Figure 6-4 (b), the Cu-rich liquid film exists in the interdendritic regions where the cracks initiate. As shown schematically in Figure 6-6(e), this Cu-rich liquid film forms between the columnar dendritic structures that align with the thermal gradient [128][129]. In general, solidification cracking occurs during the final stages of solidification, when f_s ranges between 0.9 and 0.99, labelled as vulnerable stage [130]. The directional growth of these dendrites, during the vulnerable stage, can restrict the flow of the liquid, leaving the Cu-rich liquid films trapped in interdendritic region. These trapped films are unable to accommodate the tensile stresses arising during cooling, ultimately resulting in crack initiation [128]. Here, the interplay between dendritic growth and the presence of specific amount of Cu-rich liquid films creates an ideal environment for crack initiation. The following section will shed light on the interaction of the crack with the microstructure in Cu50 and Cu75 regions.



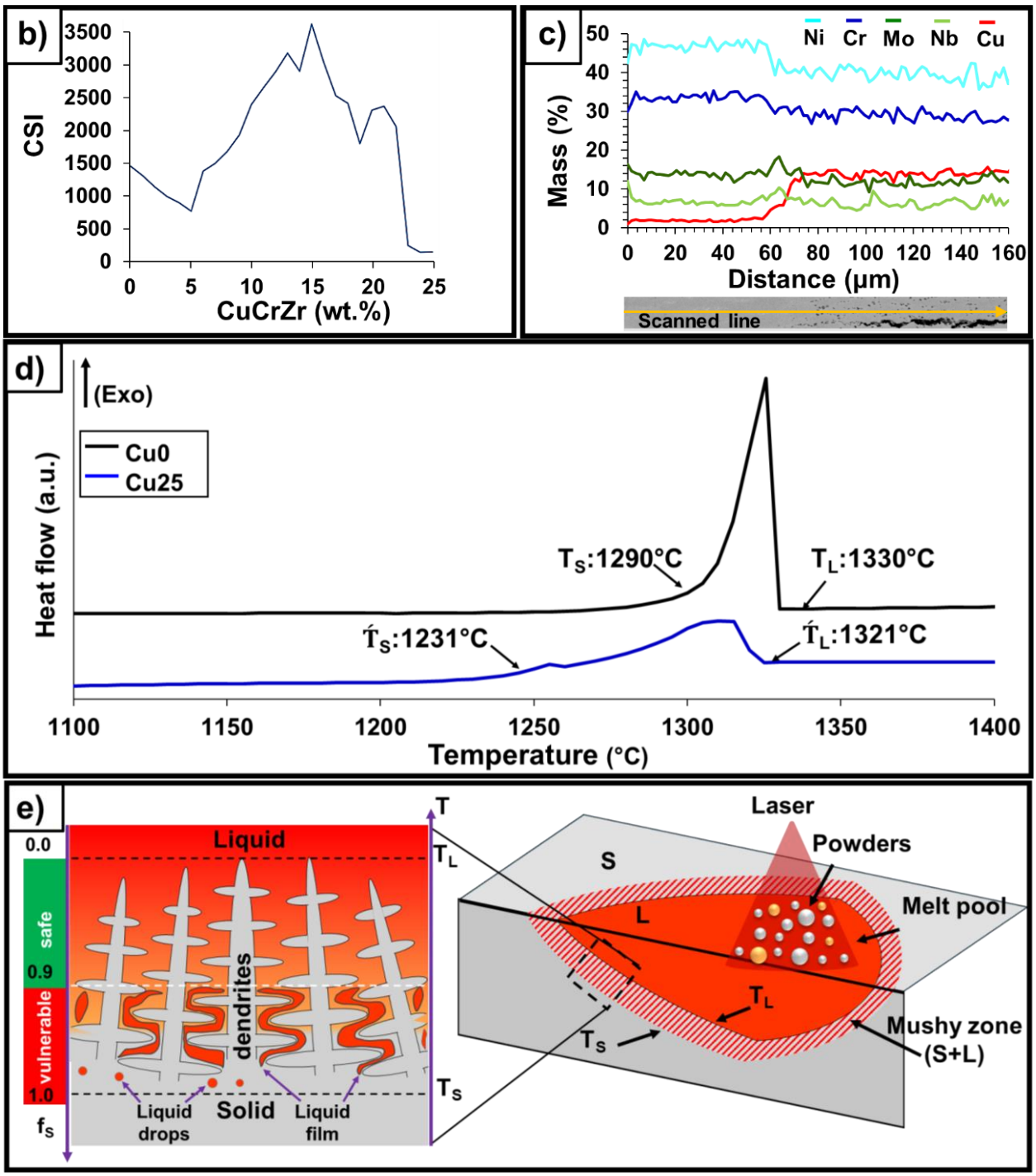
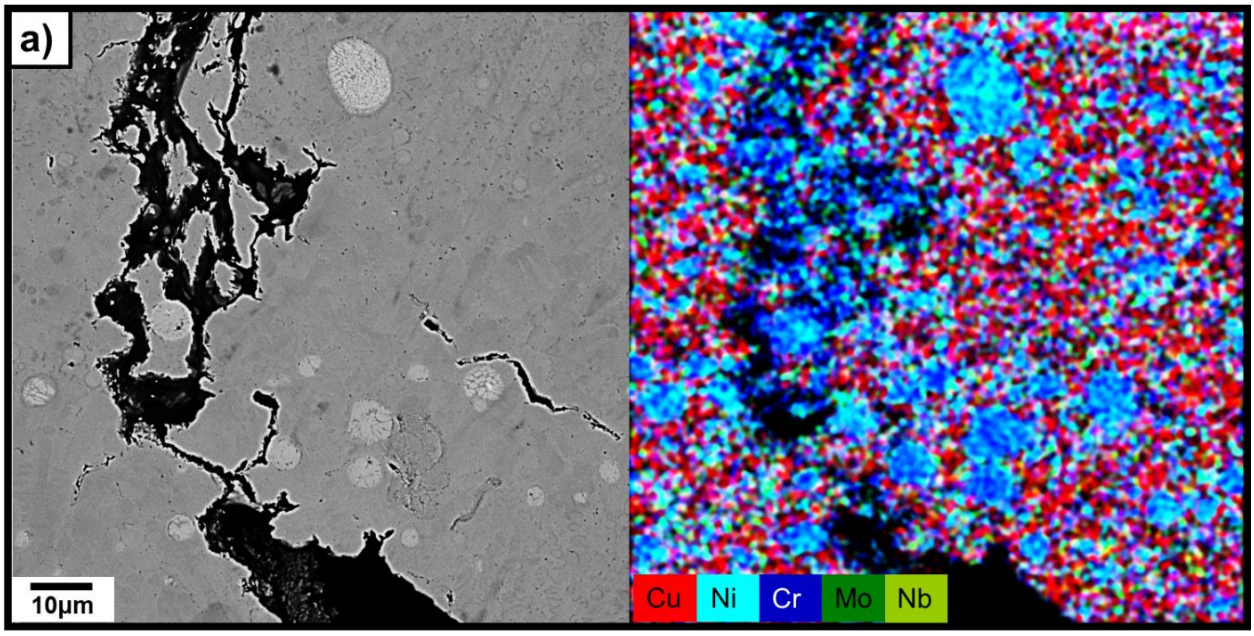


Figure 6-6 The effect of composition on solidification cracking in FGAM of IN625-CuCrZr,(a) BSE and EDS elemental map from the interface of Cu0 and Cu25 where the crack initiates, (b) Kou's CSI calculated based on amount of CuCrZr alloy in the composition and maximized at around 15% wt. CuCrZr, (c) EDS line scan in the vicinity of the crack shown in BSE of (a) shows around 15% wt. of Cu element, (d) DSC cooling curves of Cu0 and Cu25 compositions highlighting larger solidification range

of Cu25, (e) schematic of the solidification in the mushy zone of Cu25 highlighting interdendritic Cu liquid film that results in cracking.

Solidification and cracking behavior in Cu50 and Cu75

Figure 6-7 provides a detailed analysis on the interaction between the cracks and microstructure of Cu50 and Cu75 regions. As seen from the micrograph of Figure 6-7(a), the crack propagation path is significantly altered upon encountering the bright Cu-lean spheroids with branching and navigating around these spheroids that prevent its straight-line propagation. Figure 6-7(b) shows the X-CT analysis results, which provide 3D distribution of cracks, color-coded across the compositional gradient, alongside Cu-lean spheroids shown in grayscale in the upper regions. The magnified view of a crack (depicted in green) illustrates its interaction with Cu-lean spheroids (shown in gray), around which the crack navigates instead of penetrating. This behavior is primarily attributed to the metastable miscibility gap, as shown in Figure 6-5(e) [86], [91]. The synergistic effect of the miscibility gap and the solidification phenomenon in both Cu50 and Cu75 regions influences the cracking behavior in these areas. Therefore, it is essential to investigate the solidification phenomena of these compositions in detail, as discussed in the following section.



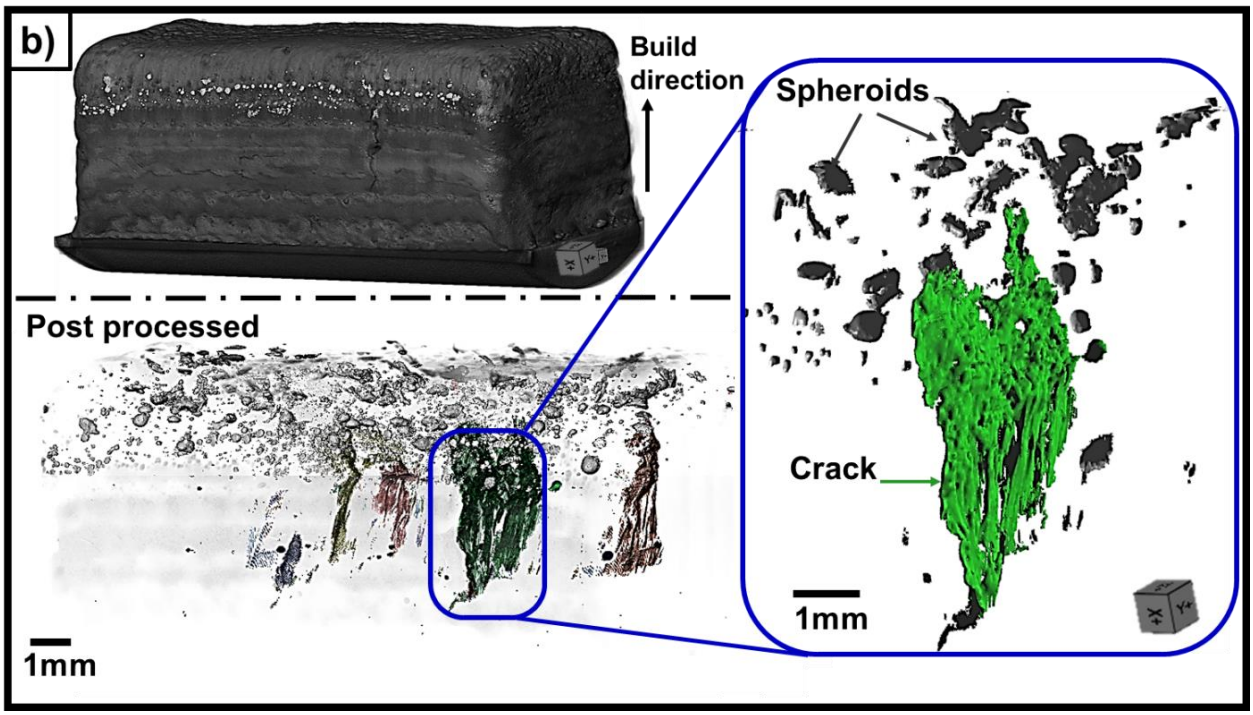
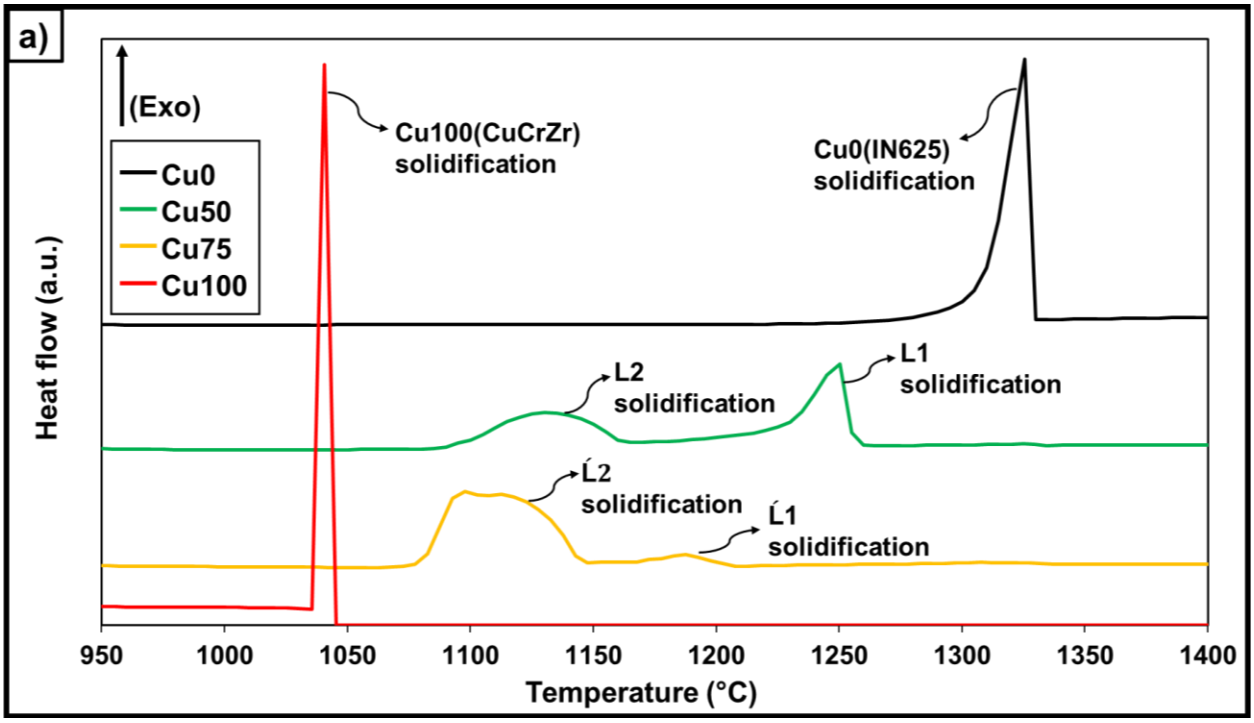


Figure 6-7 Cracking behavior and solidification phenomena in Cu50 and Cu75 regions; (a) BSE and EDS mixed elemental map illustrating crack branching and navigating around the Cu-lean spheroids, (b) X-CT analysis of the FGAM cuboid sample representing cracks in 3D, navigating around Cu-lean spheroids without penetrating them

The solidification phenomena in the Cu50 and Cu75 regions were investigated in detail, with the results presented in Figure 6-8. Figure 6-8(a) represents the DSC results that were conducted on these compositions as well as each of Cu0 (IN625) and Cu100 (CuCrZr). Unlike the single solidification peaks for Cu0 and Cu100, both Cu50 and Cu75 compositions are comprised of two distinct solidification peaks. The consecutive peaks in the cooling curves of Cu50 are annotated with L_1 (Cu-lean) and L_2 (Cu-rich), which denotes solidification of the Cu-lean and Cu-rich liquids, respectively. Similar phenomena can be seen for the cooling curve of Cu75 with the $\acute{L}_1$ and $\acute{L}_2$ peaks highlighting the solidification of Cu-lean and Cu-rich liquids, respectively. However, the cooling rate of 10°C/min in DSC is significantly slower than the actual rates in the L-DED process, which range from $10^3 - 10^5$ °C/s [131], [132]. Besides, the undercooling experienced during the L-DED process strongly influences the solidification behavior [26]. Therefore, to better approximate the rapid solidification conditions of the process, Scheil solidification simulations were performed for both Cu-lean and Cu-rich liquids, with the results presented in Figure 6-8(b) for Cu75 composition. As highlighted in the diagram, the solidification of Cu-rich liquid (L_2) begins at 1130°C where around 75% volume fraction of the Cu-lean liquid (L_1) is solidified. These

highlights separate consecutive solidification of the two liquids within the mushy zone of Cu75 region as shown schematically in Figure 6-8(c). The miscibility gap between the two liquids starts after a critical temperature (Tc:1920°C) where the liquid begins to separate into two liquids L_1 (Cu-lean) and L_2 (Cu-rich), each of them have their own solidification path. L_1 solidifies between TL_1:1230°C and TS_1:1056°C while L_2 solidifies from TL_2:1130°C to TS_2:1040°C. These distinct solidification paths result in forming a mixed morphology of dendrites and Cu-lean spheroids dispersed in a Cu-rich matrix [86], [87], [91]. The Cu-lean spheroids form prior to the solidification of the Cu-rich liquid and act as the nucleation site for the Cu-rich liquid, as shown in the OM micrograph from a lightly etched region of Cu75. Therefore, their early formation establishes them as distinct robust inclusions within the Cu-rich liquid in which the crack propagates.

Overall, these findings reveal the interplay between compositional and microstructural evolution during solidification, highlighting the role of the miscibility gap in determining cracking behavior in Cu50 and Cu75. The next section will explore how compositional changes affect grain structure across the gradient and their synergistic impact on cracking behavior.



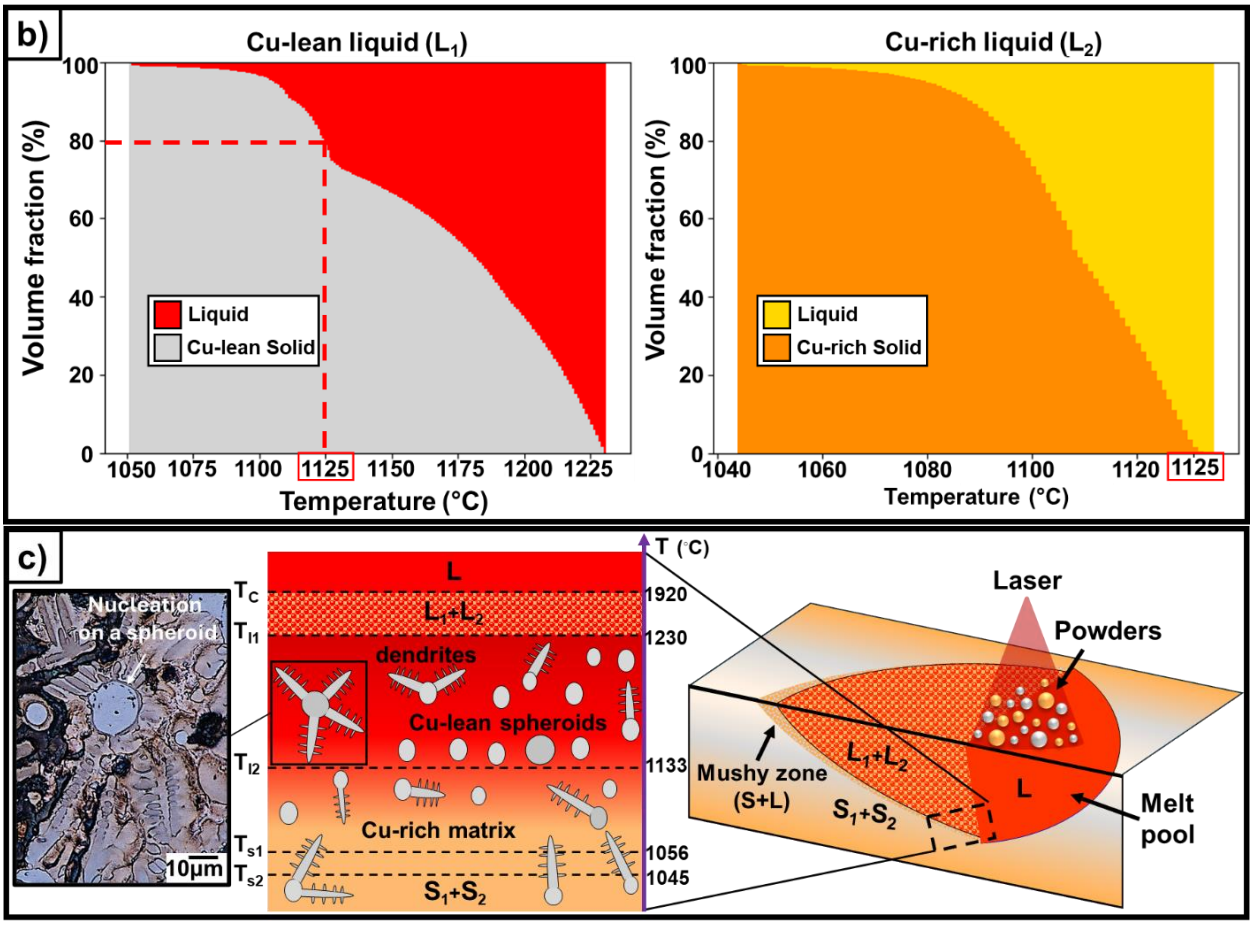


Figure 6-8 solidification phenomena in Cu50 and Cu75 regions; (a) DSC cooling curves highlighting two distinct consecutive solidification peaks in Cu50 and Cu75 compositions as a result of the miscibility gap between the liquids of IN625 and CuCrZr alloys, (b) ThermoCalc's Scheil solidification calculations for each of Cu-lean and Cu-rich liquids of Cu75 composition, (c) schematic of the mushy zone in Cu75 composition demonstrating distinct solidification paths of each liquids that results in the mixed dendritic and spheroidal microstructure along with OM of a lightly etched melt pool splash of Cu75 composition highlighting the nucleation of Cu-rich liquid on a Cu-lean spheroid

6.3.5 Impact of Grain Structure on Cracking Behavior

To explore the impact of grain structure on cracking behavior across the compositional gradient of the sample, EBSD analysis was conducted, and the results are shown in Figure 6-9. Figure 6-9(a) shows the micrograph of the cross section of sample No. 4 and the different regions that underwent the analysis. As can be seen from the micrograph, all the cracks initiated from Cu25 region some of which propagated to the upper compositions and ultimately closed in Cu75. The EBSD IPF (Y) map in Figure 6-9(b) provides a detailed observation of the crack initiation in Cu25. As expected, solidification cracks are intergranular and propagate through high-angle grain boundaries (HAGBs) [125] characterized by misorientation angles exceeding 15° (e.g. 39°,41°,44°). Figure

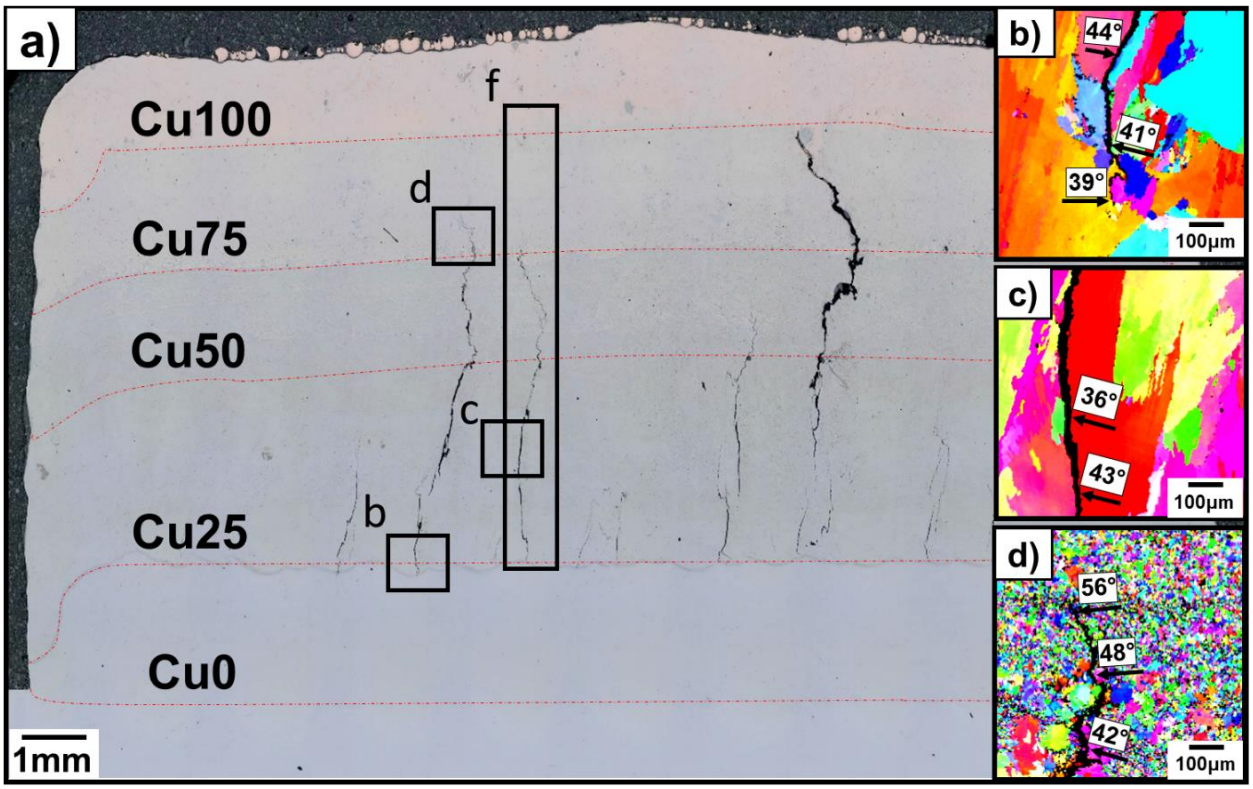
6-9(c) shows the analysis around the upper region of a crack, which denotes the propagation path along HAGBs. This trend extends up to Cu75 region, where the crack still exists between HAGBs, yet eventually arrests among them as shown in Figure 6-7(d). This behavior suggests that HAGBs are key sites for crack initiation and propagation, driven by localized stress concentrations and microstructural characteristics.

Figure 6-9(e) schematically represents how the cracks initiate and propagate through HAGBs. During the final stage of solidification, the remaining liquid phase evolves through three distinct stages: (1) the formation of a liquid channel with efficient liquid feeding when the f_s is less than 0.9. This stage is labeled as “safe” as the surrounding liquid fills any shrinkage. (2) the development of a thin residual liquid film when f_s is between 0.9 and 0.99 with restricted liquid feeding that can contribute to crack initiation under high stress conditions and labeled as “vulnerable”; and (3) the emergence of isolated liquid droplets resulting from dendrite branch coalescence that can transfer stress through the solid skeleton, causing minimal weakening and not prone to cracking [133]. In terms of the development of a thin residual liquid film or isolated liquid droplets, Rappaz [134] introduced a theory that describes dendrite coalescence between growing dendrites either “attractive” or “repulsive” which is influenced by the misorientation angle. In fact, at low misorientation angles ($\theta<15°$), dendrite growing boundaries are attractive and dendrite branches coalesce early. Therefore, the liquid film breaks into isolated droplets in low angle grain boundaries (LAGBs). In contrast, high misorientation angle results in "repulsive" boundaries between dendrites that retain a thin liquid film until coalescence occurs at lower temperatures. Therefore, in HAGBs ($\theta>15°$), this stable liquid film in conjunction with high thermal stresses cause crack initiation [133], [135]. In addition, the stress accumulates more in HAGBs due to the incompatibility in strain accommodation across the grain boundary. This strain incompatibility, coupled with the reduced mobility of the stable liquid film, results in higher susceptibility in crack initiation [130].

Figure 6-9(f) shows the stitched IPF (Y) maps along the entire crack, highlighting how the transition from coarse columnar grains to fine equiaxed grains across the compositional gradient contributes to the crack behavior. In the Cu25 region (Figure 6-9(c)), columnar grains oriented along the <001> direction grew by epitaxy across several layers along the build direction corresponding to the main direction of the thermal gradient. The successive depositing and re-

melting of several layers promotes this epitaxial growth [69]. This dominant columnar grain structure provides pathways for crack propagation due to the inability to effectively redistribute thermal strains generated during the rapid heating and cooling cycles of the L-DED process [129]. This inability to accommodate thermal strain leads to the accumulation of high thermal stresses within the microstructure, which tend to concentrate along the columnar grain boundaries [136], acting as a mechanical factor to drive crack initiation and propagation [13], [26]. The alignment of these columnar grains with the thermal gradient further exacerbates the situation by providing a continuous and preferential path for crack propagation [137].

In contrast, as the crack propagated to the Cu50 region, it is faced with the fine equiaxed microstructure region, having grains with ~25μm average size and 0.63 aspect ratio (Figure 6-9(g)) due to the heterogenous nucleation associated with the metastable miscibility gap [112]. As shown in Figure 6-8(e), this miscibility gap results in grain refinement by the formation of Cu-lean spheroids, acting as nucleation sites during solidification [110], [111]. The similar mechanism led to even finer grain structure in Cu75 region with average size of ~4μm and 0.76 aspect ratio. As shown in Figure 6-9(d), this is the region the crack is ultimately closed. In general, the increased grain boundary area enhances the ability of the microstructure to redistribute and accommodate thermal strain during solidification [138]. This results in lowering the thermal stress levels [137], [139]. Besides, the higher density of grain boundaries and their random orientations disrupt the alignment of crack pathways [106], [107]. This explains the transitioning of the crack's morphology from a relatively straight trajectory in Cu25 to a zigzag pattern in Cu50 and Cu75 regions, as shown in Figure 6-9(a). Therefore, compared with the coarse columnar grains of Cu25, the fine equiaxed grains of Cu50 and especially Cu75 are more likely to accommodate thermal stress and offer more tortuous crack paths that ultimately closes the cracks in Cu75 region. This highlights the critical role of the fine equiaxed grains in mitigating crack propagation and facilitating crack elimination mechanism [124], [140].


a)
Cu100
Cu75
Cu50
Cu25
Cu0
f
d
c
b
1mm
b)
44°
41°
39°
100µm
c)
36°
43°
100µm
d)
56°
48°
42°
100µm

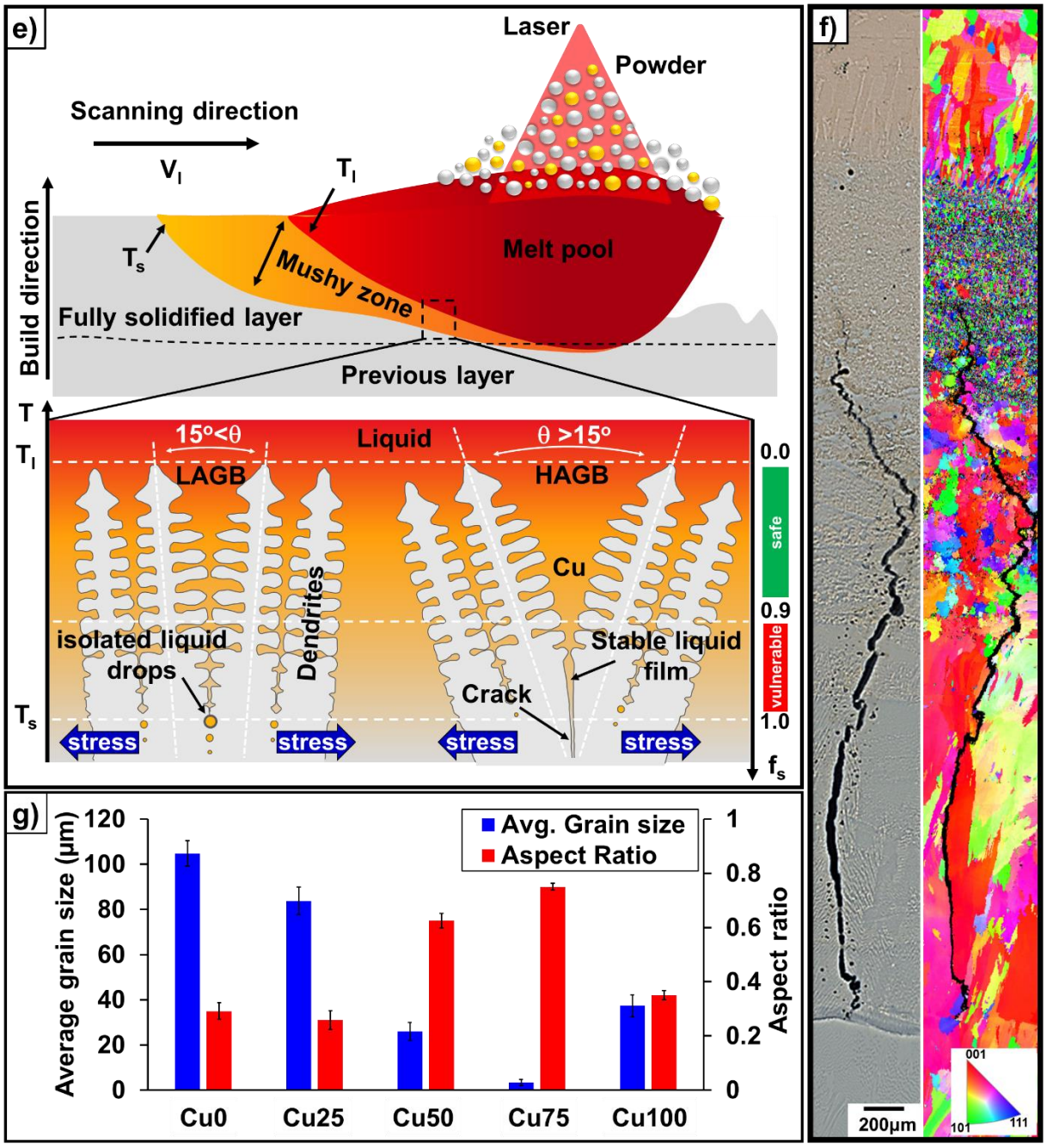


Figure 6-9 Impact of grain structure on the cracking behavior across different regions of FGAM IN625-CuCrZr cuboid; (a) OM of sample No. 4 and the different regions that underwent the EBSD analysis, (b) IPF (Y) map of the crack initiation in Cu25, (c) IPF (Y) map of the crack propagation path along HAGBs, (d) IPF (Y) map of the crack in Cu75 highlighting its elimination among fine equiaxed grain structure, (f) stitched IPF (Y) maps from the entire of a crack underscoring the contribution of the grain structure transition along the compositional gradient to the cracking behavior, (g) average grain size and aspect ratio of grain structure in each composition.

6.4 Conclusions

In this study, the defect types and formation mechanisms in FGAM of IN625-CuCrZr cuboids have been studied comprehensively. Defects were categorized into two main groups: porosity and cracks, with porosity primarily consisting of lack-of-fusion (LoF) defects and minor gas pores. Cracks were investigated in detail to identify the mechanisms behind their initiation, propagation, and arrest. Thermodynamic simulations and advanced characterization techniques elucidated the interplay between compositional gradients and microstructural evolution on cracking behavior. The key conclusions emerging from this work are summarized as follows:

1. Optimized process parameters significantly reduced the LoF porosity in FGAM of IN625-CuCrZr cuboid samples.
2. Solidification cracks formed between dendrites in Cu25 region, driven by presence of a Cu-rich liquid film that initiated the cracks formation.
3. The formation of a liquid-state miscibility gap at Cu50 and Cu75 regions results in the separation of the liquid into the Cu-rich and Cu-lean liquids, each of them follows its distinct solidification path, where the Cu-lean liquid solidifies prior to the Cu-rich liquid.
4. The liquid state miscibility gap led to a grain refinement mechanism where the Cu-lean spheroids act as nucleation sites for the Cu-rich liquid, resulting in a highly fine equiaxed grain structure in Cu50 and Cu75.
5. Grain structure evolution across the compositional gradient influenced cracking behavior, with cracks initiating along HAGBs in coarse columnar grains of Cu25, while the refined equiaxed grains in Cu50 and Cu75 promoted crack arrest by accommodating thermal stress and deflecting crack paths.

The findings of this work highlight that the precise control of the process parameters and compositional transitions enables an effective design of Ni-based superalloys and Cu alloys FGMs for L-DED. While LoF defects can be mitigated through process optimization and cracks tend to heal through compositional gradients, crack initiation remains a key challenge. Future efforts should aim to prevent the crack formation at its source by tailoring composition and process conditions through thermodynamic modeling and implementing preheating techniques to avoid the formation of the liquid film at the final stage of solidification, refine grain structure, and reduce thermal stress.

Chapter 7: A geometrically-optimized heat source model for FE thermal simulation of laser directed energy deposition

7.1 Introduction

This chapter presents a comprehensive thermal finite element (FE) modeling framework for the Laser Directed Energy Deposition (L-DED) process. To accurately simulate thermal histories and predict melt pool geometry, a hybrid statistical-numerical approach is implemented that integrates experimentally validated deposition geometries with a customized moving heat source model. Initially, single-track depositions of Inconel 625 alloy were fabricated using a wide range of process parameters, including laser power, scanning speed, and powder feed rate. The geometrical characteristics of the resulting tracks, specifically height, width, and penetration depth, were precisely measured and used to develop a predictive statistical model. This model captures the dependence of deposition geometry on process parameters via empirical functions, and its output is directly employed to define the shape and size of the heat-affected zone in subsequent numerical simulations.

To reduce the time and cost required to determine optimal process parameters and forecast temperature profiles, various numerical modeling techniques have been employed in the literature [141], [142].

A three-dimensional (3D) transient FE model is then developed in Abaqus, using a quarter-ellipsoidal deposition region activated dynamically by a hybrid quiet/inactive element technique. The heat source is modeled as a moving cylindrical-Gaussian distribution with spatial and temporal evolution, implemented via a custom DFLUX subroutine. To incorporate the realistic evolution of thermal conductivity post-solidus temperature, the model adjusts conductivity values to mimic convective effects within the melt pool. Boundary conditions include a temperature-dependent effective heat transfer coefficient derived from radiation and convection are applied at nodal points through FILM subroutine to ensure thermal losses are realistically captured on the deposition.

Compared to conventional 3D modeling approaches [39], [74] this work provides a more geometrically-resolved and experimentally calibrated strategy for simulating L-DED in the scale of single track deposition. The proposed modeling framework is validated experimentally via cross-sectional measurements of melt pool geometry and in-situ thermal data acquisition using an embedded thermocouple. The predicted melt pool dimensions and transient temperature fields

exhibit excellent agreement with experimental observations, with deviations consistently below 10%.

7.2 Materials and Experimental Methods

This section in detail describes (i) the feedstock material used for the deposition of the single tracks, (ii) design of experiment (DoE) and statistical modeling method, and (iii) L-DED processing and experimental validations of the FE thermal model.

7.2.1 Powders

Gas-atomized IN625 powders (Carpenter Additive, Bruceton Mills, WV, USA) and SS304L plate were used in this study as the feedstock material and substrate, respectively. The chemical compositions of the powder and substrate are shown in Table 7-1. The morphology of the powder is mainly spherical, and the PSD of the powders is in the range of 50 to 125 μm for IN625 (D50 = 75 μm) recommended for L-DED processing.

Table 7-1 Chemical composition of the IN625 powders and SS 304L substrate (wt.%).

Material	Ni	Cr	Mo	Nb	Fe	Si	Mn
IN625 powders	Bal.	20.0	8.0	3.0	2.0	-	-
SS 304L plate	8.8	18.18	-	-	Bal.	0.6	1.8

7.2.2 Statistical modeling & design of experiment

Empirical-statistical modeling was used to study the effect of the key parameters of the L-DED process, including the laser power (*P*), scanning speed (*V*), and powder feeding rate (*F)* in the fabrication of single tracks, on the geometrical characteristics of the depositions: the height (*h*), width (*W*) and the melt pool's penetration depth to the substrate (*b*). In that regard, a full factorial design of experiments (DoE) was applied, and the relationships between the deposition geometry and process parameters were described using the following exponential function [143], [144]:

$$y = \left(\frac{P}{\sqrt{v}}\right)^{\alpha} \times \left(\frac{F}{V}\right)^{\beta} \quad \text{(equation 7-1)}$$

Linear regression analysis was conducted to fit the model by maximizing the coefficient of determination (indicated by R^2) using the scattered experimental data, and the function constants corresponding to each geometrical characteristic were identified.

7.2.3 L-DED processing & Experimental validation

An in-house developed robotic L-DED system (shown in Figure 7-1 (a)) was used to deposit the DoE's single tracks with a length of 30 mm on the substrate. The system is equipped with a coaxial nozzle and a fiber laser with TEM00 mode and a capacity of up to 1000 W, as well as a dual hopper powder feeder system. More details about the setup can be found in [145]. During the experiments, the laser spot size was maintained at 1.2 mm, and the ranges of the main process parameters namely, laser power, scanning speed, and powder feed rate are shown in Table 7-2.

Table 7-2 the DOE's input process parameters and measured responses

Track NO.	**Process parameters (input variables)**			**Geometrical measurements (output responses)**		
	***P* (W)**	***F* (g/min)**	***V* (mm/s)**	***h* (µm)**	***w* (µm)**	***b* (µm)**
1	300	3	3	601	936	60
2	300	3	5	360	845	41
3	300	3	7	242	801	41
4	500	3	3	695	1490	106
5	500	3	5	477	1348	102
6	500	3	7	305	1291	123
7	700	3	3	741	2033	243
8	700	3	5	481	1859	151
9	700	3	7	333	1703	198
10	300	5	3	932	740	19
11	300	5	5	614	806	16

12	300	5	7	457	754	17
13	500	5	3	1086	1513	113
14	500	5	5	677	1422	115
15	500	5	7	523	1336	109
16	700	5	3	1186	1932	143
17	700	5	5	766	1748	162
18	700	5	7	567	1623	140
19	300	7	3	1178	837	20
20	300	7	5	845	810	7
21	300	7	7	605	740	12
22	500	7	3	1578	1462	117
23	500	7	5	938	1298	89
24	500	7	7	709	1194	79
25	700	7	3	1518	1849	156
26	700	7	5	1046	1712	143
27	700	7	7	675	1645	149

Figure 7-1(b) schematically shows the L-DED process and the geometrical characteristics (*h, W,* and *b*) of the depositions which were measured for both statistical analysis and validation of the FE thermal model. In that regard, the DoE samples were cross sectioned from the mid-length by electric discharge machining then samples were hot-mounted in a conductive epoxy resin followed by grinding and polishing on a Struers Labopol-20 auto-polisher using SiC grinding papers from 120 to 4000 grit sizes and the 1μm alumina slurry, respectively. Finally, the height, width, and the depth of penetration of the depositions were measured using a Keyence VHX-7000 digital microscope. In addition, the thermal validation was performed by recording the thermal history during the process from a certain location in the substrate, 1mm from the top surface and the middle

of the deposition path by a data acquisition device (DAQ, National Instruments) with a pre-installed K-type thermocouple (Figure 7-1 (c)) and comparing it with the corresponding location in the model.

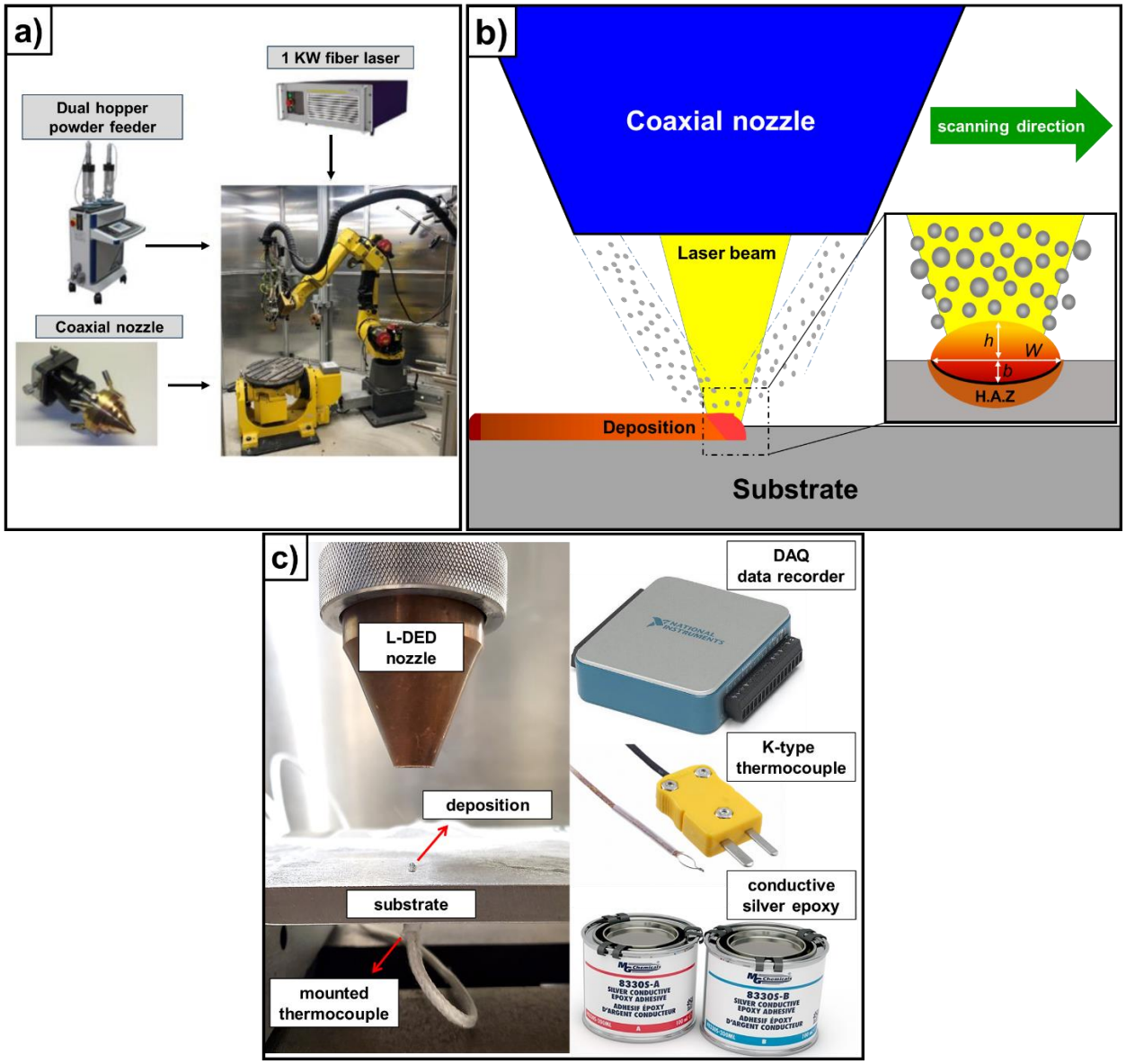


Figure 7-1 (a) L-DED setup, (b) schematic of the deposition process and its geometrical characteristics, (c) thermal validation setup including DAQ data recorder, thermocouple, and conductive silver epoxy to mount the thermocouple into the substrate

7.3 Finite element (FE) modeling

This section provides a detailed explanation of the finite element (FE) numerical modeling approach, covering the computational domain, governing equations and boundary conditions, meshing strategy, and material deposition method.

The proposed numerical model for the L-DED process prioritizes accurate thermal field simulation while simplifying melt pool fluid flow and powder dynamics to minimize computational expense. The method discretizes the continuous laser metal deposition process into a series of sequential simulation steps, each corresponding to a specific segment of the laser path. At each step, comprehensive thermal analyses are conducted, and the resulting time-temperature data are recorded for every node. This strategy enables precise prediction of the deposition dimensions in the L-DED process.

7.3.1 Model geometry

The commercial FE software Abaqus 2023 was used to simulate the depositions and temperature distribution during the L-DED process of IN625 alloy samples. To reduce computational effort, the model leveraged the process's geometric symmetry by simulating only half of the substrate and a single-track deposition. The substrate domain was defined as 5 × 5 × 15 mm, with the deposition track placed on top and measuring 2 × 2 × 10 mm. The simulation employed DC3D8 hexahedral elements. To balance computational efficiency and accuracy in regions near the laser-material interaction, a finer mesh was applied in these critical zones. This targeted mesh refinement is crucial for capturing the detailed thermal behavior during laser processing, as shown in Figure 7-2.

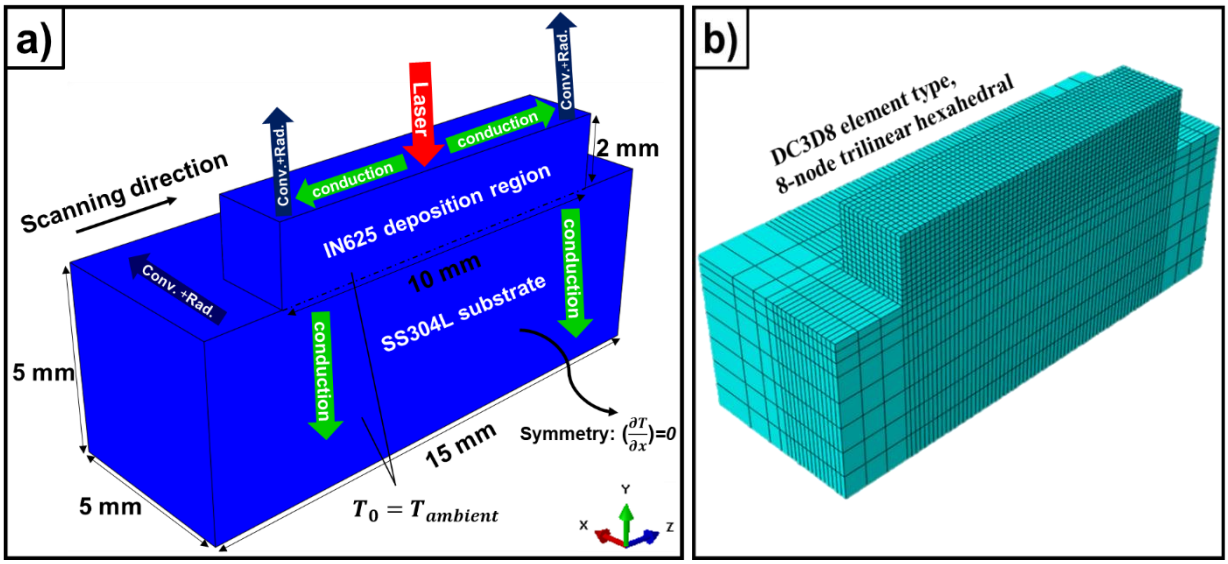


Figure 7-2 FE numerical model, (a) x-symmetry computational domain for thermal modeling of IN625

single track fabrication by L-DED, (b) meshing layout applied for the model where element size is reduced toward the deposition for high-precision calculations

7.3.2 Material properties

The temperature-dependent thermophysical properties of SS304L steel and IN625 superalloy (Table 7-3) were assigned to the substrate and deposition regions, respectively. It is assumed that the absorption coefficient is a fixed value and not affected by temperature or phase change for simplicity of the computation. In order to account for the role of fluid flow convection in the melt pool, the thermal conduction coefficient of the materials was multiplied by the constant of 4 after the liquidus temperature (1623 K) [146].

Table 7-3 Thermophysical properties of IN625

Material	Thermal conductivity (W/m K)	Specific heat (J/kg K)	Density (kg/m3)	Liqu. Temp. (K)	Solid. Temp. (K)
IN625	K_{IN625}=0.014T+7.78	Cp_{IN625}=0.16T+387.1	ρ_{IN625}=-0.8T+8903	1610	1563
SS304L	K_{SS304L}=0.015T+9.51	Cp_{IN625}=0.14T+455.2	ρ_{SS304L}=-0.3T+7916	1727	1673

7.3.3 Heat transfer governing equation and boundary conditions

The governing equation of heat transfer can be described as follows [39]:

$$\rho(T)\ Cp(T)\frac{dT}{dt} = -\nabla \cdot q(r,t) + Q(r,t) \quad \text{(equation 7-2)}$$

where T is the temperature, t is the time, q is the heat flux, Q is absorbed heat input, and r is the relative coordinate from the reference. The heat dissipation through the substrate is described by Fourier's conduction equation as follows:

$$q = -k(T)\nabla T(r, T) \quad \text{(equation 7-3)}$$

where k is the isotropic thermal conductivity coefficient, which is temperature-dependent. To solve the above equations, one must consider boundary conditions as well as apply a proper heat input model that matches the actual laser-powder interaction. The correct boundary condition should include the initial temperature in the model as well as the heat losses from the surfaces of the

substrate and deposition through radiation and convection as expressed in equations (7-4) and (7-5), respectively:

$$T(x, y, z, 0) = T_a \quad \text{(equation 7-4)}$$

$$k\left(\frac{\partial \mathrm{T}}{\partial \mathrm{n}}\right) + h_c(T - T_a) + \sigma\varepsilon(\mathrm{T}^4 - T_a^4) - \mathrm{q} = 0 \quad \text{(equation 7-5)}$$

where T_a is the ambient temperature (298 K), k is the thermal conductivity, n is surface normal, h_c is convection coefficient, σ is the Stephen–Boltzmann constant, ε is emissivity and q is the heat flux generated by the laser beam. Obviously, for surfaces other than those irradiated by the laser beam, the amount of q is zero in Eq. (7-5). It should be noted that for convenience and to avoid high nonlinearity due to the radiation heat loss, the third term in Eq. (7-5) was removed, and instead of h_c a previously developed effective heat transfer coefficient (h_e) [147] was used, which is a combination of both:

$$h_e = h_c + \sigma\varepsilon(T^3 + T^2T_a + T_a^2T + T_a^3) \quad \text{(equation 7-6)}$$

A user subroutine FILM is developed and applied to the model to account for the variation of the $h_e$with time for the top surface of the deposition.

7.3.4 Heat source model

A moving heat source with a cylindrical-Gaussian shape was applied for predicting the melt pool dimensions and temperature distributions precisely. Generally, in FE modeling of additive manufacturing processes the laser beam that irradiates on the powder particles is modeled as a volumetric heat flux that follows a Gaussian intensity distribution [13], [42]. Figure 3 schematically shows the cylindrical heat source model and its 2D Gaussian intensity distribution which follows the below equations:

$$I\,(x, y) = q_0.\exp\left[-2\frac{x^2+y^2}{r^2}\right] \quad \text{(equation 7-7)}$$

While,

$$\beta.P/V = \int_{-\infty}^{\infty}\int_{-\infty}^{\infty} q_0.\exp\left[-2\frac{x^2+y^2}{r^2}\right] dxdy \quad \text{(equation 7-8)}$$

The q_0 will be equal to:

$$q_0 = \frac{3\beta P}{\pi r^2 h} \quad \text{(equation 7-9)}$$

Where $I\,(x,y)$, q_0, r, β, P, V, h are the heat intensity distribution, maximum value of heat intensity, radius of the laser beam, laser's absorptivity coefficient, laser power, the volume of the irradiated region in the deposition, and the height of the deposition.

To implement the heat source model as a thermal load in the model, a user subroutine DFLUX was used to define the moving laser's heat flux in a cylindrical distribution along the deposition path, according to equations (7-6) and (7-9).

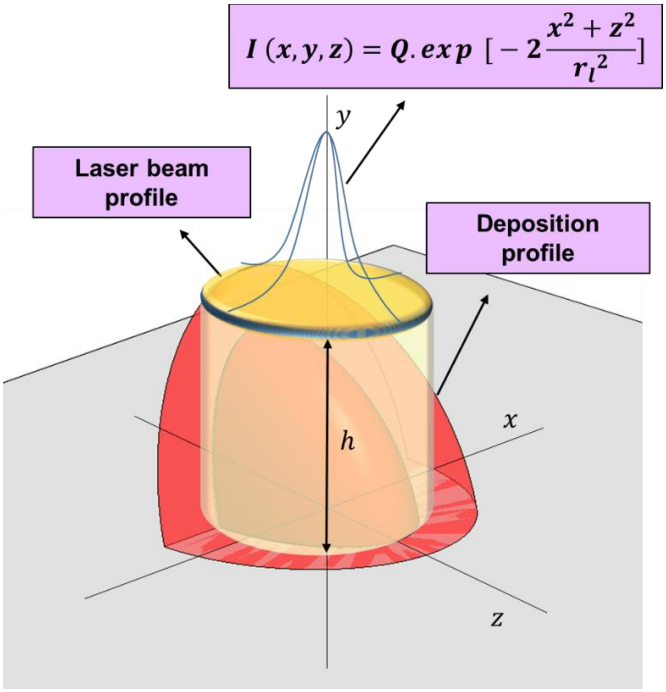


Figure 7-3 Schematic of the cylindrical heat source model with Gaussian distribution interacting with the deposition profile

7.3.5 Material deposition modeling

Finite element techniques for continuous material deposition modelling in heat transfer analyses of additive manufacturing involve discrete and sequential activation of individual FE segments. Two famous metal deposition methods in the literature for modeling material deposition are: (1) the quiet elements method and (2) the inactive elements strategy (i.e., the birth and death technique) [148]. In this section, first, these methods are described briefly then the hybrid inactive/quiet element approach which applied in this study is explained in detail.

7.3.6 Quiet element method

In the quiet element method, the elements representing metal deposition regions are present from the start of the analysis. However, they are assigned properties so they do not affect the analysis. For heat transfer analyses, the thermal conductivity k is set to a lower value to minimize conduction into the quiet elements, and the specific heat Cp is set to a lower value to adjust energy transfer to the quiet elements:

$$k_{quiet} = S_k k \qquad \text{(equation 7-10)}$$

$$C_{p\,quiet} = S_{Cp} C_p \qquad \text{(equation 7-11)}$$

where, k_{quiet} and $C_{p\,quiet}$ are the thermal conductivity and specific heat used for quiet elements, and S_k (10^{-6}) and $\mathrm{S_{Cp}}$ (10^{+6}) are the scaling factors used for the thermal conductivity and specific heat, respectively.

7.3.7 Inactive element method

In the inactive element method, the elements representing metal deposition regions are removed from the analysis and only nodal degrees of freedom corresponding to active elements are considered. The numerical implementation involves solving the thermal analyses for the active elements only considering the active nodal degrees of freedom only.

7.3.8 Hybrid inactive/quiet element approach

The hybrid inactive/quiet element method is proposed for modeling additive manufacturing. As shown in Figure 7-4, in this approach, elements corresponding to the deposition region are initially inactive, then, they are switched to quiet on a step-by-step basis. During the thermal analysis of the deposition the USFLD subroutine change the artificial material properties of the quiet elements to their real ones for the areas that are about to be scanned by the heat source. This approach has been reported to benefit from both material deposition methods in terms of providing accuracy and run times [149], [150].

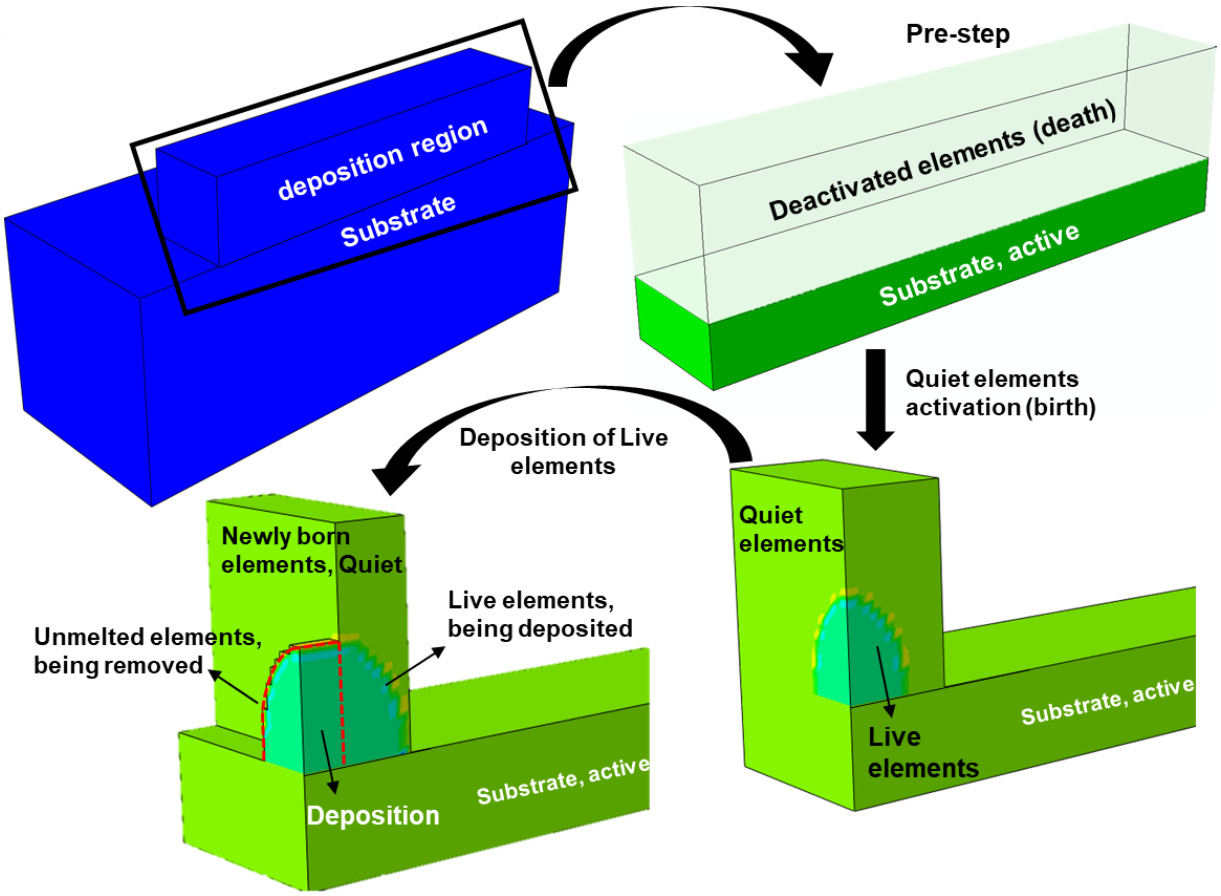


Figure 7-4 Hybrid inactive/quiet element activation approach

7.4 Outline of the statistical-numerical approach

The flowchart in Figure 7-5 outlines the comprehensive workflow employed in this work for finite element (FE) thermal modeling of the L-DED process. At the core of the framework is the implementation of material deposition, thermal loads, and convective and radiative heat interactions, which are facilitated through USDFLD, DFLUX, and FILM user-defined subroutines in Fortran. During modeling the deposition process, a set of elements in the deposition region activates first with quiet properties, then the implementation of material properties from artificial to actual values into the elements is achieved by programming the material properties as functions of selected field variables within the USDFLD user subroutine. As schematically showed in Figure 7-4, the outcome of the regression through the statistical analysis which is a mathematical equation that defines each geometrical characteristics (*h, W, b*) based on the main process parameters (*P, V, F*) will be used in USDFLD subroutine code to define the deposition area to which the actual properties will be given. A full-factorial Design of Experiments (DoE), coupled with statistical

analysis of printed results, supports the calibration and validation of the model. Once all inputs are defined, the FE heat transfer analysis is conducted, resulting in a detailed thermal history and distribution throughout the simulated domain. This structured approach ensures high-fidelity modeling of thermal phenomena during L-DED.

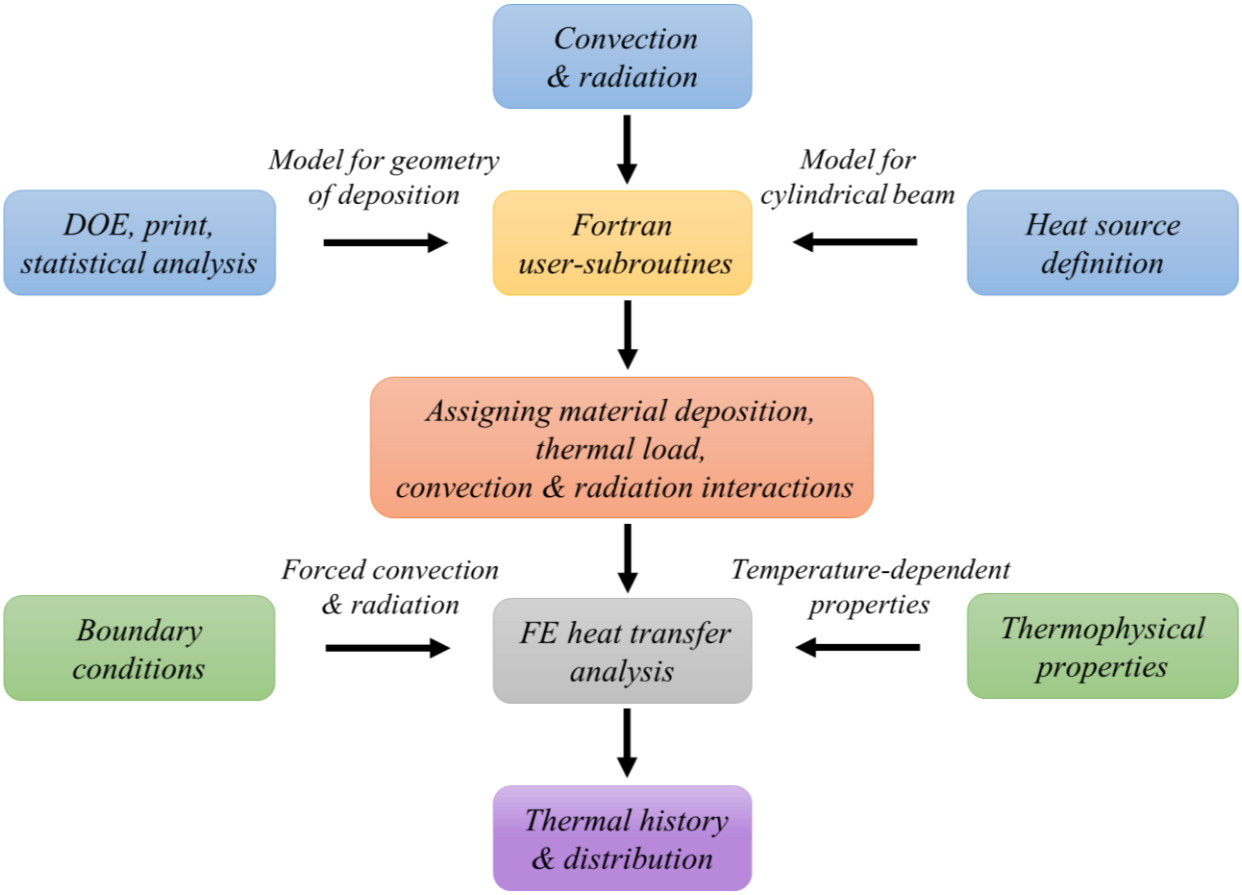


Figure 7-5 Outline of the statistical-numerical approach to study temperature distribution of the L-DED deposition.

7.5 Results and Discussions

7.5.1 Statistical analysis of geometrical characteristics

The measurement results of the geometrical characteristics, including the height, width, and penetration depth of the depositions, are presented separately in Table 7-2. The statistical analysis and regression results for each variable of *h, W,* and *b* are briefly summarized by the analysis of variance (ANOVA) Tables 7-4 to 7-6.

Table 7-4. Analysis of variance (ANOVA) for the height *(h)*.

	Sum of squares	*Df*	*f-ratio*	*p-value*
$\left(\frac{P}{\sqrt{v}}\right)^{0.25} \times (\frac{F}{V})$	3.02×10^6	1	1.02×10^3	7.08×10^{-6}
Total error	3.1×10^6			
Coefficient of determination (R^2) = 97.59 %				
Adjusted (R^2) = 97.50 %.				
Standard Error = 54.59				

Table 7-5. Analysis of variance (ANOVA) for the width *(w)*.

	Sum of squares	*Df*	*f-ratio*	*p-value*
$(\frac{P}{\sqrt{v}}) \times \left(\frac{F}{V}\right)^{-0.2}$	4.43×10^6	1	5.27×10^2	2.88×10^{-3}
Total error	4.64×10^6			
Coefficient of determination (R^2) = 95.48 %				
Adjusted (R^2) = 95.29 %.				
Standard Error = 91.65				

Table 7-6. Analysis of variance (ANOVA) for the depth *(b)*.

	Sum of squares	*Df*	*f-ratio*	*p-value*
$(\frac{P}{\sqrt{v}}) \times \left(\frac{F}{V}\right)^{-0.3}$	9.15×10^4	1	2.39×10^2	4.31×10^{-6}
Total error	1.01×10^5			

Coefficient of determination (R^2) = 90.54 %

Adjusted (R^2) = 90.16 %.

Standard Error = 19.55

Figure 7-6 illustrates the empirical correlation between the geometrical characteristics of the deposited track, the height (h), width (W), and depth of peneration (b), versus the combined process parameter ratios of $\frac{P}{\sqrt{V}}$ and $\frac{F}{V}$. As shown in Figure 7-6(a), the height of the deposition increases with rising laser power and decreasing scanning speed, which results in greater heat input per unit length. A higher powder feed rate also contributes to an increased track height due to the larger volume of material available for melting. Figure 7-6(b) reveals that while higher laser power promotes broader melt pools and thus wider tracks, an increased powder feed rate appears to have a counteracting effect. Specifically, the excessive powder influx limits the lateral spread of the molten pool by localizing the heat and restricting its diffusion, thereby reducing the overall width of the deposit. Lastly, Figure 7-6(c) confirms a positive correlation between energy input and melt pool penetration depth. Increased laser power intensifies the thermal gradient and enhances substrate melting, while slower scanning speeds prolong exposure time, both leading to deeper penetration. However, excessive powder feed may cause a slight reduction in penetration by obstructing the energy transfer to the substrate surface.

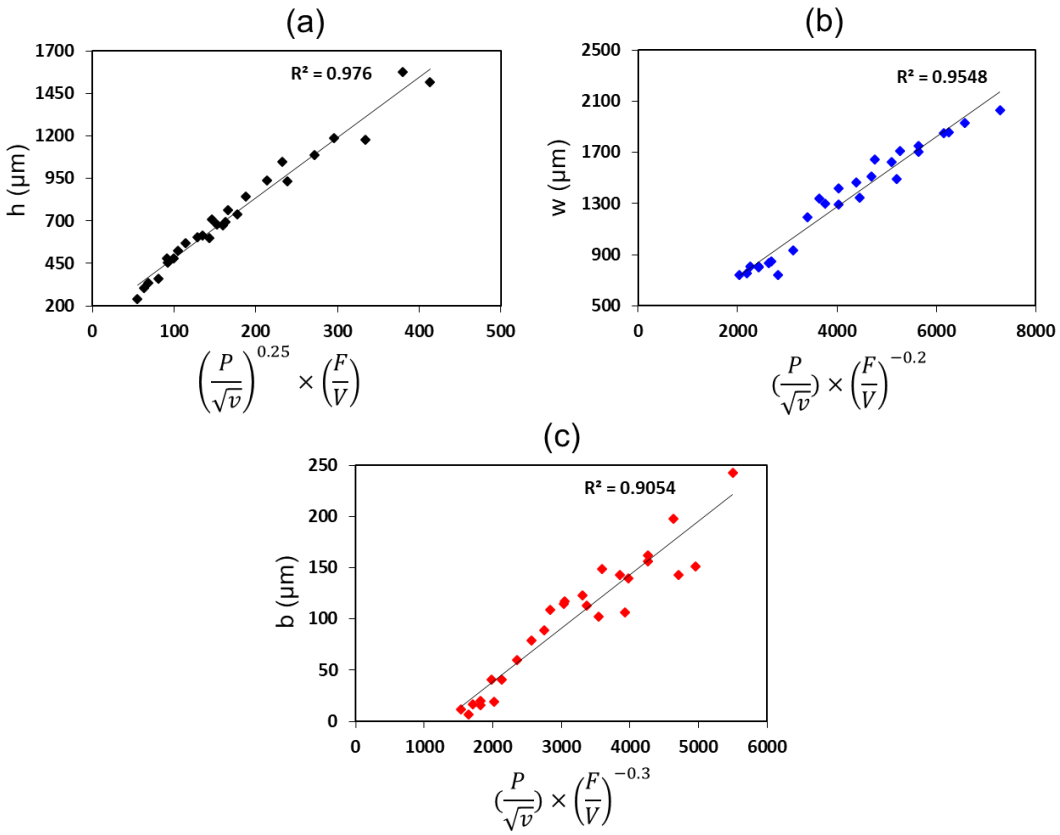


Figure 7-6 The correlation of the geometrical characteristics of a) height, b) width, c) depth of deposition and the combination of process parameters (P/√V, F/V)

7.5.2 Element size optimization

Figure 7-7 illustrates the mesh sensitivity analysis conducted to ensure the accuracy and stability of the FE thermal model. As shown in Figure 7-7(a), a line probe was defined across the melt pool cross-section to extract the temperature distribution along a representative path. Figure 7-7(b) presents the variation of predicted temperature profiles along this path for different element sizes (50 µm, 75 µm, 100 µm, and 150 µm). The results indicate that while finer meshes (50 µm and 75 µm) yield similar temperatures along the path, coarser meshes (100 µm and 150 µm) underestimate the peak temperatures. Based on the trade-off between computational cost and accuracy, an element size of 75 µm was selected for subsequent simulations to achieve reliable thermal predictions without excessive computational burden.

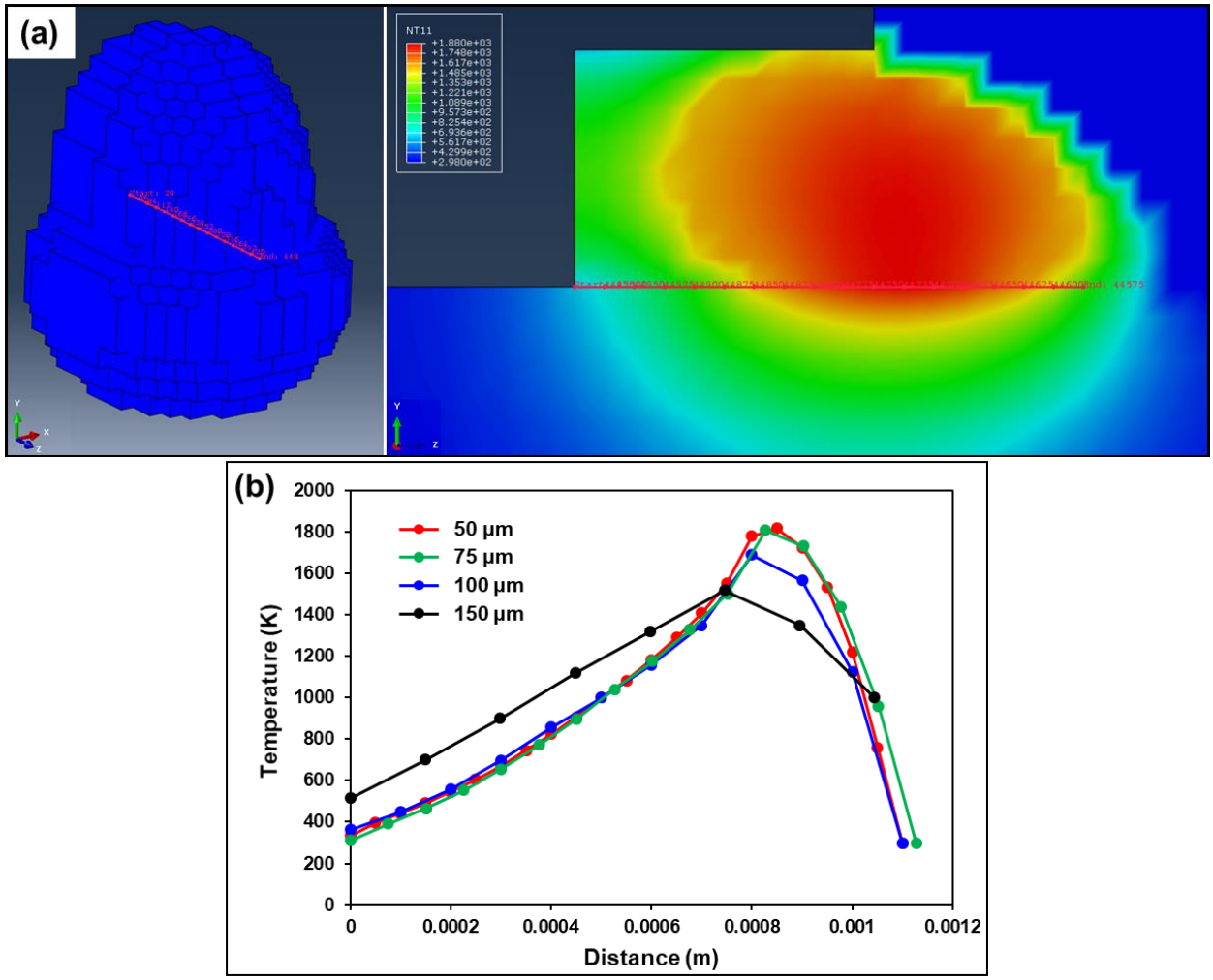


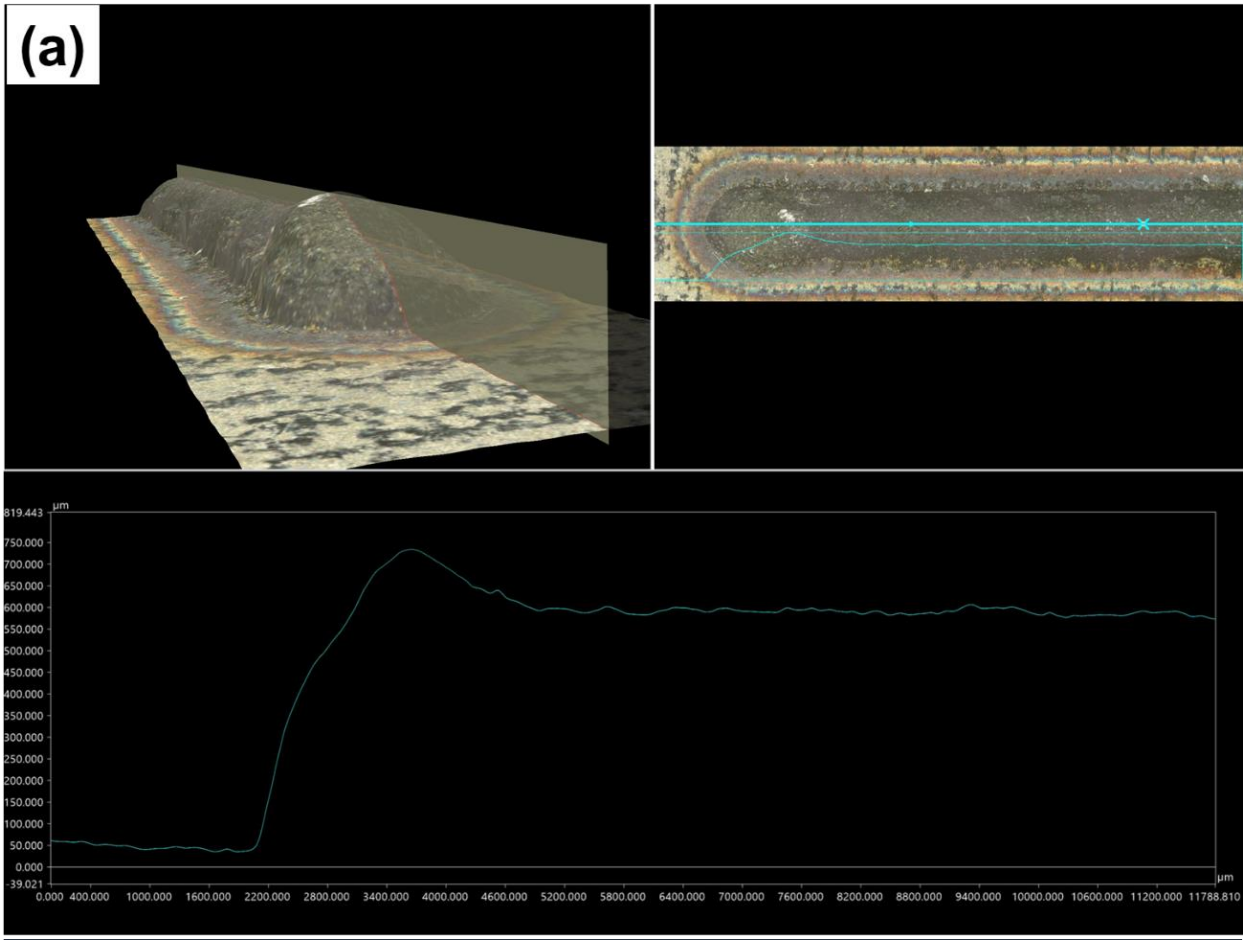
Figure 7-7 Mesh sensitivity analysis; a) measurement result's path, b) temperature distribution along the path for different element sizes

7.5.3 Experimental measurements of the melt pool, calibration, and validation results

Comparison Between Experimental Deposition Profile and Simulated Thermal Field

Figure 7-8 provides a combined experimental and numerical perspective on the thermal and geometric characteristics of a single-track L-DED deposition. Figure 7-8(a) presents the 3D topography and the extracted height profile along the scan direction of the deposited track obtained through optical profilometry. Figure 7-8(b) illustrates the simulated temperature distribution using the FE thermal modeling under identical processing conditions (P = 500 W, F = 5 g/min, V = 5 mm/s). As illustrated in Figure 7-8(a), the front of the deposited track displays a semi-ellipsoidal shape, which reflects the natural curvature of the deposition during solidification. This characteristic geometry is well replicated in the numerical model shown in Figure 7-8(b), where

the high-temperature region and the surrounding isothermal contours also exhibit a semi-ellipsoidal distribution. It is worth mentioning that the top surface of the deposition region appears slightly colder than the central regions. This is because the nodes at the top surface are activated within recently deposited elements that have not yet completed the heat transfer calculations; as the heat source continues to move, these nodes require additional time to reach their peak temperatures. This comparison confirms that the simulation appropriately captures the heat transfer within the depositions, effectively representing the physical shape of the deposition front observed in the experimental data.



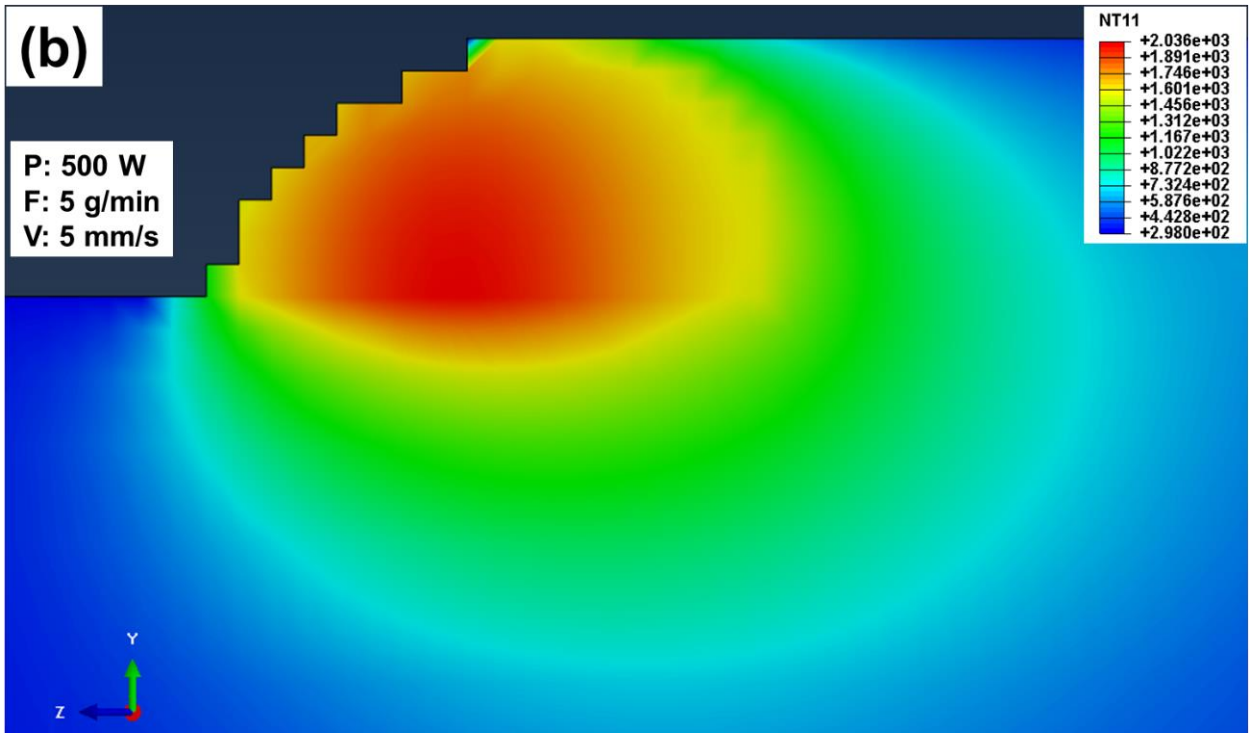


Figure 7-8 Geometrical characteristics of depositions in experiments vs. FE results

Figure 7-9 presents a direct comparison between experimentally measured melt pool cross-sections and numerically predicted temperature fields under various laser powers, scanning speeds, and powder feed rates during L-DED of IN625. The top row of each set shows the optical macrographs of cross-sectioned single-track depositions, highlighting the measured height, width, and penetration depth for each track. The bottom row displays the corresponding FE-predicted deposition's characteristics. Across different process parameters, the numerical predictions closely match the experimental measurements, particularly in capturing the overall depositions' width and bead. It is important to note that the top surface of the simulated deposition appears slightly cooler than the central regions. This occurs because the outer corner nodes of the recently deposited elements initially retain artificial material properties, while only the inner nodes of the same elements are assigned the actual material properties upon activation. As a result, these corner nodes do not fully participate in the thermal conduction and exhibit lower temperatures compared to the adjacent inner regions. This transient discrepancy arises from the way material activation is implemented in the hybrid quiet/inactive element method. Minor deviations can be observed in the measured penetration depth, which may be attributed to the assumptions inherent in the thermal

modeling such as constant laser beam's absorptivity. Overall, the strong agreement validates the robustness of the developed hybrid statistical-numerical framework in accurately predicting melt pool geometry for a range of L-DED process parameters.

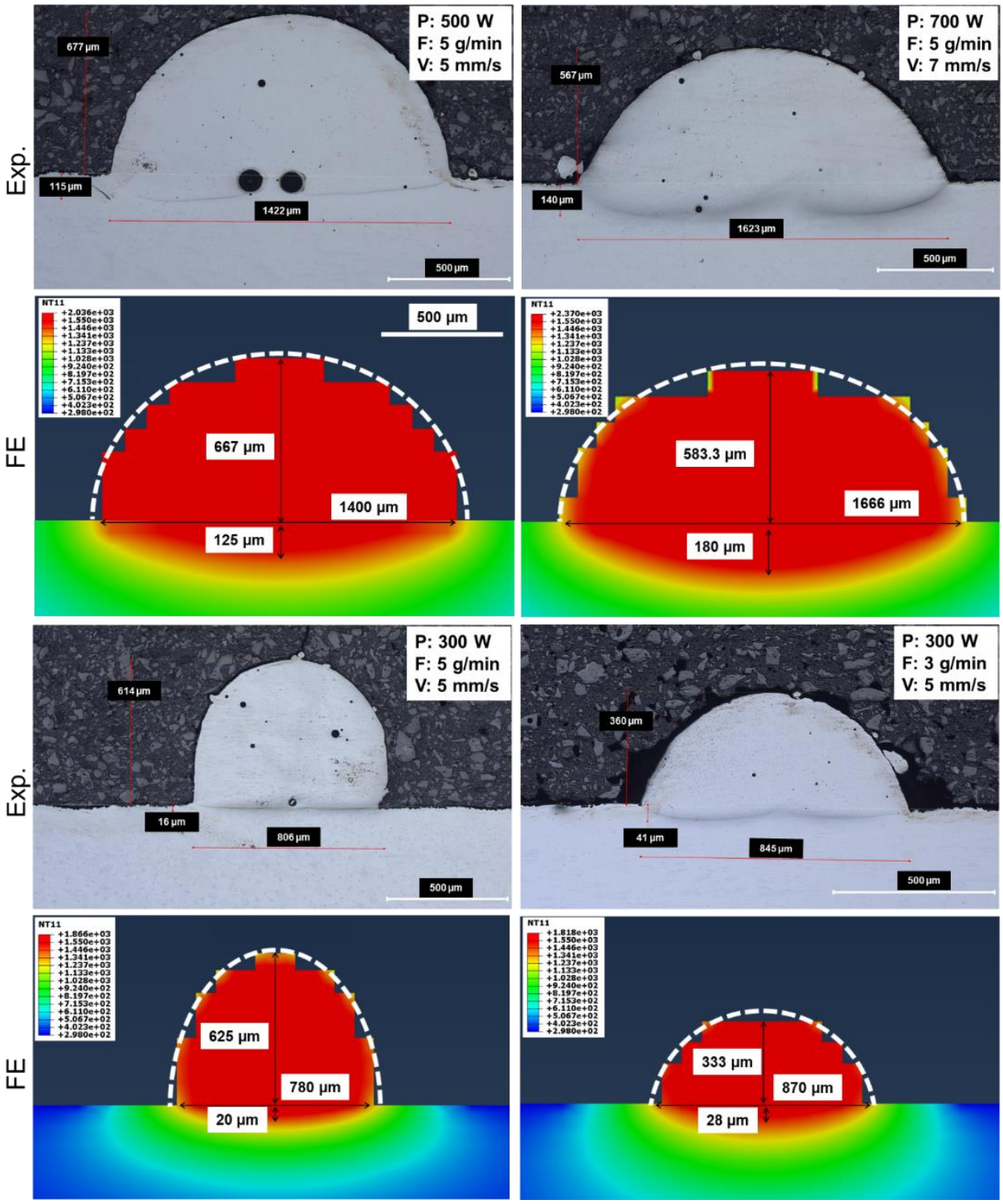


Figure 7-9 Geometrical characteristics of depositions in experiments vs. FE results

7.5.4 Effect of process parameters on the deposition's dimensions

Figure 7-10 compares the experimentally measured and numerically simulated geometrical characteristics, including the height (h), width (W), and depth of penetration (b) under four different sets of process parameters. Each plot demonstrates a strong correlation between finite element (FE) predictions and experimental results, with both datasets following a consistent trend across different parameter ranges. For the melt pool height (h), as the amount of powder feed rate per unit length ($\frac{F}{V}$) increases the deposition's height rises significantly while increasing energy input ($\frac{P}{\sqrt{V}}$) have similar effect with less pronounced impact and FE simulations closely tracked the experimental data. The penetration depth (b) also increases with rising ($\frac{P}{\sqrt{V}}$) as greater laser energy penetration results in deeper substrate melting. However, higher ($\frac{F}{V}$) can slightly reduce penetration depth due to the more fed powder absorbing part of the laser energy [143], a phenomenon captured to some extent in the FE model. The melt pool width (W) exhibits a steady rise with increasing ($\frac{P}{\sqrt{V}}$) though higher ($\frac{F}{V}$) appears to slightly constrain lateral spreading, likely due to enhanced thermal localization within the deposition region and reduced substrate melting [48]. The model again shows good agreement with experimental observations, particularly in capturing the width response to process variations. Together, these results emphasize that both ($\frac{P}{\sqrt{V}}$) and ($\frac{F}{V}$) are critical parameters governing deposition's geometry in L-DED. The close match between experimental and simulated data across all three dimensions demonstrates the model's capability to accurately capture the underlying thermal-physical interactions.

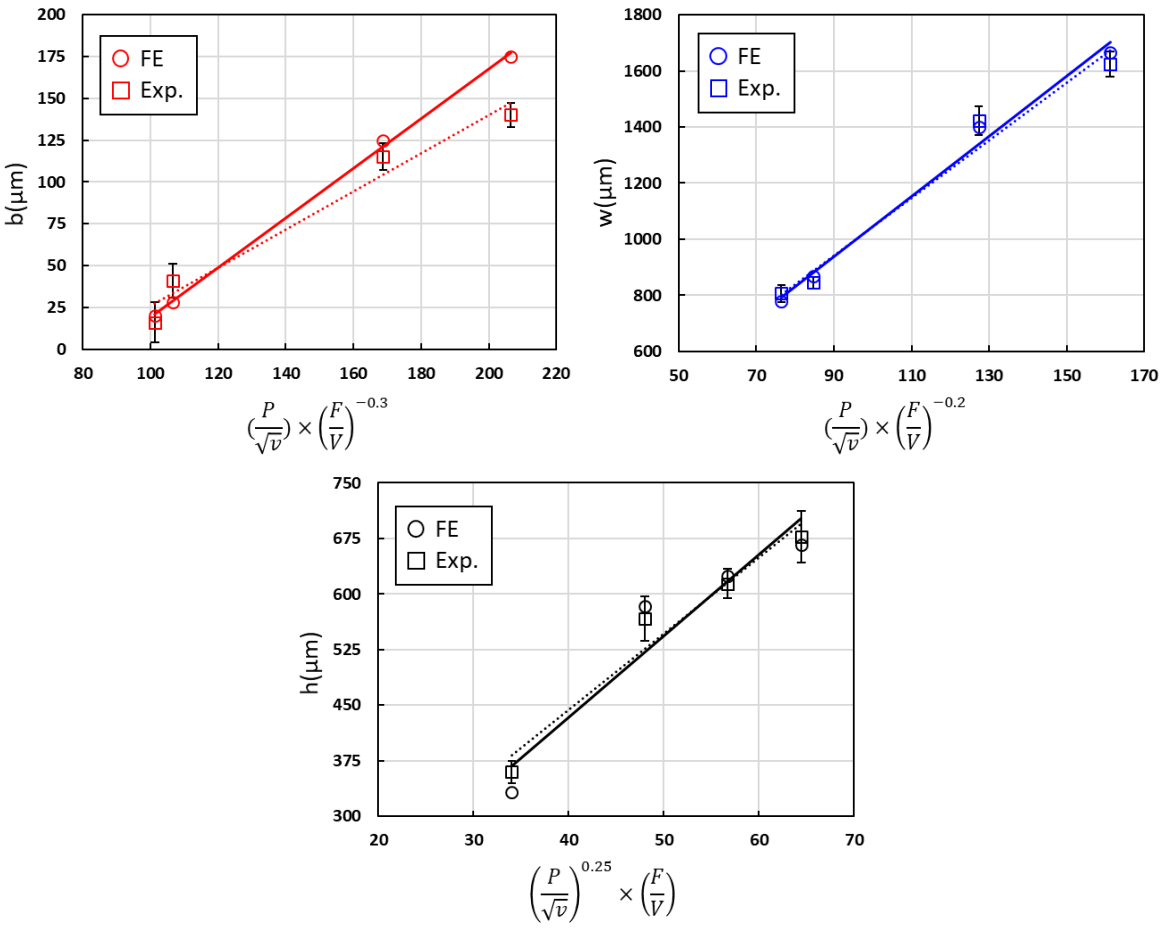


Figure 7-10 Geometrical characteristics of depositions in experiments vs. FE results

7.5.5 Experimental validation through in-situ temperature measurement

To validate the accuracy of the developed FE thermal model, an in-situ temperature measurement was performed during the L-DED process using a K-type thermocouple. Figure 11(a) shows the steady-state temperature distribution around the melt pool, with a highlighted probe location positioned 1 mm below the deposition surface. The average temperature recorded at this location in the FE model is approximately 606 K, as extracted from multiple nodes in the simulation domain. Figure 7-11(b) displays the experimentally recorded temperature profile over time using a thermocouple placed at the corresponding location. The temperature curve reveals a rapid rise from room temperature to 623 K, followed by a gradual cooling trend. Although minor discrepancies exist due to factors such as thermocouple response time, contact resistance, and heat losses not fully captured, the overall agreement validates the fidelity of the thermal model.

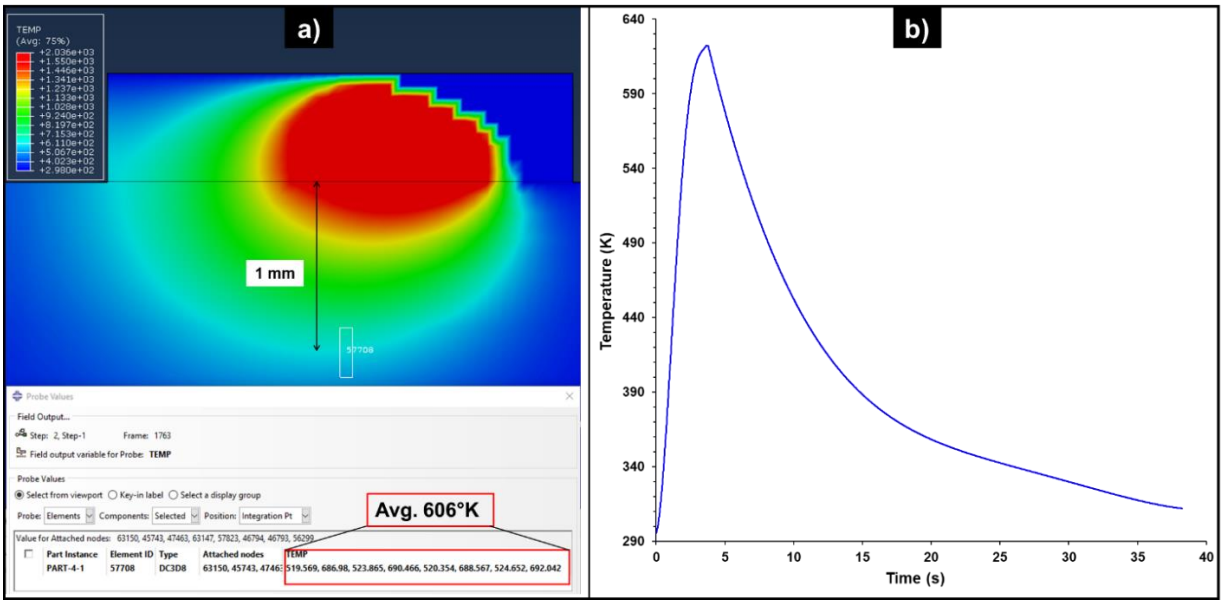


Figure 7-11 The validation of temperature distribution: (a) predicted in FE vs. (b) experimentally measured results via thermocouple

7.6 Summary

This chapter presents a hybrid statistical-numerical finite element (FE) thermal modeling framework for simulating the Laser Directed Energy Deposition (L-DED) process using Inconel 625 powder. The methodology integrated empirical-statistical modeling with a customized cylindrical-Gaussian heat source implemented in Abaqus via user subroutines (DFLUX, FILM, USDFLD), enabling high-fidelity prediction of melt pool geometry temperature distribution. The main findings are summarized below:

1. A full factorial DoE was conducted using varying process parameters. The resulting single-track geometries, height *(h)*, width *(W)*, and penetration depth *(b)*, were used to derive empirical equations as functions of combined efficient process parameters $(\frac{P}{\sqrt{V}})$ and $(\frac{F}{V})$ with R^2>90% for all geometrical features.
2. A quarter-ellipsoidal thermal model was developed using fine-meshed DC3D8 elements. A hybrid inactive/quiet element activation strategy was used to sequentially simulate material deposition. The model was validated first by comparing the simulated geometrical characteristics with experimental measurements across different process settings. The in-situ temperature measurements from a thermocouple embedded below the deposition surface showed excellent agreement with FE-predicted thermal histories. Maximum

deviations were consistently below 10%, validating the robustness of the proposed heat source model and material activation scheme.

3. Increasing $(\frac{P}{\sqrt{V}})$ led to larger melt pool dimensions in all directions. A higher $(\frac{F}{V})$ significantly increased height but reduced width and penetration depth due to thermal localization and powder-laser energy shielding. Among the parameters, laser power had the most dominant influence on melt pool depth.

The current model is primarily focused on accurately capturing the temperature distribution across single-track L-DED depositions. Future studies could build upon this by deriving cooling rates and thermal gradients to establish correlations with microstructural evolution within the deposited material. Additionally, the developed framework can be extended to simulate multi-track, multi-layer builds, enabling investigation into the effects of hatch spacing, interlayer thermal interactions, and the evolution of porosity throughout the process.

Chapter 8: On the Cracking Behavior in Functionally Graded Additive Manufacturing of IN625–CuCrZr: A Comprehensive Experimental and Thermal Finite Element Study

8.1 Introduction

Functionally graded additive manufacturing (FGAM) offers the ability to spatially tailor material composition within a single component, enabling the combination of dissimilar metals to meet diverse property requirements. Among various alloy pairings, the integration of Inconel 625 (IN625) and CuCrZr is particularly attractive due to the high-temperature strength of IN625 and the superior thermal conductivity of CuCrZr. However, the mismatch in thermophysical properties between these alloys poses serious challenges during fabrication, including poor printability, crack formation, and delamination. These challenges are particularly prominent during FGAM processing of complex geometries, where local heat accumulation and thermal gradients play a crucial role in determining the final microstructure and defects [1], [2].

The purpose of this chapter is to compare the FGAM of IN625–CuCrZr for two representative geometries, a thin wall and a cube. First, the influence of the geometry on process-induced defects, particularly hot cracks, was assessed through detailed experimental characterization. The findings indicate a clear correlation between part geometry, thermal behavior, and crack formation. For instance, the hot cracks are prominent in the cube sample, while there is no trace of them in the thin wall specimen. As discussed in detail in chapter 6, the hot cracks are formed during the end of solidification which is affected by composition and thermal history. While the compositional transition steps and process parameters are the same in both geometries, the difference in the heat dissipation and heat accumulation results in a notable difference in the thermal history of these samples. These observations highlight the necessity of analytical tools such as thermal simulations that consider geometry-specific effects to ensure reliable fabrication in FGAM.

To further elucidate the origin of these differences, we perform finite element (FE) thermal simulations to model the transient temperature fields and cooling rates experienced by both geometries during the deposition process. The simulation results reveal significant variations in thermal gradients and cooling histories between the cube and thin wall structures, which align closely with experimentally observed defect trends. This integrated experimental and FE

simulation-based approach provides a deeper understanding of cracking behavior in FGAM and can be used to study future strategies for defect mitigation in the manufacturing of functionally graded components.

8.2 Materials and methods

Functionally graded IN625–CuCrZr samples were fabricated as shown in Figure 8-1. A five-step compositional gradient (Cu0 → Cu25 → Cu50 → Cu75 → Cu100) was implemented by adjusting the hoppers' parameter every four layers along the build direction. The L-DED printing was performed under a constant powder feed rate and scanning speed, yet the laser power was adjusted based on the compositional transition. To investigate the effect of geometry on thermal history and defect formation, two sample types, cube and thin wall (Figure 8-1(b)), were printed using identical process parameters and compositional transitions. After fabrication, the samples were sectioned, polished, and analyzed using OM, SEM, and EDS, and their thermal histories were simulated using finite element (FE) thermal modeling, which is explained in detail in the following section.

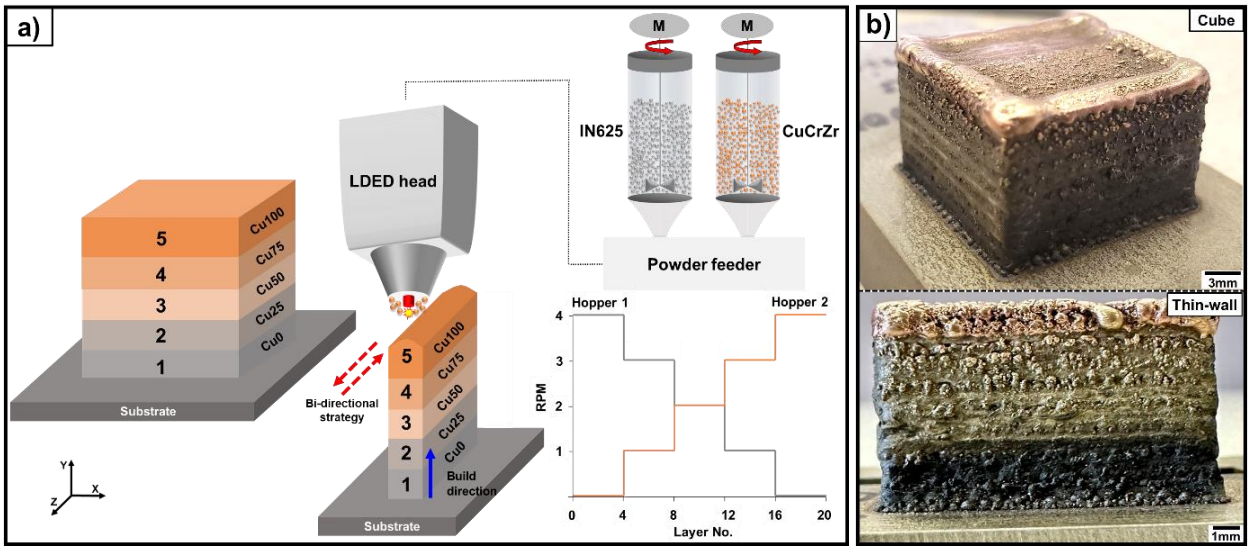


Figure 8-1 (a) Schematic of FGAM processing IN625-CuCrZr alloys for (b) cuboid and thin-wall geometries

8.3 Finite element (FE) modeling approach and model geometry

The proposed FE thermal model for the L-DED process of IN625-CuCrZr functionally graded materials focuses on accurately simulating thermal fields while simplifying melt-pool fluid and powder dynamics to reduce computational costs [3]. The methodology discretizes the continuous physical process of laser metal deposition into sequential simulation steps, corresponding to each interval of laser travel. During these intervals, detailed thermal analyses are performed step-by-

step, and the resulting time-temperature fields are stored for each node. The resultant nodal time-temperature data generated by the model will be used to estimate the cooling rates at different locations/compositions of the printed geometry. Figure 8-2 illustrates the model geometries used in the transient FE thermal simulations to represent the functionally graded IN625–CuCrZr samples. Two geometries were analyzed: (a) the thin wall with a length of 10 mm and a width of 1.6 mm, and (b) the cube with 10 mm length and 10 mm width, both built on an SS304L substrate with dimensions of 50 mm × 50 mm × 10 mm. An average layer thickness of 400 µm was considered for each compositional region, yielding a total build height of 8 mm. Each sample consists of five distinct compositional zones: Cu0, Cu25, Cu50, Cu75, and Cu100 along the build direction (Y-axis) with their specific thermophysical properties, which are described in detail in the following section.

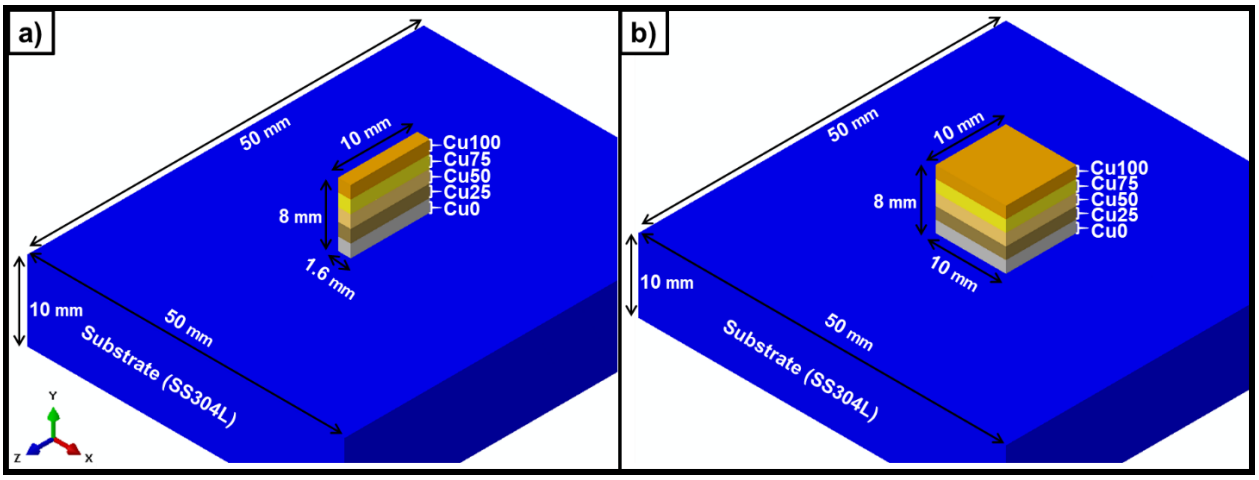


Figure 8-2 FE thermal model geometry of the FGAM processing of IN625-CuCrZr; (a) Thin-wall, (b) cube

8.3.1 Thermophysical material properties

In the FGAM processing of IN625–CuCrZr via powder-fed L-DED technique, transitional regions are built from the progressive mixing of the two base powders. The spatially varying composition between these dissimilar alloys leads to continuous changes in thermal and mechanical properties, which need to be obtained for the simulation. As previously demonstrated, there is a miscibility gap between IN625 and CuCrZr in the compositional transition regions, resulting instead in physical mixtures of the two base materials. Moreover, the microstructural analysis has shown that these regions consist of coexisting Cu-rich and Cu-lean regions, without significant emergence of

other phases. Therefore, it is reasonable to assume that the effective properties of the transition regions can be approximated using the rule of mixtures interpolation [151], [152], [153].
In that regard, both IN625 and CuCrZr are treated as isotropic materials with temperature-dependent properties. The transitional region is modeled by assigning effective material properties computed as a function of the volume fraction of each base alloy. The volume fraction of IN625 and CuCrZr in a given element is denoted by f_{IN} and f_{Cu}, respectively, where $f_{IN} + f_{Cu} = 1$.

The following expressions are used to compute the effective properties in transitional zones:

$$X(T) = f_{IN}.X_{IN}(T) + f_{Cu}.X_{Cu}(T) \quad \text{equation (8-1)}$$

Where X (ρ, k, C_p, E, ν, and σ_Y) is the property to be estimated for the mixed compositional regions.

$$\alpha(T) = \frac{f_{IN}.\alpha_{IN}(T).K_{IN}(T)+f_{Cu}.\alpha_{Cu}(T).K_{Cu}(T)}{f_{IN}.K_{IN}(T)+f_{Cu}.K_{Cu}(T)} \quad \text{equation (8-2)}$$

Where $K = \frac{E}{3(1-\nu)}$ is the bulk modulus.

To convert experimentally available weight fraction data into volume fractions (required in simulations), the following relation is used:

$$f_{IN} = \frac{w_{IN}}{w_{IN}+w_{Cu}.(\frac{\rho_{IN}}{\rho_{Cu}})},\ f_{Cu} = 1 - f_{IN} \quad \text{equation (8-3)}$$

Here, T is the temperature, ρ, k, C_p, E, ν, α, and σ_Y are the density, thermal conductivity, specific heat capacity, Young's modulus, Poisson's ratio, thermal expansion coefficient, and yield strength, respectively and w_{IN} and w_{Cu} are the weight fractions of IN625 and CuCrZr, respectively.
It is assumed that the absorption coefficient is a fixed value and not affected by temperature or phase change for simplicity of the computation. In order to account for the role of fluid flow convection in the melt pool, the thermal conduction coefficient of the materials was multiplied by the constant of 4 after the liquidus temperature [146].

8.3.2 Governing equation and boundary conditions

The cylindrical heat source model that was developed previously and discussed in detail in Chapter 7 was employed to apply the laser beam's heat flux as the thermal load. The governing equation and boundary conditions were also defined in the previous chapter.

8.3.3 Outline of the FE transient thermal modeling of FGAM process

The modeling workflow for predicting temperature distribution during the FGAM of IN625-CuCrZr involves defining a moving laser heat source and incorporating convection and radiation effects, typically implemented using DFLUX and FILM user-subroutines, respectively. Boundary conditions and temperature-dependent thermophysical properties of the materials are defined to accurately represent the actual process. These inputs feed into the FE heat transfer analysis, which computes the nodal temperature distribution over time.

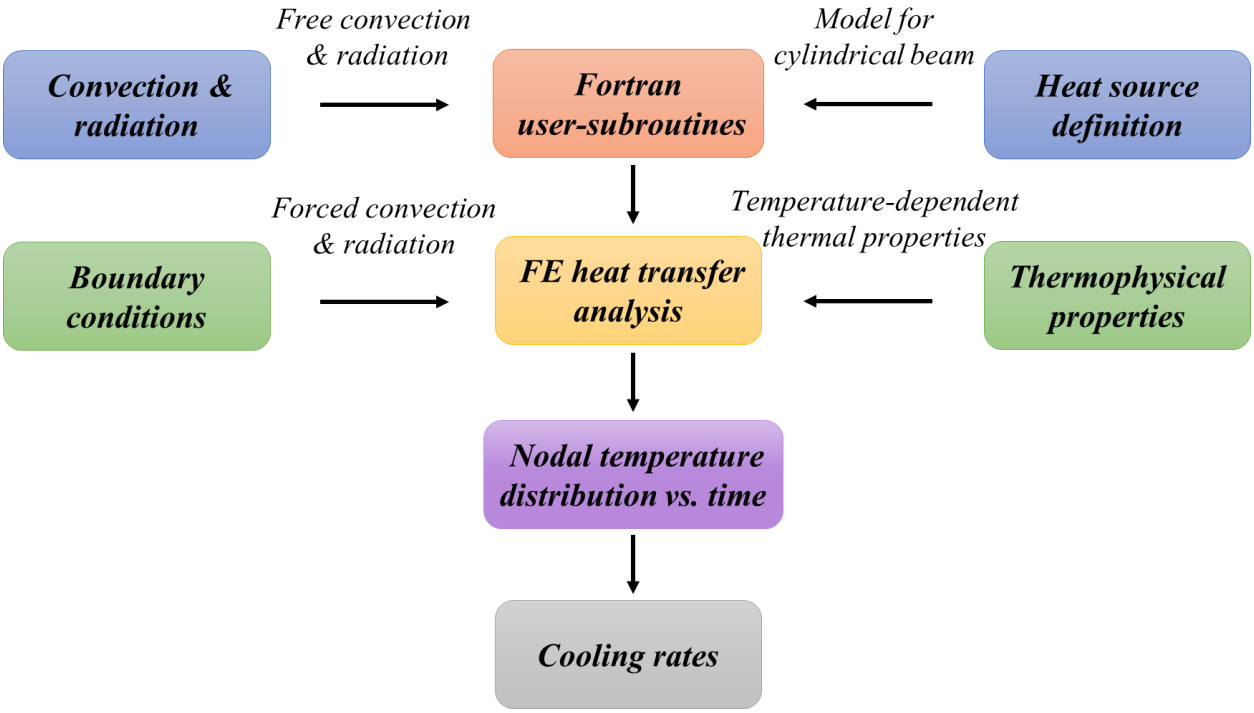


Figure 8-3 Outline of the FE transient thermal modeling workflow to study temperature distribution in FGAM processing of IN625-CuCrZr.

8.4 Results and Discussions

8.4.1 Cross sectional view of the thin wall and cube and CT scan results

Figure 8-4 presents cross-sectional micrographs of the fabricated FGAM samples, comparing the cube geometry and the thin-wall geometries. Both samples exhibit the intended five-step compositional gradient from Cu0 (bottom) to Cu100 (top), labelled in the figure. As can be seen from Figure 8-4(a), a high density of solidification cracks is observed, all initiated from Cu25 and propagated along the build direction Cu50 regions, consistent with the direction of thermal gradients during solidification [71]. As the process parameters and compositional transitions are

the same in both samples, it seems that the difference in geometry has manipulated the thermal gradient in a way that promoted the formation of hot cracks in susceptible composition zone (Cu25) in cube. In contrast, the thin-wall sample, Figure 8-4(b) shows a crack-free microstructure across all compositional zones, which is attributed to the difference in thermal gradient and cooling rate. This can be as a result of smaller heat sink effect due to its slender geometry. This geometry-dependent cracking behavior is further investigated in 3D through X-ray CT analysis, discussed in the following.

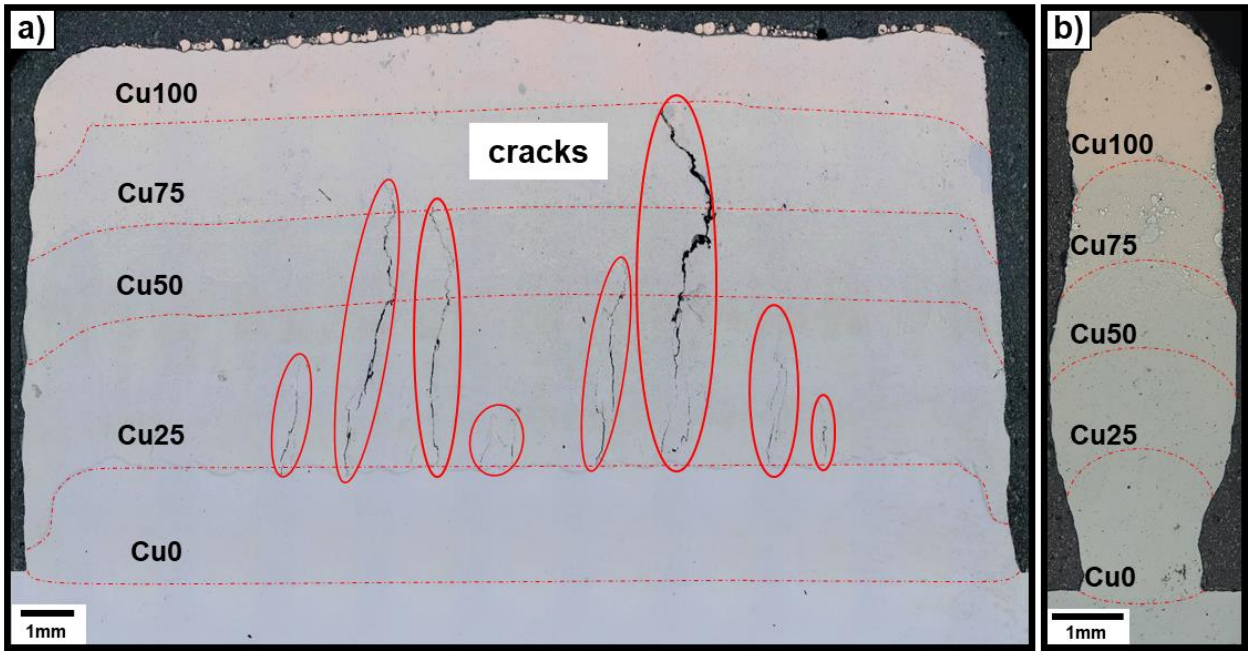


Figure 8-4 Cross sectional view of the FGAM IN625-CuCrZr samples; (a) cuboid geometry with cracks highlighted, (b) Thin-wall geometry

Figure 8-5 presents the 3D X-ray computed tomography (XCT) analysis of the cube and thin-wall geometries. Figure 8-5(a) exhibits pronounced solidification cracks that extend along the build direction (Z), particularly concentrated within the Cu25 and Cu50 regions. The high-resolution inset confirms the observation in Figure 8-4 that these cracks are initiated from Cu25 regions. Additionally, gas porosity is observed in the sample though less prevalent than the cracking. In contrast, Figure 8-5(b) shows the CT scan of the thin-wall sample, which exhibits only small porosity and no evidence of cracking throughout the graded structure. These CT results strongly confirm the 2D metallographic observations and emphasize that geometry-affected thermal history plays a dominant role in governing crack formation in FGAM structures.

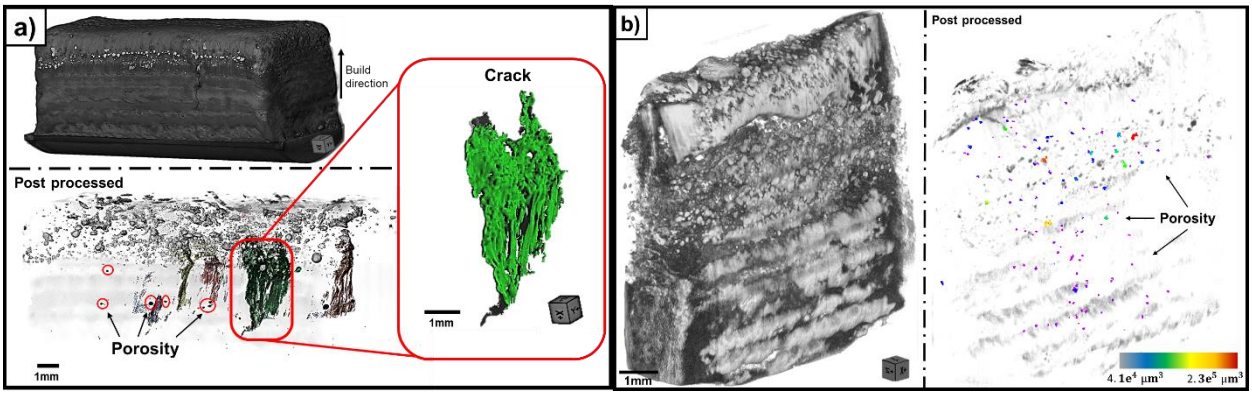


Figure 8-5 X-CT analysis of the defects on the FGAM IN625-CuCrZr samples; (a) cuboid geometry with highlighted cracks and porosity, (b) Thin-wall geometry with highlighted porosity

8.4.2 Simulated temperature distribution in the thin wall

Figure 8-6 illustrates the simulated temperature distributions during laser scanning of the last layer of each composition from Cu0 (100% IN625) to Cu100 (100% CuCrZr). As can be seen from the figure, there is a clear trend in melt pool size (gray region) and peak temperature with the amount of copper alloy. As the composition changes from Cu0 to Cu100 the melt pool size and the peak temperature progressively decreases. Although the less laser energy absorption is compensated by increasing the laser power, this behavior is attributed to the significantly higher thermal diffusivity of copper alloy, which results in less energy absorption and localized heating and more heat dissipation in the Cu-rich zones resulting in shallower melt pools and lower peak temperatures in Cu-rich regions. This variation in thermal behavior strongly follows the composition-dependent thermophysical properties change across different layers in the simulation.

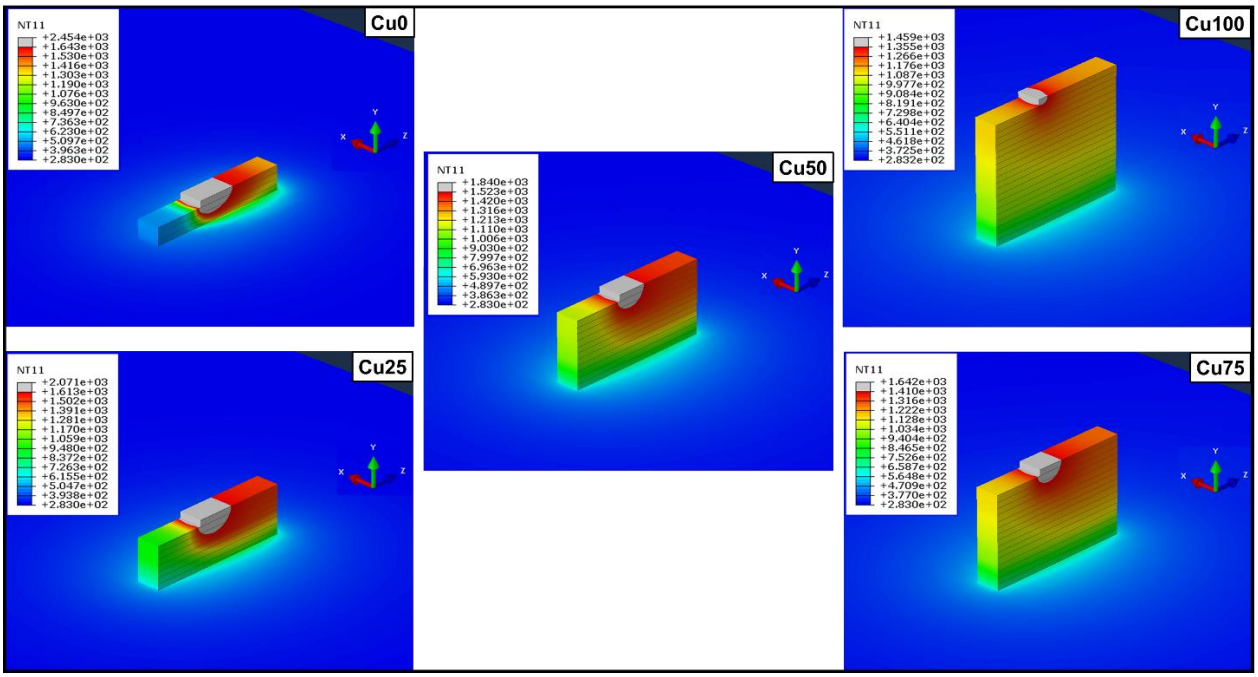


Figure 8-6 Simulated temperature distributions in the thin wall geometry during laser scanning of the final layer for each composition from Cu0 to Cu100. The gray regions correspond to temperatures exceeding the liquidus point of the respective composition, representing the extent of the simulated melt pool.

8.4.3 Simulated temperature distribution in the cube

Figure 8-7 illustrates the simulated temperature distributions during the deposition of the final layer across the compositional gradient from Cu0 to Cu100 in the cube geometry. Similar to the thin wall geometry, a clear trend is observed with increasing copper content, where both the melt pool size and peak temperature decrease progressively from Cu0 to Cu100. The Cu0 region, composed entirely of IN625, exhibits a larger and deeper melt pool with a higher peak temperature (~2165 K), whereas in the Cu100 region, the melt pool is significantly smaller and shallower, with a peak temperature dropping to ~1390 K. This behavior is primarily governed by the increasing thermal diffusivity with addition of copper alloy, which facilitates faster heat conduction and dissipation away from the melt pool, thereby limiting localized heat accumulation, leading to variations in thermal gradients and melt pool morphology across the graded structure.

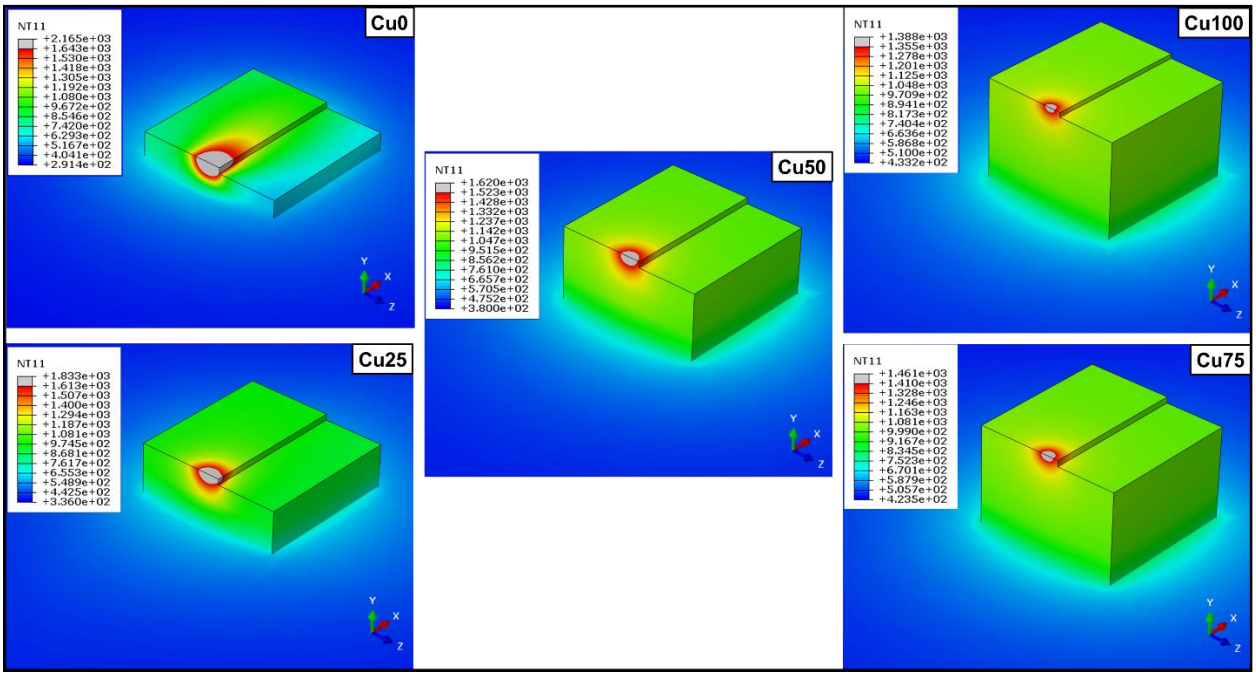


Figure 8-7 Simulated temperature distributions in the cube geometry during deposition of the final layer for each composition from Cu0 to Cu100. The gray regions correspond to temperatures exceeding the liquidus point of the respective composition, representing the extent of the simulated melt pool.

8.4.4 Experimental measurement of cooling rate from primary dendrite arm spacing and comparison of the cooling rate between thin wall and cube

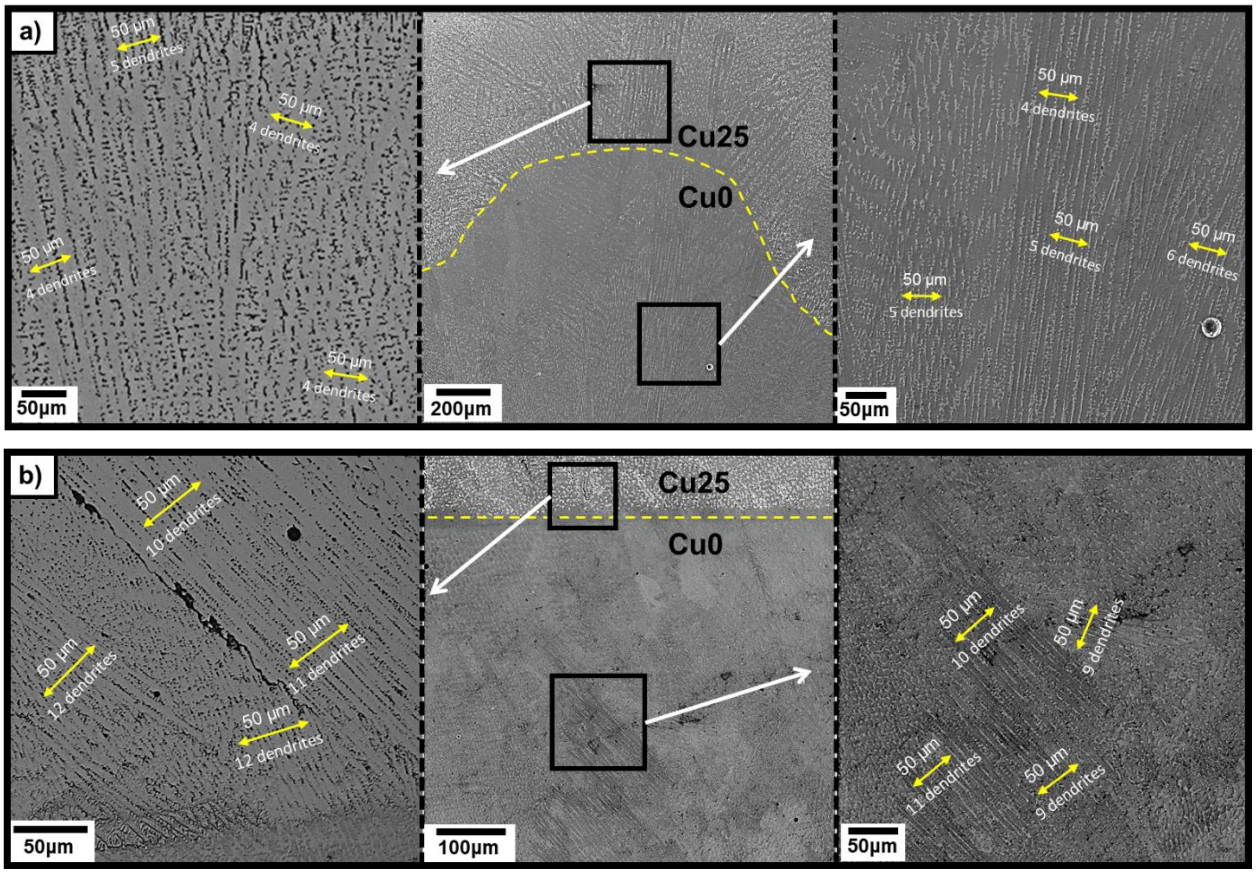
The cooling rate during solidification significantly influences the susceptibility of alloys to solidification cracking, especially in laser-based additive manufacturing processes [129]. As the cooling rate increases, the mushy zone, the temperature range over which solid and liquid coexist, narrows [154]. This reduces the time available for liquid redistribution, hindering adequate liquid feeding into the interdendritic region, leading to the formation of solidification cracks, particularly in compositions with broad solidification ranges like Cu25 in here [155], [156].

The cooling rate during solidification also defines the microstructure of additively manufactured alloys, particularly the primary dendrite arm spacing (PDAS)[157]. Rapid cooling promotes finer microstructures by reducing the time available for dendritic growth, resulting in smaller PDAS values. This inverse relationship is well established and is commonly described by empirical power-law equation as follows for Ni-based super alloys (Cu0) [158]:

$$\lambda_1 = 97\dot{T}^{-0.36} \qquad \text{(equation 8-4)}$$

where λ_1 is the PDAS and $\dot{T}$ is the cooling rate during the solidification.

In that regard, Figure 8-8 presents SEM images of the etched microstructures in the Cu0 and Cu25 regions, offering a comparative assessment of primary dendrite arm spacing (PDAS) between the thin wall (Figure 8-8(a)) and cube (Figure 8-8(b)) geometries. As quantified in Figure 8-8(c), the PDAS is noticeably finer in the cube samples compared to the thin wall for both compositions. Specifically, in the Cu0 region, the average PDAS is ~5µm in the cube, whereas it increases to around 10µm in the thin wall. A similar contrast is observed in the Cu25 region, where the average PDAS in the cube is ~4µm compared to ~12µm in the thin wall. This significant difference is inversely correlated with cooling rate, the finer dendritic spacing in the cube indicates a higher cooling rate relative to the thin wall. Further, as shown in Figure 8-8(d), the calculated cooling rates for the Cu0 (IN625) composition, using (equation 8-4), are approximately 3800 K/s for the cube and 700 K/s for the thin wall, quantitatively showing that the cube experiences substantially higher cooling rates than the thin wall. This disparity explains the differences in susceptibility to cracking observed across the two geometries.



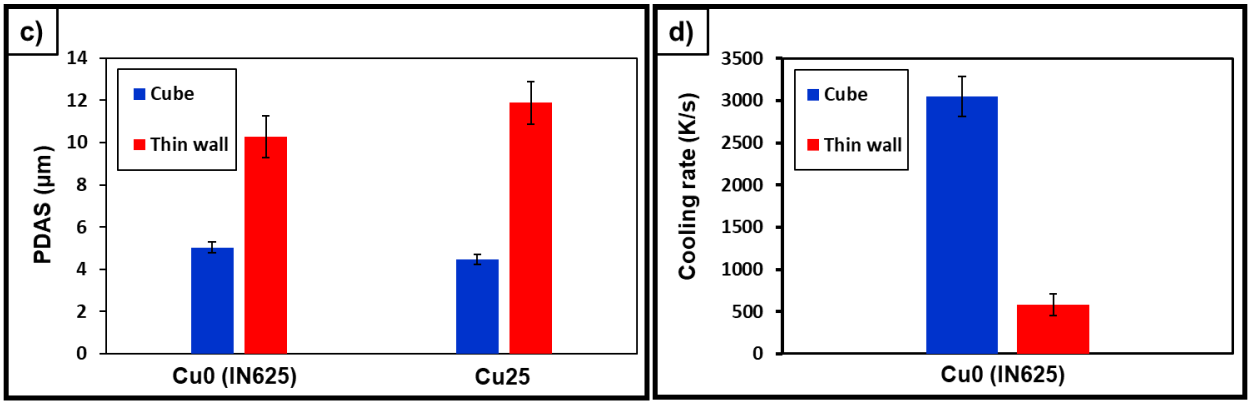


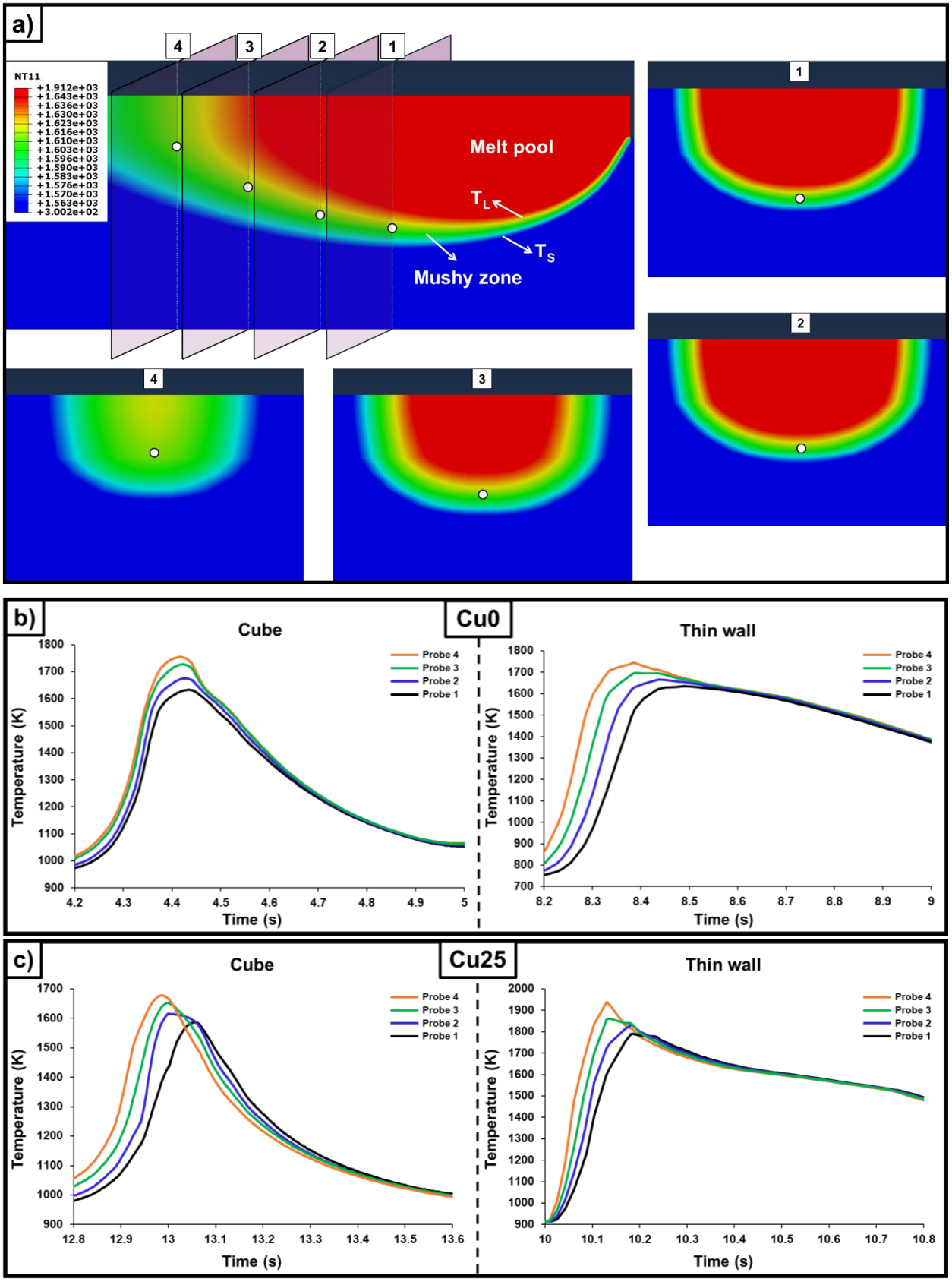
Figure 8-8 Primary dendrite arm spacing measured from high magnification SEM images from the cross-section of the Cu25 and Cu0 (IN625) regions in: (a) Thin wall and (b) cuboid samples. (d) comparison of the PDAS between thin wall and cube geometries in both compositions, highlighting finer microstructure in cube and (e) higher cooling rates

8.4.5 Comparison of the cooling rate between thin wall and cube in the crack prone regions in the model

Figure 8-9 presents the simulated thermal history within both cube and thin-wall geometries during the FGAM process, specifically at the crack-prone compositional interface between Cu0 and Cu25. Figure 8-9(a) depicts the simulated temperature distribution within a longitudinal cross-section of the melt pool obtained from finite element analysis. The melt pool region, shown in red, corresponds to temperatures exceeding the liquidus temperature (T_L), which is 1643°C for IN625, while the mushy zone spans the temperature interval between the liquidus (T_L) and solidus temperatures (T_S), which is 1563°C for IN625, isotherms. The fully solidified region is indicated in blue, corresponding to temperatures below T_S. Four probe points, indicated by white spots, are positioned along the solidification front to extract nodal temperature histories. Their spatial locations are illustrated in both the longitudinal view and the corresponding transverse cross-sections at each probe position. These probe trajectories serve as the basis for quantifying local cooling rates, which are subsequently correlated with solidification microstructure, including the PDAS. Figures 8-9(b) and (c) show the simulated nodal temperature histories at four probe locations for the Cu0 and Cu25 compositions, respectively, in both cube (left) and thin wall (right) geometries. Each curve corresponds to a probe point along the solidification front, as defined in Figure 8-9(a). In both compositions, the temperature profiles exhibit a sharp heating phase followed by cooling, with variations in peak temperature and cooling rate among the probes. The cube geometry consistently exhibits steeper thermal gradients and higher cooling rates compared to the thin wall. These thermal histories serve as the basis for quantifying local cooling rates and

interpreting their influence on microstructural features such as PDAS and cracking susceptibility at the Cu0–Cu25 interface. Figure 8-9(d) compares the average cooling rates extracted from the nodal temperature histories of the FEA simulations and experimental measurements for the Cu0 composition in both cube and thin-wall geometries. The simulated cooling rates were computed from nodal temperature histories at the probe points shown in Figure 8-9(a), while the experimental values were estimated based on microstructural measurements of PDAS. In both cases, the cube geometry exhibits significantly higher cooling rates than the thin wall, consistent with the experimental results with 14.32% error in the cube geometry and 6.54% error in the thin wall geometry. The close agreement between simulated and experimental trends validates the thermal model. Figure 8-9(e) shows the predicted average cooling rates for the Cu25 composition in both cube and thin-wall geometries, as obtained from FEA simulations. Consistent with the thermal trends observed in Figure 8-9(d), the cube geometry exhibits substantially higher cooling rates than the thin wall, attributed to its enhanced thermal conduction and larger heat sink volume. In addition, the cooling rates in Cu25 are around 10% higher in both geometries compared to the ones in Cu0, due to the addition of copper alloy, which increased the thermal diffusivity of the composition. This pronounced difference in cooling rate, therefore, has impacted the resulting microstructure and solidification cracking in the interface of Cu0 and Cu25.

In general, rapid cooling accelerates the movement of the solid–liquid interface; as a result, the mushy zone exists for only a short time and within a narrow spatial region, leaving insufficient time for the liquid metal to redistribute between growing dendrites [155], [159]. In addition, studies show that during the process, the molten alloy in one layer cannot adequately refill pre-existing cracks in the layer below if cooling is too rapid [154]. Therefore, the higher cooling rate in the cube geometry not only promotes crack initiation but also hinders the opportunity for most cracks to refill.


a)
NT11
+1.912e+03
+1.643e+03
+1.636e+03
+1.630e+03
+1.623e+03
+1.616e+03
+1.610e+03
+1.603e+03
+1.596e+03
+1.590e+03
+1.583e+03
+1.576e+03
+1.570e+03
+1.563e+03
+3.002e+02
4
3
2
1
Melt pool
T_L
T_S
Mushy zone
1
2
4
3
b)
Cube
Cu0
Thin wall
Probe 4
Probe 3
Probe 2
Probe 1
Temperature (K)
Time (s)
c)
Cube
Cu25
Thin wall
Probe 4
Probe 3
Probe 2
Probe 1
Temperature (K)
Time (s)

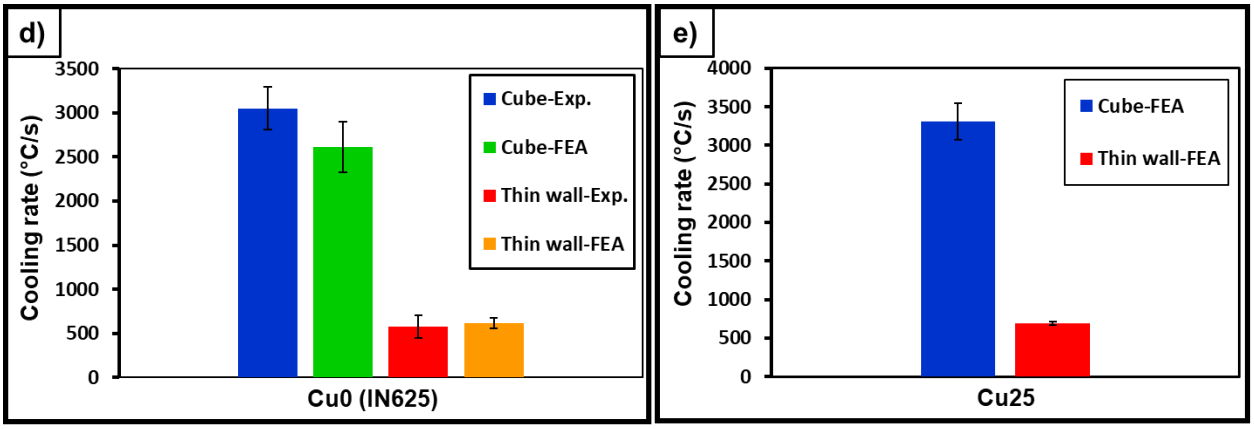


Figure 8-9 Simulated thermal behavior at the Cu0–Cu25 interface in cube and thin-wall geometries during FGAM; (a) Temperature distribution in the melt pool cross-section with probe locations. (b–c) Nodal temperature histories at probes for Cu0 and Cu25, respectively, showing higher cooling rates in the cube geometry. (d) Comparison of simulated and experimental cooling rates for Cu0. (e) Predicted cooling rates for Cu25 from simulations. Cube geometry consistently exhibits faster cooling rates

8.4.6 The mechanism behind the difference in cooling rate between thin wall and cube

The observed disparity in cooling rates between the cube and thin wall geometries can be fundamentally attributed to differences in their heat dissipation characteristics, as illustrated in the schematic of Figure 8-10. The cube geometry possesses a substantially larger heat sink area (100 mm^2) through its broad contact with the substrate and surrounding material, allowing more efficient heat conduction away from the melt pool. Additionally, each layer in the cube requires a longer build time (9 s), enabling longer heat extraction during solidification. In contrast, the thin wall has a much smaller heat sink area (16 mm^2) due to its slender cross-section, limiting conductive pathways near the melt pool. In addition, its shorter layer build time (1 s) further restricts the heat dissipation and exacerbates heat accumulation, which consequently leads to slower cooling rates [160]. Therefore, during solidification, a melt pool in the cube sample experiences significantly higher cooling rate than the one in the thin wall sample.

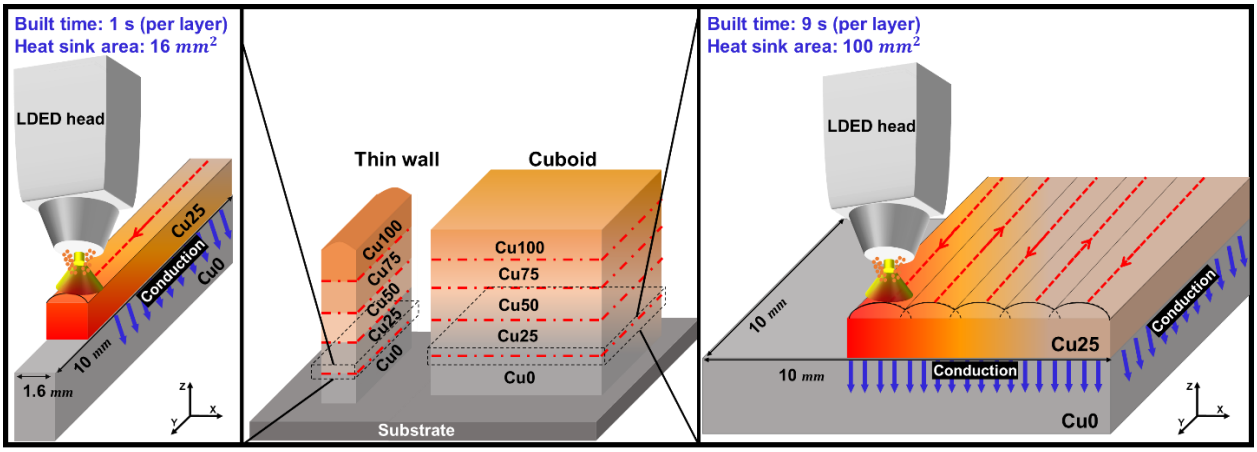


Figure 8-10 Effect of the print geometry on heat dissipation characteristics during the L-DED process

8.5 Summary

This chapter presents a comprehensive investigation into the cracking behavior of functionally graded IN625–CuCrZr alloys fabricated via L-DED, focusing on the influence of build geometry on thermal behavior and solidification phenomenon. Two representative geometries, a cube and a thin wall, were examined under identical processing and compositional transition parameters. Despite the uniform process parameters, significant differences were observed in cracking behavior, with the cube geometry exhibiting extensive solidification cracking in the Cu25 region, while the thin wall remained crack-free.

Further, the FEA thermal simulations revealed that these differences arise from geometry-dependent thermal histories. Specifically, the cube geometry demonstrated significantly higher cooling rates than the thin wall, attributed to its larger heat sink area and longer layer build time. These thermal characteristics were validated both experimentally, via microstructural analysis of PDAS, and numerically, through nodal temperature histories extracted from FE simulations.

A close agreement between simulated and experimentally derived cooling rates confirms the validation of the thermal model and underscores the critical role of cooling rate in governing solidification behavior and defect formation. These findings highlight the necessity of incorporating FE thermal modeling into the FGAM process design to mitigate defects and enable reliable fabrication of compositionally graded structures.

Chapter 9: Conclusions and future work

9.1 Conclusions

This work presented a comprehensive investigation into the process development, microstructural evolution, defect mechanisms, and thermal modeling of Functionally Graded Additive Manufacturing (FGAM) using the L-DED process. The thesis specifically focused on the challenging IN625–CuCrZr alloy system, which presents a big mismatch in thermophysical properties and processability. The research aimed to establish a systematic framework that would enable the fabrication of compositionally graded structures with minimal defects.

To address the inherent complexities of dissimilar material deposition, a hierarchical approach was employed, beginning with the optimization of process parameters for each alloy separately in the scales of single-track and multi-track. The results of these investigations were further applied to multi-layer deposition, enabling the identification of appropriate process windows for both IN625 and CuCrZr. Additionally, for the first time in literature, a processability map for L-DED of CuCrZr was developed. Complementary toolpath optimization strategies, including raster orientation and contouring, were implemented to ensure geometric accuracy and uniform deposition across multiple layers.

Beyond macroscale process development, extensive microstructural characterization and thermodynamic modeling were conducted to elucidate the influence of compositional gradients on solidification behavior. The findings revealed a strong interplay between liquid-phase miscibility gaps and the evolution of microstructure. These insights were critical in understanding the formation and distribution of defects such as solidification cracks, particularly within the transitional regions of the gradient. The study also showed that the miscibility gap provides a natural grain refinement mechanism within the mixed-phase regions.

Complementing the experimental findings, a high-fidelity finite element (FE) thermal model was developed using a hybrid statistical–numerical framework. This model accurately predicted melt pool geometry and transient thermal history by integrating an empirically calibrated heat source and an element activation scheme in Abaqus. The thermal simulations demonstrated strong agreement with in-situ thermocouple data and experimental melt pool dimensions. Further, this

model was used as an essential tool for interpreting geometry-dependent differences in thermal behavior, particularly in the cube versus thin wall geometries, which linked the difference in geometry to the differences in thermal history and cracking susceptibility. Together, these combined experimental and modeling efforts contributed to a deeper understanding of FGAM processing of dissimilar alloy systems and provide a foundation for process-informed design and defect mitigation. The major conclusions drawn from this thesis are summarized as follows:

1. Process parameter optimization and toolpath development were successfully conducted using a single-track to multi-track strategy combined with response surface methodology (RSM). Optimized parameters showed strong agreement with experimental results (within ~95% confidence interval). The implementation of a zigzag raster toolpath with 90° rotation and perimeter contouring ensured improved geometric accuracy and surface quality.

2. A general processability map for CuCrZr was established for the first time in literature, presenting a practical reference based on laser power (P) vs. feed rate/scan speed ratio (F/V), thereby addressing a key gap in L-DED knowledge for this alloy.

3. FGAM fabrication between IN625 and CuCrZr via a sharp compositional transition induced severe macrocracking and delamination, attributed to incompatible process parameters and thermophysical mismatches. A successful solution was achieved using a stepwise composition gradient (25 wt.% increments) and synchronized laser power modulation, enabling defect-free deposition at the macroscale.

4. CALPHAD-based thermodynamic simulations revealed a liquid-state miscibility gap in the Cu50–Cu75 composition range, which significantly influenced the resulting microstructure. Phase separation into Cu-rich and Cu-lean liquids, followed by rapid solidification, led to dual-phase microstructures and the formation of M_2C precipitate-rich spheroidal regions.

5. The miscibility gap enhanced grain refinement by promoting heterogeneous nucleation on semi-solidified Cu-lean spheroids. This led to the formation of highly equiaxed, ultrafine grains in 50% and 75% wt. CuCrZr/IN625 compositional mixtures regions, despite the coarse columnar grains in Cu25.

6. The cracking behavior in cube samples was dominated by solidification cracks initiated at 25% wt. CuCrZr/IN625, driven by interdendritic Cu-rich liquid films. However, the fine equiaxed grain structure in 75% wt. CuCrZr/IN625 aided in crack deflection and arrest, offering a natural toughening mechanism across the gradient.

7. A custom finite element (FE) thermal model was developed using a hybrid statistical-numerical framework and implemented in Abaqus via user subroutines. The model accurately predicted melt pool geometries and transient temperature profiles using a cylindrical-Gaussian heat source and the hybrid quiet/birth-and-death element activation technique. The model was validated against experimental melt pool dimensions and embedded thermocouple readings, with deviations consistently below 10%.

8. FE simulations demonstrated that increasing P/VP/\sqrt{V}P/V enlarged melt pool dimensions, while higher F/VF/VF/V increased height but reduced width and depth due to powder shielding effects. Laser power had the most dominant effect on penetration depth.

9. The comparative microstructural and FE thermal study between cube and thin wall geometries revealed that the build geometry significantly influences thermal history. The cube geometry

exhibited steeper cooling rates, leading to finer PDAS as a result of higher cooling rates and severe cracking, whereas the thin wall cooled more gradually and remained crack-free.

9.2 Recommendations and Future Work

Based on the results and discussions detailed in the above sections, the research goals that were defined for the thesis were successfully met. However, the work also revealed several opportunities for further exploration and enhancement. Future studies may focus on the following aspects:

1. Mechanical characterization of the gradient microstructure: While the present work focused on microstructure and defect mechanisms, future investigations should assess the mechanical performance of the mixed compositional regions, particularly in 50% and 75% wt. CuCrZr/IN625. This includes micro/nanoindentation to extract quasi static, dynamic, and creep mechanical properties.

2. Extension of post-heating or remelting strategies: The successful formation of highly fine grains in the 75% wt. CuCrZr/IN625 suggests a promising new alloy for additive manufacturing with excellent mechanical properties. Further alloy development studies should focus on this promising composition.

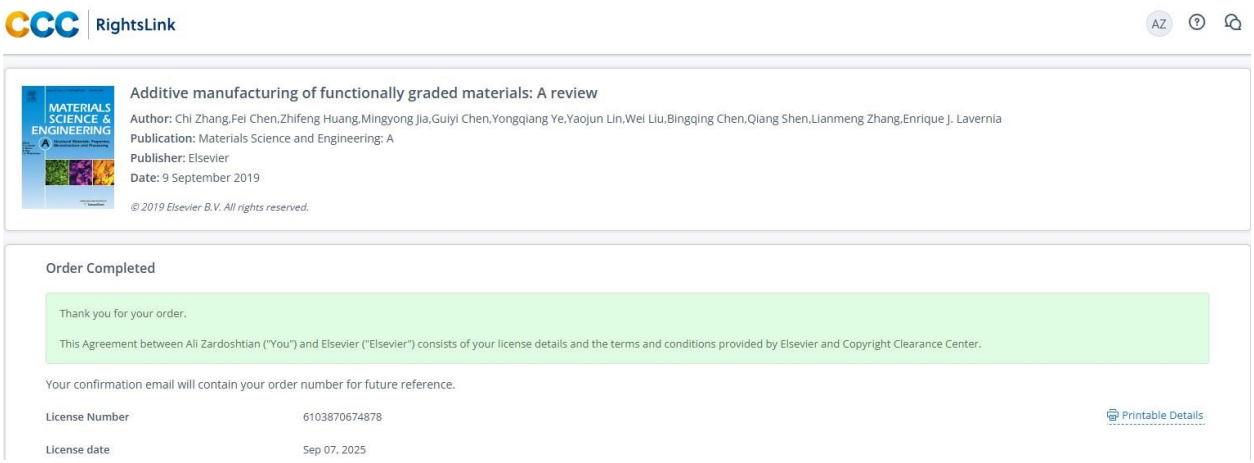
3. Crack modeling and prediction: Building on the validated thermal model, the nodal thermal histories can be coupled to a mechanical simulation framework to predict residual stress fields and their correlation with crack initiation. This would allow a more robust prediction of crack-prone regions based on both thermal history and stress evolution.

4. Adaptation to other dissimilar systems: The gradient transition and process development strategy presented here can be extended to other critical alloy systems, such as Ni-based to

steels, Ti-steels, Ti-Al, or Ni-Ti. Exploring the generalizability of the concept of miscibility gap between different alloys would broaden its industrial applicability.

5. Last but not least, investigating the role of post-process heat treatment on microstructure and mechanical properties: While this thesis focused on in-situ microstructural evolution during deposition, post-deposition heat treatment remains a powerful tool for tailoring phase composition, relieving residual stresses, and enhancing mechanical performance. Future studies could explore optimized heat treatment protocols for the IN625–CuCrZr gradient, particularly in regions affected by the liquid-phase miscibility gap. This includes evaluating homogenization effects, precipitation behavior (e.g., M_2C), and grain growth in both compositional mixtures and single-alloy regions, using advanced characterization techniques such as TEM and EBSD. Understanding the response of the gradient microstructure to thermal post-processing will be critical for developing robust, application-ready FGAM components.

Letter of Copyright Permission



CCC RightsLink

Additive manufacturing of functionally graded materials: A review

Author: Chi Zhang,Fei Chen,Zhifeng Huang,Mingyong Jia,Guiyi Chen,Yongqiang Ye,Yaojun Lin,Wei Liu,Bingqing Chen,Qiang Shen,Lianmeng Zhang,Enrique J. Lavernia
Publication: Materials Science and Engineering: A
Publisher: Elsevier
Date: 9 September 2019

© 2019 Elsevier B.V. All rights reserved.

Order Completed

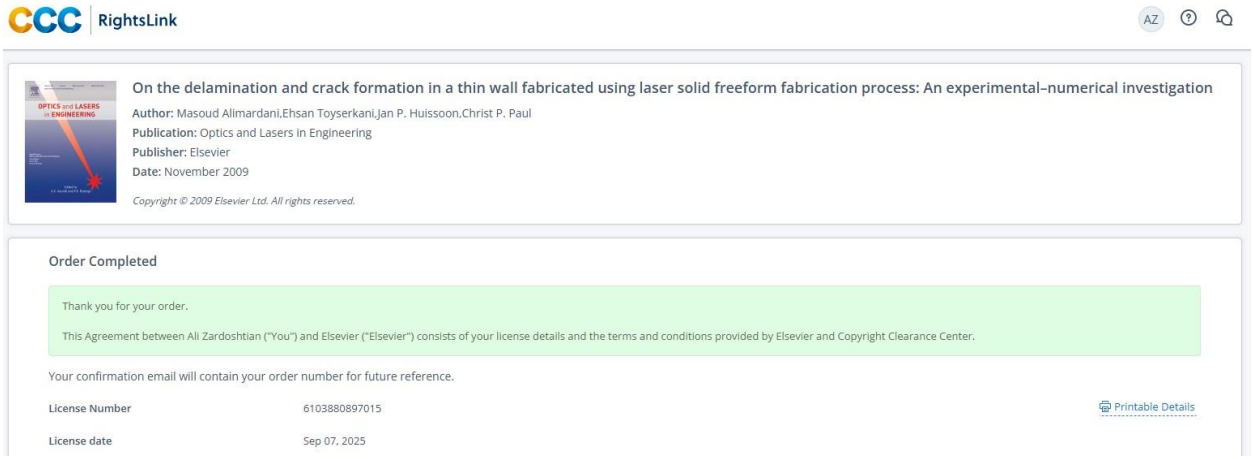
Thank you for your order.

This Agreement between Ali Zardoshtian ("You") and Elsevier ("Elsevier") consists of your license details and the terms and conditions provided by Elsevier and Copyright Clearance Center.

Your confirmation email will contain your order number for future reference.

License Number	6103870674878
License date	Sep 07, 2025

Printable Details



CCC RightsLink

On the delamination and crack formation in a thin wall fabricated using laser solid freeform fabrication process: An experimental–numerical investigation

Author: Masoud Alimardani,Ehsan Toyserkani,Jan P. Huissoon,Christ P. Paul
Publication: Optics and Lasers in Engineering
Publisher: Elsevier
Date: November 2009

Copyright © 2009 Elsevier Ltd. All rights reserved.

Order Completed

Thank you for your order.

This Agreement between Ali Zardoshtian ("You") and Elsevier ("Elsevier") consists of your license details and the terms and conditions provided by Elsevier and Copyright Clearance Center.

Your confirmation email will contain your order number for future reference.

License Number	6103880897015
License date	Sep 07, 2025

Printable Details

RightsLink



Comparison of microstructure features and mechanical properties for additive manufactured and wrought nickel alloys 625

Author: J. Nguejio,F. Szmytka,S. Hallais,A. Tanguy,S. Nardone,M. Godino Martinez
Publication: Materials Science and Engineering: A
Publisher: Elsevier
Date: 9 September 2019

© 2019 Elsevier B.V. All rights reserved.

Review Order

Please review the order details and the associated terms and conditions.

No royalties will be charged for this reuse request although you are required to obtain a license and comply with the license terms and conditions. To obtain the license, click the Accept button below.

Licensed Content

Licensed Content Publisher	Elsevier
Licensed Content Publication	Materials Science and Engineering: A
Licensed Content Title	Comparison of microstructure features and mechanical properties for additive manufactured and wrought nickel alloys 625
Licensed Content Author	J. Nguejio,F. Szmytka,S. Hallais,A. Tanguy,S. Nardone,M. Godino Martinez
Licensed Content Date	9 September 2019
Licensed Content Volume	764
Licensed Content Issue	n/a
Licensed Content Pages	1

Order Details

Type of Use	reuse in a thesis/dissertation
Portion	figures/tables/illustrations
Number of figures/tables/illustrations	2
Format	electronic
Are you the author of this Elsevier article?	No
Will you be translating?	No

About Your Work

Title of new work	Functionally graded additive manufacturing of Inconel 625 and CuCrZr alloys
Institution name	University of Waterloo
Expected presentation date	Sep 2025

Additional Data

Portions	Fig.5 and Fig.7
The Requesting Person / Organization to Appear on the License	Ali Zardoshtian

RightsLink

Taylor & Francis
Taylor & Francis Group

Modulated Structures in Cu-32Ni-3Cr and Cu-46Ni-17Cr Alloys

Author: F. Findik
Publication: Canadian Metallurgical Quarterly
Publisher: Taylor & Francis
Date: Jul 18, 2013

Rights managed by Taylor & Francis

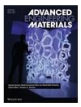
Quick Price Estimate

Taylor & Francis will be pleased to grant permission at no cost for use of content in a Master's Thesis and/or Doctoral Dissertation, subject to the following limitations.

You may use a single excerpt, up to 400 words and up to 3 figures/tables, on the condition that your acknowledgement must be included showing article title, author, full Journal title, and © copyright # [year], reprinted by permission of Informa UK Limited, trading as Taylor & Francis Group, https://www.tandfonline.com

If you use more than those limits, or intend to distribute or sell your Master's Thesis/Doctoral Dissertation to the general public through print or website publication, further permission will be required.

CCC | RightsLink



Residual Stress in Engineering Materials: A Review

Author: Mohammad Fotouhi, Mohammad Baraheni, Bahareh Marzbanrad, et al
Publication: Advanced Engineering Materials
Publisher: John Wiley and Sons
Date: Nov 14, 2021

© 2021 Wiley-VCH GmbH

Review Order

Please review the order details and the associated terms and conditions.

No royalties will be charged for this reuse request although you are required to obtain a license and comply with the license terms and conditions. To obtain the license, click the Accept button below.

Licensed Content

Licensed Content Publisher	John Wiley and Sons
Licensed Content Publication	Advanced Engineering Materials
Licensed Content Title	Residual Stress in Engineering Materials: A Review
Licensed Content Author	Mohammad Fotouhi, Mohammad Baraheni, Bahareh Marzbanrad, et al
Licensed Content Date	Nov 14, 2021
Licensed Content Volume	24
Licensed Content Issue	3
Licensed Content Pages	28

Order Details

Type of use	Dissertation/Thesis
Requestor type	University/Academic
Format	Electronic
Portion	Figure/table
Number of figures/tables	1
Will you be translating?	No

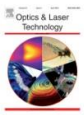
About Your Work

Title of new work	Functionally graded additive manufacturing of Inconel 625 and CuCrZr alloys
Institution name	University of Waterloo
Expected presentation date	Sep 2025

Additional Data

Portions	Fig.1
The Requesting Person / Organization to Appear on the License	Ali Zardoshtian

CCC | RightsLink



3-Dimensional heat transfer modeling for laser powder-bed fusion additive manufacturing with volumetric heat sources based on varied thermal conductivity and absorptivity

Author: Zhidong Zhang,Yuze Huang,Adhitan Rani Kasinathan,Shahriar Imani Shahabad,Usman Ali,Yahya Mahmoodkhani,Ehsan Toyserkani
Publication: Optics & Laser Technology
Publisher: Elsevier
Date: January 2019

© 2018 Elsevier Ltd. All rights reserved.

Order Completed

Thank you for your order.

This Agreement between Ali Zardoshtian ("You") and Elsevier ("Elsevier") consists of your license details and the terms and conditions provided by Elsevier and Copyright Clearance Center.

Your confirmation email will contain your order number for future reference.

License Number	6103891363528
License date	Sep 07, 2025

Printable Details

Licensed Content

Licensed Content Publisher	Elsevier
Licensed Content Publication	Optics & Laser Technology
Licensed Content Title	3-Dimensional heat transfer modeling for laser powder-bed fusion additive manufacturing with volumetric heat sources based on varied thermal conductivity and absorptivity
Licensed Content Author	Zhidong Zhang,Yuze Huang,Adhitan Rani Kasinathan,Shahriar Imani Shahabad,Usman Ali,Yahya Mahmoodkhani,Ehsan Toyserkani
Licensed Content Date	Jan 1, 2019
Licensed Content Volume	109
Licensed Content Issue	n/a
Licensed Content Pages	16

Order Details

Type of Use	reuse in a thesis/dissertation
Portion	figures/tables/illustrations
Number of figures/tables/illustrations	1
Format	electronic
Are you the author of this Elsevier article?	No
Will you be translating?	No

About Your Work

Title of new work	Functionally graded additive manufacturing of Inconel 625 and CuCrZr alloys
Institution name	University of Waterloo
Expected presentation date	Sep 2025

Additional Data

Portions	Fig.1
The Requesting Person / Organization to Appear on the License	Ali Zardoshtian

CCC | RightsLink

SPRINGER NATURE

Laser-directed energy deposition of CuCrZr alloy: from statistical process parameter optimization to microstructural analysis

Author: Ali Zardoshtian et al
Publication: The International Journal of Advanced Manufacturing Technology
Publisher: Springer Nature
Date: Apr 18, 2023

Copyright © 2023, The Author(s), under exclusive licence to Springer-Verlag London Ltd., part of Springer Nature

Order Completed

Thank you for your order.

This Agreement between Ali Zardoshtian ("You") and Springer Nature ("Springer Nature") consists of your license details and the terms and conditions provided by Springer Nature and Copyright Clearance Center.

Your confirmation email will contain your order number for future reference.

License Number	6103900173503
License date	Sep 07, 2025

Printable Details

Licensed Content

Licensed Content Publisher	Springer Nature
Licensed Content Publication	The International Journal of Advanced Manufacturing Technology
Licensed Content Title	Laser-directed energy deposition of CuCrZr alloy: from statistical process parameter optimization to microstructural analysis
Licensed Content Author	Ali Zardoshtian et al
Licensed Content Date	Apr 18, 2023

Order Details

Type of Use	Thesis/Dissertation
Requestor Type	academic/university or research institute
Format	electronic
Portion	figures/tables/illustrations
Number of figures/tables/illustrations	1
Will you be translating?	no
Circulation/distribution	1 - 29
Author of this Springer Nature content	yes

About Your Work

Title of new work	Functionally graded additive manufacturing of Inconel 625 and CuCrZr alloys
Institution name	University of Waterloo
Expected presentation date	Sep 2025

Additional Data

Portions	Fig.1 to Fig.10
The Requesting Person / Organization to Appear on the License	Ali Zardoshtian

References

[1] A. Reichardt, *Additive Manufacturing of Metal-Based Functionally Graded Materials*. University of California, Berkeley, 2017.

[2] A. Reichardt *et al.*, "Advances in additive manufacturing of metal-based functionally graded materials," *International Materials Reviews*, vol. 66, no. 1, pp. 1–29, 2021.

[3] C. Schneider-Maunoury, L. Weiss, D. Boisselier, and P. Laheurte, "Crystallographic analysis of functionally graded titanium-molybdenum alloys with DED-CLAD® process," *Procedia CIRP*, vol. 74, pp. 180–183, Jan. 2018, doi: 10.1016/J.PROCIR.2018.08.089.

[4] A. Thiriet, C. Schneider-Maunoury, P. Laheurte, D. Boisselier, and L. Weiss, "Multiscale study of different types of interface of a buffer material in powder-based directed energy deposition: Example of Ti6Al4V/Ti6Al4V - Mo/Mo - Inconel 718," *Addit Manuf*, vol. 27, no. February, pp. 118–130, 2019, doi: 10.1016/j.addma.2019.02.007.

[5] G. Anné, J. Vleugels, and O. Van Der Biest, "Functionally graded ceramics," *Ceramic-Matrix Composites: Microstructure, Properties and Applications*, pp. 575–596, Jan. 2006, doi: 10.1533/9781845691066.5.575.

[6] M. Koizumi and M. Niino, "Overview of FGM research in Japan," *MRS Bull*, vol. 20, no. 1, pp. 19–21, 1995.

[7] C. Zhang *et al.*, "Additive manufacturing of functionally graded materials: A review," *Materials Science and Engineering: A*, vol. 764, p. 138209, 2019.

[8] D. C. Hofmann *et al.*, "Developing Gradient Metal Alloys through Radial Deposition Additive Manufacturing," 2014, doi: 10.1038/srep05357.

[9] G. J. Brentrup and J. N. DuPont, "Fabrication and characterization of graded transition joints for welding dissimilar alloys," *Weld. J*, vol. 92, pp. 72–79, 2013.

[10] B. Onuike, B. Heer, and A. Bandyopadhyay, "Additive manufacturing of Inconel 718—Copper alloy bimetallic structure using laser engineered net shaping (LENS^{TM})," *Addit Manuf*, vol. 21, pp. 133–140, 2018, doi: https://doi.org/10.1016/j.addma.2018.02.007.

[11] Y. Wang, Y. Gao, Y. Li, W. Zhai, L. Sun, and C. Zhang, "Review of preparation and application of copper–steel bimetal composites," *Emerging Materials Research*, vol. 8, no. 4, pp. 538–551, 2019.

[12] S. Shakerin, M. Sanjari, H. Pirgazi, B. S. Amirkhiz, and M. Mohammadi, "On the bending of MS1-P20 hybrid steels additively manufactured using laser powder bed fusion," *Materialia (Oxf)*, vol. 24, p. 101501, Aug. 2022, doi: 10.1016/J.MTLA.2022.101501.

[13] E. Toyserkani, D. Sarker, O. O. Ibhadode, F. Liravi, P. Russo, and K. Taherkhani, "Metal Additive Manufacturing," 2021.

[14] T. DebRoy *et al.*, "Additive manufacturing of metallic components – Process, structure and properties," *Prog Mater Sci*, vol. 92, pp. 112–224, Mar. 2018, doi: 10.1016/J.PMATSCI.2017.10.001.

[15] A. Reichardt *et al.*, “Development and characterization of Ti-6Al-4V to 304L stainless steel gradient components fabricated with laser deposition additive manufacturing,” *Mater Des*, vol. 104, pp. 404–413, Aug. 2016, doi: 10.1016/J.MATDES.2016.05.016.

[16] K. Shah, I. ul Haq, A. Khan, S. A. Shah, M. Khan, and A. J. Pinkerton, “Parametric study of development of Inconel-steel functionally graded materials by laser direct metal deposition,” *Materials & Design (1980-2015)*, vol. 54, pp. 531–538, 2014, doi: https://doi.org/10.1016/j.matdes.2013.08.079.

[17] A. Thiriet, C. Schneider-Maunoury, P. Laheurte, D. Boisselier, and L. Weiss, “Multiscale study of different types of interface of a buffer material in powder-based directed energy deposition: Example of Ti6Al4V/Ti6Al4V - Mo/Mo - Inconel 718,” *Addit Manuf*, vol. 27, no. September 2018, pp. 118–130, 2019, doi: 10.1016/j.addma.2019.02.007.

[18] M. K. Imran, S. H. Masood, and M. Brandt, “Direct metal deposition of H13 tool steel on copper alloy substrate: parametric investigation,” *Lasers in Manufacturing and Materials Processing*, vol. 2, no. 4, pp. 242–260, 2015.

[19] P. R. Gradl and C. S. Protz, “Technology advancements for channel wall nozzle manufacturing in liquid rocket engines,” *Acta Astronaut*, vol. 174, pp. 148–158, Sep. 2020, doi: 10.1016/J.ACTAASTRO.2020.04.067.

[20] P. Gradl *et al.*, *Additive Manufacturing of Liquid Rocket Engine Combustion Devices: A Summary of Process Developments and Hot-Fire Testing Results*. 2018. doi: 10.2514/6.2018-4625.

[21] Y. Bai, C. Zhao, Y. Zhang, J. Chen, and H. Wang, “Additively manufactured CuCrZr alloy: Microstructure, mechanical properties and machinability,” *Materials Science and Engineering: A*, vol. 819, p. 141528, Jul. 2021, doi: 10.1016/J.MSEA.2021.141528.

[22] T. Pan *et al.*, “Characteristics of Inconel 625—copper bimetallic structure fabricated by directed energy deposition,” *The International Journal of Advanced Manufacturing Technology*, vol. 109, no. 5, pp. 1261–1274, 2020.

[23] K. J. A. Kundig and R. D. Weed, “Copper and copper alloys,” *Mech. Eng. Handb., fourth ed., John Wiley & Sons Inc, Hoboken, New Jersey*, pp. 117–227, 2015.

[24] F. Singer, D. C. Deisenroth, D. M. Hymas, and M. M. Ohadi, “Additively manufactured copper components and composite structures for thermal management applications,” in *2017 16th IEEE Intersociety Conference on Thermal and Thermomechanical Phenomena in Electronic Systems (ITherm)*, IEEE, 2017, pp. 174–183.

[25] K. Jahns, R. Bappert, · Peter, and · Ulrich Krupp, “Additive manufacturing of CuCr1Zr by development of a gas atomization and laser powder bed fusion routine”, doi: 10.1007/s00170-020-04941-7.

[26] S. Kou, “Welding Metallurgy, 2nd Edition.” [Online]. Available: www.mrs.org/meetings/spring2004/

[27] M. Karmuhilan and S. Kumanan, “A Review on Additive Manufacturing Processes of Inconel 625,” *J Mater Eng Perform*, vol. 31, no. 4, pp. 2583–2592, 2022, doi: 10.1007/s11665-021-06427-3.

[28] Y.-C. Zhang, W. Jiang, S.-T. Tu, X.-C. Zhang, Y.-J. Ye, and R.-Z. Wang, “Experimental investigation and numerical prediction on creep crack growth behavior of the solution treated Inconel 625 superalloy,” *Eng Fract Mech*, vol. 199, pp. 327–342, 2018.

[29] I. S. Cinoglu, A. Charbal, and N. Vermaak, “Towards exploiting inelastic design for Inconel 625 under short-term cyclic loading at 600∘ C,” *Mechanics of Materials*, vol. 140, p. 103219, 2020.

[30] X. Xu, G. Mi, L. Xiong, P. Jiang, X. Shao, and C. Wang, “Morphologies, microstructures and properties of TiC particle reinforced Inconel 625 coatings obtained by laser cladding with wire,” *J Alloys Compd*, vol. 740, pp. 16–27, 2018.

[31] F. Findik, “Modulated structures in Cu-32Ni-3Cr and Cu-46Ni-17Cr alloys,” *Canadian metallurgical quarterly*, vol. 41, no. 3, pp. 337–347, 2002.

[32] J. O’Flynn, C. A. Whitman, and S. F. Corbin, “Thermal property measurements of metal injection moulded Inconel 625 and Inconel 718 using combined thermal analysis techniques,” *Powder Metallurgy*, vol. 63, no. 4, pp. 277–287, 2020.

[33] Z. Ren, G. Fu, D. Z. Zhang, K. Zhang, and M. Zhao, “Thermal flow characteristics and the evolution of laser absorption in laser powder bed fusion of Cu-Cr-Zr alloy,” *Int J Mech Sci*, vol. 216, p. 106957, 2022.

[34] T. Ungár and A. Borbély, “The effect of dislocation contrast on x-ray line broadening: A new approach to line profile analysis,” *Appl Phys Lett*, vol. 69, no. 21, pp. 3173–3175, Nov. 1996, doi: 10.1063/1.117951.

[35] G. K. Williamson and W. H. Hall, “X-ray line broadening from filed aluminium and wolfram,” *Acta Metallurgica*, vol. 1, no. 1, pp. 22–31, Jan. 1953, doi: 10.1016/0001-6160(53)90006-6.

[36] A. Tabatabaeian, A. R. Ghasemi, M. M. Shokrieh, B. Marzbanrad, M. Baraheni, and M. Fotouhi, “Residual Stress in Engineering Materials: A Review,” *Adv Eng Mater*, vol. 24, no. 3, pp. 1–28, 2022, doi: 10.1002/adem.202100786.

[37] M. Manjgo, G. Lojen, N. Gubeljak, B. Karpe, and T. Vuherer, “Comparison of Three Methods of Measuring Residual Stresses in Welded Joints of High-Strength Steel S960QL,” *Materials*, vol. 18, no. 5, pp. 7–9, 2025, doi: 10.3390/ma18050950.

[38] T. Klein, P. Spoerk-Erdely, C. Schneider-Broeskamp, J. P. Oliveira, and G. Abreu Faria, “Residual Stresses in a Wire and Arc-Directed Energy-Deposited Al–6Cu–Mn (ER2319) Alloy Determined by Energy-Dispersive High-Energy X-ray Diffraction,” *Metall Mater Trans A Phys Metall Mater Sci*, vol. 55, no. 3, pp. 736–744, 2024, doi: 10.1007/s11661-023-07279-3.

[39] M. Gouge and P. Michaleris, *Thermo-mechanical modeling of additive manufacturing*. Butterworth-Heinemann, 2017.

[40] H. Fayazfar *et al.*, “A critical review of powder-based additive manufacturing of ferrous alloys: Process parameters, microstructure and mechanical properties,” *Mater Des*, vol. 144, pp. 98–128, Apr. 2018, doi: 10.1016/J.MATDES.2018.02.018.

[41] M. Bayat, W. Dong, J. Thorborg, A. C. To, and J. H. Hattel, “A review of multi-scale and multi-physics simulations of metal additive manufacturing processes with focus on modeling strategies,” *Addit Manuf*, vol. 47, p. 102278, Nov. 2021, doi: 10.1016/J.ADDMA.2021.102278.

[42] Z. Zhang *et al.*, “3-Dimensional heat transfer modeling for laser powder-bed fusion additive manufacturing with volumetric heat sources based on varied thermal conductivity and absorptivity,” *Opt Laser Technol*, vol. 109, pp. 297–312, Jan. 2019, doi: 10.1016/J.OPTLASTEC.2018.08.012.

[43] H. C. Degroh Iii, D. L. Ellis, and W. S. Loewenthal, “Comparison of GRCop-84 to Other Cu Alloys with High Thermal Conductivities”, doi: 10.1007/s11665-007-9175-3.

[44] Y. Pang *et al.*, “Effects of Zr and (Ni, Si) additions on properties and microstructure of Cu–Cr alloy,” *J Alloys Compd*, vol. 582, pp. 786–792, Jan. 2014, doi: 10.1016/J.JALLCOM.2013.08.146.

[45] T. J. Horn and D. Gamzina, “Additive manufacturing of copper and copper alloys,” 2020.

[46] P. Lassègue *et al.*, “Laser powder bed fusion (L-PBF) of Cu and CuCrZr parts: Influence of an absorptive physical vapor deposition (PVD) coating on the printing process,” *Addit Manuf*, vol. 39, p. 101888, Mar. 2021, doi: 10.1016/J.ADDMA.2021.101888.

[47] Y. Sun and M. Hao, “Statistical analysis and optimization of process parameters in Ti6Al4V laser cladding using Nd:YAG laser,” *Opt Lasers Eng*, vol. 50, no. 7, pp. 985–995, Jul. 2012, doi: 10.1016/J.OPTLASENG.2012.01.018.

[48] M. Ansari, R. Shoja Razavi, and M. Barekat, “An empirical-statistical model for coaxial laser cladding of NiCrAlY powder on Inconel 738 superalloy,” *Opt Laser Technol*, vol. 86, pp. 136–144, Dec. 2016, doi: 10.1016/J.OPTLASTEC.2016.06.014.

[49] M. Ansari, R. Shoja Razavi, and M. Barekat, “An empirical-statistical model for coaxial laser cladding of NiCrAlY powder on Inconel 738 superalloy,” *Opt Laser Technol*, vol. 86, pp. 136–144, Dec. 2016, doi: 10.1016/J.OPTLASTEC.2016.06.014.

[50] A. Dass and A. Moridi, “coatings State of the Art in Directed Energy Deposition: From Additive Manufacturing to Materials Design,” 2019, doi: 10.3390/coatings9070418.

[51] M. Ansari, A. Mohamadizadeh, Y. Huang, V. Paserin, and E. Toyserkani, “Laser directed energy deposition of water-atomized iron powder: Process optimization and microstructure of single-tracks,” *Opt Laser Technol*, vol. 112, pp. 485–493, Apr. 2019, doi: 10.1016/J.OPTLASTEC.2018.11.054.

[52] X. Wang, B. Zheng, K. Yu, S. Jiang, E. J. Lavernia, and J. M. Schoenung, “The role of cell boundary orientation on mechanical behavior: A site-specific micro-pillar characterization study,” *Addit Manuf*, vol. 46, p. 102154, Oct. 2021, doi: 10.1016/J.ADDMA.2021.102154.

[53] Z. Zhang, P. Farahmand, and R. Kovacevic, “Laser cladding of 420 stainless steel with molybdenum on mild steel A36 by a high power direct diode laser,” *Mater Des*, vol. 109, pp. 686–699, Nov. 2016, doi: 10.1016/J.MATDES.2016.07.114.

[54] S. Uchida *et al.*, “Microstructures and electrical and mechanical properties of Cu-Cr alloys fabricated by selective laser melting,” *Mater Des*, vol. 175, p. 107815, 2019, doi: https://doi.org/10.1016/j.matdes.2019.107815.

[55] R. Esmaeilizadeh, U. Ali, A. Keshavarzkermani, Y. Mahmoodkhani, E. Marzbanrad, and E. Toyserkani, “On the effect of spatter particles distribution on the quality of Hastelloy X parts

made by laser powder-bed fusion additive manufacturing," *J Manuf Process*, vol. 37, pp. 11–20, Jan. 2019, doi: 10.1016/J.JMAPRO.2018.11.012.

[56] A. Segerstark, J. Andersson, and L. E. Svensson, "Investigation of laser metal deposited Alloy 718 onto an EN 1.4401 stainless steel substrate," *Opt Laser Technol*, vol. 97, pp. 144–153, Dec. 2017, doi: 10.1016/J.OPTLASTEC.2017.05.038.

[57] H. L. Wei, T. Mukherjee, and T. Debroy, "Grain growth modeling for additive manufacturing of nickel based superalloys," in *Proceedings of the 6th international conference on recrystallization and grain growth (ReX&GG 2016)*, Springer, 2016, pp. 265–269.

[58] A. Keshavarzkermani *et al.*, "An investigation into the effect of process parameters on melt pool geometry, cell spacing, and grain refinement during laser powder bed fusion," *Opt Laser Technol*, vol. 116, pp. 83–91, Aug. 2019, doi: 10.1016/J.OPTLASTEC.2019.03.012.

[59] S. Sreekanth, E. Ghassemali, K. Hurtig, S. Joshi, and J. Andersson, "metals Effect of Direct Energy Deposition Process Parameters on Single-Track Deposits of Alloy 718", doi: 10.3390/met10010096.

[60] E. O. Hall, "Variation of hardness of metals with grain size," *Nature*, vol. 173, no. 4411, pp. 948–949, 1954.

[61] C. Meriç, E. Atik, and T. Engez, "Application of the hall-petch relation to microhardness measurement on AA 1030, Cu, CuSn7, CuZn30 and 6114 alloys," *Mathematical and Computational Applications*, vol. 2, no. 2, pp. 71–77, 1997.

[62] M. Pouranvari and S. P. H. Marashi, "Critical review of automotive steels spot welding: process, structure and properties M Pouranvari & S P H Marashi Critical review of automotive steels spot welding: process, structure and properties," 2013, doi: 10.1179/1362171813Y.0000000120.

[63] G. E. Dieter and D. Bacon, *Mechanical metallurgy*, vol. 3. McGraw-hill New York, 1976.

[64] X. Wang, B. Zheng, K. Yu, S. Jiang, E. J. Lavernia, and J. M. Schoenung, "The role of cell boundary orientation on mechanical behavior: A site-specific micro-pillar characterization study," *Addit Manuf*, vol. 46, p. 102154, Oct. 2021, doi: 10.1016/J.ADDMA.2021.102154.

[65] M. Tang, P. C. Pistorius, and J. L. Beuth, "Prediction of lack-of-fusion porosity for powder bed fusion," *Addit Manuf*, vol. 14, pp. 39–48, 2017.

[66] W. M. Steen and J. Mazumder, *Laser material processing*. springer science & business media, 2010.

[67] I. Yadroitsev, A. Gusarov, I. Yadroitsava, and I. Smurov, "Single track formation in selective laser melting of metal powders," *J Mater Process Technol*, vol. 210, no. 12, pp. 1624–1631, Sep. 2010, doi: 10.1016/J.JMATPROTEC.2010.05.010.

[68] P. Kiani, A. D. Dupuy, K. Ma, and J. M. Schoenung, "Directed energy deposition of AlSi10Mg: Single track nonscalability and bulk properties," *Mater Des*, vol. 194, p. 108847, 2020, doi: 10.1016/j.matdes.2020.108847.

[69] H. L. Wei, G. L. Knapp, T. Mukherjee, and T. DebRoy, “Three-dimensional grain growth during multi-layer printing of a nickel-based alloy Inconel 718,” *Addit Manuf*, vol. 25, pp. 448–459, Jan. 2019, doi: 10.1016/J.ADDMA.2018.11.028.

[70] M. Ansari, A. Martinez-Marchese, M. Khamooshi, A. Keshavarzkermani, R. Esmaeilizadeh, and E. Toyserkani, “Analytical modeling of multi-track powder-fed laser directed energy deposition: On the relationships among process, deposition dimensions, and solidification microstructure in additively manufactured near-β titanium alloy,” *J Mater Process Technol*, vol. 306, p. 117643, Aug. 2022, doi: 10.1016/J.JMATPROTEC.2022.117643.

[71] A. Keshavarzkermani, M. Sadowski, and L. Ladani, “Direct metal laser melting of Inconel 718: Process impact on grain formation and orientation,” *J Alloys Compd*, vol. 736, pp. 297–305, Mar. 2018, doi: 10.1016/J.JALLCOM.2017.11.130.

[72] M. Ansari, A. Martinez-Marchese, M. Khamooshi, A. Keshavarzkermani, R. Esmaeilizadeh, and E. Toyserkani, “Analytical modeling of multi-track powder-fed laser directed energy deposition: On the relationships among process, deposition dimensions, and solidification microstructure in additively manufactured near-β titanium alloy,” *J Mater Process Technol*, vol. 306, no. May, p. 117643, Aug. 2022, doi: 10.1016/j.jmatprotec.2022.117643.

[73] A. Keshavarzkermani *et al.*, “Controlling mechanical properties of additively manufactured hastelloy X by altering solidification pattern during laser powder-bed fusion,” *Materials Science and Engineering A*, vol. 762, no. June, p. 138081, 2019, doi: 10.1016/j.msea.2019.138081.

[74] B. J. Paudel, “Thermal Modeling and Simulation of Metals Additive Manufacturing,” 2019.

[75] R. P. Martukanitz, R. M. Melnychuk, M. S. Stefanski, and S. M. Copley, “Dynamic absorption of a powder layer,” *ICALEO 2004 - 23rd International Congress on Applications of Laser and Electro-Optics, Congress Proceedings*, pp. 2–7, 2004, doi: 10.2351/1.5060217.

[76] Z. Ren, G. Fu, D. Z. Zhang, K. Zhang, and M. Zhao, “Thermal flow characteristics and the evolution of laser absorption in laser powder bed fusion of Cu-Cr-Zr alloy,” *Int J Mech Sci*, vol. 216, no. August 2021, p. 106957, 2022, doi: 10.1016/j.ijmecsci.2021.106957.

[77] S. Chen, M. Xu, T. Yuan, X. Jiang, H. Zhang, and X. Zheng, “Thermal–microstructural analysis of the mechanism of liquation cracks in wire-arc additive manufacturing of Al–Zn–Mg–Cu alloy,” *Journal of Materials Research and Technology*, vol. 16, pp. 1260–1271, 2022, doi: 10.1016/j.jmrt.2021.12.016.

[78] S. Chen, H. Gao, Y. Zhang, Q. Wu, Z. Gao, and X. Zhou, “Review on residual stresses in metal additive manufacturing: formation mechanisms, parameter dependencies, prediction and control approaches,” *Journal of Materials Research and Technology*, vol. 17, pp. 2950–2974, 2022, doi: 10.1016/j.jmrt.2022.02.054.

[79] E. Tejado, A. V Müller, J. H. You, and J. Y. Pastor, “Evolution of mechanical performance with temperature of W/Cu and W/CuCrZr composites for fusion heat sink applications,” *Materials Science and Engineering: A*, vol. 712, pp. 738–746, 2018.

[80] O. Craig, “MATERIAL CHARACTERIZATION OF DIRECTED ENERGY DEPOSITION OF H13 TOOL STEEL AND FUNCTIONALLY GRADED H13-COPPER,” 2022.

[81] A. Zardoshtian, M. Ansari, R. Esmaeilzadeh, A. Keshavarzkermani, H. Jahed, and E. Toyserkani, "Laser-directed energy deposition of CuCrZr alloy: from statistical process parameter optimization to microstructural analysis," *The International Journal of Advanced Manufacturing Technology*, vol. 126, no. 9, pp. 4407–4418, 2023.

[82] A. Zardoshtian, R. Esmaeilizadeh, M. Ansari, M. K. Keshavarz, H. Jahed, and E. Toyserkani, "On the Processability and Microstructural Evolution of CuCrZr in Multilayer Laser-Directed Energy Deposition Additive Manufacturing via Statistical and Experimental Methods," 2023. doi: 10.3390/jmmp7040151.

[83] I. G. Akande, O. O. Oluwole, O. S. I. Fayomi, and O. A. Odunlami, "Overview of mechanical, microstructural, oxidation properties and high-temperature applications of superalloys," *Mater Today Proc*, vol. 43, pp. 2222–2231, Jan. 2021, doi: 10.1016/J.MATPR.2020.12.523.

[84] I. Ohnuma *et al.*, "Microstructural evolution of alloy powder for electronic materials with liquid miscibility gap," *J Electron Mater*, vol. 38, no. 1, pp. 2–9, 2009, doi: 10.1007/s11664-008-0537-x.

[85] C. P. Wang, X. J. Liu, I. Ohnuma, R. Kainuma, and K. Ishida, "Formation of immiscible alloy powders with egg-type microstructure," *Science (1979)*, vol. 297, no. 5583, pp. 990–993, 2002.

[86] J. Preis, D. Xu, B. K. Paul, P. A. Eschbach, and S. Pasebani, "Effect of Liquid Miscibility Gap on Defects in Inconel 625–GRCop42 Joints through Analysis of Gradient Composition Microstructure," *Journal of Manufacturing and Materials Processing*, vol. 8, no. 1, 2024, doi: 10.3390/jmmp8010042.

[87] J. Preis *et al.*, "Effect of laser power and deposition sequence on microstructure of GRCop42 - Inconel 625 joints fabricated using laser directed energy deposition," *Mater Des*, vol. 241, no. January, 2024, doi: 10.1016/j.matdes.2024.112944.

[88] A. Pinkerton, "Advances in the modeling of laser direct metal deposition," *J Laser Appl*, vol. 27, p. S15001, Feb. 2015, doi: 10.2351/1.4815992.

[89] X. Song *et al.*, "Advances in additive manufacturing process simulation: Residual stresses and distortion predictions in complex metallic components," *Mater Des*, vol. 193, p. 108779, Aug. 2020, doi: 10.1016/J.MATDES.2020.108779.

[90] W. Li, J. Zhang, X. Zhang, and F. Liou, "Effect of optimizing particle size on directed energy deposition of Functionally Graded Material with blown Pre-Mixed Multi-Powder," *Manuf Lett*, vol. 13, pp. 39–43, Aug. 2017, doi: 10.1016/J.MFGLET.2017.07.001.

[91] A. Munitz, A. Venkert, P. Landau, M. J. Kaufman, and R. Abbaschian, "Microstructure and phase selection in supercooled copper alloys exhibiting metastable liquid miscibility gaps," *J Mater Sci*, vol. 47, no. 23, pp. 7955–7970, 2012, doi: 10.1007/s10853-012-6354-x.

[92] M. Bellet, "Mcwaspxi_3," vol. 6, pp. 513–520, 2006.

[93] M. Bayat, V. K. Nadimpalli, D. B. Pedersen, and J. H. Hattel, "A fundamental investigation of thermo-capillarity in laser powder bed fusion of metals and alloys," *Int J Heat Mass Transf*, vol. 166, p. 120766, Feb. 2021, doi: 10.1016/J.IJHEATMASSTRANSFER.2020.120766.

[94] T. N. Le, Y. L. Lo, and Z. H. Lin, “Numerical simulation and experimental validation of melting and solidification process in selective laser melting of IN718 alloy,” *Addit Manuf*, vol. 36, p. 101519, Dec. 2020, doi: 10.1016/J.ADDMA.2020.101519.

[95] J. Brillo and I. Egry, “Surface tension of nickel, copper, iron and their binary alloys,” *J Mater Sci*, vol. 40, no. 9, pp. 2213–2216, 2005, doi: 10.1007/s10853-005-1935-6.

[96] M. J. Assael *et al.*, “Reference Data for the Density and Viscosity of Liquid Copper and Liquid Tin,” *J Phys Chem Ref Data*, vol. 39, no. 3, p. 33105, Aug. 2010, doi: 10.1063/1.3467496.

[97] H. Kobatake and J. Brillo, “Density and viscosity of ternary Cr–Fe–Ni liquid alloys,” *J Mater Sci*, vol. 48, no. 19, pp. 6818–6824, 2013, doi: 10.1007/s10853-013-7487-2.

[98] M. Sundararaman, P. Mukhopadhyay, and S. Banerjee, “Precipitation of the δ-Ni3Nb phase in two nickel base superalloys,” *Metallurgical Transactions A*, vol. 19, no. 3, pp. 453–465, 1988, doi: 10.1007/BF02649259.

[99] S. Antonov *et al.*, “σ and η Phase formation in advanced polycrystalline Ni-base superalloys,” *Materials Science and Engineering: A*, vol. 687, pp. 232–240, Feb. 2017, doi: 10.1016/J.MSEA.2017.01.064.

[100] Z. Li, J. Chen, S. Sui, C. Zhong, X. Lu, and X. Lin, “The microstructure evolution and tensile properties of Inconel 718 fabricated by high-deposition-rate laser directed energy deposition,” *Addit Manuf*, vol. 31, p. 100941, Jan. 2020, doi: 10.1016/J.ADDMA.2019.100941.

[101] L.-S.-B. Ling *et al.*, “Effects of the γ″-Ni3Nb Phase on Mechanical Properties of Inconel 718 Superalloys with Different Heat Treatments,” 2020. doi: 10.3390/ma13010151.

[102] X. Liu, J. Bi, H. Zhao, R. Li, and T. Zhang, “Rapidly screening out refractory metallic alloys with high glass-forming ability by laser surface remelting,” *Mater Today Adv*, vol. 21, p. 100462, Mar. 2024, doi: 10.1016/J.MTADV.2023.100462.

[103] M. Ansari, A. Martinez-Marchese, M. Khamooshi, A. Keshavarzkermani, R. Esmaeilizadeh, and E. Toyserkani, “Analytical modeling of multi-track powder-fed laser directed energy deposition: On the relationships among process, deposition dimensions, and solidification microstructure in additively manufactured near-β titanium alloy,” *J Mater Process Technol*, vol. 306, p. 117643, 2022, doi: https://doi.org/10.1016/j.jmatprotec.2022.117643.

[104] V. B. Biscuola and M. Martorano, “Mechanical Blocking Mechanism for the Columnar to Equiaxed Transition,” *Metallurgical and Materials Transactions A*, vol. 39, pp. 2885–2895, Dec. 2008, doi: 10.1007/s11661-008-9643-x.

[105] T. DebRoy *et al.*, “Additive manufacturing of metallic components–process, structure and properties,” *Prog Mater Sci*, vol. 92, pp. 112–224, 2018.

[106] H. B. Dong and P. D. Lee, “Simulation of the columnar-to-equiaxed transition in directionally solidified Al–Cu alloys,” *Acta Mater*, vol. 53, no. 3, pp. 659–668, Feb. 2005, doi: 10.1016/J.ACTAMAT.2004.10.019.

[107] P. Karimi *et al.*, “Columnar-to-equiaxed grain transition in powder bed fusion via mimicking casting solidification and promoting in situ recrystallization,” *Addit Manuf*, vol. 46, no. October 2020, p. 102086, 2021, doi: 10.1016/j.addma.2021.102086.

[108] R. Haghayeghi and L. Nastac, “An investigation on grain refinement of Al alloys through liquid shearing,” *Materials Science and Technology Conference and Exhibition 2012, MS and T 2012*, vol. 1, no. October 2012, pp. 73–79, 2012.

[109] W. Kurz, D. Fisher, and M. Rappaz, “Fundamentals of solidification,” 2023.

[110] I. T. Ho, K. C. Chang, D. Tiparti, A. C. Yeh, and S. Tin, “Insight to agglomeration and chemical reactions of CoAl2O4 inoculants in IN718 processed by selective laser melting,” *J Alloys Compd*, vol. 883, p. 160753, 2021, doi: 10.1016/j.jallcom.2021.160753.

[111] J.-Z. Zhao, T. Ahmed, H.-X. Jiang, J. He, and Q. Sun, “Solidification of immiscible alloys: a review,” *Acta Metallurgica Sinica (English Letters)*, vol. 30, pp. 1–28, 2017.

[112] R. N. Grugel and A. H. Well, “Alloy solidification in systems containing a liquid miscibility gap,” *Metallurgical Transactions A*, vol. 12, no. 4, pp. 669–681, 1981, doi: 10.1007/BF02649742.

[113] A. Gamon *et al.*, “Microstructure and hardness comparison of as-built inconel 625 alloy following various additive manufacturing processes,” *Results in Materials*, vol. 12, p. 100239, Dec. 2021, doi: 10.1016/J.RINMA.2021.100239.

[114] “Thermo-Calc Software TCCU5 Cu-based Alloys Database”.

[115] “Thermo-Calc Software TCNI12 Nickel-based Superalloys Database Database.”.

[116] G. K. L. Ng, A. E. W. Jarfors, G. Bi, and H. Y. Zheng, “Porosity formation and gas bubble retention in laser metal deposition,” *Applied Physics A*, vol. 97, no. 3, pp. 641–649, 2009, doi: 10.1007/s00339-009-5266-3.

[117] T. I. El-Wardany, Y. She, V. N. Jagdale, J. K. Garofano, J. J. Liou, and W. R. Schmidt, “Challenges in Three-Dimensional Printing of High-Conductivity Copper,” *J Electron Packag*, vol. 140, no. 2, pp. 1–12, 2018, doi: 10.1115/1.4039974.

[118] M. Liu, A. Kumar, S. Bukkapatnam, and M. Kuttolamadom, “A review of the anomalies in directed energy deposition (DED) processes & potential solutions - Part quality & defects,” *Procedia Manuf*, vol. 53, no. 2020, pp. 507–518, 2021, doi: 10.1016/j.promfg.2021.06.093.

[119] A. Zardoshtian, R. Esmaeilizadeh, M. Ansari, M. K. Keshavarz, H. Jahed, and E. Toyserkani, “On the Processability and Microstructural Evolution of CuCrZr in Multilayer Laser-Directed Energy Deposition Additive Manufacturing via Statistical and Experimental Methods,” 2023. doi: 10.3390/jmmp7040151.

[120] Q. Wei, Y. Xie, Q. Teng, M. Shen, S. Sun, and C. Cai, “Crack Types , Mechanisms , and Suppression Methods during High-Energy Beam Additive Manufacturing of Nickel-based Superalloys : A Review Abstract : Nickel-based superalloys have been widely used in aerospace fields , especially for engine,” *Chinese Journal of Mechanical Engineering: Additive Manufacturing Frontiers*, p. 100055, 2022, doi: 10.1016/j.cjmeam.2022.100055.

[121] T. Li, Z. Wang, S. Hu, Z. Yang, and Y. Wang, “Hot cracking during the fabrication of Inconel 625/stainless steel 308 L functionally graded material by dual-wire arc additive manufacturing,” *J Manuf Process*, vol. 82, pp. 461–473, Oct. 2022, doi: 10.1016/J.JMAPRO.2022.08.018.

[122] F. F. Noecker and J. N. DuPont, “Microstructural development and solidification cracking susceptibility of Cu deposits on steel: Part I,” *J Mater Sci*, vol. 42, no. 2, pp. 495–509, 2007, doi: 10.1007/s10853-006-1258-2.

[123] M. Grandhi, V. Nguyen, Z. Liu, C. O. Romo-De-La-cruz, and X. Song, “Copper-nickel functionally magnetic gradient material fabricated via directed energy deposition,” *J Manuf Process*, vol. 100, pp. 47–54, Aug. 2023, doi: 10.1016/J.JMAPRO.2023.05.014.

[124] T. Wen *et al.*, “From crack-prone to crack-free: Eliminating cracks in additively manufacturing of high-strength Mg2Si-modified Al-Mg-Si alloys,” *J Mater Sci Technol*, vol. 204, pp. 276–291, 2025, doi: 10.1016/j.jmst.2024.04.009.

[125] N. Lu *et al.*, “Hot cracking behavior and mechanism of a third-generation Ni-based single-crystal superalloy during directed energy deposition,” *Addit Manuf*, vol. 34, no. November 2019, p. 101228, 2020, doi: 10.1016/j.addma.2020.101228.

[126] S. Kou, “A criterion for cracking during solidification,” *Acta Mater*, vol. 88, pp. 366–374, 2015, doi: 10.1016/j.actamat.2015.01.034.

[127] Z. Yang, H. Sun, Z. K. Liu, and A. M. Beese, “Design methodology for functionally graded materials: Framework for considering cracking,” *Addit Manuf*, vol. 73, p. 103672, Jul. 2023, doi: 10.1016/J.ADDMA.2023.103672.

[128] N. Wang, S. Mokadem, M. Rappaz, and W. Kurz, “Solidification cracking of superalloy single- and bi-crystals,” *Acta Mater*, vol. 52, no. 11, pp. 3173–3182, 2004, doi: 10.1016/j.actamat.2004.03.047.

[129] N. J. Harrison, I. Todd, and K. Mumtaz, “Reduction of micro-cracking in nickel superalloys processed by Selective Laser Melting: A fundamental alloy design approach,” *Acta Mater*, vol. 94, pp. 59–68, Aug. 2015, doi: 10.1016/J.ACTAMAT.2015.04.035.

[130] M. Rappaz, J. M. Drezet, and M. Gremaud, “A new hot-tearing criterion,” *Metall Mater Trans A Phys Metall Mater Sci*, vol. 30, no. 2, pp. 449–455, 1999, doi: 10.1007/s11661-999-0334-z.

[131] T. F. Babuska, B. A. Krick, D. F. Susan, and A. B. Kustas, “Comparison of powder bed fusion and directed energy deposition for tailoring mechanical properties of traditionally brittle alloys,” *Manuf Lett*, vol. 28, pp. 30–34, 2021.

[132] A. Saboori, G. Piscopo, M. Lai, A. Salmi, and S. Biamino, “An investigation on the effect of deposition pattern on the microstructure, mechanical properties and residual stress of 316L produced by Directed Energy Deposition,” *Materials Science and Engineering: A*, vol. 780, p. 139179, 2020, doi: https://doi.org/10.1016/j.msea.2020.139179.

[133] J. A. Dantzig and M. Rappaz, *Solidification: -Revised & Expanded*. EPFL press, 2016.

[134] M. Rappaz, A. Jacot, and W. J. Boettinger, “Last-stage solidification of alloys: Theoretical model of dendrite-arm and grain coalescence,” *Metallurgical and Materials Transactions A*, vol. 34, no. 3, pp. 467–479, 2003, doi: 10.1007/s11661-003-0083-3.

[135] M. Rappaz, J.-M. Drezet, and M. Gremaud, “A new hot-tearing criterion,” *Metallurgical and Materials Transactions A*, vol. 30, no. 2, pp. 449–455, 1999, doi: 10.1007/s11661-999-0334-z.

[136] I. Serrano-Munoz *et al.*, “On the interplay of microstructure and residual stress in LPBF IN718,” *J Mater Sci*, vol. 56, no. 9, pp. 5845–5867, 2021, doi: 10.1007/s10853-020-05553-y.

[137] P. Kontis *et al.*, “Atomic-scale grain boundary engineering to overcome hot-cracking in additively-manufactured superalloys,” *Acta Mater*, vol. 177, pp. 209–221, Sep. 2019, doi: 10.1016/J.ACTAMAT.2019.07.041.

[138] J. Zhang *et al.*, “A novel crack-free Ti-modified Al-Cu-Mg alloy designed for selective laser melting,” *Addit Manuf*, vol. 38, p. 101829, Feb. 2021, doi: 10.1016/J.ADDMA.2020.101829.

[139] E. Chauvet *et al.*, “Hot cracking mechanism affecting a non-weldable Ni-based superalloy produced by selective electron Beam Melting,” *Acta Mater*, vol. 142, pp. 82–94, 2018, doi: 10.1016/j.actamat.2017.09.047.

[140] M. Opprecht, J. P. Garandet, G. Roux, C. Flament, and M. Soulier, “A solution to the hot cracking problem for aluminium alloys manufactured by laser beam melting,” *Acta Mater*, vol. 197, pp. 40–53, Sep. 2020, doi: 10.1016/J.ACTAMAT.2020.07.015.

[141] L. Isidore Besong and J. and Buhl, “A review of constitutive models used in macroscale finite element analysis of additive manufacturing and post-processing of additively manufactured components,” *Virtual Phys Prototyp*, vol. 19, no. 1, p. e2356079, Dec. 2024, doi: 10.1080/17452759.2024.2356079.

[142] X. Guan and Y. F. Zhao, “Modeling of the laser powder–based directed energy deposition process for additive manufacturing: a review,” *The International Journal of Advanced Manufacturing Technology*, vol. 107, no. 5, pp. 1959–1982, 2020, doi: 10.1007/s00170-020-05027-0.

[143] M. Alizadeh-Sh, S. P. H. Marashi, E. Ranjbarnodeh, and R. Shoja-Razavi, “Laser cladding of Inconel 718 powder on a non-weldable substrate: Clad bead geometry-solidification cracking relationship,” *J Manuf Process*, vol. 56, pp. 54–62, Aug. 2020, doi: 10.1016/J.JMAPRO.2020.04.045.

[144] R. Ghanavati, H. Naffakh-Moosavy, M. Moradi, and M. Eshraghi, “Printability and microstructure of directed energy deposited SS316l-IN718 multi-material: numerical modeling and experimental analysis,” *Sci Rep*, vol. 12, no. 1, pp. 1–16, 2022, doi: 10.1038/s41598-022-21077-8.

[145] F. Kaji *et al.*, “Robotic laser directed energy deposition-based additive manufacturing of tubular components with variable overhang angles: Adaptive trajectory planning and characterization,” *Addit Manuf*, vol. 61, p. 103366, 2023, doi: https://doi.org/10.1016/j.addma.2022.103366.

[146] S. I. Shahabad *et al.*, “Heat source model calibration for thermal analysis of laser powder-bed fusion,” *The International Journal of Advanced Manufacturing Technology*, vol. 106, no. 7, pp. 3367–3379, 2020, doi: 10.1007/s00170-019-04908-3.

[147] I. F. Z. Fanous, M. Y. A. Younan, and A. S. Wifi, “3-D finite element modeling of the welding process using element birth and element movement techniques,” *Journal of Pressure Vessel Technology, Transactions of the ASME*, vol. 125, no. 2, pp. 144–150, 2003, doi: 10.1115/1.1564070.

[148] P. Michaleris, “Modeling metal deposition in heat transfer analyses of additive manufacturing processes,” *Finite Elements in Analysis and Design*, vol. 86, pp. 51–60, 2014, doi: 10.1016/j.finel.2014.04.003.

[149] P. Michaleris, “Modeling metal deposition in heat transfer analyses of additive manufacturing processes,” *Finite Elements in Analysis and Design*, vol. 86, pp. 51–60, Sep. 2014, doi: 10.1016/J.FINEL.2014.04.003.

[150] Z. Wang, E. Denlinger, P. Michaleris, A. D. Stoica, D. Ma, and A. M. Beese, “Residual stress mapping in Inconel 625 fabricated through additive manufacturing: Method for neutron diffraction measurements to validate thermomechanical model predictions,” *Mater Des*, vol. 113, pp. 169–177, 2017, doi: 10.1016/j.matdes.2016.10.003.

[151] T. Mukherjee, J. S. Zuback, W. Zhang, and T. DebRoy, “Residual stresses and distortion in additively manufactured compositionally graded and dissimilar joints,” *Comput Mater Sci*, vol. 143, pp. 325–337, 2018, doi: 10.1016/j.commatsci.2017.11.026.

[152] R. Ghanavati, H. Naffakh-Moosavy, M. Moradi, E. Gadalińska, and A. Saboori, “Residual stresses and distortion in additively-manufactured SS316L-IN718 multi-material by laser-directed energy deposition: A validated numerical-statistical approach,” *J Manuf Process*, vol. 108, no. October, pp. 292–309, 2023, doi: 10.1016/j.jmapro.2023.11.018.

[153] L. Li, X. Zhang, W. Cui, F. Liou, W. Deng, and W. Li, “Temperature and residual stress distribution of FGM parts by DED process: modeling and experimental validation”, doi: 10.1007/s00170-020-05673-4/Published.

[154] W. Pan, Z. Zhai, Y. Liu, B. Liang, Z. Liang, and Y. Zhang, “Research on Microstructure and Cracking Behavior of Al-6.2Zn-2Mg-xSc-xZr Alloy Fabricated by Selective Laser Melting,” *Crystals (Basel)*, vol. 12, no. 10, 2022, doi: 10.3390/cryst12101500.

[155] S. Kou, “Predicting susceptibility to solidification cracking and liquation cracking by calphad,” *Metals (Basel)*, vol. 11, no. 9, 2021, doi: 10.3390/met11091442.

[156] L. Wang, Y. Yao, B. Liu, B. Zhong, and J. Dong, “Effect of cooling rate on the phase transformation and stability of the mushy zone during the solidification of Waspaloy,” *International Journal of Minerals, Metallurgy, and Materials*, vol. 17, no. 4, pp. 464–469, 2010, doi: 10.1007/s12613-010-0342-4.

[157] G. Agarwal *et al.*, “Study of Solidification Cracking in a Transformation-Induced Plasticity-Aided Steel,” *Metallurgical and Materials Transactions A*, vol. 49, no. 4, pp. 1015–1020, 2018, doi: 10.1007/s11661-018-4505-7.

[158] H. Davies, “The structures of rapidly quenched nickel-based superalloy ribbons produced by melt spinning,” *Rapid Solidification Processing, Principles and Technologies.--II*, pp. 153–164, 1980.

[159] K. Darvish, Z. W. Chen, M. A. L. Phan, and T. Pasang, “Selective laser melting of Co-29Cr-6Mo alloy with laser power 180–360 W: Cellular growth, intercellular spacing and the related thermal condition,” *Mater Charact*, vol. 135, no. November 2017, pp. 183–191, 2018, doi: 10.1016/j.matchar.2017.11.042.

[160] S. I. Shahabad *et al.*, “On the effect of thin-wall thickness on melt pool dimensions in laser powder-bed fusion of Hastelloy X: Numerical modeling and experimental validation,” *J Manuf Process*, vol. 75, pp. 435–449, Mar. 2022, doi: 10.1016/J.JMAPRO.2022.01.029.